

PL-TR-96-2185

## STUDY OF THE ORIGINS AND INTERPLANETARY PROPAGATION OF GEOEFFECTIVE DISTURBANCES

John Campbell  
Louise Gentile  
M. Patricia Hagan  
Stephen Kahler  
David Webb

Boston College  
Institute for Scientific Research  
Chestnut Hill, MA 02167

15 April 1996

FINAL REPORT  
13 December 1989 - 15 March 1996

DTIC QUALITY INSPECTED 2

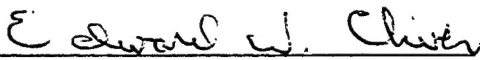
Approved for public release; distribution unlimited.




PHILLIPS LABORATORY  
Directorate of Geophysics  
AIR FORCE MATERIEL COMMAND  
HANSCOM AIR FORCE BASE, MA 01731-3010

19970218 063

"This technical report has been reviewed and is approved for publication"

  
EDWARD W. CLIVER  
Contract Manager

  
MARK D. CONFER, Major  
Acting Branch Chief

  
DAVID A. HARDY  
Division Director

This report has been reviewed by the ESC Public Affairs Office (PA) and is releasable to the National Technical Information Service (NTIS).

Qualified requestors may obtain additional copies from the Defense Technical Information Center (DTIC). All others should apply to the National Technical Information Service (NTIS).

If your address has changed, if you wish to be removed from the mailing list, or if the addressee is no longer employed by your organization, please notify PL/IM, 29 Randolph Road, Hanscom AFB, MA 01731-3010. This will assist us in maintaining a current mailing list.

Do not return copies of this report unless contractual obligations or notices on a specific document require that it be returned.



REPORT DOCUMENTATION PAGE			Form Approved OMB No. 0704-0188	
Public reporting burden for this collection of information is estimated to average 1 hour per response, including the time for reviewing instructions, searching existing data sources, gathering and maintaining the data needed, and completing and reviewing the collection of information. Send comments regarding this burden estimate or any other aspect of this collection of information, including suggestions for reducing this burden, to Washington Headquarters Services, Directorate for Information Operations and Reports, 1215 Jefferson Davis Highway, Suite 1204, Arlington, VA 22202-4302, and to the Office of Management and Budget, Paperwork Reduction Project (0704-0188), Washington, DC 20503.				
1. AGENCY USE ONLY (Leave blank)	2. REPORT DATE 15 Apr 96	3. REPORT TYPE AND DATES COVERED Final (13 Dec 89 - 15 Mar 96)		
4. TITLE AND SUBTITLE STUDY OF THE ORIGINS AND INTERPLANETARY PROPAGATION OF GEOEFFECTIVE DISTURBANCES		5. FUNDING NUMBERS PE 61102F PR 2311 TA G4 WU CA		
6. AUTHOR(S) John Campbell Stephen Kahler Louise Gentile David Webb M. Patricia Hagan		Contract: F19628-90-K-0006		
7. PERFORMING ORGANIZATION NAME(S) AND ADDRESS(ES) Boston College Institute for Scientific Research 140 Commonwealth Avenue Chestnut Hill MA 02167		8. PERFORMING ORGANIZATION REPORT NUMBER		
9. SPONSORING/MONITORING AGENCY NAME(S) AND ADDRESS(ES) Phillips Laboratory 29 Randolph Road Hanscom AFB MA 01731-3010 Contract Manager: Edward Cliver/GPSG		10. SPONSORING/MONITORING AGENCY REPORT NUMBER PL-TR-96-2185		
11. SUPPLEMENTARY NOTES				
12a. DISTRIBUTION/AVAILABILITY STATEMENT  Approved for public release; distribution unlimited.			12b. DISTRIBUTION CODE	
13. ABSTRACT (Maximum 200 words)  This contract has provided a program of research whose overall goal has been a better understanding of the origins and interplanetary propagation of geomagnetic disturbances and also the dynamics of Solar Energetic Particle events (SEPs). The research built on addressing several areas: the solar eruptive phenomena which lead to sporadic geomagnetic storms; analyses of SEPs to identify particle injection profiles at the Sun; the role of Coronal Mass Ejections (CMEs) in the production of SEPs and shocks at 1 AU; view of the heliospheric current sheet and coronal streamer belt; identification of CMEs in the interplanetary medium, and establishment of their heliospheric characteristics; magnetic clouds as interplanetary signatures of CMEs; solar flare/CME relationships; e-folding decay time of intense soft x-ray burts as a forecaster of significant proton events at 1 AU; CMEs as a tracking mechanism for the solar activity cycle; systematic search for candidate disconnection structures in the wake of CMEs; and the development of a Ground Level Event (GLE) database with access by GLEINFO; Shuttle Potential and Return Electron Experiment (SPREE) measurements and analysis.				
14. SUBJECT TERMS Tethered Satellite System (TSS), Combined Release and Radiation Effects Satellite (CRRES), Shuttle Potential and Return Electron Experiment (SPREE), Solar Energetic Particle (SEP) Events, Coronal Mass Ejection (CME), Interplanetary (IP) Shock Waves, Ground Level Event (GLE)			15. NUMBER OF PAGES 178	
			16. PRICE CODE	
17. SECURITY CLASSIFICATION OF REPORT UNCLASSIFIED	18. SECURITY CLASSIFICATION OF THIS PAGE UNCLASSIFIED	19. SECURITY CLASSIFICATION OF ABSTRACT UNCLASSIFIED	20. LIMITATION OF ABSTRACT SAR	

## TABLE OF CONTENTS

<i>Section</i>	<i>Page</i>
1. INTRODUCTION	1
2. PROGRAM RESULTS	2
2.1. Results on Solar and Interplanetary Sources of Geomagnetic Storms	2
2.2. Results on Solar Energetic Particle Events and Interplanetary Shocks	2
2.3. Results on Ground-Level Enhancements	3
2.4. Shuttle Potential and Return Electron Experiment (SPREE)	5
2.5. Results on Combined Release and Radiation Effects Satellite (CRRES)	8
2.6. The WIND Satellite	8
2.7. Results on Modification/In-Scope Change to Contract	8
3. PRESENTATIONS	10
4.. PUBLICATIONS	17
5. REPRINTS OF SELECTED PUBLICATIONS	23

## 1. INTRODUCTION

This contract with Boston College has provided a significant research program utilizing satellite and ground-based observations of solar, interplanetary, and geomagnetic measurements to improve understanding of the origins and interplanetary propagation of geomagnetic disturbances as well as the dynamics of solar energetic particle events.

The research addressed several areas: the solar eruptive phenomena which lead to sporadic geomagnetic storms; analyses of SEPs to identify particle injection profiles at the Sun; the role of Coronal Mass Ejections (CMEs) in the production of SEPs and shocks at 1 AU; view of the heliospheric current sheet and coronal streamer belt; identification of CMEs in the interplanetary medium, and establishment of their heliospheric characteristics; magnetic clouds as interplanetary signatures of CMEs; solar flare/CME relationships; e-folding decay time of intense soft x-ray bursts as a forecaster of significant proton events at 1 AU; CMEs as a tracking mechanism for the solar availability cycle; systematic search for candidate disconnection structures in the wake of CMEs; and the development of a Ground Level Event (GLE) database with access by GLEINFO; Shuttle Potential and Return Electron Experiment (SPREE) measurements and analysis.

Specific research projects included:

- Studies of solar sources of activity leading to geomagnetic storms, principally the origin, early development, and characteristics of CMEs;
- Studies of electron and proton association with solar activity and interplanetary activity;
- Generation of a solar relativistic proton database for the GLEs of Solar Cycle 22, with plot programs and interactive procedures for access;
- SPREE studies: wave-particle interaction, electron beam propagation, ionization effects, MHz modulations in electron flux, ion beam arc distributions;
- Generation of CRRES electric field database, with interactive plot programs for quick surveys;
- Interactive program for access to DMSP data;
- Studies of interaction of the auroral ionosphere and the magnetosphere;
- Provision of mission support for the SPREE science team for the Tethered Satellite System reflight

Section 2 provides a brief summary of the primary research results of this contractual effort. Section 3 lists presentations made at both national and international scientific meetings, workshops, and conferences, Section 4 lists publications generated under the contract; and Section 5 is comprised of reprints of twelve publications selected from the list in Section 4, as being of particularly high interest to the scientific community.

## **2. PROGRAM RESULTS**

### **2.1. Solar and Interplanetary Sources of Geomagnetic Storms**

Studies in this area emphasized the sources at the Sun of activity which leads to geomagnetic storms and the signatures of IP disturbances which link the solar ejections to storms. Because of its importance as a link between solar activity and storms at Earth, CMEs and the IP shock waves driven by them were primary focuses of our research.

Invited review presentations and published papers on the origins, properties and IP aspects of CMEs and related activity: Kahler (1992c, 1992d) and Webb (1992, 1993, 1994, 1995a, 1995b, 1996a, 1996b). In addition Webb was a Team Leader at Workshops on Flares22 (Webb et al., 1994) and on the Solar Radio Telescope.

A major focus of the research was on the origin and early development of CMEs and their association with other forms of activity near the sun. Papers highlighting these aspects included St. Cyr and Webb (1991), Webb (1991), Kahler (1992a), Webb (1992), Webb and Howard (1994) and Webb et al. (1994). A major effort was a study of evidence for the disconnection of magnetic field lines involved in CMEs near the sun (Webb et al., 1994; Webb and Cliver, 1995), and the topology of CME fields in the IP medium (Kahler and Reames, 1991; Lin and Kahler, 1992; and Webb et al., 1993a).

Another focus was on the IP manifestations of geoeffective disturbances, in particular CMEs. Webb collaborated with B. Jackson and others on studies of the IP signatures of CMEs using HELIOS spacecraft in-situ and photometer data to identify and study CMEs between 0.3 and 1 AU from the sun. A comprehensive catalog of the photometer identifications was published by Jackson et al. (1994). Papers on results of the general characteristics of IP CMEs were by Webb and Jackson (1990, 1992, 1993) and Webb et al. (1993a). The masses and kinetic energies of CMEs observed by HELIOS were discussed by Jackson and Webb (1994) and Webb, Howard and Jackson (1996). An important paper by Crooker et al. (1993) suggests that the base of the heliospheric current sheet may encompass multiple helmet streamers and, therefore, may act as a conduit for CMEs. The specific association of HELIOS CMEs aimed at the Earth and geomagnetic storms was discussed by Webb, Jackson and Hick (1996a, 1996b).

Finally, during this period some contract work was performed as a target of opportunity on the conceptual design of an Earth-orbiting instrument to detect and study CMEs approaching the Earth. The experiment, called the Solar Mass Ejection Imager (SMEI), will be used as an operational sensor to forecast the occurrence of geomagnetic storms and related disturbances at Earth. This program is now being supported by external Air Force and NASA funds. Papers relating to SMEI are Jackson et al. (1992, 1994, 1996a, 1996b, 1996c) and Keil et al. (1996).

### **2.2. Solar Energetic Particle Events and Interplanetary Shocks**

Studies in this area involved analyses of SEP data from several spacecraft and from the ground to identify the particle injection profiles at the Sun and to examine different kinds of particle events. The studies fell into two general categories: 1) the determination of the acceleration and injection profiles of electrons and protons and their association with solar activity and IP disturbances, and 2) study of the profiles of solar relativistic events using a standardized data base of ground-level events (GLEs) compiled under the contract.

The central role of CMEs in geoeffective disturbances was also a focus of the studies of SEP events, since long-duration SEP events are strongly associated with IP shocks driven by CMEs.

Results supporting this conclusion are: large, long-duration SEP events are nearly always associated with fast CMEs, they are not well correlated with the amplitude of a flare's impulsive phase, their abundances and ionization states are typical of ambient coronal rather than flare-heated plasma, and isolated erupting filaments can also produce SEPs (reviewed by Kahler, 1992d). Possibly even high energy SEPs ( $>1$  GeV) can be accelerated by CME-driven IP shocks. Kahler (1994) showed that the injection intensities of  $\sim 1$  GeV proton events reach maximum when the associated CME is at  $\sim 10$  Rs, not earlier at the onset of the associated flare or its impulsive phase.

The association of CMEs with long-rise injection profiles of some SEP events were studied by Kahler (1991, 1993a, 1994). They concluded that the long risetime profiles were a combination of two separate SEP injections from two CMEs.

Most of the earlier SEP/CME studies had involved proton SEPs. Kahler et al. (1991, 1994) examined nonrelativistic electron events and concluded that the population of shock-accelerated electrons is comparable to the flare-associated population. Finally, Kahler and Reames (1991) used SEPs as probes of magnetic clouds, considered a subset of IP CMEs. They concluded that the cloud topology was like a bottle, with the field lines still connected back to the sun, rather than like a disconnected plasmoid.

A study of coronal mass ejection (CME) activity and cosmic ray modulation from 1979-1989 was completed. Histograms of CME speeds and of solar latitude distribution were plotted for 3-month intervals from an extensive list of CMEs to determine the spatial distribution of CMEs for various speed ranges in order to gain insight into the role of CMEs in cosmic ray modulation. The daily rate of CMEs was compared with the Deep River galactic cosmic ray counting rate to study two specific periods of change in cosmic ray modulation, early 1982 and late 1988, in relation to the current models of galactic cosmic ray modulation.

Plots of solar flare time and location vs sudden commencement time and location were prepared for a study of  $> 10$  MeV solar energetic proton events associated with eastern limb eruptive flares. Such events can rapidly propagate from a wide range of heliolongitudes. The study used multi-spacecraft data to examine the observational evidence that such rapid propagation of solar energetic protons is dependent on widespread acceleration of coronal mass ejection-driven interplanetary shocks.

A study was completed of the large soft x-ray bursts of Solar Cycle 22 to examine the relationship between these events and the occurrence of major ( $>10$  MeV) proton events. This was an extension of a study done by Cliver and Cane for Solar Cycle 21 which examined the e-folding decay time of the soft x-ray emission and found that major proton events rarely originated in impulsive flares. The continuance of this characteristic during the first half of Solar Cycle 22 reinforces the usefulness of the soft x-ray time scale as a tool for forecasting solar proton events. This study was presented at the Solar-Terrestrial Predictions Workshop in Ottawa, Canada.

### **2.3. Ground-Level Enhancements (GLEs)**

1) A solar relativistic proton database for the Ground-Level Enhancements (GLEs) of Solar Cycle 22 was compiled and has been maintained for the duration of this contract. The objective of this effort was to make the data readily available to the international scientific community for research studies of these unusual events. The remarkable cooperation of the international scientific community contributed greatly to the success of this project. Russian scientists in particular made a concerted effort to contribute their data despite limited resources.



GLEs are marked by the observation of secondary particles generated by high energy protons (>450 MeV) interacting at the top of the atmosphere. Fifteen events were observed during this solar cycle and many of them were highly significant. The 29 September 1989 event, with increases > 350 % above background recorded at several high latitude stations, was the largest GLE observed since February 1956. During the GLEs on 19, 22, and 24 October 1989, measured proton fluxes reached record high levels. The GLEs of 11 and 15 June 1991 occurred during a period of intense solar activity which included a remarkable cosmic ray intensity low on 13 June 1991.

The complete GLE Database for Solar Cycle 22 resides on a VAX 7620 at the Geophysics Directorate of Phillips Laboratory at Hanscom AFB and is available online. Two separate software applications provide access, GLE and GLEINFO. GLE has been available for five years and has been used successfully by scientists from Australia, Canada, Finland, France, Italy, Japan, South Africa, Switzerland, and the US. GLE allows authorized users complete access to the data, including the capability to copy data files and event information. Upon request, data for specific GLEs have been sent to scientists who could not log in to the database directly. GLEINFO allows unrestricted access to the database to examine data and event information. No special password is required. The paper entitled Relativistic Solar Proton Database for the Ground-Level Enhancements During Solar Cycle 22 by L. C. Gentile which describes GLEINFO was published as a Brief Data Report in the Journal of Geophysical Research-Space Physics for December 1993.

The database has a separate subdirectory for each event. In addition to the data files, each event subdirectory has a brief summary file for the event which includes the associated flare information and preliminary estimates of the event onset and maximum observed at each station, the station latitude, longitude, altitude, type of monitor, and effective vertical cutoff rigidity calculated using the 1980 International Geomagnetic Reference Field Model. An additional subdirectory includes event dates, baselines and times selected for hourly and small-time data for each event, and a complete description of the GLE standard format. Having all this information readily available in concise tables has been beneficial in the analysis of these events, particularly for new users of the database.

2) After several years of painstaking work, the GLE Database for 1956-1984 has been compiled and computerized in a standard format suitable for scientific analysis. These data were previously found primarily in the form of printed records, many of which were incomplete or not fully documented. We have computerized these data in a standard format as accurately as possible with the information available to us. Individual station sets have been checked for consistency and those with unresolved discrepancies were documented both in the data file and in the GLE catalog. Principal investigators have been given the latest catalog lists for their stations and have been asked for their help in resolving the discrepancies found in the data and in completing data sets. This has enabled us to provide a more accurate and consistent database for scientific study of the processes involved in solar proton acceleration and propagation. Scientists from Oulu, Finland, and Potchefstroom, South Africa, made exceptional efforts to provide complete and verified data for all events for which their stations were operating.

3) Work was also completed on a comprehensive check of both GLE databases with the full GLE catalog for 1956-1992. Each catalog entry was checked and verified with the accompanying data file, and the catalog is now an up-to-date record of the computerized database. Catalog entries were checked for consistency station by station and event by event. A complete station listing was made and filed in a notebook for reference. All catalog files were moved to an updated computer system which could accommodate the extensive complete catalog files.

4) A significant number of plot programs and interactive procedures were written for use with the GLE databases. These procedures allow the users to select parameters from a menu of plotting options to plot six different types of rigidity and energy spectra or to create plots of either single or multiple data sets in both hourly data and small-time formats for data analysis. A number of FORTRAN programs and DCL procedures were also written to facilitate updating the GLE data files and catalog. Many are interactive, allowing the user to select the type of change to be made, to enter the necessary information, and then to add the modified file to the database.

5) Data were also gathered and analyzed for significant Forbush decreases during this solar cycle. These decreases occurred during periods of intense cosmic ray activity. The additional data were reformatted in the GLE standard format, printed, and plotted for further study of these unusual periods of cosmic ray activity.

6) An extensive series of plots were prepared for a study of coronal mass ejection (CME) activity and cosmic ray modulation from 1979-1989. Histograms of CME speeds and of solar latitude distribution were plotted for 3-month intervals from an extensive list of CMEs to determine the spatial distribution of CMEs for various speed ranges in order to gain insight into the role of CMEs in cosmic ray modulation. The daily rate of CMEs was compared with the Deep River galactic cosmic ray counting rate to study two specific periods of change in cosmic ray modulation, early 1982 and late 1988, in relation to the current models of galactic cosmic ray modulation.

7) Plots of solar flare time and location vs sudden commencement time and location were prepared for a study of  $> 10$  MeV solar energetic proton events associated with eastern limb eruptive flares. Such events can rapidly propagate from a wide range of heliolongitudes. The study used multi-spacecraft data to examine the observational evidence that such rapid propagation of solar energetic protons is dependent on widespread acceleration of coronal mass ejection-driven interplanetary shocks.

## **2.4 Shuttle Potential and Return Electron Experiment (SPREE)**

The Shuttle Potential and Return Electron Experiment (SPREE) flew on the first Tethered Satellite System mission (TSS 1) from 31 July to 8 August 1992 and again on the TSS 1 reflight (TSS 1R) from 22 February to 9 March 1996. SPREE, which measured fluxes of electrons and ions with energies between 10 eV and 10 keV, was designed to measure the shuttle potential during tether operations and to determine the wave-particle interactions in the plasma environment surrounding the shuttle. A number of studies of the SPREE data from TSS 1 were undertaken and completed. Electron beam firings from the shuttle simulated conditions observed along auroral field lines during magnetic storms. Data obtained from these experiments contributed to a better understanding of beam propagation and interactions with the ionosphere. SPREE frequently detected increased ionization during thruster firings, operation of the flash evaporator system, and water dumps. Studies of these SPREE results have provided a more detailed assessment of the effects the shuttle systems have on the shuttle environment.

1) The study of electron beam propagation following Fast Pulsed Electron Generator (FPEG) emissions perpendicular to the Earth's magnetic field during TSS 1 was published in the November 1995 Journal of Geophysical Research. Electrons fired from FPEG nearly perpendicular to the Earth's magnetic field were observed by SPREE after completing  $\sim 1$  gyrocycle. The decrease in the beam intensity between emission and detection ( $100 \text{ mA cm}^{-2}$  to  $18 \text{ nA cm}^{-2}$ ) indicates that the electrons cannot reach SPREE along unperturbed trajectories. The creation of a virtual cathode near FPEG was suggested as a reasonable explanation for the SPREE observations.

A FORTRAN program was written to calculate the X and Z coordinates of the FPEG beam spread for various colatitude angles to determine particle access to the SPREE detectors. Two events in particular during which FPEG fired a 1 keV electron beam almost perpendicular to the Earth's magnetic field and SPREE detected beam electrons after almost 1 full gyrocycle were studied. An interactive version of the program was created to provide more flexibility in selecting time intervals for future studies.

2) A FORTRAN program was written to calculate and plot the interplanetary magnetic field magnitude and direction for the duration of the TSS 1 mission. In addition, the program provides an option to plot the electron pitch angle, gyroradius, and gyrofrequency to study particle access to the SPREE detectors during firing of FPEG.

3) The study of increased ionization effects observed during thruster firings by SPREE during TSS 1 was published in the October 1995 Journal of Geophysical Research. Significant ion flux enhancements were observed when the shuttle was flying approximately perpendicular to the Earth's magnetic field and SPREE was looking in the ram direction.

In one case, the shuttle was flying bay-to-earth with the left wing forward and the rear right thrusters fired. Both SPREE electrostatic analyzers (ESAs) detected ions in the 10 eV to 60 eV range when looking toward the left wing. Ions were also detected by the QINMS (Quadrupole Ion-Neutral Mass Spectrometer) which was mounted in the aft section of the shuttle payload bay. The mass spectrometer indicated the increased presence of ions in the 12-44 amu range. The model devised for the collisionless trajectories of pickup ions that could be detected by SPREE confirms the ion energy distribution observed by SPREE and indicates that significant scattering must be taking place both immediately after thruster emission and later after particles become ionized and the new pickup ions cross the path of the oncoming particle stream before reaching the SPREE detectors.

In another case, the shuttle was flying bay-to-ram and the forward thrusters fired. Ions were promptly detected by SPREE which was then looking perpendicular to the magnetic field. A third type of event occurred when the shuttle was flying bay-to-ram in a vertical attitude. When thrusters on the right side fired along the magnetic field lines, SPREE did not record the firing. When the rear thrusters fired perpendicular to the magnetic field lines, SPREE detected increased ion fluxes. In all cases, SPREE detected ions in the 10-100 eV range, suggesting that the majority of the ions SPREE detected were pickup ions.

4) The study of MHz modulations in the electron flux observed during FPEG dc firings during TSS 1 was published in the November 1995 Journal of Geophysical Research. Modulations in the 0-10 MHz electron flux were recorded by SPACE (Space Particle Correlator Experiment) an integral component of the SPREE data processor unit. The study focused on 2-4 MHz modulations observed when FPEG was firing in dc mode at pitch angles close to 90 degrees.

Several FORTRAN programs were written to support this study. Programs were written to plot the electron differential number flux, distribution function, Fast Fourier Transforms, and Auto Correlation Functions calculated by the SPREE SIDAT software. Additional programs plot differential number flux spectra from 3-5 different zones of the SPREE ESAs for comparison of the beam observations at the varying look angles of SPREE.

5) The study of ion beam arc distributions observed by SPREE during TSS 1 was accepted for publication in the Journal of Geophysical Research. This paper is a comprehensive study of increased ion fluxes recorded by SPREE when the ESAs were looking in the ram direction and approximately perpendicular to the Earth's magnetic field. Operation of the flash evaporator system, water dumps, and thruster firings enhanced the ion distributions. The collisionless trajectory model developed for the thruster effects study, was generalized and applied to the



trajectories of these beam arc ions. This study characterizes the observed ion beam arc distributions for these shuttle operating conditions and models their effects in the vicinity of the shuttle.

6) The paper describing thruster firing effects on the shuttle potential during the deployed phase of the TSS 1 mission when the shuttle was negatively charged was accepted for publication in the Journal of Geophysical Research. This study identifies 13 events when the shuttle was flying with the engine bells in the ram direction, the tether was electrically connected to the shuttle by a low-impedance shunt, and the shuttle charged negatively. We examined the effects of thruster firings on the shuttle potential. Our observations indicate that the thruster firings either did not affect the tether circuit or caused the tether current to diminish and the shuttle to become more negatively charged. The aft vernier thrusters which fire toward the wings caused the most significant effects.

7) Work is continuing on an extensive study of low frequency modulation effects in wave-particle interactions observed during DC firings of the Fast Pulsed Electron Generator (FPEG) during the TSS 1 mission. The study describes low frequency modulations in the electron flux observed by SPREE and SPACE (Space Particle Correlator Experiment) over a wide range of pitch angles when FPEG was firing in DC mode. A comprehensive table was prepared for this study, including shuttle location, attitude, and velocity, magnetic field measurements, FPEG pitch angle, and the frequency and energy range of the modulations measured during each event. Approximately two thirds of the events occur at night. SPREE often observes the beam after it has lost its parallel kinetic energy. There is a marked transition from thermal to power law distributions as the SPREE pitch angle decreases from 90 degrees.

#### *SPREE Briefings for TSS 1R*

8) Briefings on the progress of the SPREE data analysis were prepared for the Tethered Satellite System Reflight Investigator Working Group Meetings held in Turin, Italy in October 1994, at NASA Marshall Space Flight Center in Huntsville, Alabama, in February 1995, and in Rome, Italy, in May 1995. Our studies of electron beam propagation, ion beam arc distributions, thruster firing effects, and negative shuttle charging were discussed. Results of these studies provided extremely valuable insights as scientists designed and modified experiments planned for the reflight.

9) A brief report on SPREE including a description of the instrumentation, the scientific objectives, and the scientific results from the TSS 1 data analysis was written and submitted for publication in the third edition of the Tethers in Space Handbook. SPREE Support in Preparation for TSS 1R Shuttle Mission

10) Support was provided for several pre-flight simulations, hardware tests, and Investigator Working Group Meetings in preparation for TSS 1R. Projects included preparing experiment documentation for the reflight, writing and revising the SPREE scientific functional objectives and checking operational and malfunction procedures for consistency. A functional objective summary list which included all the mission science experiment functional objectives and indicated those for which SPREE operations were required was prepared as a quick reference list for the mission support team.

11) As a direct result of the thruster firing study, several experiments were designed to observe the duration of the increased ionization effects following controlled thruster firings at specified attitudes. Experiments were planned with and without FPEG electron beam emissions.

## **2.5. Combined Release and Radiation Effects Satellite (CRRES)**

1) Support was provided for the project to create a database of the CRRES electric field data. CRRES (Combined Release and Radiation Effects Satellite) flew for more than 1 year in 1990-1991, and during its more than 1000 orbits recorded a substantial amount of data. Printed plots filed in notebooks are now available for quick surveys of the data and for selecting time intervals for further study. Programs and procedures written to plot these data for selected orbits have been documented and maintained to ensure the data are accessible to scientists. Electric field and magnetic field data for specific orbits have been provided to Phillips Lab and NASA GSFC scientists for research studies.

2) A FORTRAN program was written to extract specific parameters from the DMSP F08 data which are stored on optical disk. The software combines the three DMSP files per month into one file and extracts the polar cap potential data. An additional interactive program was written to enable the user to select a day at a time for detailed study. These data are being used for a study of the LEPA data from the CRRES mission in 1990-1991.

## **2.6. WIND**

Procedures to maintain the WIND satellite real-time data link and to obtain ascii data files and plots for selected days from the database at NASA Goddard Space Flight Center have been documented and implemented as needed.

## **2.7. Modification/In-Scope Change to Contract**

### *2.7.1 Study of Importance of Magnetic Field Complexity for CME Source Regions*

As discussed above we have learned much about the origins and development of CMEs. However, recent work indicates that the underlying, large-scale solar magnetic fields appear to be more complex than previously thought. During the extended period of performance we studied Yohkoh spacecraft images of eruptive events as tracers of the CME fields visible against the solar disk and compared them with global surface magnetic field patterns. The results suggesting that multipolar magnetic systems are a common configuration of the source fields of many CMEs are discussed by Webb et al. (1996).

Also during this period Webb presented a review paper on CMEs (Webb, 1996b) and a contributed paper (Webb, Jackson and Hick, 1996b) at a predictions Workshop in Japan. Both papers will be published in the Proceedings of the Workshop.

### *2.7.2. Study of the Characteristics of Disturbed Magnetospheric Plasma*

Studying the predictability of the strength and direction of the interplanetary magnetic field during geomagnetic disturbances requires data generally available only when such disturbances naturally occur. Because of the effects of such storms on orbiting spacecraft and communications capabilities, NASA conducts active shuttle-based controlled experiments and invited Air Force participation in the Tethered Satellite System Reflight. This provided a free and worthwhile opportunity for the Air Force. Through the use of electron beam firings from the shuttle, conditions along auroral field lines during magnetic storms were simulated.

This was a unique opportunity for our scientists under this contract, who have the expertise to take advantage of the data obtained from these experiments to better understand the interaction of the auroral ionosphere and the magnetosphere. Mission support was provided for the Shuttle

Potential and Return Electron Experiment (SPREE) science team for the Tethered Satellite System reflight (TSS 1R) which was launched on Columbia 22 February 1996. Primary objective of the mission was to characterize the electrodynamic effects of deploying and retrieving an electrically conducting satellite connected to the shuttle by a conducting tether. SPREE was designed to measure the shuttle potential during tether operations and to determine the wave-particle interactions in the plasma environment surrounding the shuttle.

SPREE was activated on the second day of the mission and performed exceptionally well. Preliminary data from the deployed phase of the mission are quite extraordinary, and it is most unfortunate that the tether broke at 19.7 km, just before reaching the full 20.7 km planned for the deployment. However, in cooperation with other experiment support teams, we rescheduled electron beam experiments to take advantage of the additional time for electron beam emission and propagation studies. SPREE recorded an extensive set of electron beam experiments conducted throughout full orbits of the mission.

In one particular experiment, the shuttle was aligned with the long axis along the Earth's magnetic field and the fast pulsed electron generator (FPEG) fired at a pitch angle of  $\sim 90$  degrees to the magnetic field. The sequence included 28 beam firings while the shuttle maintained this attitude. In this configuration SPREE was able to view the interior structure of the beam and specify the wave-particle interactions (WPI) within a beam with a gyroradius of a few meters. This experiment simulated very narrow auroral arc beams identified in optical and sounding rocket experiments. Studies of the data from this and other beam firing experiments will contribute to our research involving disturbed magnetospheric conditions.

Also included in the TSS 1R experiments were several that were developed as a direct result of the thruster firing study. These were designed to observe the duration of increased ionization effects following controlled thruster firings at specified attitudes. Experiments were conducted for two different shuttle attitudes in relation to the Earth's magnetic field with and without FPEG electron beam emissions. A preliminary survey of the real-time data from the mission has been completed. Plots of 15-minute electron and ion differential flux spectrograms were prepared for initial studies of this extensive and valuable new data set.

### 3. PRESENTATIONS

15 December 1989 - 15 March 1996

1. Hildner, E. and S. Kahler, Coronal Structure and Development Following CMEs, Seventh Quadrennial Symposium on Solar-Terrestrial Physics (in conjunction with XXVIII COSPAR), The Hague, The Netherlands, 23 June - 5 July 1990. Presented by E. Hildner. (Invited)
2. Webb, D.F., The Coronal Mass Ejection as a Geoeffective Agent, Seventh Quadrennial Symposium on Solar-Terrestrial Physics (in conjunction with XXVIII COSPAR Meeting), The Hague, The Netherlands, 23 June - 5 July 1990. Presented by D.F. Webb.
3. Webb, D.F., The Solar Cycle Variation of CMEs and Related Activity, Symposium 9 on Space Observations of the Solar Corona and the Origin of the Solar Wind (in conjunction with XXVIII COSPAR Meeting), The Hague, The Netherlands, 23 June - 5 July 1990. Presented by D.F. Webb.
4. Gentile, L.C., M.A. Shea, and D.F. Smart, Compiling a Computerized Database of Solar Relativistic Proton Data for the Ground-Level Enhancements of Solar Cycle 22, 1990 Fall Meeting of the American Geophysical Union, San Francisco, California, 3-7 December 1990. Abstract published in EOS, Transactions, AGU, 71, 43, p. 1514, October 23, 1990. Presented by L.C. Gentile.
5. Webb, D.F., S.W. Kahler, K.L. Harvey, and E.W. Cliver, The Scale Sizes of CMEs and Associated Surface Activity, 21st Solar Physics Division Meeting of the American Astronomical Society, Huntsville, Alabama, 9-11 April 1991. Presented by D. Webb.
6. Smart, D.F., M.A. Shea, Margaret D. Wilson, and L.C. Gentile, Preliminary Analysis of the 29 September 1989 High Energy Solar Proton Event Using the World-Wide Cosmic Ray Network, 1991 Spring Meeting of the American Geophysical Union, Baltimore, Maryland, 28-31 May 1991. Abstract published in EOS, Transactions, AGU, 72, 17, p. 222, April 23, 1991. Presented by D.F. Smart.
7. Kahler, S., A Comparison of the SMS/GOES and Solrad X-Ray Detectors for Quiet-Sun Studies, SOLERS 22, Boulder, Colorado, 3-7 June 1991. Presented by S. Kahler.
8. Webb, D.F., S.F. Martin, D. Moses, and J.W. Harvey, The Correspondence Between X-Ray Bright Points and Evolving Magnetic Features in the Quiet Sun, 21st General Assembly of the International Astronomical Union, Session on High Resolution Observations and Theory of Solar Magnetism and Convection, Buenos Aires, Argentina, 29 July 1991. Presented by D.F. Webb.
9. Jackson, B., R. Altrock, R. Gold, and D. Webb, The Solar Mass Ejection Imager, International Astronomical Union Colloquium 133, Iguazu Falls, Argentina, 2-6 August 1991. Presented by B. Jackson.
10. Webb, D.F., Solar Sources of Coronal Mass Ejections, International Astronomical Union Colloquium 133, Iguazu Falls, Argentina, 2-6 August 1991. Presented by D.F. Webb. (Invited)
11. Gentile, L.C., Accessing the Computerized Database of Solar Relativistic Proton Data for the Ground-Level Enhancements of Solar Cycle 22, 22nd International Cosmic Ray Conference, Dublin, Ireland, 11-23 August 1991. Presented by L.C. Gentile.

12. Kahler, S.W., M.A. Shea, D.F. Smart, and E.W. Cliver, Ground-Level Events from Impulsive Solar Flares, 22nd International Cosmic Ray Conference, Dublin, Ireland, 11-23 August 1991. Presented by S.W. Kahler.
13. Kahler, S.W., E.I. Daibog, V.G. Kurt, and V.G. Stolpovsky, A Comparison of Nonrelativistic Electron Escape Factors Between Solar Flares with and without Coronal Mass Ejections, 22nd International Cosmic Ray Conference, Dublin, Ireland, 11-23 August 1991. Presented by S.W. Kahler.
14. Kahler, S.W., The Double Coronal Mass Ejection Event and Long Rise Time of the Energetic Particle Event of 12 August 1989, 22nd International Cosmic Ray Conference, Dublin, Ireland, 11-23 August 1991. Presented by S.W. Kahler.
15. Kananen, H., P.J. Tanskanen, L.C. Gentile, M.A. Shea, and D.F. Smart, A Quarter of a Century of Relativistic Solar Cosmic Ray Events Recorded by the Oulu Neutron Monitor, 22nd International Cosmic Ray Conference, Dublin, Ireland, 11-23 August 1991. Presented by M.A. Shea.
16. Shea, M.A., D.F. Smart, and L.C. Gentile, The Benefits of Assembling a Database of Relativistic Solar Proton Events, 20th General Assembly of the IUGG, Vienna, Austria, 11-23 August 1991. Poster Presentation.
17. Smart, D.F., M.A. Shea, Margaret D. Wilson, and L.C. Gentile, Solar Cosmic Rays on 29 September 1989; An Analysis Using the World-Wide Network of Cosmic Ray Stations, 22nd International Cosmic Ray Conference, Dublin, Ireland, 11-23 August 1991. Presented by D.F. Smart.
18. Webb, D.F., S.W. Kahler, K.L. Harvey, and E.W. Cliver, The Scale Sizes of CMEs and Associated Activity, Solar Wind Seven, Goslar, Germany, 16-20 September 1991. Presented by D.F. Webb.
19. Webb, D.F., N.U. Crooker, and S. Shodhan, Structure and Dynamics of the Coronal Streamer Belt, Solar Wind Seven, Goslar, Germany, 16-20 September 1991. Presented by D.F. Webb.
20. Webb, D.F., and B.V. Jackson, Characteristics of CMEs Observed in the Heliosphere Using Helios Photometer Data, Solar Wind Seven, Goslar, Germany, 16-20 September 1991. Presented by D.F. Webb.
21. Gentile, L. C., J.M. Campbell, N.A. Vickers, S.M. Jacavano, M.A. Shea, and D.F. Smart, Compilation and Distribution of Relativistic Solar Proton Data, First SOLTIP Symposium, Liblice, Czechoslovakia, 30 September - 5 October 1991. Presented by M.A. Shea.
22. Kahler, S., Solar Coronal Structures Following Mass Ejections, First SOLTIP Symposium, Liblice, Czechoslovakia, 30 September - 5 October 1991. Presented by S. Kahler.
23. Gentile, L.C., M.A. Shea, and D.F. Smart, Preliminary Assessment of the Ground-Level Enhancements in June 1991, 1991 Fall Meeting of the American Geophysical Union, San Francisco, California, 9-13 December 1991. Abstract published in EOS, Transactions, AGU, 72, 44, p. 383, October 29, 1991. Presented by L.C. Gentile.
24. Kahler, S.W., Solar Energetic Particle Events with Long Rise Times and Pairs of Associated Coronal Mass Ejections, American Geophysical Union Meeting, Montreal, Canada, 12-16 May 1992. Presented by S.W. Kahler.

25. Cliver, E., S. Kahler, and J. Campbell, An Investigation of the Relationship Between the Microwave Spectra of Solar Flares and the Delay to Maximum of Associated Proton Events at 1 AU, Solar-Terrestrial Predictions Workshop IV, Ottawa, Canada, 18-22 May 1992. Presented by L.C. Gentile.
26. Gentile, L.C., J.M. Campbell, E.W. Cliver, H.V. Cane, X-Class Soft X-Ray Bursts and Major Proton Events During Solar Cycle 22 (1987-1991), Solar-Terrestrial Predictions Workshop IV, Ottawa, Canada, 18-22 May 1992. Presented by L.C. Gentile.
27. Webb, D.F., The Heliospheric Manifestations and Geoeffectiveness of Solar Mass Ejections, Solar-Terrestrial Predictions Workshop IV, Ottawa, Canada, 18-22 May 1992. Presented by D.F. Webb. (Invited)
28. Webb, D.F., and B.V. Jackson, Characteristics of CMEs Observed in the Heliosphere Using Helios Photometer and In-Situ Data, Solar-Terrestrial Predictions Workshop IV, Ottawa, Canada, 18-22 May 1992. Presented by D.F. Webb.
29. Kahler, S.W., and G.D. Fleishman, Microwave Transition Radiation in Solar Flares and Astrophysics, American Astronomical Society Meeting, Columbus, Ohio, 7-11 June 1992. Presented by S.W. Kahler.
30. Webb, D.F., B.V. Jackson, and D.V. Reames, Study of CMEs Observed in the Heliosphere Using Helios Photometer, Magnetic Field and Plasma Data, 180th Meeting of the American Astronomical Society, Columbus, Ohio, 7-11 June 1992. Presented by D.F. Webb.
31. Webb, D.F., Introductory and Summary Plenary invited talks given as co-leader of Team 5 on Material Ejection, Flares 22 Workshop, Ottawa, Canada, 13-16 July 1992. Presented by D.F. Webb.
32. Webb, D.F., D.V. Reames, and B.V. Jackson, Study of the Structure of CMEs Observed in the Heliosphere Using Helios Photometer and Bidirectionally Streaming Ion Data, 1992 STEP Symposium, Program Guide and Abstracts, 31 (abstract), JHU Applied Physics Lab., Laurel, MD, 24-28 August 1992. Presented by D.F. Webb.
33. Webb, D.F., N.U. Crooker, G.L. Siscoe, S. Shodhan, and J.T. Gosling, Evolution of the Coronal Streamer Belt on the Inner Heliosphere, First SOHO Workshop, Annapolis, MD, 25-28 August 1992. Presented by D.F. Webb.
34. Webb, D.F., D.V. Reames, and B.V. Jackson, Study of the Structure of CMEs Observed in the Heliosphere Using Helios Photometer and Bidirectionally Streaming Ion Data, First SOHO Workshop, Annapolis, MD, 25-28 August 1992. Presented by D.F. Webb.
35. Jackson, B., P. Hick, and D. Webb, Co-Rotating Structures of the Inner Heliosphere From Helios Photometer and In-Situ Data, Symposium on Fundamental Problems in Solar Activity, World Space Congress/29th COSPAR meeting, Washington, D.C., 28 August - 5 September 1992. Presented by B.V. Jackson.
36. Webb, D., B. Jackson, P. Hick, R. Schwenn, V. Bothmer, and D. Reames, Comparison of CMES, Magnetic Clouds, and Bidirectionally Streaming Proton Events in the Heliosphere Using Helios Data, Symposium on Fundamental Problems in Solar Activity, World Space Congress/29th Plenary Meeting of COSPAR, Washington, D.C., 28 August - 5 September 1992. Presented by B.V. Jackson.



37. Jackson, B.V., P.L. Hick, and D.F. Webb, Co-Rotating Structures of the Inner Heliosphere From Helios Photometer and In-Situ Data, Fall AGU Meeting, San Francisco, CA, 7-11 December 1992. Presented by B.V. Jackson.
38. Webb, D.F., B.V. Jackson, P. Hick, R. Schwenn, V. Bothmer, and D.V. Reames, CMEs in the Heliosphere - Helios Photometer and In-Situ Data, Fall AGU Meeting, San Francisco, CA, 7-11 December 1992. Presented by D.F. Webb.
39. Smart, D. F., M.A. Shea, and L.C. Gentile, The Relativistic Solar Proton Ground-Level Enhancements Associated with the Solar Neutron Events of 11 June and 15 June 1991, AIP Workshop on High Energy Physics of Solar Flares, Waterville Valley, NH, 2-5 March 1993. Presented by D.F. Smart.
40. Shodhan-Shah, S., N.U. Crooker, W.J. Hughes, D.F. Webb, B.V. Jackson, and G.L. Siscoe, Streamer Belt Variability and Heliospheric Current Sheet Stability Near Solar Maximum, Spring AGU meeting, Baltimore, MD, 24-28 May 1993. Presented by S. Shodhan-Shah.
41. Webb, D.F., Introductory and Summary Plenary Invited Talks, Team 5, Flares 22 Workshop, Ottawa, Canada, 24-28 May 1993. Presented by D.F. Webb.
42. Cook, J.W., D. Moses, G.E. Brueckner, K.P. Dere, D.F. Bartoe, D.F. Webb, J.M. Davis, J.W. Harvey, F. Recely, S.F. Martin, and H. Zirin, Transition Region Explosive Events in an X-ray Dark Lane Region of the Quiet Sun, 24th Solar Physics Div. meeting, Stanford, CA, 13-16 July 1993. Presented by J.W. Cook.
43. Hick, P.L., B.V. Jackson, and D.F. Webb, Observations of Solar Wind 'Halo' Electrons, 24th Solar Physics meeting, Stanford, CA, 13-16 July 1993. Presented by P.L. Hick.
44. Jackson, B.V., A. Buffington, S.W. Kahler, D.F. Webb, R. Altrock, and R. Gold, The Solar Mass Ejection Imager, 24th Solar Physics Div. meeting, Stanford, CA, 13-16 July 1993. Presented by B.V. Jackson.
45. Webb, D.F., P.S. McIntosh, and S.W. Kahler, The Locations of CMEs Compared With Coronal Streamers and the Large-Scale Magnetic Field, 24th Solar Physics Div. meeting, Stanford, CA, 13-16 July 1993. Presented by D.F. Webb.
46. Gentile, L.C., Ground-Level Enhancement Database for Solar Cycle 22: An Update, 23rd International Cosmic Ray Conference, Calgary, Canada, 19-30 July 1993. Presented by L.C. Gentile.
47. Gentile, L.C., J.M. Campbell, N.A. Vickers, S.M. Jacavano, M.A. Shea, and D.F. Smart, A Relativistic Solar Proton Database for the Ground-Level Enhancements of 1956-1984, 23rd International Cosmic Ray Conference, Calgary, Canada, 19-30 July 1993. Presented by L.C. Gentile.
48. Kudela, K., M.A. Shea, D.F. Smart, and L.C. Gentile, Relativistic Solar Particle Events Recorded by the Lomnický štít Neutron Monitor, 23rd International Cosmic Ray Conference, Calgary, Canada, 19-30 July 1993. Presented by K. Kudela.
49. Smart, D.F., M.A. Shea, and L.C. Gentile, The Relativistic Solar Proton Event of 11 June 1991, 23rd International Cosmic Ray Conference, Calgary, Canada, 19-30 July 1993. Presented by D.F. Smart.

50. Smart, D.F., M.A. Shea, and L.C. Gentile, The Relativistic Solar Proton Event of 15 June 1991, 23rd International Cosmic Ray Conference, Calgary, Canada, 19-30 July 1993. Presented by D.F. Smart.
51. Gentile, L. C., J. M. Campbell, M. A. Shea, and D. F. Smart, A Database for Relativistic Solar Proton Events, IAGA 7th Scientific Assembly, Buenos Aires, Argentina, 8-20 August 1993. Presented by M. A. Shea.
52. Smart, D. F., M. A. Shea, L. C. Gentile, J. M. Campbell, H. Coffey, Difficulties with the Comprehensive Flare Index, IAGA 7th Scientific Assembly, Buenos Aires, Argentina, 8-20 August 1993. Presented by D. F. Smart.
53. Webb, D.F., B.V. Jackson, and P.L. Hick, Geomagnetic Storms and Heliospheric CMEs as Viewed from Helios, Fall Meeting of the American Geophysical Union, San Francisco, California, 6-10 December 1993. Presented by D.F. Webb.
54. Webb, D.F., Kahler, S.W., Klimchuk, J., and McIntosh, P., The Source Regions of CMEs and the Large-Scale Magnetic Field Using Yohkoh SXT Data. EOS, 75, 262 (abstract), Spring AGU Meeting, Baltimore, MD, 23-27 May 1994. Presented by D.F. Webb.
55. Kahler, S.W., Webb, D.F., Klimchuk, J., and McIntosh, P., The Source Regions of CMEs and the Large-Scale Magnetic Field Using Yohkoh SXT Data, Book of Abstracts of the Eighth International Symposium on Solar Terrestrial Physics, 7 (abstract), Symposium on Solar Terrestrial Physics, Sendai, Japan, 5-10 June 1994. Presented by S.W. Kahler.
56. Webb, D.F., Solar and Geomagnetic Disturbances During the Declining Phase of Recent Solar Cycles, Book of Abstracts of the 30th COSPAR Scientific Assembly, 151 (abstract), COSPAR Assembly, Hamburg, Germany, 11-21 July 1994. Presented by D.F. Webb. (Invited)
57. Webb, D.F., Kahler, S.W., Klimchuk, J., and McIntosh, P., The Source Regions of CMEs and the Large-Scale Magnetic Field Using Yohkoh SXT Data, Book of Abstracts of the 30th COSPAR Scientific Assembly, 254 (abstract), COSPAR Assembly, Hamburg, Germany, 11-21 July 1994. Presented by D.F. Webb.
58. Jackson, B.V. and Webb, D.F., CME Masses Measured in the Inner Heliosphere From the Helios Spacecraft Photometers, Third SOHO Workshop, Estes Park, CO, 26-29 September 1994. Presented by B.V. Jackson.
59. Webb, D.F. and Jackson, B.V., Comparison of CME Masses Measured Near the Sun and in the Inner Heliosphere, Third SOHO Workshop, Estes Park, CO, 26-29 September 1994. Presented by D.F. Webb.
60. Gentile, L.C., W.J. Burke, J.S. Machuzak, D.A. Hardy, and D.E. Hunton, Thruster Pickup Ions Detected during TSS 1, 1994 Fall Meeting of the American Geophysical Union, San Francisco, California, 5-9 December 1994. Abstract published in EOS, Transactions, AGU, 75, 44, p. 499, 1 November 1994. Presented by L.C. Gentile.
61. Gough, M. P., D. A. Hardy, M. R. Oberhardt, W. J. Burke, L. C. Gentile, B. McNeil, K. Bounar, D. C. Thompson, and W. J. Raitt, Particle Modulations at kHz and MHz Measured by the Shuttle Potential and Return Electron Experiment (SPREE) During STS-46, 1994 Fall Meeting of the American Geophysical Union, San Francisco, California, 5-9 December 1994. Abstract published in EOS, Transactions, AGU, 75, 44, p. 499, 1 November 1994. Presented by M. P. Gough.



62. Gentile, L. C., W. J. Burke, J. S. Machuzak, D. A. Hardy, and D. E. Hunton, Thruster Pickup Ions Detected by SPREE during TSS 1, Fourth International Conference on Tethers in Space, Smithsonian Institution, Washington, D.C., 10-14 April 1995. Presented by L. C. Gentile.
63. Gough, M. P., D. A. Hardy, M. R. Oberhardt, W. J. Burke, L. C. Gentile, Correlator Measurements of MHz Wave-Particle Interactions during TSS 1 Electron Beam Operations, Fourth International Conference on Tethers in Space, Smithsonian Institution, Washington, D.C., 10-14 April 1995. Presented by W. J. Burke.
64. Hardy, D. A., M. R. Oberhardt, W. J. Burke, D. C. Thompson, W. J. Raitt, and L. C. Gentile, Electron Beam Propagation Observed during TSS 1, Hardy, D. A., M. R. Oberhardt, W. J. Burke, D. C. Thompson, W. J. Raitt, and L. C. Gentile, Electron Beam Propagation Observed during TSS 1, Fourth International Conference on Tethers in Space, Smithsonian Institution, Washington, D.C., 10-14 April 1995. Presented by W. J. Burke.
65. Webb, D.F., Summary Plenary talk given as Leader of the Group on Large-Scale Structures at the Solar Radio Telescope Workshop, San Juan Capistrano, CA, 17-20 April 1995. Presented by D.W. Webb. (Invited)
66. Jackson, B.V., and Webb, D.F., "The Mass and Energy Distributions of CMEs Measured by Solwing and HELIOS", EOS, 76, S224 (abstract), Spring AGU Meeting, Baltimore, MD, 23-27 May 1995. Presented by B.V. Jackson.
67. Webb, D.F., "Heliospheric Observations of Coronal Mass Ejections". EOS, 76, S225 (abstract), Spring AGU Meeting, Baltimore, MD, 23-27 May 1995. Presented by D.F. Webb. (Invited)
68. Jackson, B.V. and Webb, D.F., "CME Masses and Energies Measured by the HELIOS Spacecraft Photometers", Solar Wind Eight, Dana Point, CA, 25-30 June 1995. Presented by B.V. Jackson.
69. Jackson, B.V., A. Buffington, P.L. Hick, S.W. Kahler, R.C. Altrock, R.E. Gold and D.F. Webb, "The Solar Mass Ejection Imager", Solar Wind Eight, Dana Point, CA, 25-30 June 1995. Presented by B.V. Jackson.
70. Webb, D.F., Howard, R.A., and Jackson, B.V., "Comparison of CME Mass and Kinetic Energies Near the Sun and in the Inner Heliosphere", Solar Wind Eight, Dana Point, CA, 25-30 June 1995. Presented by D.F. Webb.
71. Shea, M. A., D. F. Smart, L. C. Gentile, and J. M. Campbell, Review of Ground-Level Solar Cosmic Ray Enhancements during the 22nd Solar Cycle, 24th International Cosmic Ray Conference, Rome, Italy, 28 August - 8 September 1995. Presented by M. A. Shea.
72. Keil, S.L., R.C. Altrock, S.W. Kahler, B.V. Jackson, A. Buffington, P. Hick, G. Simnett, C. Eyles, D.F. Webb, and P. Anderson, "The Solar Mass Ejection Imager (SMEI): Development and Use in Space Weather Forecasting", 16th NSO/Sacramento Peak International Workshop on Solar Drivers of Interplanetary and Terrestrial Disturbances, Sunspot, NM, 16-20 October 1995. Presented by S.L. Keil.
73. Webb, D.F., "CMEs as solar drivers of interplanetary and terrestrial disturbances", 16th NSO/Sacramento Peak International Workshop on Solar Drivers of Interplanetary and Terrestrial Disturbances, Sunspot, NM, 16-20 October 1995. Presented by D.F. Webb.

74. Webb, D.F., B.V. Jackson, and P. Hick, "Geomagnetic storms and heliospheric CMEs as viewed from HELIOS", 16th NSO/Sacramento Peak International Workshop on Solar Drivers of Interplanetary and Terrestrial Disturbances, Sunspot, NM, 16-20 October 1995. Presented by D.F. Webb.
75. Webb, D.F., "CMEs and their relation to other disturbances", Workshop on Solar Flares and Related Disturbances, Hitachi, Japan, 23-27 January 1996. Presented by D.F. Webb.
76. Webb, D.F., B.V. Jackson, and P. Hick, "Effects of CMEs on the heliosphere and geomagnetic storms using HELIOS data", Solar-Terrestrial Predictions-V Workshop, Hitachi, Japan, 23-27 January 1996. Presented by D.F. Webb.
77. Jackson, B.V., A. Buffington, P. Hick, S.W. Kahler, S.L. Keil, R.C. Altrock, G.M. Simnett and D.F. Webb, "The Solar Mass Ejection Imager", SPIE meeting, San Diego, May 1996. Presented by B.V. Jackson.
78. Jackson, B.V., A. Buffington, P. Hick, S.W. Kahler, S.L. Keil, R.C. Altrock, G.M. Simnett and D.F. Webb, "The Solar Mass Ejection Imager", Small Mission Opportunities and the Scientific Community Workshop, Colleferro, Italy, 1996. Presented by G.M. Simnett.

## **Publications:**

13 December 1989 - 15 March 1996

1. Webb, D.F., and B.V. Jackson, The Identification and Characteristics of Solar Mass Ejections Observed in the Heliosphere by the Helios 2 Photometers, *J. Geophys. Res.*, 95, 20641, 1990.
2. Gentile, L.C., Accessing the Computerized Database of Solar Relativistic Proton Data for the Ground-Level Enhancements of Solar Cycle 22, 22nd International Cosmic Ray Conference, Conference Papers, 3, 149-152, 1991.
3. Kahler, S.W., M.A. Shea, D.F. Smart and E.W. Cliver, Ground-Level Events from Impulsive Flares, 22nd International Cosmic Ray Conference, Conference Papers, 3, 21-24, 1991.
4. Kahler, S.W., E.I. Daibog, V.G. Kurt, and V.G. Stolpovsky, A Comparison of Nonrelativistic Electron Escape Factors Between Solar Flares with and Without Coronal Mass Ejections, 22nd International Cosmic Ray Conference, Conference Papers, 3, 85, 1991.
5. Kahler, S.W., The Double Coronal Mass Ejection Event and Long Rise Time of the Energetic Particle Event of 12 August 1989, 22nd International Cosmic Ray Conference, Conference Papers, 3, 133, 1991.
6. Kahler, S.W., and R.W. Kreplin, The NRL Solrad X-Ray Detectors: A Summary of the Observations and a Comparison with the SMS/GOES Detectors, *Solar Phys.*, 133, 371, 1991.
7. Kahler, S.W., and D.V. Reames, Probing the Magnetic Topologies of Magnetic Clouds by Means of Solar Energetic Particles, *J. Geophys. Res.*, 96, 9419, 1991.
8. Kananen, H., P.J. Tanskanen, L.C. Gentile, M.A. Shea, and D.F. Smart, A Quarter of a Century of Relativistic Solar Cosmic Ray Events Recorded by the Oulu Neutron Monitor, 22nd International Cosmic Ray Conference, Conference Papers, 2, 145-148, 1991.
9. Smart, D.F., M.A. Shea, Margaret D. Wilson, and L.C. Gentile, Solar Cosmic Rays on 29 September 1989; An Analysis Using the World-Wide Network of Cosmic Ray Stations, 22nd International Cosmic Ray Conference, Conference Papers, 3, 97-100, 1991.
10. St. Cyr, O.C., and D.F. Webb, Activity Associated with Coronal Mass Ejections at Solar Minimum: SMM Observations from 1984-1986, *Solar Physics*, 136, 379-394, 1991.
11. Webb, D.F., The Solar Cycle Variation of the Rates of CMEs and Related Activity, *Adv. Space Res.*, 11, (1)37, 1991.
12. Fleishman, G.D. and S.W. Kahler, Microwave Transition Radiation in Solar Flares and in Astrophysics, *Astrophys. J.*, 394, 688, 1992.
13. Gentile, L.C., J.M. Campbell, N.A. Vickers, S.M. Jacavano, M.A. Shea, and D.F. Smart, Compilation and Distribution of Relativistic Solar Proton Data, Proceedings of the First SOLTIP Symposium at Liblice, Edited by S. Fischer and M. Vandas, 2, 50-55, 1992.
14. Jackson, B.V., D.F. Webb, R.C. Altrock and R. Gold, Considerations of a Solar Mass Ejection Imager in a Low-Earth Orbit, Eruptive Solar Flares (Proceedings of Colloquium No. 133), Edited by Z. Svestka, B.V. Jackson, and M.E. Machado, Springer-Verlag, Berlin, 322, 1992.

15. Kahler, S., Solar Coronal Structures Following Mass Ejections, Proceedings of the First SOLTIP Symposium at Liblice, Edited by S. Fischer and M. Vandas, 2, 92, 1992.
16. Kahler, S.W., A Comparison of the SMS/GOES and Solrad X-ray Detectors for Quiet-Sun Studies, Proceedings of the Workshop on the Solar Electromagnetic Radiation Study for Solar Cycle 22, Edited by R.F. Donnelly, 426, 1992.
17. Kahler, S.W., Coronal Mass Ejections, The Astronomy and Astrophysics Encyclopedia, Edited by S.P. Maran, Van Nostrand Reinhold, New York, 631, 1992.
18. Kahler, S.W., Solar Flares and Coronal Mass Ejections, Annual Review of Astronomy and Astrophysics, Edited by G. Burbidge, D. Layzer, and J.G. Phillips, 30, 113, 1992.
19. Lin, R.P., and S.W. Kahler, Interplanetary Magnetic Field Connection to the Sun During Electron Heat Flux Dropouts in the Solar Wind, J. Geophys. Res., 97, A6, 8203-8209, 1992.
20. Webb, D.F., The Solar Sources of Coronal Mass Ejections, Eruptive Solar Flares (Proceedings of Colloquium No. 133), Edited by Z. Svestka, B.V. Jackson, and M.E. Machado, Springer-Verlag, Berlin, 234, 1992.
21. Webb, D.F., and B.V. Jackson, Characteristics of CMEs Observed in the Heliosphere Using Helios Photometer Data, Solar Wind Seven, edited by E. Mausch and R. Schwenn, Pergamon, Oxford, 681, 1992.
22. Crooker, N.U., G.L. Siscoe, S. Shodhan, D.F. Webb, J.T. Gosling, and E. J. Smith, Multiple Heliospheric Current Sheets and Coronal Streamer Belt Dynamics, J. Geophys. Res., 98, 9371-9381, 1993.
23. Gentile, L.C., Relativistic Solar Proton Database for the Ground Level Enhancements During Solar Cycle 22, J. Geophys. Res., 98, 21, 107-21, 109, 1993.
24. Gentile, L.C., Ground-Level Enhancement Database for Solar Cycle 22: An Update, 23rd International Cosmic Ray Conference, Conference Papers, 3, 63-66, 1993.
25. Gentile, L.C., J.M. Campbell, N.A. Vickers, S.M. Jacavano, M.A. Shea, and D.F. Smart, A Relativistic Solar Proton Database for the Ground-Level Enhancements of 1956-1984, 23rd International Cosmic Ray Conference, Conference Papers, 3, 67-70, 1993.
26. Jackson, B.V., P. Hick, and D.F. Webb, Co-Rotating Structures of the Inner Heliosphere From Helios Photometer and In-Situ Data, Adv. Space Res., 13, (9)43-46, 1993.
27. Kahler, S.W., Coronal Mass Ejections and Long Rise Times of Solar Energetic Particle Events, J. Geophys. Res., 98, 5607, 1993.
28. Kudela, K., M.A. Shea, D.F. Smart, and L.C. Gentile, Relativistic Solar Particle Events Recorded by the Lomnický Stit Neutron Monitor, 23rd International Cosmic Ray Conference, Conference Papers, 3, 71-74, 1993.
29. Smart, D.F., M.A. Shea, and L.C. Gentile, The Relativistic Solar Proton Event of 11 June 1991, 23rd International Cosmic Ray Conference, Conference Papers, 3, 55-58, 1993.
30. Smart, D.F., M.A. Shea, and L.C. Gentile, The Relativistic Solar Proton Event of 15 June 1991, 23rd International Cosmic Ray Conference, Conference Papers, 3, 59-62, 1993.

31. Webb, D.F., The Heliospheric Manifestations and Geoeffectiveness of Solar Mass Ejections, Solar-Terrestrial Predictions Workshop: IV, Edited by A. Hruska, M. Shea, D. Smart, and G. Heckman, NOAA, Boulder, CO, 2, 71, 1993.
32. Webb, D.F., and B.V. Jackson, Characteristics of CMES Observed in the Heliosphere using Helios Photometer and IN-Situ Data, Solar-Terrestrial Predictions Workshop: IV, Edited by A. Hruska, M. Shea, D. Smart, and G. Heckman, NOAA, Boulder, CO, 2, 381, 1993.
33. Webb, D., B. Jackson, P. Hick, R. Schwenn, V. Bothmer, and D. Reames, Comparison of CMES, Magnetic Clouds, and Bidirectionally Streaming Proton Events in the Heliosphere Using Helios Data, *Advances in Space Research*, 13, (9)71-74, 1993.
34. Webb, D.F., S.F. Martin, D. Moses, and J.W. Harvey, The Correspondence Between X-ray Bright Points and Evolving Magnetic Features in the Quiet Sun, *Solar Phys.*, 144, 15-35, 1993.
35. Cliver, E.W., S.W. Kahler, and J.M. Campbell, An Investigation of the Relationship Between the Microwave Spectra of Solar Flares and the Delay to Maximum of Associated Proton Events at 1 AU, Solar-Terrestrial Predictions Workshop: IV, Edited by A. Hruska, M. Shea, D. Smart, and G. Heckman, NOAA, Boulder, CO, 2, 113, 1993.
36. Gentile, L.C., J.M. Campbell, E.W. Cliver, and H.V. Cane, X-Class Soft X-Ray Bursts and Major Proton Events During Solar Cycle 22 (1987-1991), Solar-Terrestrial Predictions Workshop: IV, Edited by A. Hruska, M. Shea, D. Smart, and G. Heckman, NOAA, Boulder, CO, 2, 153, 1993.
37. Gough, M. P., D. A. Hardy, M. R. Oberhardt, W. J. Burke, L. C. Gentile, B. McNeil, K. Bounar, D. C. Thompson, and W. J. Raitt, Correlator Measurements of MHz Wave-Particle Interactions during Electron Beam Operations of STS, *Journal of Geophysical Research*, 100, 21,561-21,575, 1995.
38. Jackson, B.V., A. Buffington, P.L. Hick, S.W. Kahler and D.F. Webb, A spaceborne near-Earth asteroid detection system, *Astronomy and Astrophys. Suppl. Ser.*, 108, 279, 1994.
39. Jackson, B.V., D.F. Webb, P.L. Hick, and J.L. Nelson, Catalog of Helios 90° Photometer Events, PL-TR-94-2040, Phillips Lab, Hanscom AFB, MA, 1994.
40. Jackson, B.V. and D.F. Webb, "The Masses of CMEs Measured in the Inner Heliosphere", in *Solar Dynamic Phenomena and Solar Wind Consequences*, Third SOHO Workshop, ESA SP-373, ESTEC, The Netherlands, p. 233-238, 1994.
41. Kahler, S., Injection Profiles of Solar Energetic Particles as Functions of Coronal Mass Ejection Heights, *Astrophys. J.*, 428, 837-842, 1994.
42. Kahler, S.W., E.I. Daibog, V.G. Kurt and V.G. Stolpovskii, A Comparison of Nonrelativistic Electron Escape Efficiencies for Solar Flares With and Without Coronal Mass Ejections, *Astrophys. J.*, 422, 394-399, 1994.
43. Moses, D., J.W. Cook, J. Bartoe, G.E. Brueckner, K.P. Dere, D.F. Webb, J.M. Davis, J.W. Harvey, F. Recely, S.F. Martin, S.F., and H. Zirin, Solar Fine Scale Structures in the Corona, Transition Region, and Lower Atmosphere, *Astrophys. J.*, 430, 913-924, 1994.

44. Smart, D. F., M.A. Shea, and L.C. Gentile, The Relativistic Solar Proton Ground-Level Enhancements Associated with the Solar Neutron Events of 11 June and 15 June 1991, High Energy Solar Phenomena - A New Era of Spacecraft Measurements, Edited by J.M. Ryan and W.T. Vestrand, AIP Conference Proceedings 294, American Institute of Physics, New York, 222-229, 1994. (PL-TR-94-2074, AD A278671)
45. Waljeski, K., D. Moses, K.P. Dere, J.L.R. Saba, K.T. Strong, D.F. Webb, and D.M. Zarro, The Composition of a Coronal Active Region, *Astrophys. J.*, 429, 909-923, 1994.
46. Webb, D.F. and R.A. Howard, The Solar Cycle Variation of Coronal Mass Ejections and the Solar Wind Mass Flux, *J. Geophys. Res.*, 99, 4201-4220, 1994.
47. Webb, D.F., T.G. Forbes, H. Aurass, J. Chen, P. Martens, B. Rompolt, V. Rusin, and S.F. Martin, Material Ejection, *Solar Phys.*, 153, 73-89, 1994.
48. Webb, D.F., Coronal Mass Ejections, in (J. Bergeron, ed.) Reports on Astronomy, International Astronomical Union, The Netherlands, 27A, p. 64-67, 1994.
49. Webb, D.F., Coronal Mass Ejections: The Key to Major Interplanetary and Geomagnetic Disturbances, The U.S. National Report to the IUGG (1991-1994), *Rev. of Geophys. (Suppl.)*, 33, 577-583, July 1995.
50. Shea, M.A., D.F. Smart, L.C. Gentile and J.M. Campbell, Review of Ground-Level Solar Cosmic Ray Enhancements during the 22nd Solar Cycle, 24th International Cosmic Ray Conference, Contributed Papers, 4, 244-247, 1995.
51. Burke, W.J., L.C. Gentile, J.S. Machuzak, D.A. Hardy and D.E. Hunton, Energy distributions of thruster pickup ions detected by the Shuttle Potential and Return Electron Experiment during TSS 1, *J. Geophys. Res.*, 100, 19,773-19,790, 1995.
52. Gentile, L. C., W. J. Burke, J. S. Machuzak, D. A. Hardy, and D. E. Hunton, Thruster Pickup Ions Detected by SPREE during TSS 1, Proceedings of the Fourth International Conference on Tethers in Space, Smithsonian Institution, Washington DC, 10-14 April 1995, I, 267, 1995.
53. Gough, M. P., D. A. Hardy, M. R. Oberhardt, W. J. Burke, L. C. Gentile, Correlator Measurements of Megahertz Wave-Particle Interactions during Electron Beam Operations on STS, Proceedings of the Fourth International Conference on Tethers in Space, Smithsonian Institution, Washington DC, 10-14 April 1995, I, 299, 1995.
54. Hardy, D. A., M. R. Oberhardt, W. J. Burke, D. C. Thompson, W. J. Raitt, and L. C. Gentile, Electron Beam Propagation Observed during TSS 1, Proceedings of the Fourth International Conference on Tethers in Space, Smithsonian Institution, Washington DC, 10-14 April 1995, I, 283, 1995.
55. Hardy, D. A., M. R. Oberhardt, W. J. Burke, D. C. Thompson, W. J. Raitt, and L. C. Gentile, Observations of Electron Beam Propagation Perpendicular to the Earth's Magnetic Field during the TSS 1 Mission, *Journal of Geophysical Research*, 100, 21,523-21,534, 1995.
56. Hardy, D.A., D.E. Hastings, D.R. Rivas, W.J. Burke, D.L. Cooke and L.C. Gentile, Beam arc distributions of shuttle pickup ions and their instabilities, *J. Geophys. Res.*, (in press), 1996.
57. Webb, D.F. and E.W. Cliver, Evidence for Magnetic Disconnection of Mass Ejections in the Corona, *J. Geophys. Res.*, 100, 5853-5870, 1995.

58. Webb, D.F., Solar and Geomagnetic Disturbances During the Declining Phase of Recent Solar Cycles, *Advances in Space Res.*, 16, (9)57-69, 1995.
59. Jackson, B.V., A. Buffington, P.L. Hick, S.W. Kahler, R.C. Altrock, R.E. Gold and D.F. Webb, The Solar Mass Ejection Imager, in *Proceedings of Solar Wind 8*, Edited by D. Winterhalter et al., NASA Jet Propulsion Lab. Pasadena, CA, (in press) 1996.
60. Jackson, B.V., A. Buffington, P. Hick, S.W. Kahler, S.L. Keil, R.C. Altrock, G.M. Simnett and D.F. Webb, The Solar Mass Ejection Imager, in *Proceedings of Small Mission Opportunities and the Scientific Community Workshop*, Colleferro, Italy, W. Pecorella and R. Mura, eds., (in press) 1996.
61. Jackson, B.V., A. Buffington, P. Hick, S.W. Kahler, S.L. Keil, R.C. Altrock, G.M. Simnett and D.F. Webb, The Solar Mass Ejection Imager, in *Proceedings of the Instrument Society of America*, San Diego, (in press) 1996.
62. Keil, S.L., R.C. Altrock, S.W. Kahler, B.V. Jackson, A. Buffington, P. Hick, G. Simnett, C. Eyles, D.F. Webb, and P. Anderson, The Solar Mass Ejection Imager (SMEI): Development and Use in Space Weather Forecasting, in *Solar Drivers of Interplanetary and Terrestrial Disturbances*, edited by K.S. Balasubramaniam, Stephen L. Keil, and Raymond N. Smartt, Astronomical Society of the Pacific, San Francisco, 158-166, 1996.
63. Machuzak, J.S., W.J. Burke, L.C. Gentile, V.A. Davis, D.A. Hardy and C.Y. Huang, Thruster effects on the shuttle potential during TSS 1, *J. Geophys. Res.*, 101, 13,437 - 13,444, 1996.
64. Webb, D.F., R.A. Howard, and B.V. Jackson, Comparison of CME masses and kinetic energies near the sun and in the inner heliosphere, in *Proceedings of Solar Wind 8*, Edited by D. Winterhalter et al., NASA Jet Propulsion Lab. Pasadena, CA, (in press) 1996.
65. Webb, D.F., CMEs as solar drivers of interplanetary and terrestrial disturbances, in *Solar Drivers of Interplanetary and Terrestrial Disturbances*, edited by K.S. Balasubramaniam, Stephen L. Keil, and Raymond N. Smartt, Astronomical Society of the Pacific, San Francisco, 219-228, 1996.
66. Webb, D.F., B.V. Jackson, and P. Hick, Geomagnetic storms and heliospheric CMEs as viewed from HELIOS, in *Solar Drivers of Interplanetary and Terrestrial Disturbances*, edited by K.S. Balasubramaniam, Stephen L. Keil, and Raymond N. Smartt, Astronomical Society of the Pacific, San Francisco, 167-170, 1996.
67. Jackson, B.V., and D.F. Webb, CME Masses and Energies Measured by the HELIOS Spacecraft Photometers, *Proceedings of Solar Wind Eight*, (In Press) 1996.
68. Webb, D.F., CMEs and their relation to other disturbances, in *Proceedings of the Workshops on Solar Flares and Related Disturbances and on Solar-Terrestrial Predictions-V*, Hiraiso Solar-Terrestrial Research Center, CRL, Isozaki, Japan, (in press) 1996.

69. Webb, D.F., B.V. Jackson, and P. Hick, Effects of CMEs on the heliosphere and geomagnetic storms using HELIOS data, in Proceedings of the Workshops on Solar Flares and Related Disturbances and on Solar-Terrestrial Predictions-V, Hiraiso Solar-Terrestrial Research Center, CRL, Isozaki, Japan, (in press) 1996.

70. Webb, D.F., S.W. Kahler, P.S. McIntosh and J.A. Klimchuck, Large-scale structures and multiple neutral lines associated with CMEs, J. Geophys. Res., submitted, 1996.



## 5. REPRINTS OF SELECTED PUBLICATIONS

The reprints in this section are in numerical order, and refer to the following numbers in the Publication List of Section 4:

Pub. No.	Page
1	24
7	45
18	51
22	66
23	77
36	80
46	89
49	109
53	116
55	131
57	143
58	161

# The Identification and Characteristics of Solar Mass Ejections Observed in the Heliosphere by the Helios 2 Photometers

D. F. WEBB

*Institute for Space Research, Boston College, Newton Center, Massachusetts*

B. V. JACKSON

*University of California at San Diego, La Jolla*

We describe the use of Helios 2 zodiacal light photometer data to identify, classify, and determine the characteristics of significant white light transient events observed in the interplanetary medium. Data from the north ecliptic pole (+90°) photometer were used to identify transient flux increases which are interpreted as plasma "clouds" of Thomson-scattered radiation from electrons which enveloped the spacecraft or passed north of it. A subset of these events was classified by examining the lower-latitude Helios photometers to determine the temporal evolution and spatial extent of each event. We also examined the in situ plasma and magnetic field data during the time of the white light events. Both the white light and in situ data sets were used to study the characteristics of heliospheric white light transients during a 4-year period from solar minimum (1976) to solar maximum (through 1979). Eighty percent of the classified transient events moved progressively outward from the Sun to the east and/or west of the Helios spacecraft and were classified as solar coronal mass ejections (CMEs). We determined the frequency of occurrence of these CMEs and found that they increased by at least an order of magnitude from solar minimum to maximum. In 1979, most of the Helios events were found to be associated with major CMEs observed near the Sun by the Solwind coronagraph. We used the photometers to determine the brightnesses, durations, outward speeds, and scale sizes for each of the heliospheric mass ejections. The average CME had a brightness increase of 2.3 S10 units in the 90° photometer. It had an average duration of 37 hours and speed  $\approx 500$  km/s, implying a radial "flow" dimension of  $\sim 0.4$  AU, and a longitudinal width near the Sun of  $\approx 50^\circ$ . These results suggest that typical heliospheric CMEs have large dimensions, encompassing large volumes and supplying significant amounts of mass to the inner heliosphere, especially around the solar activity maximum. Because of their large size and our selection criteria, nearly all of the white light transients were detected at the spacecraft as in situ density enhancements. Most were also associated with significant enhancements and rotations of the interplanetary magnetic field, and many showed evidence for the passage of "magnetic clouds." About half were associated with fast MHD shocks. A small subset (27%) of the white light events showed evidence of corotation from east to west in the lower-latitude photometers and may represent the detection of coronal streamers in the interplanetary medium.

## 1. INTRODUCTION

Coronal mass ejections (CMEs) from the Sun are now considered to be an important aspect of the physics of the corona. CMEs are also important to our understanding of heliospheric disturbances because they can involve the injection of significant amounts of mass and energy into large volumes of the interplanetary medium. CMEs may also provide a key link between geomagnetic effects such as storms and supposedly independent classes of "geoeffective" solar activity. For instance, most, if not all transient interplanetary shocks are associated with energetic CMEs [Sheeley *et al.*, 1985; Cane *et al.*, 1987]. Solar energetic protons, which often accompany geomagnetic storms, are probably accelerated in the coronal shocks associated with CMEs [Kahler *et al.*, 1978]. Also, erupting prominences and large optical and X ray flares are well associated with CMEs (see Kahler [1987] for a review).

CMEs have been well studied near the Sun ( $<10 R_s$ ) by Earth-orbiting coronagraphs operating at high cadences producing images of white light emission due to Thomson-scattered electron radiation [e.g., Kahler, 1987; Hund-

hausen, 1988]. Spacecraft nearer the Sun and not in Earth orbit have recently provided in situ evidence of the propagation of CMEs as they move outward from the Sun [e.g., Dryer *et al.*, 1982; Burlaga *et al.*, 1982; Sheeley *et al.*, 1985]. Earth-based remote sensing techniques such as interplanetary scintillation [Watanabe and Kakinuma, 1984; Woo *et al.*, 1985] and kilometric type II data [Cane, 1985] also detect plasma disturbances at large distances from the Sun. But these observations contain limited spatial information and are only indirectly sensitive to electron density and therefore mass. Our knowledge of the manifestations and effects of CMEs in the heliosphere remains very uncertain. Even near the Sun the three-dimensional shapes and line-of-sight positions of CMEs are ambiguous from coronagraph observations alone, and their characteristics farther out are poorly known. Our knowledge of the geometry of CMEs is so crude that after 15 years of coronagraph observations we still do not know whether CMEs emerge from the Sun primarily as planar loops or spherical bubbles [Kahler, 1987; Webb, 1988].

The Helios zodiacal light photometers measured brightness variations globally around the spacecraft with varying spatial resolution. Richter *et al.* [1982] first described the use of these data to follow plasma ejections detected by electron scattering out to 90° solar elongation and beyond. More

Copyright 1990 by the American Geophysical Union.

Paper number 90JA01988.

0148-0227/90/90JA-01988\$05.00

The U.S. Government is authorized to reproduce and sell this report. Permission for further reproduction by others must be obtained from the copyright owner.

recently, Jackson and colleagues [e.g., Jackson, 1985; Jackson *et al.*, 1985, 1988; McCabe *et al.*, 1986] have used the Helios photometer data to study the gross features of a number of individual mass ejections within the spacecraft orbits from 0.3 to 1 AU. Most of these studies involved events observed in 1979 and 1980 when they could be directly compared with coronagraph images of CMEs near the Sun. Because the Helios spacecraft orbited the Sun inside of 1 AU, the photometer experiments viewed heliospheric events from a unique perspective which, when combined with Earth-based and/or other spacecraft data, could better determine the three-dimensional structure and mass content of the events. Polarization data obtained with the photometer experiments are also potentially useful in determining structural dimensions but were not used in our study.

In this study we performed a comprehensive survey of all electron plasma events detected above a given threshold by the Helios 2 photometers. These photometers pointed north of the ecliptic plane, whereas the Helios 1 photometers pointed south. The Helios 2 experiment operated for nearly four consecutive years from early 1976 to the end of 1979 during a long gap in conventional coronagraph observations between Skylab, which ceased operations in January 1974, and Solwind which began observations in March 1979. The major goals of this study were to use these data as a way of identifying coronal mass ejections in the interplanetary medium, to establish their heliospheric characteristics and compare them with those of CMEs observed near the Sun, and to determine the frequency of occurrence of CMEs during the long gap in coronagraph coverage.

We note in passing that our use of the term "CME" is generic. It is clear from this and previous studies that the Helios photometers are sensitive to Thomson-scattered photospheric radiation from massive ejections of material from the solar atmosphere. However, we are not sure that this material is entirely coronal in origin. In addition, the generation of interplanetary shock waves, expansion, and other forms of interaction of this material with the ambient solar wind undoubtedly transform it on its journey through the heliosphere. Although we would prefer a more general term such as "solar mass ejection" to describe the heliospheric manifestations of these events, here we will follow convention and refer to these events as coronal mass ejections.

Other than CMEs and interplanetary dust, possible sources of interplanetary white light enhancements include corotating structures possibly related to coronal streamers (B. V. Jackson, Helios spacecraft photometer observations of elongated rotating structures in the interplanetary medium, submitted to *Journal of Geophysical Union*, 1990) shock-related compression regions [Jackson, 1986], comets [Jackson and Benensohn, 1990], and density enhancements at sector boundaries (this paper). As the references indicate, possible detections of these phenomena have now been made using the Helios photometers data. For the initial selection of events we used flux time series plots obtained only with the +90° photometer, which always pointed at the north ecliptic pole. This method was chosen to minimize the background contribution and confusion arising from complex events occurring near the ecliptic plane. Because of the other potential sources of interplanetary white light enhancements, we then used the lower-latitude photometer time

series data during a majority of the 90° events to classify them in terms of their temporal evolution and spatial extent outward from the Sun. We found that 80% of these events could be classified as coronal mass ejections and their basic characteristics determined. We also found that during 1979 most of the Helios events we classified as CMEs could be associated with Solwind CMEs near the Sun at an earlier time and that the annualized occurrence rate of the Helios CMEs agreed favorably with that of the Solwind CMEs.

In section 2 we describe the characteristics of the Helios zodiacal light experiment important for our study, and in section 3 we discuss our methods of selecting and analyzing the data. The results are summarized in section 4 in terms of a statistical analysis of the white light events, determination of some of the basic characteristics of the subset of the events classified as CMEs, and a summary of a study of the characteristics of the in situ solar wind plasma and magnetic field data during the times of the white light events. In section 5 we summarize the results and discuss our conclusions.

## 2. INSTRUMENTAL BACKGROUND

The Helios 2 spacecraft, launched in January 1976, was fitted with three zodiacal light photometers originally intended to measure the distribution of dust in the interplanetary medium between the Sun and the Earth [Leinert *et al.*, 1975, 1981a]. However, these photometers can also be used to measure the variations of brightness produced by large-scale differences in the interplanetary electron content. The three Helios photometers were fixed on the spacecraft and rotated at its 1 s spin period on an axis perpendicular to the plane of the ecliptic; they pointed 16°, 31°, and 90° north of the ecliptic plane and had apertures of 1°, 2°, and 3°, respectively. Data from the 16° and 31° photometers were binned into 32 longitude sectors at constant ecliptic latitude, relative to the spacecraft, around the sky. The 16 sectors within 45° of the Sun subtended angles of 5.6° in ecliptic longitude; angles of 11.2° and 22.4° were formed for sectors at more distant longitudes. The spacecraft photometer data were integrated over an 8.6-min period in turn from each of the three photometers through a set of broadband ultraviolet, blue, and visual light and polarizing filters, with a time interval of 5.2 hours between similar filter sequences. The Helios photometry was stable with time over several years and could be calibrated to about 5% in absolute intensity [Leinert *et al.*, 1981a]. The zodiacal light was found to be constant at this level and was described quantitatively by Leinert *et al.* [1981b]. Relative comparisons of data over short intervals of time are far more precise. The photometer intensities are calibrated in S10 units. One S10 corresponds to the intensity of one solar type star with a V magnitude of 10 per square degree. The best observations of the background noise indicate that over short intervals of a few days the photometer observations were accurate to better than 1 S10 unit [Jackson, 1988].

Residual brightness variations can be studied after the zodiacal light and stellar contributions have been removed from the photometer data. Richter *et al.* [1982] showed that these variations are caused primarily by discrete changes in the electron density, which they called plasma clouds, in the interplanetary medium. By combining observations from each photometer sector interpolated at a given instant in

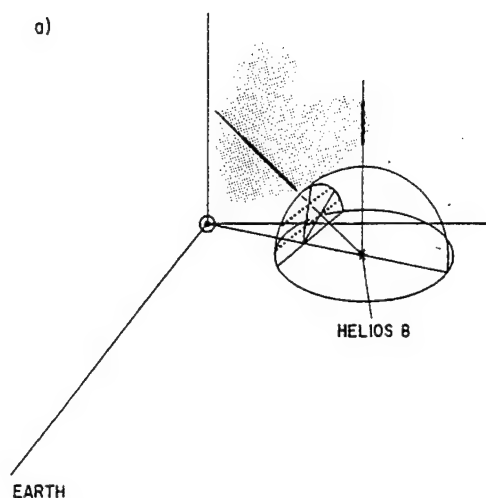


Fig. 1a. Three-dimensional Sun-centered schematic view of the Earth, Sun, and Helios 2 spacecraft configuration. The ecliptic celestial sphere around the Helios 2 spacecraft is depicted and the positions of the photometer sector centers (dots) within  $45^\circ$  solar elongation are shown. The schematic has lines of sight from the spacecraft drawn through one of the  $16^\circ$  photometer sector centers and through the Helios spacecraft zenith (the  $90^\circ$  photometer).

time, these data can be used to form images of the plasma in the heliosphere in a way similar to the images obtained from Earth-orbiting coronagraphs. Because the Helios spacecraft orbited the Sun, not the Earth, these data have serendipitously provided a unique stereoscopic view of an entire hemisphere of the inner heliosphere.

Figure 1a depicts the three-dimensional configuration of the Earth, Sun, and the direction to the centers of the photometer sectors at one position in the Helios 2 spacecraft orbit. Figure 1b gives the spatial coverage of the Helios 2 photometers within  $90^\circ$  of the Sun as viewed from the spacecraft. The Helios photometer data are available on computer tapes from the National Space Science Data Center (NSSDC). An image processing system developed at the University of California at San Diego to access these

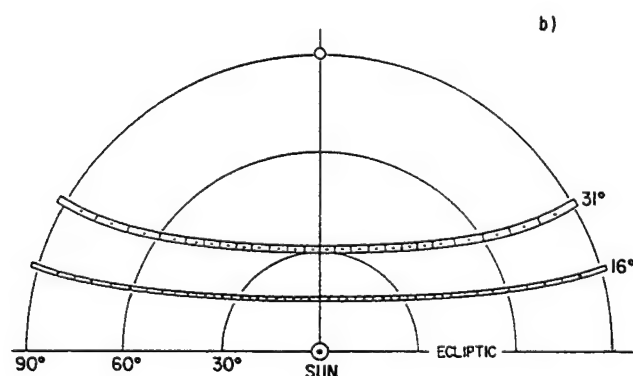


Fig. 1b. View of the spatial photometer coverage near the Sun as observed from the Helios 2 spacecraft. In this view, the Sun is centered on the ecliptic plane depicted as the horizontal straight line. Semicircles denote angles of constant elongation from the Sun out to  $90^\circ$ . Photometer sector areas at  $16^\circ$  and  $31^\circ$  are depicted by the boxes, with the photometer sector centers marked by dots as in Figure 1a. The  $90^\circ$  photometer which points directly to the spacecraft zenith, the north ecliptic pole, is marked at the top by the  $3^\circ$  circle.

data constructs images of the interplanetary medium by contouring the residue brightness variation around the spacecraft in terms of columnar density (see Jackson and Leinert [1985] and Jackson [1985] for summaries of this imaging technique).

These Helios images have been used to trace the extent of CMEs as they propagate outward into the interplanetary medium over periods of days. Also present in these images are persistent elongated features that extend outward from the Sun and move systematically with time from solar east to west [Jackson, 1990]. These latter features can generally be traced to the heliospheric current sheet, and for a few corresponding observations, to coronal streamers observed by the Solwind coronagraph. Thus information about both coronal mass ejections and the corotating structures of the heliosphere exists in the Helios data.

### 3. SELECTION CRITERIA AND DATA ANALYSIS OF PHOTOMETER EVENTS

#### 3.1. Selection of $90^\circ$ Photometer Events

For the initial selection of white light events we limited our search to data obtained only with the Helios 2  $+90^\circ$  photometer. We chose this method because the star and dust background were minimal and constant for this photometer [Richter *et al.*, 1982], and we could avoid the problem of interpreting confusing or complex phenomena occurring near the ecliptic plane, especially near the maximum epoch of solar activity. A limitation of this method is that we could only select those transients which intersected or passed to the north of the spacecraft, i.e., those which were aimed in its general direction. With this criterion we will miss events which passed entirely south of or at large near-ecliptic elongations from the spacecraft.

The Helios 2  $90^\circ$  photometer data are available in strip chart form for the duration of the experiment lifetime (through the end of 1979). These data have had the zodiacal light contribution removed through use of an appropriate empirical model of its distribution [Leinert *et al.*, 1981b] and are normalized to the brightness expected of Thomson-scattered light at 1 AU. Richter *et al.* [1982] show such time series plots for three orbits of Helios 2 in their Figure 3. These charts form a unique data base with which to do comparative studies of interplanetary plasma events, presumably mostly coronal mass ejections, which occurred during the spacecraft lifetime. In Figure 2 we present examples of the time series from the  $90^\circ$  photometer for two spacecraft orbits in 1977 and 1978. These show the normalized white light intensity in S10 units plotted as a function of the spacecraft orbital position in heliocentric longitude. The events which we selected for further analysis are shown for each orbit numbered in time sequence. As stated earlier, the basic time resolution of these data is 5.2 hours. This cadence is more apparent in the enlarged portion at the bottom of Figure 2, where longitude has been converted to time.

We established a set of criteria that was used to select significant brightness enhancements from the  $90^\circ$  orbital plots for further study. We excluded brightness enhancements or dropouts consisting of a single 5.2-hour data point, such as those labeled by Leinert as being instrumental in nature. These included attitude maneuvers, transmission errors, and dark current anomalies. Others were likely

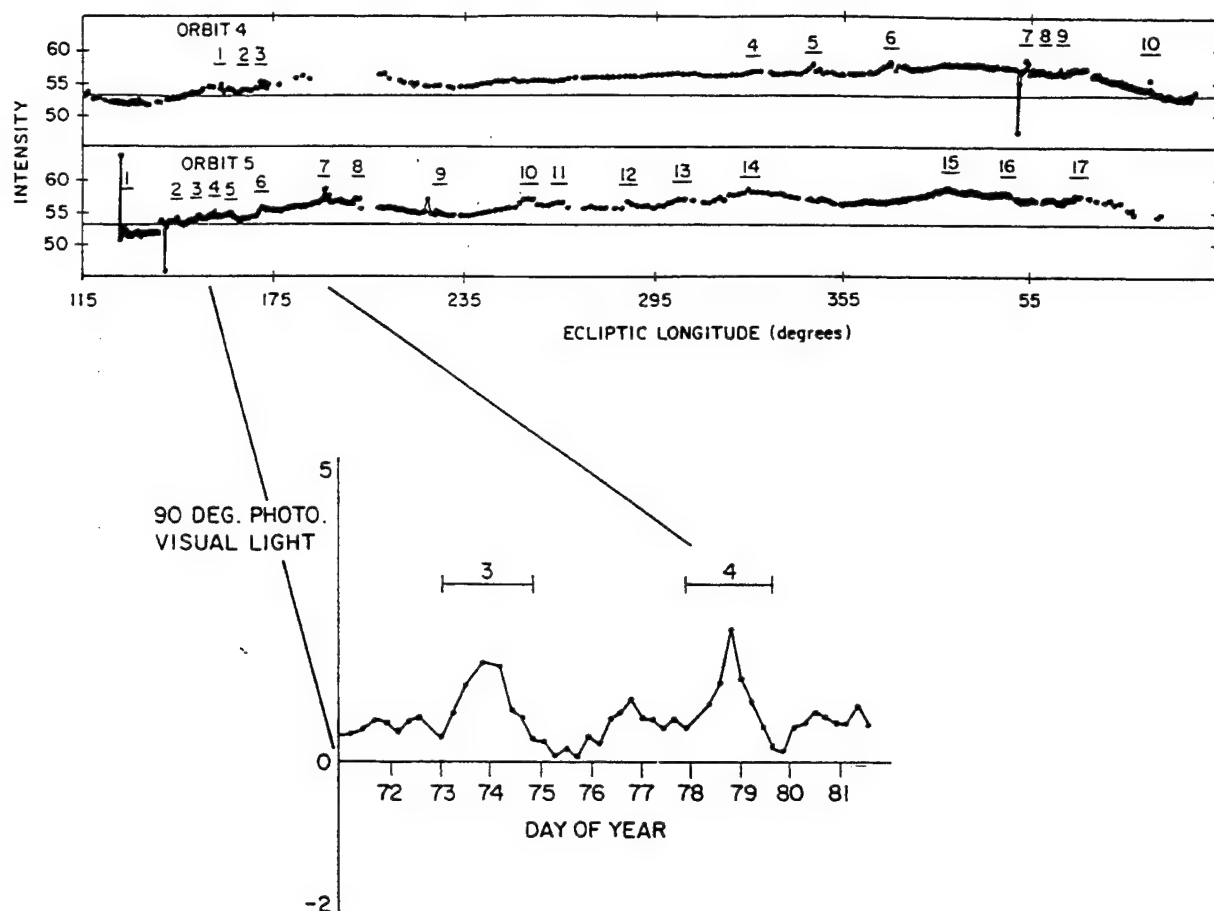


Fig. 2. White light intensity (in S10 units) time series through the blue filter of the 90° Helios 2 photometer for orbits 4 and 5. The events which were selected for further study are marked on the top plots for each orbit numbered in the sequence in which they occurred. The period of each orbit of the Helios 2 spacecraft was 186 days, or about two orbits per year. In this plot of equal intervals of spacecraft heliocentric longitude, the fixed rate photometer data points have greater spacing near perihelion (center) than near aphelion (left and right sides). The expected contribution due only to the zodiacal light model of Richter et al. [1982] is shown as the horizontal straight line on the plots. There are several examples of instrumental anomalies on these plots which we removed. The first peak on orbit 5 is a transmission error and the single dips at ~50° on orbit 4 and at ~140° on orbit 5 are dark current anomalies. An enlargement of one portion of the photometer time series through the V filter for orbit 5 is shown at the bottom, where longitude has been converted to time (day of year).

caused by instrumental glitches or particle events, which are clearly detectable as large enhancements in the 9-min time resolution data [e.g., *Leinert et al.*, 1981a]. We selected all events which exhibited distinct rise and fall flux profiles consisting of two or more data points (a time duration of at least 10.5 hours). Events with peak brightness <1.0 S10 unit above background, normalized to 1 AU, are easily discernable on these plots. Our effective brightness threshold was about 1.0 S10 unit, the lowest enhancement shown in Table 1. The typical event profile (Figure 2, bottom) exhibited a gradual rise and fall signature of 1 to 2 days duration lying atop much more gradual, longer-term orbital variations, which were probably due to small deviations from the planar dust model used [e.g., *Richter et al.*, 1982]. Although this initial selection of events was somewhat subjective, their existence, peak brightnesses, and durations were later confirmed and accurately determined from the actual data tapes (see next section).

In this manner, a list of 70 Helios 2 90° photometer events was compiled from the eight orbits (4 years) of photometer operation from January 1976 through December 1979. For

each event the ecliptic longitudes of the onset, peak and end points and the peak brightness above the average preevent background were recorded. The event longitudes were then converted to time in units of the day of the year (DOY), and the event duration calculated.

### 3.2. Selection and Analysis of Events Using Lower-Latitude Photometers

To classify the transient plasma events and, in particular, to identify those that were coronal mass ejections, it was necessary to examine the lower photometer data to determine the overall temporal evolution and spatial extent of each event. Appropriately reduced, time-series intensity plots for all three photometers were the primary data used to determine the class of event responsible for the brightness enhancement at 90°. Occasionally, sequential contour images were used in the interpretation of a given event. Such events were nearly always found to be either CMEs or bright regions corotating with the Sun.

TABLE 1. Helios 2 90° Photometer Classified Events and in Situ Associations

Date	90° Event			16° Event			31° Event			90° Event			In Situ Solar Wind Associations					Class
	Period, DOY	Peak Time, DOY	$\delta I_e$ S10	Peak Time, DOY	$\delta I_e$ S10	Peak Time	$\delta I_e$ S10	Dura- tion, days	Speed, km/s	Density Enhance- ments	Shock	Sector Boundary	Mag- netic Rota- tion	Mag- netic Cloud	$\delta B_e$ nT			
March 6-8 March 13-15 April 7-12	66.9-68.3 73.0-75.1 ≈98-≈103	? 73.0 100.5-101.8	? 15 200	? ... 100.8-101.9	1000 <3 50	67.2 73.8 101.7	1.8 1.5 ≈17	1.4 2.1 5	... ... 350	n y/y y/y	n n n	n y y	n y y	n m n	n ... ...	0 17 15	Comet West possible CRS CRS	
March 16-18 March 24-25 March 29-31 Sept. 16	75.7-77.0 83.2-84.6 88.8-90.0 259.2->259.7	74.6-75.6 82.6 88.8 257.1; 259.5	25 20 50 ...	<74.7-76.4 83.2 89.3 ?	10 15 <5 ...	76.1 ≤84.1 89.6 259.4	2.5 ≥2.1 1.0 2.5	1.3 1.4 1.2 >0.5	340 545-622 495 257	y/y y/n? y/y y/y	y/y y/n n n	n n n? n	y y m n	y y m n	18 16 11 11	CRS CME CME CRS; possible CME		
Sept. 21-22 Sept. 25-26	264.2-265.2 >268.2-269.4	263.6-264.4 268.0	35 50	<263.7-264.3 268.2; 268.6	≈4 15	264.7 268.7	2.0 3.0	1.0 <2.0	762 664-780	n y/y	n y/y	n n?	m y	n y	0 .25	Possible CME CME;		
Nov. 2-3 Nov. 7-9 Nov. 23-24 Nov. 26-28	306.2-307.4 311.0-313.6 327.4->328.5 330.0-332.4	306.2-306.4 310.8 ≈326.5 328.0-329.4	≈70 400 75 30	306.6 311.6 >326.3<327.0 328.8-330.3	≈40 150 10 10	306.8 311.9 327.8 331.2	13 8.0 4.0 1.5	1.2 2.6 >1.1 2.4	365-600 425-520 755 293	y/y y/y y/y y/y	n y/y y/y n	n y n n	y y y y	m y m n	... ≈15 27 ≈23 0	possible shock CME CME Possible CME CRS		
March 7-9 March 14-15 March 19-20 March 23-25	≤66.9-68.1 73.2-74.8 ≤78.3-79.4 ≤82.2-84.6	65.9 71.3 77.3 81.2; 82.6	20 40 40 40	66.3 72.3 77.7 82.0; 83.2	10 20 10 10	67.2 73.9 78.8 83.3	1.9 1.3 2.0 3.0	>1.2 1.6 >1.1 >2.4	812-1138 350-415 315-375 405	y/y n y/y y/y	y/y n n n	n n y n?	y n y n?	n n m m	19 0 11 20	CME/shock CME CME CRS; possible CME		
March 29-31 April 8-10	88.7-≈90.5 98.8-100.3	85.0-91.0 98.8	60 300	87.4-≈92 99.2-99.6	20 80	≈89.5 99.6	5.0 12	(1.8) 1.5	302 550	y/y y/y	n y/y	y y	y y	n y	≈7 48	CRS CME + shock		
April 12-13 April 19-20	102.4->103.4 <109.1-110.6	102.2 108.0	200 400	102.6 108.7	80 150	≥103.4 109.2; 109.9	8.0 27 10	>1.0 >1.5	315 153-620 160-533	y/y y/y y/y	y/n y/n	m n	y n	m n	15 ≈8	CME CME + shock		
April 24-25 April 25-26 April 29-30	<114->115.2 <115.7->116.9 <119.2->120.2	114.0 112-117.5 118.7-119.6	600 500 400	114.4 111.5-119 118.0-119.0	100 100 100	114.8 116.2 119.3	13 12 >16	>0.6 >1.2 >1.0	700 340 480-840	y/y y/y y/y	m/n n y/y	n n n	y n y	y n m	≈45 0 ≈50	CME CRS CME + shock		
April 30- May 2 Oct. 24-26	>120.7≈122.5 <297.2->299.7	120.2 297.0	300 200	120.3 297.1	70 110	≥121.2 297.4	>15 9.0	(1.8) >2.5	400 482-908	y/y y/y	n y/y	n n	n n	n n	... ≈30	CME CME + shock		
Oct. 31- Nov. 2 Nov. 8	<304.8>306.3 312.0->312.5	305.1 310.8-311.9	800 450	304.8-305.5 311.2-312.7	250 100	305.8 312.2	25 18	>1.5 >0.5	480-488 655-885	y/y y/y	y/y y/y	n n?	y y	y y	35 ≈85	CME + shock possible CME/ shock		

TABLE 1. (continued)

90° Event	16° Event				31° Event				90° Event				In Situ Solar Wind Associations				
Date	Period, DOY	Peak Time, DOY	$\delta I$ , S10	Peak Time, DOY	Peak Time, DOY	$\delta I$ , S10	Peak Time	$\delta I$ , S10	Duration, days	Speed, km/s	Density Enhancements	Shock	Sector Boundary	Magnetic Rotation	Magnetic Cloud	$\delta B$ , nT	Class
Nov. 16-18	320.2-322.0	317.7-321.5	350	317.0-323.7	60	321.8	7.0 > 1.8	235	n	y/y	n	m/n?	n	m	n	≈5	CRS
Nov. 18	<322.3-322.5	321.7	200	322.0	50	322.5	10 > 0.2	?	y/y	?	y/y	n	...	y	n	≈20	CME
Nov. 29-30	333.1-334.8	332.5	100	332.2	20	334.2	3.0 1.7	412-495	y/y	412-495	y/y	n	y	y	n	≈10	CME
Dec. 9-12	<343.5-346.4	343.5	70	344.4	15	345.3	2.5 > 2.9	380-530	y/y	380-530	y/y	n	y	y	n	≈8	CME
Dec. 13-15	347.3-349.5	346.5	100	347.0	40	348.0	3.0 2.2	450-610	y/y	450-610	y/y	y/n	y	y	y	≈25	CME
April 7-9	97.9-99.2	98.0	<50	98.3	98.3	98.3	1979	...	n	...	n	n	n	n	n	≈10	cannot classify
April 15-20	105.2-110.0	106.0-108.4	400	104.0-108.4	100	107.7	12 > 4.8	?	y/y	?	y/y	n	y	y	y	≈40	CRS; CME
April 23-25	<114.5-115.2	111.5-115.8	>400	112.8-115.4	180	≤114.5	≥10 > 0.7	?	y/y	?	y/y	y/y	n	y	m	≈60	CRS; CME + shock
April 28-29	118.-119.2	117.2	800	117.9	700	118.6	8.0 0.8	330-470	n	330-470	n	n	n	y	n	...	CME
May 3-4	<123.4-124.5	≈123.0	2000	123.1	550	123.6	30 > 1.1	450-778	y/y	450-778	y/y	y/y	m	y	n	≈25	CME
May 7-9	127.3-129.6	127.2	800	127.3	300	129.4	12 > 2.3	(CME)	y/y	(CME)	y/y	y/y	n	y	y	≈57	CME no. 1
May 12-14	132.9-134.7	130.3-131.9	600	130.9-132.4	600	134.0	18	208-300	y/y	208-300	y/y	n	n	y	n	120	CME no. 2
May 26-27	146.0-147.2	145.3	800	145.5	100	146.7	3.0 1.2	320	y/y	320	y/y	n	n	...	...	...	CRS
May 28-30	>148.2-150.0	147.3	900	148.3	170	148.6	10 > 1.8	410	y/y	410	y/y	n	(m)	y	...	...	CME
June 9-11	160.5-162.3	159.6	(20)	159.8	200	161.4	2.0 1.8	380-500	y/y	380-500	y/y	y/y	n?	y	y	≥25	CME
June 11-14	≥162.3-165.8	161.7	100	162.8	(10)	165.3	2.0 > 3.5	?	y/n	?	y/n	n	n	y	y	0	possible CME
June 16-19	<167-170.3	163.4-169.6	100	162.8	20	168.6	1.5 > 3.0	260-393	y/y	260-393	y/y	n	n	y	y	17	CME
Oct. 17-19	290.1-292.9	290.3	400	290.6	30	291.3	5.0 > 2.8	415-600	y/y	415-600	y/y	n	y?	y	n	≈8	possible CRS
Oct. 30-31	≤302.2-304.3	303.0	200	no data	70	303.4	13 > 1.1	686	y/y	686	y/y	y/y	m	y	n	20	CME; shock?
Nov. 1-2	≤305.4-306.8	<305.3-306.1	1000	no data	306.3	306.3	37 > 1.4	553	y/y	553	y/y	y/y	...	...	...	...	CME + shock
Nov. 3-4	≈307.2-308.3	306.8-307.6	1000	no data	307.8	307.8	20 1.1	574	y/y	574	y/y	y/y	n?	y	n	53	CME + shock
Nov. 5-6	309.0-310.2	308.7-309.2	1200	no data	309.4	309.4	30 0.8-1.2	477	y/y	477	y/y	m	...	...	...	...	CME; shock?
Nov. 6-8	310.7-312.2	<310.4-310.8	(4000)	no data	311.3	311.3	20 0.5-1.5	405	y/y	405	y/y	m	n	m	n	<5	CME; shock?
Nov. 10-12	314.3-316.8	315.7	(3000)	no data	315.8	315.8	20 < 2.5	358	y/y	358	y/y	n	n	y	y	≈20	CME
Nov. 17-18	321.2-322.0	320.3	(3000)	no data	321.3	321.3	6.0 0.8	343	n?	343	n?	n	n	m	n	≈7	CME; shock?
Nov. 21-23	325.7-327.2	326.2	(40)	no data	326.8	326.8	5.0 1.5	?	y/y	?	y/y	n	n	y	m	<5	CME; shock?
Nov. 23-26	327.9-330.6	328.0	(800)	no data	329.8	329.8	8.0 2.7	332	y/n	332	y/n	n	n	y	n	<5	CME; possible CRS
Nov. 26-28	330.6-332.0	329.9	200	no data	331.2	331.2	7.0 1.0-1.4	396	y/y	396	y/y	n	n	y	y	15	CME

DOY is day of year; y(yes), n(no), and m(maybe).



To be classified as a mass ejection, an event must move progressively outward from the Sun. Thus in the Helios view it would have to appear first in the photometer viewing  $16^\circ$  ecliptic latitude, then successively later in the  $31^\circ$  and  $90^\circ$  photometers (refer to Figure 1). The speeds represented by the successive time delays also had to be reasonable (i.e., hours to several days). Typically, mass ejections could be observed in the lower photometers to move outward simultaneously both to the east and west of the Sun prior to reaching the  $90^\circ$  photometer field of view. Corotating regions were identified as structures which moved at roughly the solar rotation rate progressively from east to west of the Sun before and after passing through the  $90^\circ$  photometer view. Operationally, this distinction was usually easily made by observing on the sector time series plots of each photometer whether the peak brightness of an event occurred at the same time in each sector (a mass ejection), or at successively later times in more westward sectors (a corotating region).

Each month of reduced Helios 2 photometer data are available on one tape from Goddard Space Flight Center (GSFC); there are a total of 43 such tapes. Since the processing of these tapes is very time consuming, we reduced the data from only a small number of them for 56 of the 70  $90^\circ$  events that were representative of the sample over the eight spacecraft orbits. These reduced data were then edited to place straight-line baselines through the time series, and the  $16^\circ$  and  $31^\circ$  photometer time series displayed for approximately 8-day stretches of the data [see Jackson, 1985]. Data for each event were analyzed using the three polaroid and clear filters in the visual waveband, whenever available, beginning  $\sim 5$  days before the event onset at  $90^\circ$  (the  $90^\circ$  time series data centered on the event interval were similarly reduced and displayed).

Figures 3 and 4 illustrate the kinds of data displays we used to identify and classify the two main types of  $90^\circ$  photometer plasma events: solar coronal mass ejections (CMEs) and corotating structures (CRSs). Figure 3 presents "stack" plots of uncorrected photometer brightness as a function of day of year during the passage of a CME (Figure 3a) and a CRS (Figure 3b). For illustration, we have plotted only the unpolarized visual light brightness, although all of the filter data were available and were displayed on our working plots. At the top right of each figure are shown the time series data for the  $90^\circ$  photometer, and at the bottom right and left are selected individual sectors for the  $31^\circ$  and  $16^\circ$  photometers, respectively. The solar elongations of these lower photometer sectors are indicated, and their positions on the Helios image plane can be determined by reference to Figure 1b. Vertical arrows on each panel indicate the times of maximum brightness in each photometer set.

Figure 4 shows representative contour, "fisheye" images of the same two events. The data used in the contour program are the brightness versus position values at each sector center, which are shown by the small crosses. Since there is only the single data point at  $+90^\circ$ , the space above the ecliptic latitude of  $31^\circ$  is grossly undersampled. However, below this latitude the spatial coverage is relatively complete; therefore such images provide a useful method of viewing the propagation of solar-initiated interplanetary disturbances. Details on the contouring program and other examples can be found in the referenced papers by Jackson and colleagues.

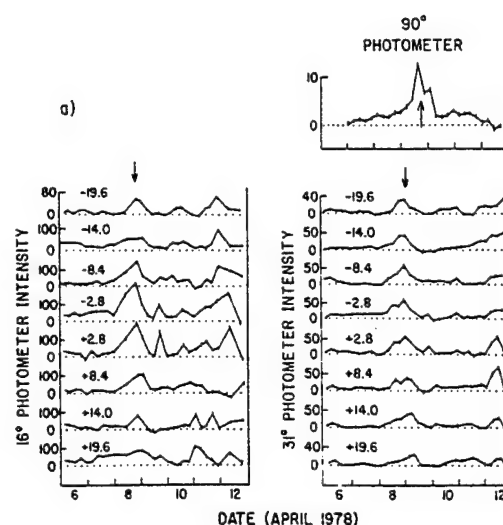


Fig. 3a. Time series intensity plots for the mass ejection of April 8–10, 1978, for the Helios 2  $16^\circ$ ,  $31^\circ$ , and  $90^\circ$  photometers. The plot ordinates are in S10 units with zero intensity denoted by the horizontal dotted lines. The stacked plots for the  $16^\circ$  and  $31^\circ$  photometers are the time series for individual sectors proceeding from east (+) to west (–) of the Sun (see Figure 1b). The ecliptic longitude in degrees of the center of each sector relative to the Sun are labeled on each graph. The short vertical bars mark the times of intensity data. The vertical arrows indicate the best estimate of the time of maximum intensity of the mass ejection in each photometer set.

The CME shown in Figures 3a and 4a exemplifies several typical characteristics of the plasma clouds we identified. As expected for material propagating rapidly outward from the Sun, the CME, as traced most easily by the times of peak brightness (Figure 3a—arrows), was observed earliest in the  $16^\circ$  sectors, then later in the  $31^\circ$  and  $90^\circ$  photometers. Its

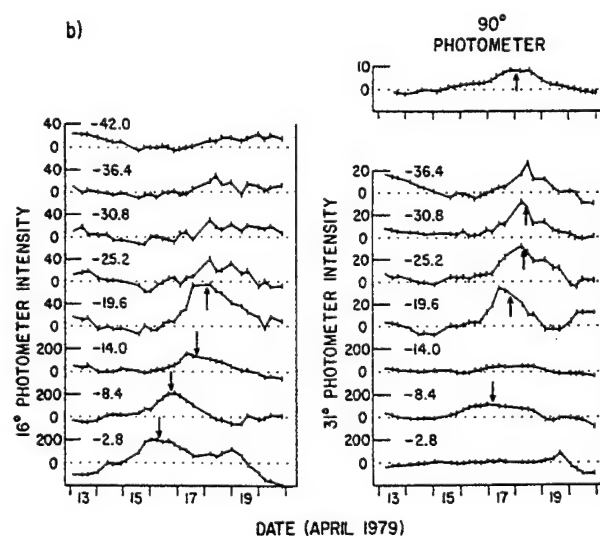


Fig. 3b. Time series plots as in Figure 3a for the corotating region of April 15–20, 1979. The vertical arrows denote the best estimates of the time of passage of the region centroid in individual photometer sectors. Note the intensity scale change as the solar elongation changes. Only the western sectors are shown here, because a CME, not clearly visible here, was also detected in the lower photometers along or just east of the Sun-spacecraft direction and obscured the data.



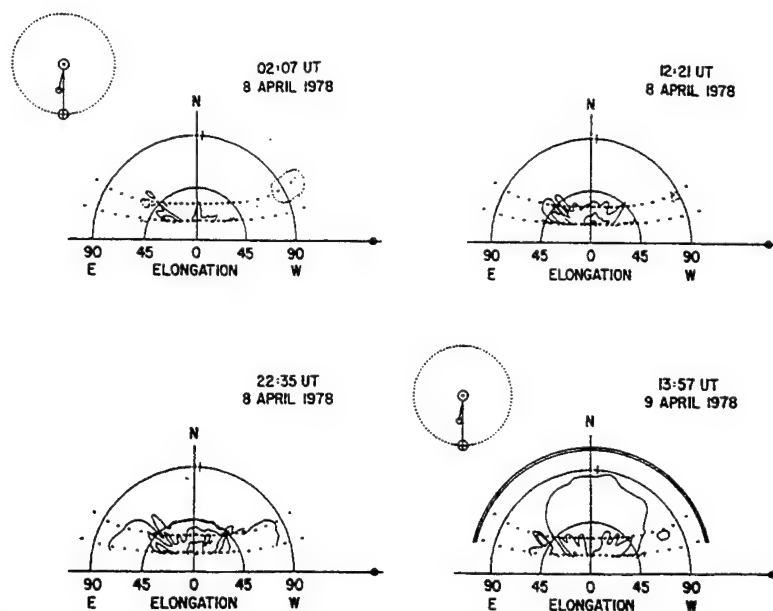


Fig. 4a. Helios 2 contour images in the same format as Figure 1b showing the evolution of the coronal mass ejection of April 8–10, 1978 (Figure 3a). In this presentation the Sun is centered and various solar elongations labeled on the abscissa in degrees form semicircles above the ecliptic plane, i.e., the horizontal line. The position of the Earth is marked “ $\oplus$ ” and the tilt angle of the solar north pole is indicated by the short line segment crossing 90° elongation. Positions of the photometer sector centers are marked by small dots. Electron column density is contoured in levels of  $3 \times 10^{14} \text{ cm}^{-2}$  increasing from a base level of  $2 \times 10^{14} \text{ cm}^{-2}$ . Negative contours below  $2 \times 10^{14} \text{ cm}^{-2}$  are dotted. The times shown are when the 31° photometer measurements were obtained. Data from the 16° and 90° photometers are interpolated to the times indicated. The small Sun-centered displays to the upper left of the images at 0207 and 1357 UT indicate the relative locations of the Earth, Sun, and Helios 2 spacecraft.

position as a function of time in a given photometer was relatively constant. The speed of 550 km/s derived for this event based on travel time between the 31° and 90° photometer elevations, and its flow duration of 1.5 days were typical of the CMEs in our study. Also, some of the CME material intersected the spacecraft where the 90° photometer measured its electron-scattered brightness as integrated along the line of sight above the spacecraft. Its primary in situ signatures at the spacecraft were density and magnetic enhancements, also typical of these events, and a preceding fast shock. The images in Figure 4a demonstrate that the CME moved out to the north of the Sun, with the larger amount of material appearing to the northeast.

The corotating structure shown in Figures 3b and 4b illustrates several typical characteristics of this class of event. As viewed in projection by Helios, these events could

be as bright and wide as the CMEs, although the best observed CRSs were elongated radially outward from the Sun and tended to be narrower. Their salient, distinguishing characteristic on the stack plots (Figure 3b) is a uniform progression in time of the bright core to successively westward sectors in a given photometer. We have shown only the western (negative) sectors for this event, because a CME obscured the CRS near the Sun. However, all of the events we identified as CRSs were observed first east then west of the Sun and therefore could not be mistaken for, say, off-limb CMEs. This characteristic movement is as expected for a streamerlike structure rooted at the Sun and rotating with it from east to west [e.g., Jackson, 1990]. When these structures swept by the spacecraft, they were typically associated in situ with density enhancements and rotations of the interplanetary magnetic field (IMF).

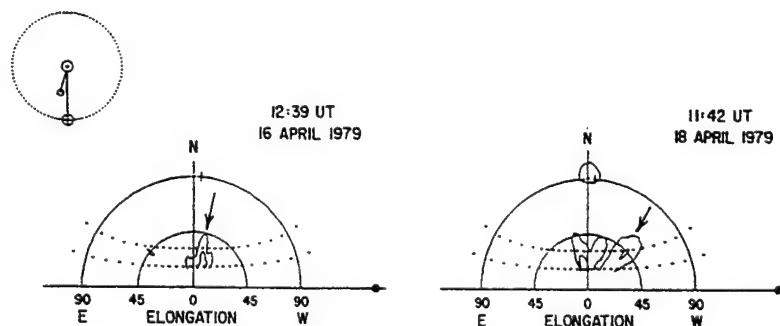


Fig. 4b. Helios 2 contour plots as in Figure 4a showing the elongated corotating region of April 15–20, 1979, shown in Figure 3b. Arrows depict the feature at the two times displayed as images demonstrating the projection effect of a relatively stationary structure corotating with the Sun.

### 3.3. Comparative Analysis of in situ Solar Wind Data During the Photometer Events

We also examined the in situ solar wind plasma and IMF data from Helios 2 and, occasionally Helios 1, during the time intervals of the 90° photometer white light events. Our purpose was to discover how many of the white light events, which were viewed remotely, actually intersected the spacecraft and what their characteristic signatures in the solar wind were. In particular, we searched for features which have been considered as possible signatures of coronal mass ejections in the solar wind, such as density enhancements, fast shocks, shock driver gas, magnetic clouds, and IMF magnitude enhancements and/or rotations [Gosling, 1990]. We also noted when the spacecraft crossed sector boundaries. The primary data we used were 1-hour averages of the Helios plasma and IMF data through 1980 that are available on a tape from the NSSDC. The plasma data are from the plasma analyzer of the Max-Planck Institute branches at Garching and Lindau, Federal Republic of Germany [Schwenn, 1983]. The IMF data are from the fluxgate magnetometers of the Institut für Geophysik und Meteorologie der Technischen Universität Braunschweig, Federal Republic of Germany, and the University of Rome and GSFC [Mariani *et al.*, 1987]. The Helios shock data are from a preliminary list of fast forward shocks provided courtesy of R. Schwenn (private communication, 1986); a description of a subset of these shocks was published by Volkmer and Neubauer [1985].

We printed out the hourly averages of all the pertinent plasma and IMF data from the Helios tape. We also produced computer plots of the plasma proton number density, temperature, and flow speed and the IMF magnitude and polar and azimuthal angles during multiple-day intervals encompassing all of the initial 70 90° events. We then examined the solar wind data during each of the white light intervals and tabulated the occurrences of the in situ transient phenomena noted above.

We selected the in situ features of interest occurring during the white light intervals as follows. Notable density enhancements were defined as distinct increases in the hourly proton number density having amplitudes above the background of at least  $10 \text{ cm}^{-3}$  (unnormalized). Most of the increases were much larger than this. Similar increases in the IMF magnitude of  $\geq 10 \text{ nT}$  were recorded, as well as large and systematic ( $\geq 50^\circ$ ) rotations of the IMF, as evidenced by changes in either or both of its polar and azimuthal components. We defined candidate "magnetic clouds" [Klein and Burlaga, 1982] to include periods of smooth, long-enduring (on the order of 10 hours or more) enhancements in the IMF magnitude associated with significant field rotations in one or both of the IMF components. Sector boundary crossings were signified by an abrupt  $\sim 180^\circ$  swing in the  $B_\phi$  IMF component and, as expected, were usually accompanied or followed by enhancements in both the density and IMF magnitude [Hundhausen, 1972]. Finally, we also noted the occurrences of evidence of so-called "driver gas" [e.g., Zwickl *et al.*, 1983]. With the parameters available to us we defined driver gas to include a period of increased  $B$ , increased flow speed, decreased temperature, and, possibly, the characteristics of a magnetic cloud.

Figure 5 provides examples of the solar wind data during the two white light events discussed above and in Figures 3

and 4. These graphs are representative of the kinds of in situ signatures we found for the two primary photometer event classes, CMEs and CRSs. Figure 5 shows the important plasma and IMF parameters during several days around the time intervals of the photometer events. The horizontal bars on the density panels indicate the uncertainty in the time of the white light peak in the 90° photometer data.

Figure 5a shows the solar wind data during the interval of passage of the CME of 8–10, April 1978, shown in Figures 3a and 4a. At the time of the peak white light brightness the in situ density and magnetic field increased following the passage of a strong shock. The IMF enhancement, which had a peak amplitude of 48 nT, was characteristic of a magnetic cloud, with a long-lived increase in the IMF magnitude from the time of shock passage through April 9 and a large, smooth rotation of the polar angle,  $B_\phi$ , from April 9, 16 hours to April 10, 3 hours. This event also exhibited a large rotation of the  $B_\phi$  component during the same period. A rotation of either or both IMF components is to be expected since a priori there is no reason to expect the loop(s) represented by the cloud or CME to lie in any preferred plane with respect to the ecliptic. The passage of the CME was accompanied by a rise in the flow speed and a decrease in the proton temperature, which is also characteristic of the passage of such clouds and of shock driver gas. The event followed, but is separate from and not to be confused with the Helios 2 crossing of an interplanetary sector boundary at 1600 UT on April 8.

The timing of the enhancement in each of the photometers and the in situ density increase and shock, and the abruptness of the white light increase suggest that the photometers detected emission from the region of compressed plasma at or just behind the shock front. Such an interpretation has been made for some other Helios photometer events [Jackson, 1986]. With these moderate time resolution data we cannot distinguish whether such abrupt photometer increases are due to the shock-compressed plasma or to the CME/driver gas following it. However, in terms of identifying a CME this difference is academic, since nearly all transient interplanetary shocks are likely driven by CMEs [Sheeley *et al.*, 1985; Cane *et al.*, 1987].

The solar wind data during the time interval of the passage of the CRS on April 15–20, 1979, illustrated in Figures 3b and 4b, is shown in Figure 5b. This figure illustrates the Helios 2 crossing of another sector boundary after 0800 UT on April 17. The 90° photometer increase was double peaked with the first rise occurring in the compression region following the crossing and accompanied by large variations in  $B_\phi$  and  $B_\theta$ . The second white light peak was associated with a sharp peak in the in situ density and possibly a small magnetic cloud. Both of the density increases were very large. No fast shock was detected during this period. One or both of these peaks were likely associated with the CRS and possibly a CME detected in the lower photometers.

## 4. RESULTS

### 4.1. Classification of the White Light Events

In this section we present the basic results of our analysis of the classification and characteristics of the Helios 2 90° photometer events. We place particular emphasis on the most common class, that of coronal mass ejections.

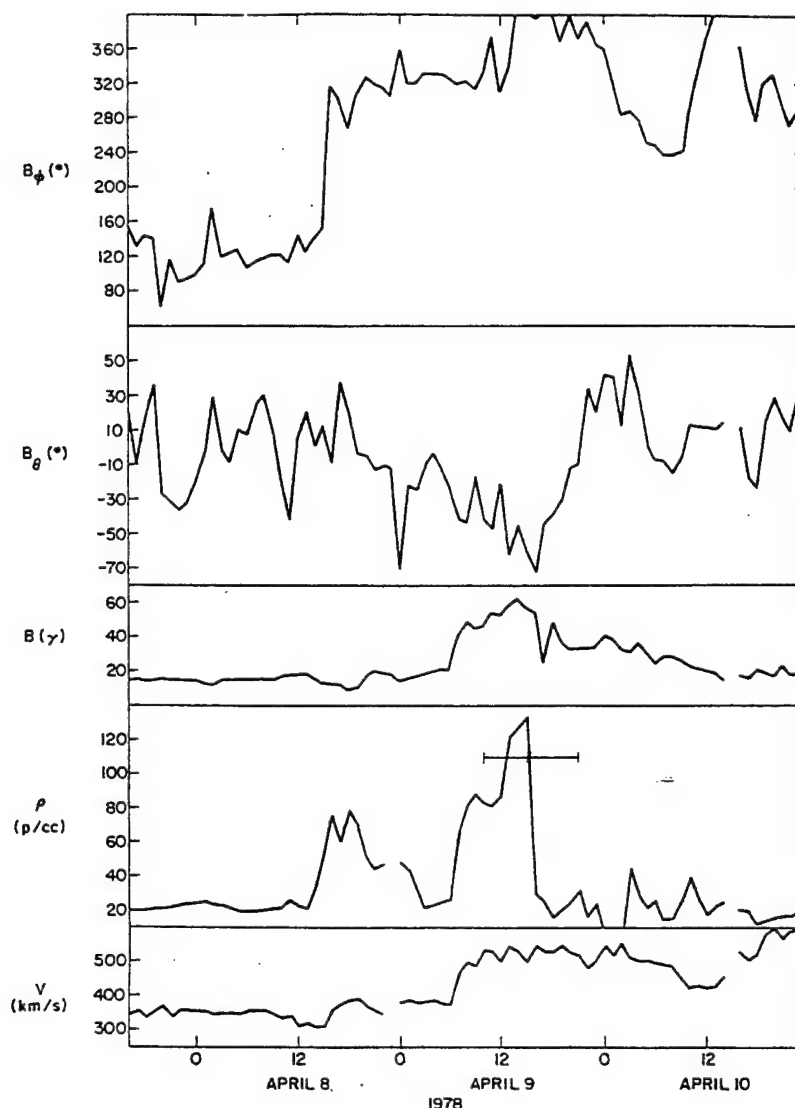


Fig. 5a. Helios 2 in situ solar wind data during the time interval of the white light mass ejection of April 8–10, 1978, viewed remotely from Helios at 0.51 AU and shown in Figures 3a and 4a. Plotted from top to bottom are 1-hour averages of the azimuthal and polar components and the amplitude of the IMF, the plasma proton density, and the flow speed. The horizontal bar on the density panel indicates the uncertainty in the time of the white light peak and extends from the last previous photometer observation to the next one following the peak value. A strong shock passed the spacecraft at 0716 UT on April 9 and was followed by a long-lived density enhancement and a magnetic cloud, signified by the long-lived enhancement of the IMF amplitude and the smooth rotation of both of the IMF components. The time of the photometer peak was coincident within the uncertainties with these in situ enhancements. Note the sector boundary crossing at 1600 UT on April 8, 15 hours before the shock and 22 hours before the white light peak. It is signified by the abrupt  $\sim 180^\circ$  swing in  $B_\phi$  and the first density enhancement.

Table 1 is a summary compilation and an event classification for the 56 events which satisfied our criteria discussed earlier. Reading from left to right, the data are presented in seven main groups. The table is keyed to the first group, the date and time of the event observed with the  $90^\circ$  photometer. In the second column the time interval from the onset to the end of the  $90^\circ$  event is listed by day of year (DOY). All times are listed in decimal parts of a day. In the next three groups we list the peak times and brightnesses of the events successively as observed in each of the photometers. The brightnesses ( $\delta I$ ) are in S10 units above the preevent background as estimated from a straight-line fit through approximately 8-day periods of the data. These values are unnor-

malized for distance from the Sun but have been corrected for zodiacal light and star background (section 2).

A given  $90^\circ$  event may be associated with one or two distinguishable lower photometer events. If there were two events or two classes of events, then two values of each parameter may be listed if they could be determined separately. A range of peak times is usually listed for the CRS events, since they were of relatively constant brightness and visible from the spacecraft over several days. There were no data available from the  $31^\circ$  photometer during most of Orbit 8, after October 1979. In the ninth column we list the event duration in days, which is the difference between the end and onset times of the  $90^\circ$  event in column 2. Estimated speeds

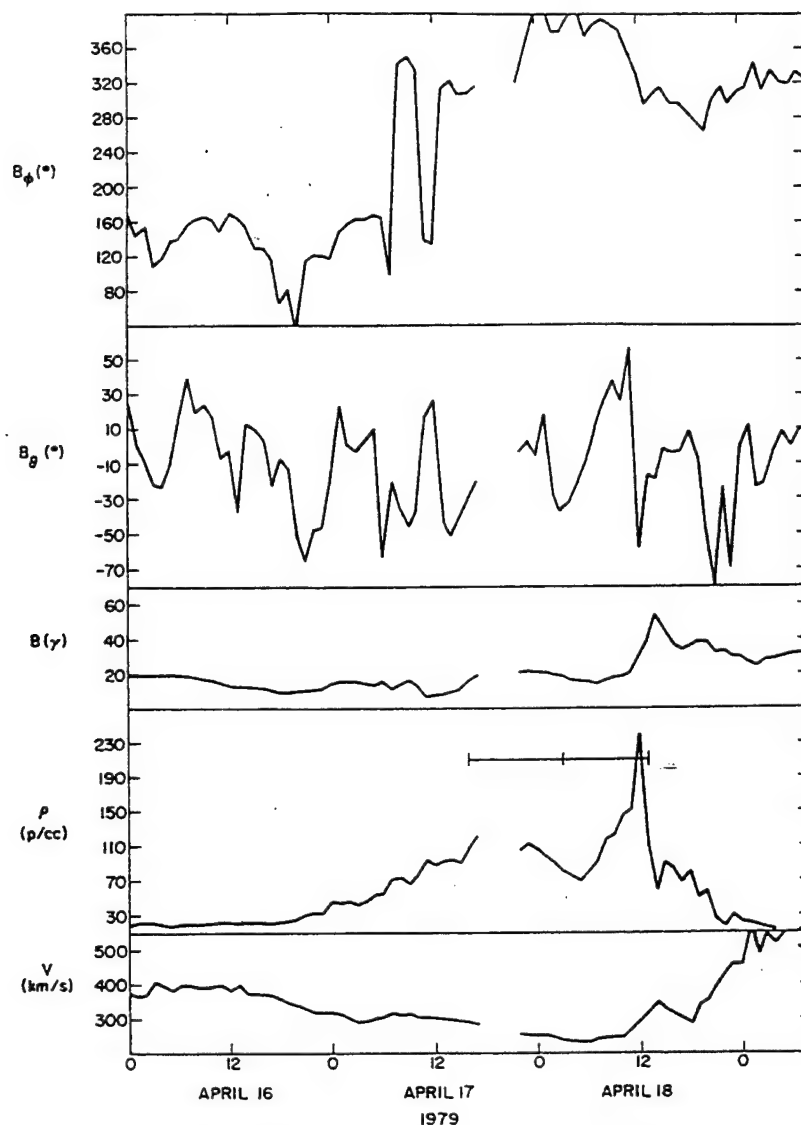


Fig. 5b. Helios 2 solar wind data, at 0.50 AU, as in Figure 5a during the time interval of the passage of the corotating white light structure on April 15–20, 1979, shown in Figures 3b and 4b. The photometer event occurred during the passage of a sector boundary at 0800 UT on April 17. There were two 90° photometer peaks which coincide with the two in situ density peaks on April 17 and 18. The first rise occurred in the compression region following the sector crossing. The second density peak was very large and sharp (note the density scale) and associated with a magnetic cloud (note the complete rotation in the IMF  $B_\theta$  component). One of the enhancements may have been associated with a CME which was detected in the lower photometers near or east of the Sun/spacecraft direction.

for the events are listed in the next column. These are based on the difference in times between the peak brightness in any two photometers: 16°–31°, 31°–90°, and 16°–90°. For CMEs a range is given denoting the extrema of the three pairs; a single speed is given if good data were available from only one pair. For CRSs a single speed is given and is derived by modeling the outward material flow of each event [see Jackson, 1990].

Group number 6 in Table 1 summarizes the results of our comparison of the in situ solar wind data during the time intervals of the white light events (section 3.3). The columns answer the question (yes, maybe, no) of whether or not at least one of the given characteristic features occurred within the time span between the onset and end of the 90° photometer event. The features of interest are a significant density enhancement, a fast forward shock, a sector boundary crossing, a smooth, large rotation of either or both of the

IMF polar and azimuthal angles, and a magnetic cloud. If a density enhancement or fast shock definitely (y) or possibly (m) occurred in the interval, then a second letter follows the first indicating whether or not the density increase or shock occurred within about  $\pm 5$  hours of the white light peak. If so, then we consider it to be within the time resolution of the photometer data and therefore coincident with the peak. Finally, the amplitudes of any relatively rapid increases in the IMF magnitude  $\delta B$  during the interval are given in the last column of the group. Dashed lines in any of these columns means that the IMF data were missing or inadequate to make an assessment. Further details of the solar wind study are discussed in section 4.4.

Finally, in the last column we give our determination of the classification of the event based on data from all of the photometers. We can see from Table 1 that nearly all of the classifiable 90° photometer events were either definite or

TABLE 2. Classification of Helios Photometer Events by Orbit

Year	Orbit	Events		CME		CRS	
		Total	Sample	Definite	Possible	Definite	Possible
1976	1	5	3*	0	0	1	1
1976	2	0					
1977	3	5	3	2	0	1	0
1977	4	10	7	3	3	2	0
1978	5	17	12	9	1	3	0
1978	6	8	8	6	1	1	0
1979	7	12	12†	8	1	4	1
1979	8	13	11	11	0	0	1
Total		70	56	39	6	12	3

\*Comet West was detected during this orbit as one of the 90° events.

†One of the events during this orbit could not be classified.

possible CMEs or CRSs. Exceptions include the observations of Comet West in March 1976 which was identified and discussed by *Jackson and Benensohn* [1990]. Also, the April 7–9, 1979, 90° event was faint and could not be clearly identified in the lower photometers, partly because of incomplete data. Therefore 54 of the 56 white light events could be classified as either CMEs or CRSs. In Table 2 we tabulate the number of events by orbit number and the breakdown by class of the 54 CME or CRS events. We conclude that at least one definite or possible CME was responsible for the 90° event in 80% (45 of 56) of the cases, and a definite or possible CRS in 27% (15 of 56). There are overlaps between the classes, since a given 90° event could be associated with one or more events of different classes. Thirty-five (7) of the 56 white light events were associated with only a single definite CME (CRS).

Thus we see that most of the white light transients detected and imaged by the Helios 2 photometers during this period could be classified as outwardly moving electron plasma clouds, or mass ejections. Also, most of these remotely imaged ejections were also detected as in situ density enhancements at the spacecraft. We are convinced from the Helios data alone that these structures are the interplanetary manifestation of the well-known solar CMEs.

However, to confirm our assessment of the Helios mass ejections as true CMEs, we performed a comprehensive survey of the association between the Helios "CME" events and CMEs detected near the Sun in 1979 by the Naval Research Laboratory's (NRL) Solwind coronagraph. Solwind was launched in March 1979 and its observations of CMEs near the Sun overlapped in time with the Helios 2 photometer observations on Orbits 7 and 8 in 1979 from March to early May and from late October to December. The field of view of the coronagraph extended to 10  $R_s$ , whereas the inner limit of the closest approach to the Sun of the line of sight of the Helios 16° photometer ranged from 17 to 57  $R_s$ . Especially during the period around perihelion, this gap was minimized and associations could be made with higher confidence. Several of the largest Helios events observed during 1979 have previously been associated with Solwind CMEs [e.g., *Jackson*, 1985; *Jackson et al.*, 1988; *Webb and Jackson*, 1988].

We began with the 19 90° photometer events in 1979 from Table 1 that included at least one event that we classified as a definite Helios CME (thus the June 9–11 event was excluded). We note that for 15 of these events (y/y in column

13) there was a density enhancement coincident with the 90° photometer peak suggesting that the plasma event intersected the spacecraft; seven of the events also had coincident fast shocks (y/y in column 14). Although not required for our association study, the occurrence and timing of the shocks and related particle events were helpful in making the solar associations.

For these 19 photometer events we constructed height/time diagrams that are similar to the one displayed in Figure 9c of *Jackson et al.* [1988] for the May 7–9 event. In these diagrams the peak times and durations of the events at each photometer height are plotted in  $R_s$ ; the time is that of the brightest signal in the sectors nearest the Sun. The heights are calculated on the assumption that the bulk of the material observed by each photometer is moving in a direction perpendicular to the closest approach of the line of sight to the Sun [*Jackson and Leinert*, 1985]. Extrapolation of a best fit line through the heights of the photometer peaks to below 10  $R_s$ , then provides a first-order indication of the temporal window in which to search for candidate associated CMEs. We also plotted the times of the shocks and prompt particle events as detected at the spacecraft. The particle data are from the Helios experiments of the Universitaet Kiel, Federal Republic of Germany (G. Wibberentz, private communication, 1988) and are useful in determining the onsets and locations of their sources at the Sun.

We then searched through a recent version of the Naval Research Lab (NRL) Solwind CME list provided by R. Howard (private communication, 1989) for CMEs which occurred at northern heliolatitudes within a time interval of about 1 day before to 1 day after the extrapolated Helios onset time. The photometer time series plots and images were helpful in estimating from which hemisphere or limb (i.e., east, west, or over the pole) the CME arose. Times of limited or missing Solwind coverage were also marked. With these restrictions there usually remained only one or two Solwind CMEs as candidates for association with the Helios event. The occurrences of large optical and/or X ray flares and metric type II bursts were also noted.

Table 3 is a list of the resulting associations between the Helios 2 events which we classified as CMEs and Solwind CMEs, flares, and type II bursts. The table contains the date and peak time of the 90° event followed by the association data for the CMEs, flares, and radio bursts. Each category is preceded by a column giving our assessment (yes, maybe, no) of whether or not the photometer event was associated

TABLE 3. Association of Helios 2 Classified CMEs in 1979 With Solwind CMEs and Other Solar Activity

90° Event		CME				Flare				Type II				
Date	Peak Time, day of year	Solwind CME	Onset Time	Position	Span, deg	Speed, km/s	Class	Flare	Onset Time	Position	Imp.	II	Onset Time	Notes
April 15-20	107.7	...	(no Solwind data)					n?	113, 0234	S35E07	1F	n	113, 0207	1
April 23-25	≤114.5	n						y	(≥112, 2200	S20E10	DSF)	y		
April 28-29	118.6	y	117, 0640	N80E	80	690P	Y, U	y	117, ≈0630	N18E17	1B, X1.5 LDE	y	117, 0644	2
May 3-4	123.6	...	(no Solwind data)					y	122, ≈1300	N45W	2B, M9 LDE	y	122, 1659	3
May 7-9	129.4	y	144, 1555	N45E	110	1000A	Y, L, H $\alpha$	n	127, 1330	N35WL	(EPL), C1.5 LDE	n		4
May 26-27	146.7	y	(same source event; see note)					n	probable backside flare			n		4
May 28-30	148.6	y	161, 0850	N75W	40	450P	Q, F	y	161, 0830	N22W46	3B, X1 LDE	y	161, 0902	
June 11-14	165.3	(m)	288, ≈1730	N85E	35	100E	Q, MS	m	290, 0040	N26E43	?N, C8 LDE	n		
Oct. 17-18	291.3		(limited Solwind coverage)					m	possible backside flare			n		
Oct. 30-31	303.4	m	302, 0730	N90	80	650F	Q, MS	m	several candidate flares; could be backside event			n		
Nov. 1-2	306.3	y	305, 0630	N65E	130	1420G	Y, CF, H $\alpha$	n	probable backside flare			n		
Nov. 3-4	307.8	y	306, 2235	N35E	100	≈1500	Q, U	n	probable backside flare			y	306, 2257	5
Nov. 5-6	309.4	y	308, 0500	N40E	100	≈1650	Y, MS	(y)	308, 0500	?	C9 LDE	y	308, 0510	6
Nov. 6-8	311.3	y	310, 0430	N30E	140	≈685	Y, CF, H $\alpha$	m	310, 0511	N19E11	IN, X1 LDE	m	310, 0516	
Nov. 10-12	315.8	y	315, 0840	N75E	50	260P	Y, SB	m	315, 0900	N15E45	-B, M2 (blend)	n		7
Nov. 17-18	321.3	y	319, 2140	N42W	110	1200G	Y, ML	(y)	319, 2130	N29W35	2B, M2 LDE	y	319, 2147	8
Nov. 21-23	326.8	(n)	(limited Solwind coverage)					y	325, 0650	?	M3 LDE	y	325, 0650	
Nov. 23-26	329.8	y	327, 0900	N75W	90	295F	Q, MS	y	327, 0904	N33W68	-F(No XR data)	n		
Nov. 26-28	331.2	y	329, 0600	N50E	40	470	Q, F	m	329, 0640	N31W90	IN, C2	n		

Here y(yes), n(no), and m(maybe). Notes are: 1, Well-studied interplanetary shock/particle event directed earthward. Source considered to be a DSF/flare near Sun center. (See discussion and references of *Cane et al.* [1986]). The Helios 2 event is described by *Jackson* [1986]; 2, Another interplanetary shock/particle event directed earthward (Discussed by *Jackson* [1988]); 3, Well-studied Helios event (see *Jackson et al.*, 1988); 4, Well-studied May 24 CME and interplanetary event [see *Sheeley et al.* 1981, 1982; *Jackson et al.*, 1985; *Jackson*, 1988]. The second Helios 2 90° event peaking at 148.6 is attributed to a later phase of the same ejection; 5, No reported H $\alpha$  flare. *Kahler et al.* [1985] suggest that this flare occurred in a backside active region  $\geq 15^\circ$  over the east limb; 6, The type II burst was associated with the flare. Since it was near Sun center, it is uncertain if the flare was associated with either the CME or Helios 2 event; 7, This flare/CME was the source of proton events at Helios 1, Helios 2, and at Earth; 8, This Helios 2 event was minor and is confused with a large earlier event seen at both Helios 1 and 2. Proton events at Helios 2 and the Earth suggest a western hemisphere source; the lack of a reported H $\alpha$  flare suggests the source region was over the west limb.



with the earlier class of solar activity. Since we believe there was a single source event for both of the May 26 and 28 photometer peaks (see note 4), we are left with 18 periods in which to search for associated solar events. From Table 3 we see that for 14 of these periods there was good Solwind coverage, for two there was limited coverage, and for two there were no Solwind data. During 12 of the 14 periods with good coverage, or in 86% of the potential cases, we found a good association between a Solwind CME and the Helios CME. In the other two cases there was evidence of possibly associated activity. No CME was observed for the April 23 event, but the source for this well-studied event is known to be a disappearing filament, flare, and type II burst from near Sun center where a CME is less likely to be detected by a coronagraph (see Table 3, note 1). The October 30 event had several candidate CMEs and flares and probably had a backside source. Nine of the 18 periods had well-associated optical and/or soft  $X$  ray flares, an expected rate for frontside versus backside near-surface events. The associated flares were energetic, typically having optical importances  $>1$  and  $X$  ray fluxes  $>M1$ , and 7 of 8 (there were no available  $X$  ray data for one event) were long duration  $X$  ray events (LDEs). Eight of the 18 periods had associated type II bursts, which are indicative of fast CMEs.

So a good association between the Helios CME and a solar CME or CME proxy was found for 13 of the 14 periods of good coverage. This degree of association is statistically highly significant. We found that major Solwind CMEs typical of these events (see below: class Y or Q, span  $\geq 45^\circ$ , northern heliolatitudes) occurred at a rate of 0.30/day in a 1979 control sample. During 14 periods of good Solwind coverage this rate would yield a random association of 4.2 CMEs, whereas 12 (of 14 or 86%) CMEs were actually found to be associated with the Helios CMEs. Therefore since nearly all of the photometer events in 1979 classified as heliospheric CMEs were, in fact, associated with CMEs near the Sun, we feel justified in making the assumption that our CME classification of the photometer events is correct. As further justification, we demonstrate in the next section that the annualized rates of occurrence of the Helios and Solwind CMEs for 1979 are consistent with each other.

It is of interest to compare some characteristics of the energetics of the associated solar events with those in other recent studies involving interplanetary disturbances. The extrapolated onset times, central axis limb positions, latitudinal spans, speeds, and morphological classes of the associated Solwind CMEs are given in columns 4–8 of Table 3. These parameters were taken directly from the NRL/CME list or were modified by M. Koomen (private communication, 1988). The NRL definitions and classifications were discussed by Howard *et al.* [1985]. The 12 well-associated Solwind CMEs were, on average, wider ( $86^\circ$ ) and faster ( $815$  km/s) than normal. They also tended to be "major" CMEs, with eight Y class events and four of Q class. In addition, as noted above, they were associated with energetic flares with long  $X$  ray durations and with type II bursts, which are indicative of coronal shocks. All of these characteristics are now known to be typical of the CMEs associated with large interplanetary disturbances, such as shocks [Sheeley *et al.*, 1985; Woo *et al.*, 1985; Cane *et al.*, 1987], interplanetary scintillation events [Watanabe and Kakinuma, 1984], and prompt proton events [Kahler *et al.*, 1978, 1984].

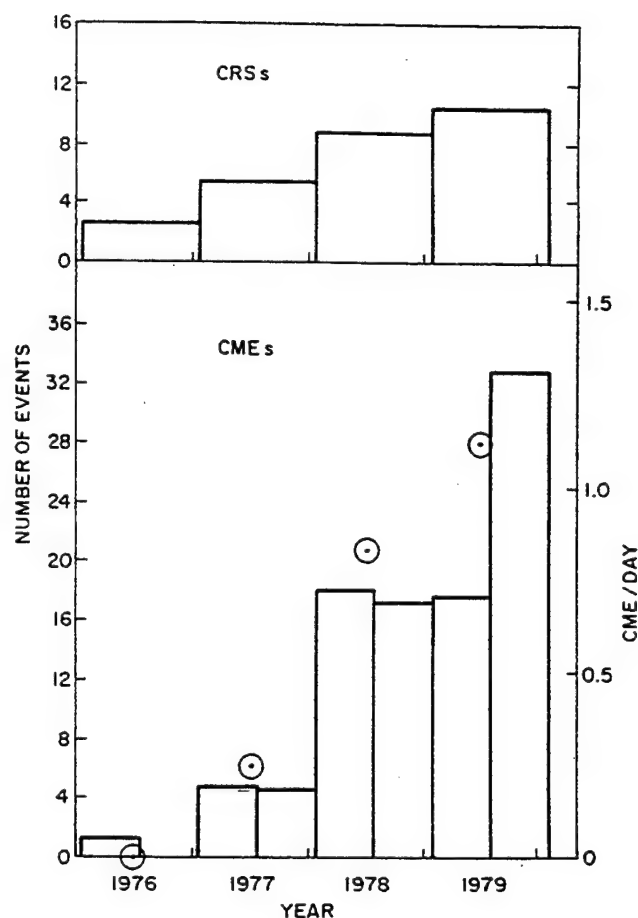


Fig. 6. Histogram showing the frequency of occurrence of coronating structures (top) and coronal mass ejections (bottom) detected by the Helios 2  $90^\circ$  photometer from 1976 through 1979. The number of CMEs is summed for each orbit of the spacecraft (left-hand scale), whereas the number of CRSs is summed in two-orbit bins for statistical purposes. All values have been corrected for the instrument duty cycle. The four circled points represent the daily Helios 2 CME occurrence rate (right-hand scale) averaged over each year and corrected for the instrument visibility function as described in the text.

#### 4.2. Annual Variation of the Helios CME Occurrence Rate

We have provided evidence that the Helios 2  $90^\circ$  photometer detected most CMEs, as well as some other plasma sources, ejected toward or passing north of the spacecraft. Likewise, with this method we will miss events passing at large near-ecliptic elongations from the spacecraft or entirely south of it. With appropriate corrections, we can use these results to estimate the frequency of occurrence of solar CMEs during the long gap in conventional coronagraph coverage from 1976 to early 1979. We will also compare the rates of occurrence obtained by the Helios and Solwind instruments in 1979 as a check on the consistency of our results.

In Figure 6 we display the frequency of occurrence of the Helios events in several ways. The number of CRS (top) and CME (bottom) events have been plotted separately. In addition, the annualized, average daily rates for the CMEs (circled points) have been plotted for ease of comparison with other published CME rate data. These data have been



corrected for the instrument and spacecraft duty cycle by accounting for segments of missing data covering periods of greater than several consecutive days. This correction could be large and increased on successive orbits because the photometer data were downlinked less often later in the mission. This is because the spacecraft solar panels produced less power as they aged, so that it was necessary to turn off some experiments, including the photometers, when the spacecraft was farthest from the Sun. The rates were also adjusted according to the observed CRS/CME fraction per orbit to account for the extra 90° events for which we did not obtain the lower photometer data. Plotted are the corrected number of CMEs per orbit and the annual (two-orbit) values of CRSs.

In addition to the duty cycle correction, the daily CME rate data include a correction for the instrument visibility function, or the reduction in sensitivity to events away from the plane of the sky and, in the case of Helios, the view angle of the 90° photometer. Such a correction is necessary to derive CME rates which are comparable with those obtained from coronagraph data. Webb [1986] and D. F. Webb and R. A. Howard (The long-term variation of the rate of occurrence of coronal mass ejections and the solar wind mass flux, submitted to *Journal of Geophysical Research*, 1990) (hereinafter referred to as Webb and Howard, 1990) have discussed such visibility function corrections for the Solar Maximum Mission (SMM) and Solwind coronagraphs. Those authors used the heliolongitude distribution of type II/H flares associated with and without CMEs to estimate the visibility functions of the coronagraphs. Because of the heliospheric perspective of Helios, we must use a different technique to estimate the actual CME rate. Our approach was to make only a single, coarse correction for the azimuthal distribution of CMEs as follows. First, we know that nearly all of the CMEs detected by the 90° photometer also encountered the spacecraft in the ecliptic plane. We then assumed that the distribution of CMEs in azimuth is uniform and that the average longitudinal width of a CME is equal to the average CME latitudinal span of 45° [e.g., Kahler, 1987]. Thus Helios should intersect in ecliptic longitude only 45/360 of all CMEs. We therefore multiplied the annualized rates by a factor of 8 to yield the total daily CME rates shown in Figure 6. (We made no other corrections, such as for the large number of CMEs that were missed because they passed south of or at large elongations from the spacecraft, for the probable expansion of CMEs in the heliosphere, or for any possible effect of detectability with the varying distance of the spacecraft from the Sun. However, to first order, these corrections must generally cancel each other, since we show next that the 1979 Helios and Solwind CME rates were in agreement.)

Webb and Howard [1990] have determined two annualized CME rates from the Solwind data, a rate for "major" (Y + Q) CMEs and a higher rate for all observed CMEs (including the "minor" events of N class). Their annualized, corrected rates for 1979 were 1.0 and 2.0 CME/day respectively. Our equivalent Helios rate is 1.1 CME/day, which lies between the two Solwind rates and thus supports our method of correction. Furthermore, the near equality of the 1979 Helios and "major" Solwind CME rates suggests that it is the larger and more energetic CMEs which result in obvious disturbances in the interplanetary medium. This is also consistent with other studies comparing interplanetary

turbances with CMEs. For example, Gosling [1990] considers bidirectional streaming electron events such as observed with ISEE 3 to be the "best" interplanetary signature of CMEs. We derive an equivalent rate of 1.1 per day if we make the same azimuthal correction to his occurrence rate of bidirectional electron events (BDEs) observed from late 1978 to late 1982. We conclude that the results from our association and occurrence rate studies lend confidence in the use of the Helios photometer data to detect and count CMEs in the heliosphere.

Figure 6 shows that the occurrence rates of both the CMEs and CRSs increased with time, with a sharp rise after 1977, from the solar activity minimum in 1976 to its maximum in 1979–1980. (Again, we emphasize that with the photometer time resolution, we cannot distinguish whether sharply peaked events are due to shock-compressed plasma or to CME/driver gas following it. But, since transient interplanetary shocks are driven by CMEs, the CME occurrence rates will be unaffected.) The importance of using the Helios photometer data to detect CMEs is exemplified by Figure 3 of Webb and Jackson [1988] in which they plotted the annualized CME rate over the last solar cycle. The Helios data provide the only CME data available during the rise of cycle 21. The Helios rates closely track the coronagraph rates near the maximum in 1979–1981, and indicate that the CME rate traced that of the solar activity cycle in general and varied from minimum to maximum by at least an order of magnitude [Webb and Howard, 1990].

The occurrence rate of the white light corotating structures definitely identified in this study increased much less during this period, by about a factor of 3. This is consistent with these features being the interplanetary manifestation of coronal streamers, since Sime [1985] found a similar increase during the same period for coronal streamers detected by the ground-based High-Altitude Observatory (HAO) *K* coronameter. However, the lower photometer data are better suited for study of these features and further discussion of CRSs is beyond the scope of this paper. In a separate study using a more complete set of the Helios photometer data, Jackson [1990] has identified and modeled many more such structures.

#### 4.3. Characteristics of the Helios Photometer Mass Ejection Events

In this section we summarize the measurements of several key CME parameters made with the photometer data and compare them with similar data obtained near the Sun from coronagraph observations. Speed and width are the two CME parameters which can be unambiguously measured on sequences of coronagraph images. These parameters represent values as projected on the plane of the sky. Speeds are determined by appropriate fits to, usually, radial measurements of the leading edge of the CME on height/time plots. A constant speed (i.e., a straight-line fit on such plots) is typical for CMEs near the Sun. CME widths or spans are measured as the difference in position angle, or latitudinal spread, between the edges or outer boundaries of the CME at a fixed height. Because of the more three-dimensional heliospheric perspective, it is difficult to derive similar measurements of these parameters with the Helios photometers which can be directly compared with the coronagraph data. In section 4.1 we discussed briefly these measurements, and here we present the detailed statistical results.

The speeds of CMEs determined from the photometer data are based on the difference in times between the peak brightnesses in the different photometers. For the 16° and 31° photometers the peak brightnesses of the CMEs were measured in sectors 1 and 32 nearest the Sun. Listed speeds measured by coronagraphs usually refer to the leading edge of the CME; however, the onset time of the CME in the photometer data cannot be as reliably determined as the peak time. The height of the material is calculated on the assumptions that the bulk of the material observed by each photometer is moving in a direction perpendicular to the closest approach of the line of sight to the Sun and that the material moves through the line of sight of the 90° photometer. These assumptions do not take into account any systematic latitudinal effects in the propagation of the bulk of the material, such as its geometrical distribution or the heliolatitude of the source region. A height/time diagram is then constructed, in which the peak times and durations of the events at each photometer height are plotted in  $R_s$ , and speeds are calculated based on straight-line fits between different photometer heights [e.g., Jackson *et al.*, 1988]. These assumptions yield underestimates of the speeds, but coronagraph speeds are also underestimated because the material is assumed to lie in the plane of the sky.

We present in Figure 7 histograms of the best-determined values of these speeds for the three pairs of the photometer data. Figure 7a shows speeds for the set closest to the Sun and Figure 7b for the pair farthest from the Sun. Figure 7c shows the values between the two extremes, for the 16° and 90° photometers, and includes speeds from Orbit 8 when the 31° data were missing. The mean speeds determined for the three data pairs are given in column 2 of Table 4 along with the mean speed of all CMEs measured near the Sun with the Solwind coronagraph during the same epoch.

The mean and, particularly the median speeds of the Helios CMEs tend to be larger with greater height, or distance from the Sun, and they are all greater than the mean Solwind speed. Both of these results provide some statistical evidence for acceleration as the CME moves out from the Sun. Evidence for such acceleration in the inner heliosphere has been noted before [Jackson *et al.*, 1985, 1988; Watanabe and Kakinuma, 1984]. Evidence in the literature for acceleration of CMEs within the field of view of coronagraphs is inconclusive, but those measurements are confined to within 10  $R_s$  of the surface, whereas the Helios observations extend out to  $>100 R_s$ . The speeds of the 12 Helios CMEs with well-associated Solwind CMEs are shaded in Figure 7 and their mean values listed in column 3 of Table 4. We note that the speeds of these events measured by Helios are much lower than the mean speed (815 km/s) measured in the Solwind field of view. There are several possible factors contributing to this discrepancy: (1) These are very fast events near the Sun, suggesting that the material decelerates later on (for example, Woo *et al.* [1985] found evidence of deceleration of fast shocks within the Helios field of view); (2) the Helios measurements are with respect to the center of mass rather than the leading edge; and 3) typically, the photometers will be viewing through the flanks of the material rather than along its axis. The latter two factors imply that for the same events the Helios speeds will be underestimated relative to the coronagraph speeds. In summary, the Helios data provide some evidence for acceleration of typical CMEs as they move out from the Sun into the helio-

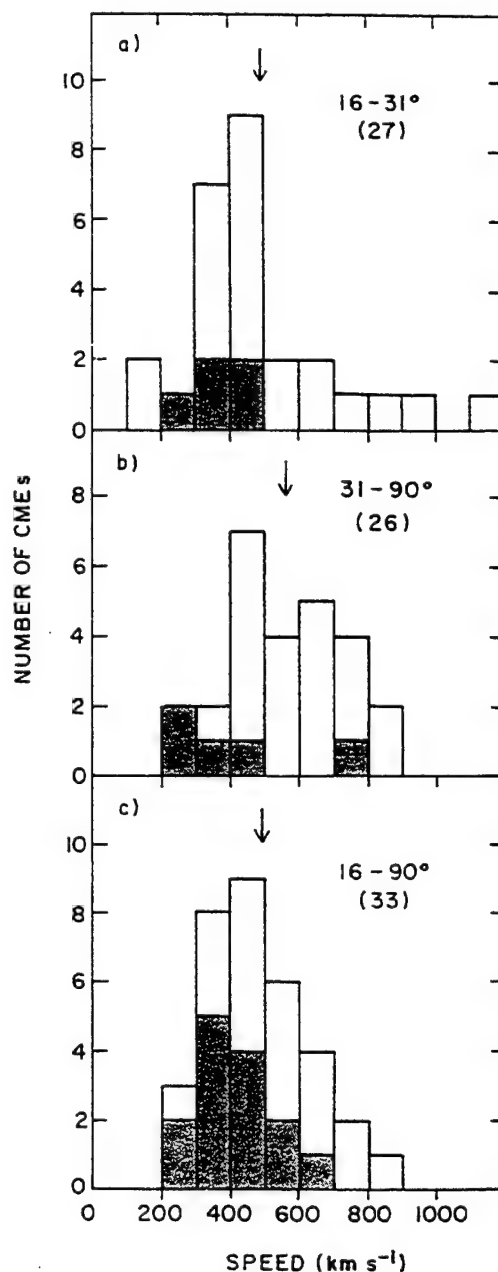


Fig. 7. Histograms of the distributions of speeds of Helios 2 CMEs determined by straight-line fits on height versus time diagrams between pairs of photometers. The heights are calculated on the assumption that the material is at the closest approach of the line of sight to the Sun. The times are those of the estimated peak intensities of the events measured in a given photometer (see Figure 3). The CME speeds are measured between the following pairs of photometers: (a) the 16° and 31° photometers, closest to the Sun; (b) the 31° and 90° photometers, farthest from the Sun; and (c) the 16° and 90° photometers. Events from Orbit 8, when the 31° data were missing, are included in Figure 7c. The arrows indicate the mean speeds of each distribution. The speeds of the 12 Helios CMEs which were well associated with Solwind CMEs are shaded.

sphere; particularly fast events may decelerate farther out. More work is required to better understand the kinematics of these CMEs.

It is difficult to determine the true "width" of a CME from the Helios data, at least one that can be compared with coronagraph measurements. This is because, unlike corona-

TABLE 4. Measured Characteristics of Helios CMEs

Instrument	Speed, km/s, All Events	Speed, km/s, Solwind Associations	Duration, days, All Events†	Duration, days, Solwind Associations‡
Helios*	491,558,487	390,422,418	1.53	1.56
Solwind	472†	815	...	...

\*Speeds determined from Helios photometer pairs are listed in the sequence: 16°–31°, 31°–90° and 16°–90°.

†Solwind CME speeds averaged over the period 1979–1981. Average speeds measured by the SMM coronagraph in 1980 were 340 km/s [from *Kahler, 1987*].

‡Durations are determined from the Helios 90° photometer data.

graph observations, the brightness of material at large elongations from the Sun is a strong function of the distance between the material and the spacecraft. In fact, as shown by the measurements with the 90° photometer, the spacecraft was eventually intercepted by the plasma from nearly every CME. However, the longitudinal extent of CME material as determined with the 16° photometer data nearest the Sun can provide a crude measure of the azimuthal width of the event. For a given event we defined this extent to be the distance in degrees between the eastmost and westmost sectors in which the event could be clearly observed. In a preliminary survey we compared the 16° photometer extents of CMEs with the average latitudinal spans of coronagraph CMEs. The mean extent of the Helios CMEs was 53°. This is similar to the mean spans of all CMEs measured by coronagraphs during the same epoch, i.e., SMM; 1980 = 41° and Solwind; 1979–1981 = 45° [*Kahler, 1987*]. We also compared the 16° photometer extents with the Solwind spans for the 12 major CMEs in 1979 that were also observed by Solwind. The mean of the spans of the associated Solwind CMEs was 86°, whereas the mean of the events measured at Helios was 65°. Thus the longitudinal extents of CMEs measured in the lower Helios photometers are reasonably consistent with the latitudinal spans of CMEs measured by coronagraphs nearer the Sun and earlier in the event evolution.

We examined the distributions of the durations and brightnesses of the CMEs as observed in the 90° photometer to better understand the size scales of the interplanetary manifestations of coronal mass ejections. The duration of an event is merely the time interval between the onset and the end of the 90° event as defined in section 3. These values are listed in the ninth column of Table 1. Figure 8 presents the distribution of these durations for the 45 events classified as definite or possible CMEs. The distribution is relatively sharply peaked with a mean of 1.53 days or 36.7 hours, as determined for the 21 CMEs without upper or lower limits. Since most of the remaining 24 events had lower limits, the typical duration is likely to be underestimated. Such long durations greatly exceed the typical observed durations of CMEs in the field of view of coronagraphs, but those durations are not well determined [e.g., *Kahler, 1987*]. The mean duration of those Helios CMEs associated with the 12 1979 Solwind CMEs is similar to that for all Helios CMEs, as shown in Table 4. It has been suggested that the Helios photometers detected enhanced plasma earlier than and for longer periods than would be estimated from Solwind observations of the same events [*Jackson and Leinert, 1985; Jackson et al., 1988*]. The mean Helios CME duration of 37 hours represents a dimension of 0.35 AU at the average solar

wind flow speed of 400 km/s, or about 0.45 AU at the mean speed of the Helios CMEs. These size scales lie at the high end of the range of average flow sizes derived for features suggested to be interplanetary manifestations of CMEs.

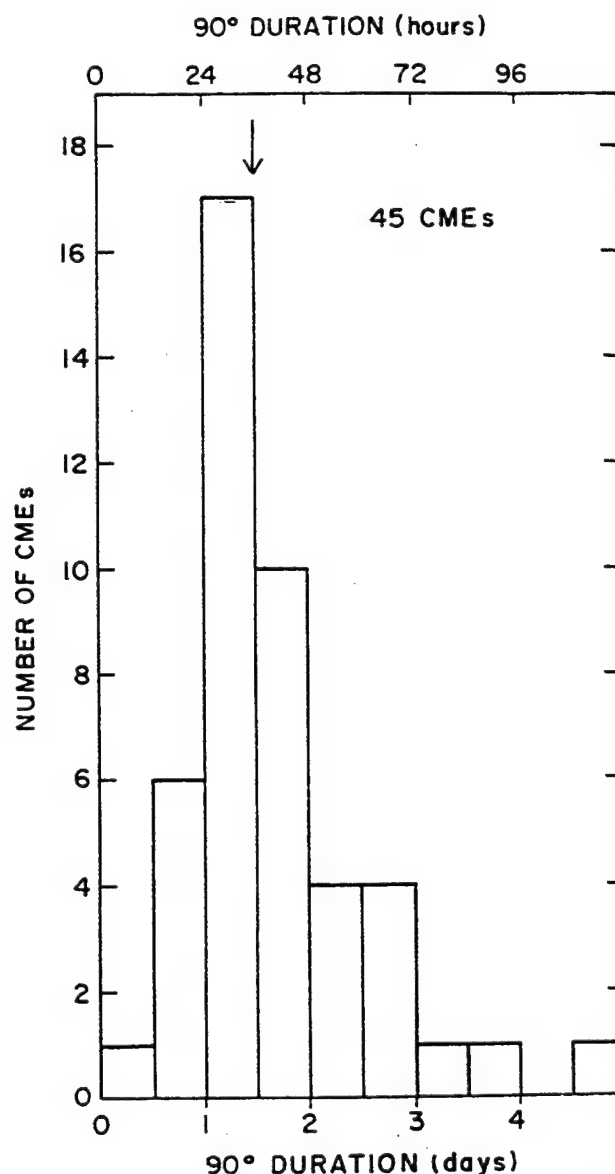


Fig. 8. Histogram of the distribution of durations of the CMEs as observed with the 90° photometer. The duration is given in hours at the top and days at the bottom. The arrow denotes the mean equal to 1.53 days of the duration distribution.

These include bidirectional streaming particle events (0.13 AU [Gosling *et al.*, 1987]), magnetic clouds (0.25 AU [Klein and Burlaga, 1982]), and helium abundance enhancements (0.4 AU [Borrini *et al.*, 1982]). It must be emphasized that these long flow times are typical of all of the photometer events, not just the largest ones.

Finally, we calculated the brightness increase above the preevent background attributable to each of the 90° events normalized to 1 AU. The mean brightness increase of all of the definite CMEs was 2.32 S10 units. The trend of the mean brightness of the CME events increased toward solar activity maximum (as did that for the CRS events) as follows: 1976 + 1977 =  $1.51 \pm 0.82$ , 1978 =  $2.50 \pm 1.34$ , and 1979 =  $2.95 \pm 1.55$  S10 units. The mean durations of the CMEs remained relatively constant over this same period. Analogous with coronagraph data, the observed brightness is a function of electron density times the depth of the material and therefore its mass [see Jackson and Leinert, 1985]. Thus brightness times duration is proportional to mass flow, which suggests that the mass, or the amount of material contained in the typical CME increased during this 4-year period. We consider this to be the first direct evidence that the mass per CME expelled into the solar wind is in phase with the solar cycle. This result appears to be consistent with the coronagraph mass estimates of Webb and Howard [1990] showing that CMEs can contribute up to 15% of the bulk solar wind ecliptic mass flux at 1 AU during solar maximum. We conclude that the typical plasma enhancements accompanying the Helios CMEs have large dimensions and therefore can supply large amounts of mass to the inner heliosphere, especially around the maximum period of solar activity.

#### 4.4. Comparative Analysis of the in situ Solar Wind During the Photometer Events

In section 3.3 we described the selection criteria and method of analysis of our study of the solar wind plasma and IMF data obtained at Helios 2 during the time intervals of the 90° photometer events. In this section we discuss the important results of that study as they pertain to the white light events, especially those classified as CMEs. Our goals were to discover how frequently material from the remotely viewed white light events actually intersected the spacecraft, what the signatures of this material were, and how the material evolved as it passed the spacecraft. We keyed on several solar wind parameters and classes of events which have been considered to be possible signatures of coronal mass ejections.

The basic results are listed by the categories of the characteristic in situ features in Table 1, which was described above. We examined the solar wind data during the intervals of all of the original 90° events, but we will limit our discussion to the results of comparison of these data with only the white light events which we classified as definite CMEs or definite CRSs (see Table 2). In Table 5 we summarize the results of this comparison during the time intervals of the white light events. In the first column we list the solar wind features of interest and in the other two columns the number and fractional percentage of white light intervals during which there was at least one occurrence of the given solar wind feature. For example, listed fast forward shocks occurred during the time interval of the 90° photometer enhancement for 18 of the 39 (46%) CMEs and 3 of the 12 (25%) CRSs.

TABLE 5. Association of Classified Photometer Events With in Situ Observations

Solar Wind Feature	Definite CMEs, 39 Events	Definite CRSs, 12 Events
Density enhancement	36/39 (92%)	12/12 (100%)
Shock	18/39 (46%)	3/12 (25%)
Sector boundary*	7/35 (20%)	3/12 (25%)
IMF rotation*	29/35 (82%)	8/12 (67%)
Magnetic cloud*	14/35 (40%)	2/12 (17%)
Average IMF $\delta B^*$	24.3 nT	15.7 nT

\*For their identification these features required IMF data, which were missing during some of the photometer events.

As we see in Table 5, significant in situ density enhancements occurred during nearly all of the white light intervals. This is perhaps not surprising since our selection criteria were biased toward events aimed in the general direction of the spacecraft. Notable density enhancements were defined as distinct increases in the hourly proton number density having amplitudes above the background of at least  $10 \text{ cm}^{-3}$  (unnormalized). Most of the increases were much larger than this. In Figure 9a we plot a histogram of the distribution of  $\Delta t$ , the difference between the white light peak time and the time of the in situ density peak. The time differences are grouped in 2-hour bins; the  $-1$  to  $+1$  hour bin includes the events for which the white light and in situ peaks coincided within the 1 hour time resolution of the solar wind data. We see that there is a sharp peak in the distribution for near-zero lag and, further, that 64% of the density peaks were within  $\pm 6$  hours of the white light peak, or essentially within the 5.2 hour time resolution of the photometer observations. Therefore we conclude that plasma associated with most of the 90° photometer events also intersected the spacecraft in the ecliptic, usually at about the same time ( $\pm 5.2$  hours) as the peak of white light brightness. Thus we are justified in using the solar wind data for these events to study the in situ characteristics of CMEs and CRSs.

Table 5 also reveals that fast forward shocks occurred during nearly half of the intervals with CMEs and 1/4 of those with CRSs. (We do not know why shocks would be physically associated with CRSs; the small number of associations could be due to chance.) Figure 9b shows the distribution of  $\Delta t$  for these shocks. This distribution is very similar to that for the density peaks, showing that 62% (16 of 26) of the shocks occurred within  $\pm 6$  hours of the white light peak. Thus in most cases involving shocks the white light brightness peak was "coincident" with the shock. Typically, in these events a sharply peaked feature was also observed earlier in the lower photometer data (e.g., Figure 3a). For these events we conclude that the most intense white light emission came from regions of compressed plasma at or just behind the shock front [e.g., Jackson, 1986]. Since flows attributed to shock sheaths can persist for several hours, with these data we cannot determine whether the abrupt white light increases are due to shock-compressed plasma, to the CME/driver gas following it, or to a regime somewhere between.

Large and systematic rotations of either or both of the polar and azimuthal components of the IMF occurred during most (82% for the CMEs and 2/3 for the CRSs) of the white light intervals. During a subset of the cases with rotations



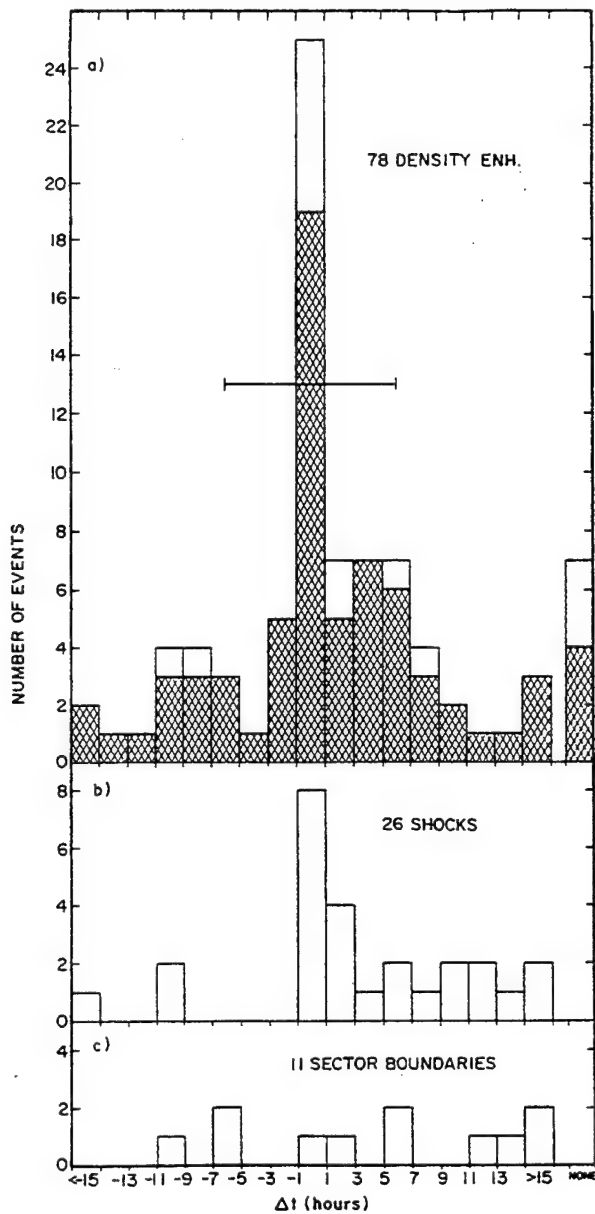


Fig. 9. Histograms of the distributions of  $\Delta t$ , the difference between the white light event peak times in the 90° photometer and the times of Helios 2 in situ (a) density peaks, (b) fast forward shocks, and (c) sector boundaries. The time differences are grouped in 2-hour bins; the -1 to +1 hour bin includes the events for which the white light and in situ peaks essentially coincided within the 1 hour time resolution of the solar wind data. Positive (negative)  $\Delta t$  means that the in situ peak preceded (followed) the white light peak. The horizontal bar denotes the time resolution of the photometer data. Time differences involving only upper or lower limits were excluded. The density time differences involving definite or possible CMEs are indicated by cross hatching. Multiple in situ events occurring within the white light intervals were included. The 78 density enhancements occurred during 49 white light intervals, the 26 shocks during 18 intervals, and the 11 sector crossings during 11 intervals.

(40% of the CMEs and 17% of the CRSs), the IMF displayed characteristics resembling those of magnetic clouds. We defined such cases of candidate clouds as having smooth, long-enduring (on the order of 10 hours or more) enhancements in the IMF intensity associated with significant field rotations in one or both of the IMF components. Typically,

these magnetic enhancements occurred during the periods with enhanced density. From Table 1 we see that during most of the white light intervals there was a significant increase in the IMF magnitude  $\delta B$  whether or not associated with any of the above features. The mean value of  $\delta B$ , uncorrected for radial distance from the Sun, is listed at the bottom of Table 5. The mean IMF amplitude during CMEs greatly exceeded that during CRSs.

Spacecraft crossings of the heliospheric current sheet in the interplanetary medium are identified as sector boundaries. From this study we conclude that: (1) None of the white light transients occurring when Helios 2 was near a sector boundary could be attributed solely to the density enhancement at that boundary; (2) CRSs and/or CMEs could be identified during each of the white light intervals occurring with a sector boundary; and (3) the rate of crossings of sector boundaries during the white light intervals is consistent with a random chance association. (For a four-sector structure, boundaries will occur on average every 7 days. CMEs or CRSs have an average duration of 1.5 days, so there should be 21% random associations with the white light intervals. This agrees with the rates shown in Table 5.) This conclusion is supported by Figure 9c, which shows that the times of crossings of the 11 definite sector boundaries in our data were broadly distributed with respect to the white light brightness peaks. These results indicate that, at least near the Sun, such interaction regions in the solar wind are not sufficiently dense along the line of sight to yield white light enhancements detectable by the photometers.

In the corona, white light streamers tend to form a belt which has been shown to overlie the computed source surface of the heliospheric neutral sheet [e.g., Bruno *et al.*, 1982]. Thus the occasional occurrence at sector boundaries of corotating structures extending from the Sun is not surprising. Since CMEs are often ejected from streamers, we should also expect that occasionally a CME will appear near a sector boundary in the ecliptic. Since we can unambiguously identify and differentiate CMEs and CRSs, we believe that our study is one of the first to demonstrate that some corotating solar structures and CMEs propagate out from the Sun in close proximity to the neutral sheet where they are observed in situ.

## 5. CONCLUSIONS

In this study we have used Helios 2 zodiacal light photometer data to identify and determine the characteristics of white light transient events observed in the interplanetary medium. Data from the north ecliptic pole (+90°) photometer were used to identify all significant electron plasma events passing north of or enveloping the spacecraft. A subset of these events was classified by examining the lower-latitude photometers to determine the temporal evolution and spatial extent of each event. The major goals of the study were to identify coronal mass ejections (CMEs) in the interplanetary medium, to establish their heliospheric characteristics and compare them with those of CMEs observed near the Sun, and to determine the frequency of occurrence of CMEs from 1976 through 1979.

We found that most (80%) of the white light transients could be classified as mass ejections moving outward from the Sun. A smaller number (27%) were elongated structures which corotated from east to west of the Sun and probably

represent the interplanetary detection of coronal streamers in the heliosphere. During the period of overlapping coverage in 1979 the Helios mass ejections were found to be well associated with Solwind CMEs observed earlier near the Sun. Their occurrence rates, speeds, and size scales were also comparable, indicating that the Helios photometers were detecting most CMEs directed through its field of view.

We were able to establish some important characteristics of the heliospheric manifestation of coronal mass ejections. Nearly all of the Helios events were accompanied by in situ density enhancements, most of which were essentially coincident with the times of the white light peak brightness. The average brightness increase attributable to the heliospheric CMEs in the 90° photometer was 2.3 S10 units. They had long durations (1.5 days) and speeds of ~500 km/s, implying radial dimensions of ~0.4 AU, and longitudinal widths near the Sun of ~50°. Taken together, these results imply that typical heliospheric CMEs have large dimensions and supply significant amounts of mass to the inner heliosphere, especially around the maximum phase of solar activity.

Other than significant density enhancements, the Helios CMEs were characterized in situ by significant increases in the magnitude of the IMF and large rotations of its polar and azimuthal components. About half of them were preceded by fast shock waves and by flows typical of magnetic clouds. The shocks tended to be coincident with or to precede the peak brightness of the white light events by up to 15 hours. This suggests that the most intense white light emission comes, in the former case, from compressed plasma at or just behind the shock front or, in the latter case, from regions within the CME itself commonly referred to as driver gas. Three quarters of the shocks in our study were followed within the photometer event interval by in situ material suggestive of driver gas. Such features were also observed during intervals without shocks.

We showed that, with appropriate corrections, we can use the Helios photometer data to estimate the frequency of occurrence of solar CMEs. The Helios 2 data discussed in this paper were particularly appropriate for this task because they permitted us to estimate CME rates during the long gap in conventional coronagraph coverage from 1976 to early 1979. Combined with coronagraph data in 1979–1981, the results indicate that during the rise of the last solar activity cycle, the CME occurrence rate generally tracked the cycle, increasing by at least an order of magnitude between cycle minimum and maximum. The Helios results also suggest that the mass per CME likewise increased during this 4-year period.

The occurrence rate of the smaller class of photometer transients, corotating structures or CRSs, increased during this period by only a factor of three. A definitive study of these structures is left to other papers [e.g., Jackson, 1990], but our preliminary results indicate that this class of transient may represent the heliospheric signature of coronal streamers. Many of these features can be mapped back to white light streamers observed by coronagraphs at the Sun. In the corona, such bright streamers tend to lie along the source surface of the current sheet in the heliosphere, where its ecliptic crossings are identified as sector boundaries. None of the white light transients, either CMEs or CRSs, occurring when Helios 2 was near a sector boundary could be attributed solely to the density enhancement at that boundary, indicating that such regions are not sufficiently

dense to yield white light enhancements detectable by the photometers. On the other hand, we have shown that some corotating solar structures and CMEs do propagate out from the sun in the vicinity of the current sheet where they can be observed in situ. We have yet to perform a more complete analysis of these features to study, for example, the white light characteristics of sector boundaries and interaction regions in general.

In conclusion, we have demonstrated that the Helios zodiacal light photometers were sufficiently sensitive to detect the electron-scattered component of most coronal mass ejections in the inner heliosphere. We have determined some important characteristics of these events and compared them with in situ solar wind data and with CMEs observed earlier near the Sun. Future studies involving these data will include: the characteristics of the corotating class of events, the characteristics of sector boundaries, the solar source regions of the white light events of this study determined by backprojection to the Sun, extension of the statistical analyses to include the Helios 1 photometer data, and comparison of the Helios CMEs with other coronagraph CME data and with transient events detected at other interplanetary spacecraft, such as Pioneer Venus and ISEE 3.

**Acknowledgments.** We are grateful to Ch. Leinert of the Max Planck Institut für Astronomie, Federal Republic of Germany, principal investigator of the Helios zodiacal light experiment, who has graciously supported our analyses of the photometer data. We thank S. Kahler of Boston College and E. Cliver of the AFSC/Geophysics Laboratory (GL) for helpful comments, and L. Dillard and M. Figueroa of UCSD, L. Gentile of Boston College and S. Bredesen of GL for their help with processing the Helios data. This work was influenced by the authors' participation in the Workshop on Solar Events and Their Influence on the Interplanetary Medium (SEIIM) organized by NOAA under the auspices of the SMM P.I.s. The Helios data were obtained by the zodiacal light experiment BMFT grant WRS 0108 and are available from the NSSDC. The work of D. Webb was supported at Emmanuel College and at Boston College by the Space Physics Division of GL under contracts AF19628-87-K-0033 and AF19628-90-K-0006, respectively. B. Jackson was supported at the University of California, San Diego by the National Science Foundation under grant ATM-88-12409 and by GL under contract AF19628-87-K-0033.

The Editor thanks J. D. Mihalov and R. S. Steinolfson for their assistance in evaluating this paper.

## REFERENCES

- Borini, G., J. T. Gosling, S. J. Bame, and W. C. Feldman, An analysis of shock wave disturbances observed at 1 AU from 1971 through 1978, *J. Geophys. Res.*, **87**, 4365, 1982.
- Bruno, R., L. F. Burlaga, and A. J. Hundhausen, Quadrupole distortions of the heliospheric current sheet in 1976 and 1977, *J. Geophys. Res.*, **87**, 10,339, 1982.
- Burlaga, L. F., L. Klein, N. R. Sheeley, Jr., D. J. Michels, R. A. Howard, M. J. Koomen, R. Schwenn, and H. Rosenbauer, A magnetic cloud and a coronal mass ejection, *Geophys. Res. Lett.*, **9**, 1317, 1982.
- Cane, H. V., The evolution of interplanetary shocks, *J. Geophys. Res.*, **90**, 191, 1985.
- Cane, H. V., N. R. Sheeley, Jr., and R. A. Howard, Energetic interplanetary shocks, radio emission, and coronal mass ejections, *J. Geophys. Res.*, **92**, 9869, 1987.
- Dryer, M., H. Perez-de-Tejada, H. A. Taylor, Jr., D. S. Intriligator, J. D. Mihalov, and B. Rompolt, Compression of the Venusian ionosphere on May 10, 1979, by the interplanetary shock generated by the solar eruption of May 8, 1979, *J. Geophys. Res.*, **87**, 9035, 1982.
- Gosling, J. T., Coronal mass ejections and magnetic flux ropes in

- interplanetary space, in *Physics of Magnetic Flux Ropes*, edited by C. T. Russell, L. C. Lee, and E. Priest, p. 343, AGU Chapman Conf., Washington, D. C., 1990.
- Gosling, J. T., D. N. Baker, S. J. Bame, W. C. Feldman, R. D. Zwickl, and E. J. Smith, Bidirectional solar wind electron heat flux events, *J. Geophys. Res.*, **92**, 8519, 1987.
- Howard, R. A., N. R. Sheeley, Jr., M. J. Koomen, and D. J. Michels, Coronal mass ejections: 1979–1981, *J. Geophys. Res.*, **90**, 8173, 1985.
- Hundhausen, A. J., *Coronal Expansion and the Solar Wind*, Springer-Verlag, New York, 1972.
- Hundhausen, A. J., The origin and propagation of coronal mass ejections, Proceedings of the Sixth International Solar Wind Conference, edited by V. Pizzo, T. E. Holzer, and D. G. Sime, *Tech. Note 306 + Proc.* p. 181, Natl. Cent. for Atmos. Res., Boulder, Colo., 1988.
- Jackson, B. V., Imaging of coronal mass ejections by the Helios spacecraft, *Sol. Phys.*, **100**, 563, 1985.
- Jackson, B. V., Helios photometer measurements of in-situ density enhancements, *Adv. Space Res.*, **6**, 307, 1986.
- Jackson, B. V., Scientific background and design specifications for a near-Earth heliospheric imager, *Tech. Rep. 88-0195*, Air Force Geophys. Lab., Hanscom Air Force Base, Mass., 1988.
- Jackson, B. V., and R. M. Benensohn, The Helios spacecraft zodiacal light photometers used for comet observations and views of the comet west bow shock, *Earth, Moon Planets*, **48**, 139, 1990.
- Jackson, B. V., and C. Leinert, Helios images of solar mass ejections, *J. Geophys. Res.*, **90**, 10,759, 1985.
- Jackson, B. V., R. A. Howard, N. R. Sheeley, Jr., D. J. Michels, M. J. Koomen, and R. M. E. Illing, Helios spacecraft and earth perspective observations of three looplike solar mass ejection transients, *J. Geophys. Res.*, **90**, 5075, 1985.
- Jackson, B. V., B. Rompolt, and Z. Svestka, Solar and interplanetary observations of the mass ejection on 7 May 1979, *Sol. Phys.*, **115**, 327, 1988.
- Kahler, S., Coronal mass ejections, *Rev. Geophys.*, **25**, 663, 1987.
- Kahler, S., Observations of coronal mass ejections near the Sun, Proceedings of the Sixth International Solar Wind Conference, edited by V. Pizzo, T. E. Holzer, and D. G. Sime, *Tech. Note 306 + Proc.* p. 215, Boulder, Colo., 1988.
- Kahler, S. W., E. Hildner, and M. A. I. van Hollebeke, Prompt solar proton events and coronal mass ejections, *Sol. Phys.*, **57**, 429, 1978.
- Kahler, S. W., N. R. Sheeley, Jr., R. A. Howard, M. J. Koomen, D. J. Michels, R. E. McGuire, T. T. von Rosenvinge, and D. V. Reames, Associations between coronal mass ejections and solar energetic proton events, *J. Geophys. Res.*, **89**, 9683, 1984.
- Klein, L. W., and L. F. Burlaga, Interplanetary magnetic clouds at 1 AU, *J. Geophys. Res.*, **87**, 613, 1982.
- Leinert, C., H. Link, E. Pitz, N. Salm, and D. Kluppelberg, Helios zodiacal light experiment, *Raumfahrtforschung*, **19**, 264, 1975.
- Leinert, C., E. Pitz, H. Link, and N. Salm, Calibration and in-flight performance of the zodiacal light experiment on Helios, *Space Sci. Instrum.*, **5**, 257, 1981a.
- Leinert, C., I. Richter, E. Pitz, and B. Planck, The zodiacal light from 1.0 to 0.3 A.U. as observed by the Helios space probes, *Astron. Astrophys.*, **103**, 177, 1981b.
- Mariani, F., et al., Magnetic field hourly averages from the Rome-GSFL experiment aboard Helios 1 and Helios 2, *Rep. IFSI-87-1*, Inst. di Fisica Dello Spazio Interplanetario, Frascati, Italy, 1987.
- McCabe, M. K., Svestka, Z. F. Howard, R. A., Jackson, B. V. and Sheeley, N. R., Jr., Coronal mass ejection associated with the stationary post-flare arch of 21/22 May 1980, *Sol. Phys.*, **103**, 399, 1986.
- Richter, I., C. Leinert, and B. Planck, Search for short term variations of zodiacal light and optical detection of interplanetary plasma clouds, *Astron. Astrophys.*, **110**, 115, 1982.
- Schwenn, R., The "average" solar wind in the inner heliosphere: Structure and slow variations, *Solar Wind Five, NASA Conf. Publ.*, **2280**, 489, 1983.
- Sheeley, N. R., Jr., R. A. Howard, M. J. Koomen, D. J. Michels, R. Schwenn, K. H. Muhlhauser, and H. Rosenbauer, Coronal mass ejections and interplanetary shocks, *J. Geophys. Res.*, **90**, 163, 1985.
- Sime, D. G., The corona and interplanetary medium during the solar cycle, Proceedings ESA Workshop on Future Missions in Solar Heliospheric and Space Plasma Physics, *Spec. Publ.* **235**, p. 23, Eur. Space Agency, Neuilly, France, 1985.
- Volkmer, P. M., and F. M. Neubauer, Statistical properties of fast magnetoacoustic shock waves in the solar wind between 0.3 AU and 1 AU: Helios-1, 2 observations, *Ann. Geophys.*, **3**, 1, 1985.
- Watanabe, T., and T. Kakinuma, Radio-scintillation observations of interplanetary disturbances, *Adv. Space Res.*, **4**, 331, 1984.
- Webb, D. F., The origin and kinematics of coronal mass ejections, in *Solar Terrestrial Physics: Proceedings of Second Indo-U.S. Workshop on Solar-Terrestrial Physics*, edited by M. R. Kundu, B. Biswas, B. M. Reddy, and S. Ramadurai, p. 283, Indoc, New Delhi, 1986.
- Webb, D. F., Erupting prominences and the geometry of coronal mass ejections, *J. Geophys. Res.*, **93**, 1749, 1988.
- Webb, D. F., and B. V. Jackson, Detection of coronal mass ejections in the interplanetary medium from 1976–1979 using Helios-2 photometer data, Proceedings of the Sixth International Solar Wind Conference, edited by V. Pizzo, T. E. Holzer, and D. G. Sime, *Tech. Note 306 + Proc.* p. 267, Natl. Cent. for Atmos. Res. Boulder, Colo., 1988.
- Woo, R., J. W. Armstrong, N. R. Sheeley, Jr., R. A. Howard, M. J. Koomen, D. J. Michels, and R. Schwenn, Doppler scintillation observations of interplanetary shocks within 0.3 AU, *J. Geophys. Res.*, **90**, 154, 1985.
- Zwickl, R. D., J. R. Asbridge, S. J. Bame, W. C. Feldman, J. T. Gosling, and E. J. Smith, Plasma properties of driver gas following interplanetary shocks observed by ISEE-3, *Solar Wind Five, NASA Conf. Publ.* **2280**, 711, 1983.
- B. V. Jackson, University of California, San Diego, La Jolla, CA 92093.
- D. F. Webb, GL(AFSC)/PHG, Hanscom Air Force Base, MA 01731.

(Received May 7, 1990;  
revised July 26, 1990;  
accepted August 16, 1990.)



## Probing the Magnetic Topologies of Magnetic Clouds by Means of Solar Energetic Particles

S. W. KAHLER

*Institute for Space Research, Boston College, Newton, Massachusetts*

D. V. REAMES

*NASA Goddard Space Flight Center, Greenbelt, Maryland*

Magnetic clouds are large ( $<0.25$  AU) interplanetary regions with topologies consistent with those of magnetic loops. They are of interest because they may be an interplanetary signature of coronal mass ejections. Clouds have been identified in solar wind data by their magnetic properties and by the presence of bidirectional particle fluxes. Two possible closed magnetic topologies have been considered for clouds: (1) an elongated bottle with field lines rooted at both ends in the Sun and (2) a detached magnetic bubble or plasmoid consisting of closed field lines. The inferred topologies are also consistent with open field lines that converge beyond 1 AU. We have used solar energetic particles (SEPs) as probes of the cloud topologies. The rapid access of SEPs to the interiors of many clouds indicates that the cloud field lines extend back to the Sun and hence are not plasmoids. The small modulation of galactic cosmic rays associated with clouds also suggests that the magnetic fields of clouds are not closed.

### 1. INTRODUCTION

The topology of magnetic field lines carried into the interplanetary medium by coronal eruptive events has been investigated for several decades. Both *Piddington* [1958] and *Gold* [1959] suggested that magnetic loops would retain their connection to the Sun and form topologically closed bottles. The observation with the Skylab coronagraph of large loop-like coronal mass ejections (CMEs) that appeared to remain connected to the Sun [*Gosling et al.*, 1974] lent further credence to the basic picture of a magnetic bottle.

The first attempt to use solar energetic particles (SEPs) to probe the topology of interplanetary fields was made by *Rao et al.* [1967]. As part of a survey of energetic storm particle events observed with detectors on the Pioneer 6 and 7 spacecraft, they found four periods of bidirectional anisotropies of 10-MeV protons. All occurred during the maximum depressions of Forbush decreases, and in at least one case, on March 23, 1966, the maximum fluxes were parallel and antiparallel to the field lines. *Rao et al.* [1967] argued that their observations were not consistent with a Gold bottle but were better explained by particles behind a blast wave in a field configuration open to the interplanetary medium.

The next attempt to deduce magnetic field topologies from energetic particle measurements was apparently that of *Palmer et al.* [1978]. They surveyed  $\sim 1$ -MeV particle data from the Explorer and Vela satellites covering a 6-year interval and found 16 periods of bidirectional fluxes, including three of  $E > 40$  keV electron events. Their event anisotropies generally occurred during the minima of Forbush decreases and for an average duration of 9 hours, implying a spatial scale of 0.13 AU. Contrary to *Rao et al.* [1967], *Palmer et al.* argued in favor of a Gold bottle as

opposed to a blast wave in an open field configuration for the magnetic topology.

*Kutcho et al.* [1982] analyzed a 1-MeV proton and alpha SEP event on October 12, 1977, that showed field-aligned bidirectional fluxes for about 5 hours. At the same time the relativistic electron fluxes were also "bidirectional" but with anisotropies peaked perpendicular to the magnetic field. These particles were associated with a solar flare which occurred earlier in the day and were therefore injected at the Sun. As candidate topologies for the interplanetary magnetic field, they compared the Gold bottle with a pinched-off bottle, or plasmoid, as shown in Figure 1. Their analysis of the plasma, field, and particle data from IMP 7 and 8 led them to conclude that the magnetic field was in a Gold bottle configuration. *Sarris and Krimigis* [1982] analyzed the pitch angle distributions of energetic electrons and protons from two solar flares observed on IMP 7. In each case the electrons and protons were inferred to bounce between magnetic mirrors. Their preferred magnetic topology was also a bottle, extending about 3.5 AU from the Sun.

The *Kutcho et al.* [1982] observations were significant for inferring the presence of a magnetic loop at the Earth during a time of relatively undisturbed solar wind conditions. In contrast, the earlier events discussed by *Rao et al.* [1967] and *Palmer et al.* [1978] generally occurred in association with Forbush decreases, which clearly implied unusual conditions for the interplanetary field. The work of *Kutcho et al.* [1982] therefore suggested particle bidirectionality as a tool for probing the magnetic structure of the interplanetary medium at any time, rather than only during disturbed conditions.

These early reports of bidirectional particle fluxes make clear that bidirectionality occurs rather infrequently in the  $>1$ -MeV energy range. At much lower energies the ubiquitous electron and proton fluxes apparently provide a more sensitive tool for detecting bidirectionality. Bidirectional proton fluxes (BDPs) observed with the low-energy ( $E > 35$

Copyright 1991 by the American Geophysical Union.

Paper number 91JA00659.  
0148-0227/91/91JA-00659\$05.00

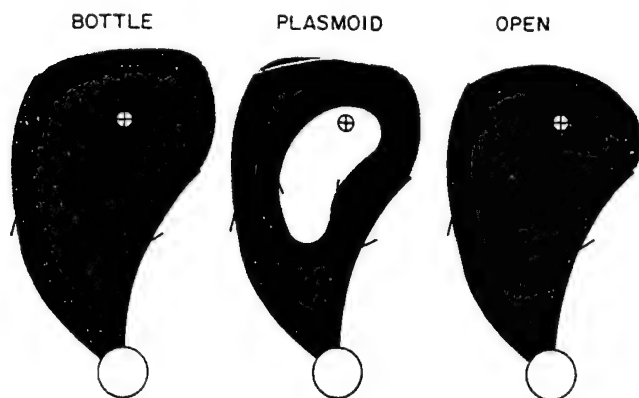


Fig. 1. Three possible topologies of magnetic clouds, as projected into the ecliptic. The circle with the cross is the Earth; the Sun is at the bottom. The heavy solid lines indicate magnetic field lines extending from the Sun into interplanetary space, and the shaded regions show the areas accessible to SEPs. In all cases a bidirectional particle flux could be observed at the Earth.

keV) proton detector on ISEE 3 were analyzed for individual events [Sanderson *et al.*, 1983; Tranquille *et al.*, 1987] and for all events found in a 45-month survey [Marsden *et al.*, 1987]. Similarly, analyses of individual events of bidirectional low-energy [ $E > 80$  eV] electron fluxes (BDEs) [Bame *et al.*, 1981; Zwickl *et al.*, 1983; Pilipp *et al.*, 1987] were followed by a survey of events in a 16-month period [Gosling *et al.*, 1987]. The BDE and BDP events often did not coincide, and when they did, they often differed by hours in their start and stop times [Gosling *et al.*, 1987].

A complementary approach to detecting magnetic loops in the solar wind was based on interplanetary magnetic field observations. Guided by the detailed observations from five spacecraft of a region interpreted as a magnetic loop [Burlaga *et al.*, 1981], Klein and Burlaga [1982] defined magnetic clouds as interplanetary regions with (1) radial dimensions of  $\approx 0.25$  AU, (2) enhanced magnetic fields of  $> 10\gamma$ , and (3) changes of magnetic field directions from large southern directions to large northern directions, or vice versa. Forty-five clouds were identified by Klein and Burlaga between 1967 and 1978. This period was extended to 1982 by Zhang and Burlaga [1988], who found 19 more clouds.

The durations of the BDE and BDP events correspond to spatial scale sizes of  $< 0.05$  to  $0.5$  AU, comparable with those of magnetic clouds. Nearly all the Zhang and Burlaga magnetic clouds can be associated with BDE events. However, the number of BDE events exceeds the number of BDP events over comparable periods of time, and the number of BDP events exceeds the number of reported magnetic clouds, both by factors of  $\approx 3$  [Gosling, 1990]. The bidirectional particle technique is therefore regarded as a more sensitive method of identifying interplanetary CMEs, particularly when the cloud consists of a peak field too weak ( $< 10\gamma$ ) to match the definition of a magnetic cloud.

The BDPs, BDEs, and magnetic clouds have all been interpreted as the interplanetary manifestations of CMEs [Marsden *et al.*, 1987; Gosling *et al.*, 1987; Klein and Burlaga, 1982; Gosling, 1990]. A good association between the magnetic clouds of Klein and Burlaga [1982] and disappearing filaments has been found [Wilson and Hildner, 1986; Marubashi, 1986], thus supporting this interpretation by linking a known solar signature of CMEs [Webb and Hund-

hausen, 1987] with clouds. One expects the interaction between the CME and the ambient plasma to produce the most enhanced magnetic field intensities ahead of and within the driver gas for the fastest CMEs [Gosling, 1990]. Thus, if the CME interpretation is correct, the original cloud criterion of a  $> 10\gamma$  field should preferentially select the most energetic of all CMEs intersecting the Earth. The speeds of most CMEs are sufficiently below the Alfvén speed [Hundhausen *et al.*, 1987] that shocks and field compressions will not be produced in interplanetary space. In these cases the BDPs and BDEs may be the only way to detect the characteristic magnetic topology of a CME.

To explain the BDPs and BDEs, Marsden *et al.* [1987] and Gosling *et al.* [1987], respectively, considered the bottle and plasmoid topologies as the only candidate topologies, and both argued in favor of the plasmoid topology. Furthermore, in their discussion of field line draping around fast CMEs, Gosling and McComas [1987] explicitly assumed a plasmoid topology for the CME. On the other hand, recent modeling efforts [Burlaga, 1988; Marubashi, 1986] have assumed that clouds are cylindrical magnetic flux ropes, consistent with the bottle topology of Figure 1. Realistic magnetic geometries, such as flux ropes, obviously involve field lines inclined to the ecliptic plane. However, the assumption of such geometries will not change the basic topologies shown in Figure 1.

Open field topologies have not been considered as candidates for BDEs and BDPs. However, Barouch and Burlaga [1976] showed that simple azimuthal variations in solar wind speeds can produce an interplanetary field configuration in which field lines converge with radial distance to produce a magnetic mirror for particles. This topology, consisting of field lines open to a distance beyond the region of convergence, as shown in Figure 1, is an alternative to the bottle and plasmoid topologies. Although Marsden *et al.* [1987] briefly considered the possibility of local mirroring, where local means a size scale much less than  $0.1$  AU, the open field configuration has apparently not been considered as an explanation for particle bidirectionality since the work of Palmer *et al.* [1978]. A special case of the open topology arises with a fast mode MHD shock, which results in a field convergence behind the shock front. This case was considered as a candidate topology by Rao *et al.* [1967].

BDEs are often found in association with other solar wind signatures of CMEs [Gosling *et al.*, 1987]. Gosling [1990] argued that all bidirectional particle events are signatures of CMEs, but he did not consider the possibility that some events may be associated with the open field topology and hence are not signatures of CMEs. In our view, the determination of the topologies of the magnetic fields associated with BDPs and BDEs remains an important problem for detecting CMEs as well as for understanding the development of solar magnetic fields.

In this work we use a simple technique to determine whether the plasmoid structure shown in Figure 1 is characteristic of BDP events. If SEPs are injected into interplanetary space from the Sun while a plasmoid is present in space, those particles should be excluded from the region of the plasmoid, as shown in Figure 1. The subsequent passage of such a region past the Earth should therefore be accompanied by a substantial reduction in SEP fluxes. The absence of such reductions implies that we can then rule out the plasmoid topology of Figure 1. Similarly, the observation of

TABLE 1. Bidirectional Proton Events and Associated SEP Events

BDP Event Interval		SEP Event			
Date	Time, hours UT	Flux	Onset, hours, UT (Date)	Flare Source	Magnetic Class*
1979 April 3	00-07	e, p	4 (3)	M4/1B 0418 UT S23 W05	2a
1979 April 4	16-24	e, p	4 (3)	same as above	2b
1980 Feb. 15	23-23 (16)	e, p	22 (15)	C5/- 2116 UT S10 W71	1a, ZB
1980 April 1	03-23	e	23 (30)	C6/- 2242 UT N10 W15	2a
1980 May 8	12-20 (9)	e	14 (7)	M4/- 1320 UT S22 W12	1b
1980 Aug. 19	19-01 (21)	e, p	4 (18)	no flare type II 0130 UT	1a
1980 Oct. 15	06-21	e, p	7 (15)	M2/3N 0524 UT N21 E55	2a
1980 Dec. 20	20-23	e	17 (20)	C4/1B 1706 UT S20 W47	3
1981 March 7	18-22	e, p	<14 (7)	M2/-N 0630 UT S22 W79	2a
1981 April 8	21-09 (9)	e, p	18 (8)	M5/1B 1638 UT N10 W06	3
1981 July 18	00-06 (19)	e	18 (17)	unknown	1a
1981 Nov. 20	20-23	e	16 (20)	C8/-B 1530 UT S20 W53	3
1981 Nov. 21	08-08 (22)	e	4 (22)	M1/1B 0323 UT S20 W74	2b
1982 Jan. 31	17-23	e, p	1 (31)	X1/2B 2344 UT S14 E13	1a
1982 Feb. 9	12-24	e, p	13 (8)	X1/1B 1223 UT S15 W88	1b
1982 Feb. 12	00-06 (13)	e, p	22 (12)	M3/-B 2158 UT S12 W22	1a, ZB

\*ZB: magnetic clouds of *Zhang and Burlaga* [1988]. 1a: events with rotational magnetic signatures characteristic of magnetic clouds and associated with interplanetary shocks. 1b: same as 1a, but without shocks. 2a: events without rotational magnetic signature characteristic of magnetic clouds and associated with interplanetary shocks. 2b: same as 2a, but without shocks. 3: events without clear isolated magnetic structure identified.

promptly arriving SEPs at the Earth while the Earth is embedded within a BDP region is inconsistent with the plasmoid topology. A preliminary version of this work was published by *Kahler and Reames* [1990].

## 2. DATA ANALYSIS

We examined energetic particle data from the Goddard Space Flight Center (GSFC) experiment [*von Rosenvinge et al.*, 1978] on the ISEE 3 spacecraft at the times of all the BDP events in the list of *Marsden et al.* [1987]. We selected those periods during which the 0.2- to 2.0-MeV electron and/or the 22- to 27-MeV proton fluxes were enhanced above background due to the occurrence of a prompt SEP event. The GSFC particle data were not available from August 14, 1979, to January 25, 1980. The 36 BDP events with associated prompt SEP events were divided into three classes defined as follows: (1) the occurrence of the SEP event appeared to precede the solar origin of the BDP region (7 events); (2) the SEP event appeared to arise in the same solar event that resulted in the BDP region (13 events); and (3) the SEP event appeared to follow the origin of the BDP region (16 events). In each case we assumed that the BDP region resulted from an eruptive solar event about 2-4 days before the BDP region was observed at the Earth. Most SEP events

included 0.2- to 2.0-MeV electrons, the onsets of which were used to constrain the associated flare timings to within 15 min.

Let us consider what the SEP signatures at 1 AU might be for the three classes. If open field lines are populated with SEP particles before the formation of a plasmoid, we might expect only minor differences between the SEP populations inside and outside the plasmoid. Hence the class 1 events are not particularly useful in detecting plasmoids. Most of the events of class 2 follow the interplanetary shocks associated with SEP flares. They may or may not be populated with SEP particles at the time of the plasmoid formation, depending on the location of the particle acceleration region. Class 2 events may serve to identify a plasmoid, but this is not clear. In class 3 events, SEPs are released at the Sun after the plasmoid has already formed. In that case the SEPs should be excluded from the plasmoid, as shown in Figure 1, resulting in a substantial drop of SEP fluxes when the plasmoid reaches 1 AU. These 16 SEP events should therefore provide the best test cases for the presence of interplanetary plasmoids.

The 16 BDP and SEP events of class 3 are listed in Table 1. In the first two columns we give the dates of the starts of the BDP events followed by the start and stop times as given

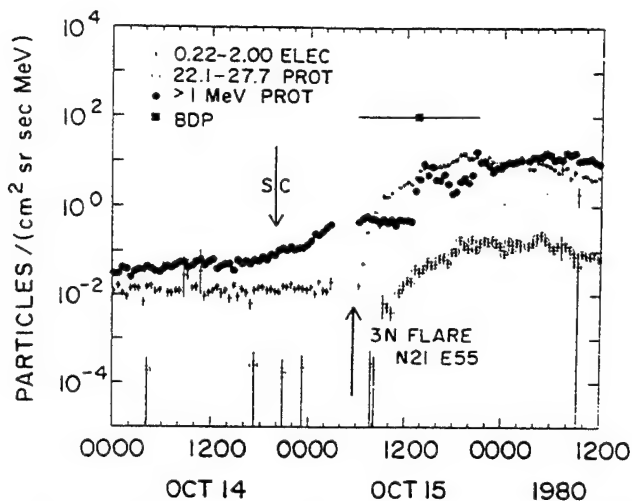


Fig. 2. The BDP event of October 15, 1980. The onset of a SEP event occurs during the BDP event. This BDP followed a geomagnetic sudden commencement (sc) indicated by the top arrow.

by Marsden *et al.* [1987]. For the accompanying SEP event we indicate whether enhanced fluxes of 0.2- to 2-MeV electrons (e) or 22- to 27-MeV protons (p) were observed. The hour and date of the particle event onset is followed by the solar flare associated with the SEP event. The flare X ray and H $\alpha$  peak brightness and H $\alpha$  maximum time are given in the first line of each entry, and the solar coordinates of the flare in the second line. In the last column we also note the classifications of events by Marsden *et al.* [1987] and Zhang and Burlaga [1988].

We examined the >1-MeV and 22- to 27-MeV proton fluxes and 0.2- to 2-MeV electron fluxes at the times of all BDP events. In none of the events of any class did we see a substantial decline and subsequent increase of SEP fluxes matching the start and end of the associated BDP event. Since many of the BDP events closely followed shocks, there was sometimes a sharp decline in SEP fluxes near the event onset, but the SEP fluxes did not increase again at the end of the BDP event. We attribute the SEP flux modulation in these events to the effects of the shocks.

We present three examples of our class 3 events. In the first, shown in Figure 2, a 3N flare at N21 E55 on October 15, 1980, was associated with a SEP event which began during the BDP event. The fluxes increased to a broad maximum at the end of the BDP event, showing little change at that time. In the second example, shown in Figure 3, the SEP event was associated with a 2B flare at S14 E13 on January 30, 1982. In this case the SEP fluxes showed no modulation at either the beginning or the end of the BDP event. We show at the top of Figure 3 the magnetic field magnitude and  $\theta$ , the inclination of the field vector out of the ecliptic. Although the gradual rotation of the field from south of the ecliptic at 1300 UT on January 31 to north at 2200 UT is a characteristic signature of magnetic clouds, this period was not selected as a cloud by Zhang and Burlaga [1988], probably because of its relatively short duration ( $\sim 10$  hours).

In the third example, shown in Figure 4, two solar electron events occurred during the February 12, 1982, BDP event, which was also listed as a magnetic cloud by Zhang and Burlaga [1988]. The cloud followed a geomagnetic sudden commencement (sc), shown in the top panel. The low-energy

proton (35-56 keV) fluxes of this event were analyzed by Sanderson *et al.* [1990b]. They found a sharp decrease in these fluxes at about 2300 UT on February 11 in association with a magnetic discontinuity marking the onset of the BDP event. This is an example of a substantial modulation of low-energy interplanetary particle fluxes by magnetic structures. However, these fluxes, which probably originated in the preceding interplanetary shock, cannot be attributed to a solar event and do not carry the information about the magnetic topology which we can derive from SEPs. Another event of Table 1 is shown in our earlier paper [Kahler and Reames, 1990]. In that event, on April 3, 1979, a SEP onset occurred near the middle of a BDP event.

### 3. DISCUSSION

Both Marsden *et al.* [1987] and Gosling *et al.* [1987] have argued that the magnetic fields in bidirectional particle events must be closed, and both favored the plasmoid topology. If we accept the idea of a closed field topology, our results argue strongly against the plasmoid topology. We find no cases that suggest that particles are excluded from a region of interplanetary space.

If we assume an interplanetary field of  $10\gamma$ , the gyroradii of the 0.2- to 2.0-MeV electrons and the 22- to 27-MeV protons are 5 orders of magnitude and 3 orders of magnitude,

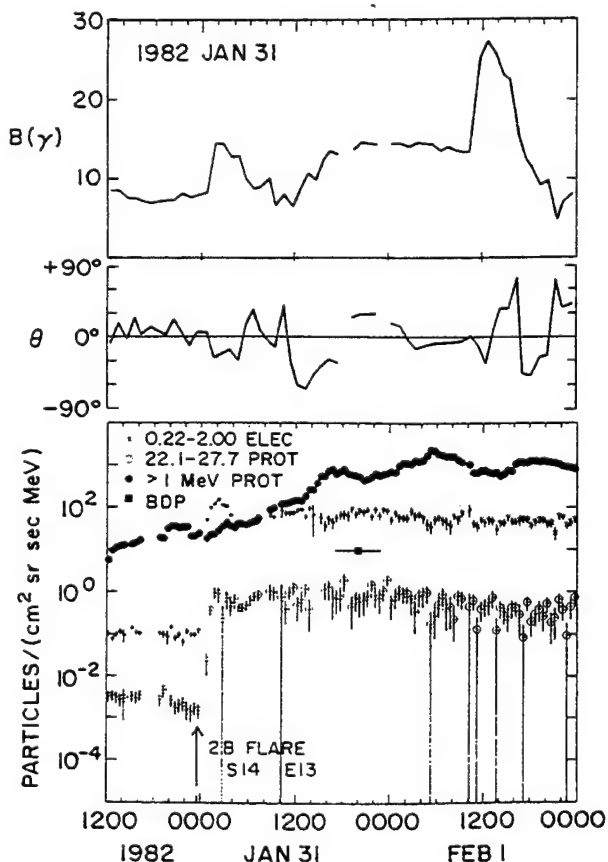


Fig. 3. The BDP event of January 31, 1982. The top panel shows the B field intensity and the inclination of the field vector to the ecliptic plane. The SEP event began before the BDP event. SEP fluxes showed no modulation at the time of the BDP.

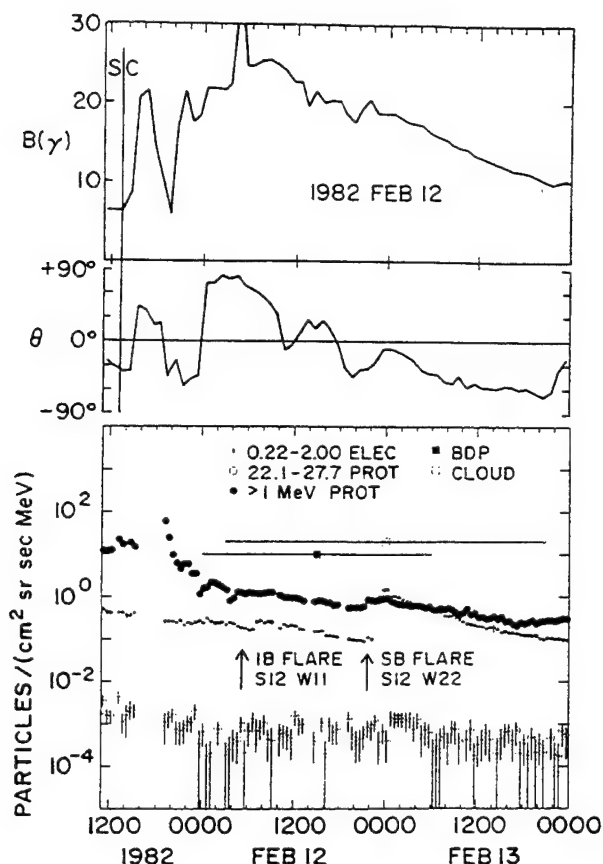


Fig. 4. The BDP and magnetic cloud event of February 12, 1982. Two solar electron events occurred during the BDP event. The top panel shows the B field intensity and the inclination of the field vector to the ecliptic plane. The time of an sc is indicated in the top panel.

respectively, smaller than the characteristic sizes of the inferred plasmoids. Thus even with substantial cross-field diffusion, a plasmoid should reveal itself with a strong decrease in SEP fluxes.

It is undoubtedly unrealistic to suppose that a large region of space is completely magnetically isolated from its surroundings, since this would require a very highly ordered geometry in the magnetic reconnection site near the Sun. It is more likely that a tightly wound helix forms with the ends of the helix connected back to the Sun, as shown in Figures 16 and 17 of Gosling [1990]. Even in this case, only a small number of field lines provide access for the SEPs to the large volume of the magnetic helix. This suggests that we may see a small population of SEPs in the helix, but the SEP event onsets and maxima should be substantially delayed when they occur in the helix, and the helix fluxes should be reduced from those outside the helix, contrary to what is observed.

The three kinds of magnetic topology that could explain the bidirectional particle events are shown schematically in Figure 1. The open configuration, in which bidirectional fluxes result from reflection or injection behind a shock [Rao *et al.*, 1967] or from a compressed region of interplanetary field [Barouch and Burlaga, 1976], has not been considered in recent studies. Our SEP observations are consistent with

such a topology, which, of course, does not require a CME for its formation.

We can use the results of recent comparisons of magnetic clouds and Forbush decreases [Badruddin *et al.*, 1986; Zhang and Burlaga, 1988; Sanderson *et al.*, 1990a] to complement our use of SEPs as probes of the magnetic topology. The goal of these studies was to determine whether the postshock turbulent region or the magnetic cloud is responsible for the Forbush decreases observed in the neutron monitor counts. We can treat the cosmic rays as a population of particles from a source in an antisolar direction and, again assuming limited cross-field diffusion, ask whether those particles will have access to the topological regions shown in Figure 1.

If either the bottle or the plasmoid topology of Figure 1 characterizes the cloud, we should expect a depression of the cosmic ray fluxes in the cloud, since the closed field lines originate in the Sun and are not directly accessible to the outer solar system source of the cosmic rays. In contrast to the case with SEPs, the cosmic rays would have 2–3 days during which they could diffuse into the bottle or plasmoid before it is observed at Earth. The cosmic ray rigidities are an order of magnitude larger than those of the 22- to 27-MeV protons of our study, but the cosmic ray gyroradii are still 2 orders of magnitude less than the inferred magnetic cloud radii.

The general result [Sanderson *et al.*, 1990a] is that the first step of the decrease is associated with the postshock turbulent region and the second step with the passage of the cloud. The maximum decrease occurs shortly after (~4 hours) the arrival of the cloud and may be due to the tangential discontinuity between the cloud and the preceding turbulent region. The small decreases (<5%) and the gradual increases, rather than decreases, in galactic cosmic ray fluxes as the Earth moves further into the cloud appear to be inconsistent with the closed topologies of the plasmoid and the bottle. In addition, Badruddin *et al.* [1986] found cases with no appreciable decrease in cosmic ray intensity with shock-associated clouds. This was also generally the case for clouds associated with cold magnetic enhancements, rather than with shocks.

We suggest that while the bidirectional particle fluxes observed by Marsden *et al.* [1987] and Gosling *et al.* [1987] are an effective tool for examining the geometrical properties of the magnetic field, such as the field direction or divergence, those fluxes cannot determine the field topology, i.e., the large-scale connections of the field lines. The fact that clouds, BDPs, and BDEs are nearly transparent to SEPs and cosmic rays suggests that we are not dealing with closed field structures. If we believe that the CME magnetic field topology must be closed, then BDPs and BDEs are not exclusively signatures of CMEs. On the other hand, if CMEs are characterized by open field topologies, a serious revision of our view of magnetic fields in CMEs may be necessary.

**Acknowledgments.** The work at Emmanuel College was funded by AFGL contract F19628-87-K-0033 and at Boston College by contract F19628-90-K006. We acknowledge useful discussions with D. Webb and E. Cliver.

The Editor thanks G. Zhang and R. G. Marsden for their assistance in evaluating this paper.



## REFERENCES

- Badrudin, R. S. Yadav, and N. R. Yadav, Influence of magnetic clouds on cosmic ray intensity variation, *Sol. Phys.*, **105**, 413, 1986.
- Bame, S. J., J. R. Asbridge, W. C. Feldman, J. T. Gosling, and R. D. Zwickl, Bi-directional streaming of solar wind electrons >80 eV: ISEE evidence for a closed-field structure within the driver gas of an interplanetary shock, *Geophys. Res. Lett.*, **8**, 173, 1981.
- Barouch, E., and L. F. Burlaga, Three-dimensional interplanetary stream magnetism and energetic particle motion, *J. Geophys. Res.*, **81**, 2103, 1976.
- Burlaga, L. F., Magnetic clouds and force-free fields with constant  $\alpha$ , *J. Geophys. Res.*, **93**, 7217, 1988.
- Burlaga, L. F., E. Sittler, F. Mariani, and R. Schwenn, Magnetic loop behind an interplanetary shock: Voyager, Helios, and IMP 8 observations, *J. Geophys. Res.*, **86**, 6673, 1981.
- Gold, T., Plasma and magnetic fields in the solar system, *J. Geophys. Res.*, **64**, 1665, 1959.
- Gosling, J. T., Coronal mass ejections and magnetic flux ropes in interplanetary space, in *Physics of Magnetic Flux Ropes*, *Geophys. Monogr. Ser.*, vol. 58, edited by C. T. Russell et al., p. 343, AGU, Washington, D. C., 1990.
- Gosling, J. T., and D. J. McComas, Field line draping about fast coronal mass ejections: A source of strong out-of-the-ecliptic interplanetary magnetic fields, *Geophys. Res. Lett.*, **14**, 355, 1987.
- Gosling, J. T., E. Hildner, R. M. MacQueen, R. H. Munro, A. I. Poland, and C. L. Ross, Mass ejections from the sun: A view from Skylab, *J. Geophys. Res.*, **79**, 4581, 1974.
- Gosling, J. T., D. N. Baker, S. J. Bame, W. C. Feldman, R. D. Zwickl, and E. J. Smith, Bidirectional solar wind heat flux events, *J. Geophys. Res.*, **92**, 8519, 1987.
- Hundhausen, A. J., T. E. Holzer, and B. C. Low, Do slow shocks precede some coronal mass ejections?, *J. Geophys. Res.*, **92**, 11,173, 1987.
- Kahler, S. W., and D. V. Reames, Solar energetic particles as probes of the structures of magnetic clouds, *Proc. Int. Cosmic Ray Conf. 21st*, **5**, 245, 1990.
- Klein, L. W., and L. F. Burlaga, Interplanetary magnetic clouds at 1 AU, *J. Geophys. Res.*, **87**, 613, 1982.
- Kutchko, F. J., R. P. Briggs, and T. P. Armstrong, The bidirectional particle event of October 12, 1977, possibly associated with a magnetic loop, *J. Geophys. Res.*, **87**, 1419, 1982.
- Marsden, R. G., T. R. Sanderson, C. Tranquille, K.-P. Wenzel, and E. J. Smith, ISEE 3 observations of low-energy proton bidirectional events and their relation to isolated interplanetary magnetic structures, *J. Geophys. Res.*, **92**, 11,009, 1987.
- Marubashi, K., Structure of the interplanetary magnetic clouds and their solar origins, *Adv. Space Res.*, **6**, 335, 1986.
- Palmer, I. D., F. R. Allum, and S. Singer, Bidirectional anisotropies in solar cosmic ray events: Evidence for magnetic bottles, *J. Geophys. Res.*, **83**, 75, 1978.
- Piddington, J. H., Interplanetary magnetic field and its control of cosmic-ray variations, *Phys. Rev.*, **112**, 589, 1958.
- Pilipp, W. G., H. Miggenrieder, M. D. Montgomery, K.-H. Muhlhauser, H. Rosenbauer, and R. Schwenn, Unusual electron distribution functions in the solar wind derived from the Helios plasma experiment: Double-strahl distributions and distributions with an extremely anisotropic core, *J. Geophys. Res.*, **92**, 1093, 1987.
- Rao, U. R., K. G. McCracken, and R. P. Bukata, Cosmic ray propagation processes, 2, The energetic storm particle event, *J. Geophys. Res.*, **72**, 4325, 1967.
- Sanderson, T. R., R. G. Marsden, R. Reinhard, K.-P. Wenzel, and E. J. Smith, Correlated particle and magnetic field observations of a large-scale magnetic loop structure behind an interplanetary shock, *Geophys. Res. Lett.*, **10**, 916, 1983.
- Sanderson, T. R., J. Beeck, R. G. Marsden, C. Tranquille, K.-P. Wenzel, R. B. McKibben, and E. J. Smith, A study of the relation between magnetic clouds and Forbush decreases, *Proc. Int. Cosmic Ray Conf. 21st*, **6**, 251, 1990a.
- Sanderson, T. R., J. Beeck, R. G. Marsden, C. Tranquille, K.-P. Wenzel, R. B. McKibben, and E. J. Smith, Cosmic ray, energetic ion and magnetic field characteristics of a magnetic cloud, *Proc. Int. Cosmic Ray Conf. 21st*, **6**, 255, 1990b.
- Sarris, E. T., and S. M. Krimigis, Evidence for solar magnetic loops beyond 1 AU, *Geophys. Res. Lett.*, **9**, 167, 1982.
- Tranquille, C., T. R. Sanderson, R. G. Marsden, K.-P. Wenzel, and E. J. Smith, Properties of a large-scale interplanetary loop structure as deduced from low-energy proton anisotropy and magnetic field measurements, *J. Geophys. Res.*, **92**, 6, 1987.
- von Rosenvinge, T. T., F. B. McDonald, J. H. Trainor, M. A. I. van Hollebeke, and L. A. Fisk, The medium energy cosmic ray experiment for ISEE-c, *IEEE Trans. Geosci. Electron.*, **GE-16**, 208, 1978.
- Webb, D. F., and A. J. Hundhausen, Activity associated with the solar origin of coronal mass ejections, *Sol. Phys.*, **108**, 383, 1987.
- Wilson, R. M., and E. Hildner, On the association of magnetic clouds with disappearing filaments, *J. Geophys. Res.*, **91**, 5867, 1986.
- Zhang, G., and L. F. Burlaga, Magnetic clouds, geomagnetic disturbances, and cosmic ray decreases, *J. Geophys. Res.*, **93**, 2511, 1988.
- Zwickl, R. D., J. R. Asbridge, S. J. Bame, W. C. Feldman, J. T. Gosling, and E. J. Smith, Plasma properties of driver gas following interplanetary shocks observed on ISEE 3, Solar Wind Five, *NASA Conf. Publ.*, **CP-2280**, 711, 1983.

S. W. Kahler, AFGL/PHG, Hanscom AFB, MA 01731.

D. V. Reames, Code 661, NASA Goddard Space Flight Center, Greenbelt, MD 20771.

(Received July 25, 1990;  
revised December 28, 1990;  
accepted February 28, 1991.)



The U.S. Government is authorized to reproduce and sell this report.  
Permission for further reproduction by others must be obtained from  
the copyright owner.

# SOLAR FLARES AND CORONAL MASS EJECTIONS

S.W. Kehler

Institute for Space Research, Boston College, Newton Center,  
Massachusetts 02159

KEY WORDS: solar wind, geomagnetic storms, filaments, solar x-ray emission,  
solar radio emission

## 1. INTRODUCTION

Attempts to clarify the nature of the terrestrial effects of solar activity and variability continue at an increasing pace. While mechanisms relating possible changes in terrestrial weather patterns to changes in solar luminosity remain elusive, it has long been thought that intense geomagnetic storms and interplanetary disturbances can be traced directly to large solar flares. To describe the basic scenario in simple terms, a large release of energy first occurs in a region of strong magnetic field. The energy release results in a rapid heating of coronal and chromospheric material, which expands outward into the interplanetary medium. In the case of the most energetic events the expanding material produces an interplanetary shock wave. The most energetic aspect of the flare, the impulsive phase, is characterized by the production of energetic ( $E > 1$  MeV) electrons and protons, some of which can be observed as a solar energetic particle (SEP) event at 1 AU.

Over the past half century attempts have been made to identify the solar flares and their particular properties that result in geomagnetic storms and SEP events. These extensive studies, of interest to both solar physicists and forecasters of effects on the terrestrial environment, seemed to lay a solid foundation for the idea that the flare itself was the cause of the subsequent activity observed in the interplanetary medium and at the Earth.

About two decades ago large coronal eruptions, now known as coronal

mass ejections (CMEs), were discovered in coronagraph observations on the *OSO-7* (Tousey 1973) and *SkyLab* (Gosling et al 1974) spacecraft. At first they were thought to be driven by large flares. Today, although the general perception continues that large flares are the primary sources of both energy release in the corona and disturbed interplanetary flows, the observational evidence indicates that it is the CMEs themselves, and not large flares, that are the sources of both the energy release and interplanetary disturbances. Flares, the objects of extensive studies for decades, are not required to produce a CME and are probably only secondary phenomena when they occur with CMEs.

This review addresses two basic questions. First, how did we form such a fundamentally incorrect view of the effects of flares after so much observational and theoretical work? Second, what is the observational and theoretical evidence to support a primary role for CMEs, and what can we say about the relationship between flares and CMEs? In Section 2 we present flare and CME observations in a historical context to show the changing perspective between the two phenomena. In Section 3 we discuss the coronal phenomena that bear on the relationship between flares and CMEs. Interplanetary effects are discussed in Section 4.

## 2. HISTORICAL PERSPECTIVE

### 2.1 *The Flare as the Source of Geomagnetic Disturbances*

The first suggestion that geomagnetic disturbances were solar in origin was the observation that frequencies of both geomagnetic storms and sunspots followed the eleven-year cycle (Sabine 1852). Later, Maunder (1904) and Greaves & Newton (1928a,b) showed that the "great" geomagnetic storms were usually accompanied on the sun by groups of spots with large projected areas. By noting that the most probable spot position was one day west of central meridian and that large storms last about a day, Greaves & Newton (1928a,b) deduced a time of one and a half days for the disturbance to travel from the sun to the Earth. The smaller storms, however, did not show a strong correlation with sunspots.

The first step in associating geomagnetic storms with flares rather than with the associated spot regions was the memorable observation by Carrington (1860) of the 1 September 1859 white-light flare that was followed about 17 hrs later by a large geomagnetic storm. Hale (1931) reviewed the spectrohelioscope observations of large flares and drew a connection between some of those events and subsequent geomagnetic storms. A solid foundation for the statistical association of large flares and storms was provided by Newton (1939, 1943) who surveyed all the large flares observed since 1892 and found a significant correlation between those flares and

subsequent geomagnetic storms. The result that the probability of a subsequent geomagnetic storm depends on the occurrence of a type IV radio burst (McLean 1959) and on the complexity of the magnetic field in the spot group associated with a flare (Bell 1961) further strengthened the tie between flares and storms.

Dellinger (1937) associated flares with another geomagnetic disturbance known as a shortwave radio fadeout or sudden ionospheric disturbance (SID). This kind of disturbance, in which an increase in atmospheric ionization and a geomagnetic disturbance occur nearly simultaneously with the flare brightening, had been tentatively associated with flares as early as the 1 September 1859 flare, but Dellinger (1937) provided the statistical foundation for the association. SIDs were attributed to ultraviolet radiation (e.g. Dellinger 1936) rather than to X rays, but the electromagnetic nature of the disturbance was correctly understood at the time.

A third kind of terrestrial disturbance, the increase of cosmic-ray intensity at the Earth, now known as a ground-level enhancement (GLE), was associated with flares by Forbush (1946). These events result when ions of energies exceeding about 1 BeV strike the Earth's atmosphere to produce secondary particles measured by detectors on the Earth. In a subsequent work Forbush et al (1949) discussed the acceleration and escape of BeV protons in terms of variable magnetic fields of sunspots. The detection of  $E < 100$  MeV proton events by riometers (Reid & Leinbach 1959) also suggested flare sources for those events. Early efforts to understand particle acceleration considered the source to lie in or near the flare plasma (e.g. Smith & Smith 1963, Kundu 1965).

Thus, we see that by about 1960 there appeared little reason to doubt that all three solar-terrestrial disturbances -- large geomagnetic storms, SIDs, and SEP events -- were directly caused by the flare itself. It is the thesis of this review that although these disturbances are usually well associated with flares, only SIDs and some aspects of SEP events can be causally related to flares.

Since it was appreciated that the expulsion of a stream of high-velocity charged particles had to accompany the flare to cause the subsequent geomagnetic storm, a mechanism was required to effect the expulsion. Milne (1926) discussed a radiation-pressure mechanism in which outwardly moving atoms see a Doppler-shifted spectrum in which the resonant radiation lies on the violet side of the absorption line of the atom and is more intense than that in the absorption line itself. He calculated a maximum velocity of 1600 km/s for the escaping atoms, similar to that required for the expelled stream. Hale (1931) suggested that the flare emission could provide increased radiation to drive the particle stream in Milne's model, but Chapman & Bartels (1940) acknowledged that the solar

phenomena giving rise to the particle stream had yet to be observed. Parker (1961) used a hydrodynamic calculation to show that a large solar flare with a temperature of  $4 \times 10^6$  K could drive a hydrodynamic blast wave to the Earth in 1–2 days. Chapman (1964) and Akasofu & Chapman (1972) adapted Kahn's (1949) ad hoc treatment of a shell of gas expelled from the H $\alpha$  flare region with a particle speed profile decreasing during the course of the flare. Again, no association with observed flare phenomena was claimed. However, by examining six major flare events observed in August 1972, Lin & Hudson (1976) provided observational support for the idea that the energy of  $E > 10$  keV flare electrons can be sufficient to provide the energy and mass for interplanetary shock waves by heating the atmospheric gas to energies sufficient to escape the solar gravitational and magnetic fields. They found that shock waves were associated only with those flares for which the  $E > 20$  keV electron energy exceeded  $10^{11}$  erg.

The numerical integration of the time-dependent hydrodynamic equations for interplanetary disturbances with shock waves was carried out by Hundhausen & Gentry (1969), who obtained solutions for piston-driven and blast waves. Although they explicitly assumed flare-driven disturbances, Hundhausen (1972a,b), in reviewing these results, expressed reservations about associating flares with interplanetary shock waves, the arguments causing geomagnetic storms. He noted 1. the imperfect correlation between large or energetic flares and interplanetary shocks, 2. the large masses and energies of the shocks compared with the flare energies, and 3. the occurrence of flares in closed magnetic field regions unrelated to solar wind flow. Thus, at the time of the *SkyLab* mission in 1973 the basic physics of interplanetary shocks was understood, but the shocks were not yet directly related to any coronal events by observations.

Solar prominences were well known and easily observed by early investigators. These cool coronal structures have typical lengths of  $2 \times 10^5$  km and heights of  $5 \times 10^4$  km. They appear as bright features on the limb and as dark ribbons called filaments when seen on the disk. We may ask why prominence eruptions were not thought to play any role in geomagnetic storms. Greaves & Newton (1928b) suggested a relationship between prominences and geomagnetic storms, but Hale (1931) pointed out that erupting prominences generally fall back to the sun, and Newton (1939) dismissed erupting prominences as the sources of high-speed streams because they rarely achieve escape velocity. An additional factor may have been that the angular extents of the streams, correctly perceived to be up to  $90^\circ$  wide (Newton 1943), were thought to be much larger than prominence eruptions.

There are two types of geomagnetic storms, which are due to different

kinds of high-speed streams (e.g. Feynman & Gii 1986). The first type arises from magnetically open, long-lived solar coronal holes and usually results in small storms with gradual commencements. Twenty-seven-day recurrences of these storms (Hundhausen 1977) were first discovered by Maunder (1905) and analyzed by superposed epoch analysis by Chree & Stagg (1927). The second type of geomagnetic storm begins with a sudden commencement—a sharp increase in the horizontal component of the geomagnetic field. These storms are relatively large and are due to interplanetary shocks preceding high-speed streams arising from the transient eruption of closed-field solar regions. Thus, if one wishes to find an association between prominence eruptions (or flares) and geomagnetic storms, it is necessary to deal only with the largest storms. The connection between prominence eruptions and geomagnetic storms was not appreciated until the work of Joselyn & McIntosh (1981). In reviewing the history of work on associations between prominences and storms, they showed how the recurrent storms confused earlier investigators and provided one more reason that prominences, an integral part of many CMEs (Webb & Hundhausen 1987), were not linked to storms.

## 2.2 Flares as Drivers for CMEs

The first summary of *SkyLab* CMEs (Gosling et al 1974) left little doubt that CMEs were the long-sought eruptions of coronal material required to produce the high-speed transient flows of solar wind which, in turn, produce geomagnetic storms. Gosling et al (1974, 1976) found that although few CMEs were accompanied by H $\alpha$  flares, those CMEs were generally much faster than CMEs without flares and were nearly always accompanied by type II or type IV metric radio bursts. They suggested two classes of nonrecurrent interplanetary disturbances: 1. those due to fast CMEs associated with flares and type II or type IV bursts, and 2. a larger class due to slower CMEs but not associated with flares or type II or type IV bursts. Their results and those of Stewart et al (1974a,b) reporting on flare-associated CMEs observed on *O5O-7* left little reason to doubt that the fastest CMEs originated in the explosive phases of flares.

The idea that CMEs are propelled by pressure forces resulting from associated flares was the basis of several kinds of CME models. The first approach used pressure pulses, usually based on associated flare X-ray flux profiles, to drive the ejections (Dryer 1982). The results of numerical codes were compared with CME observations (e.g. Wu et al 1983b), but disagreement arose about the success of this approach in matching the appearances of CMEs (Sime et al 1984, 1985; Dryer & Wu 1985). A serious problem for this model is that parametric studies of potential fields show that reasonable pressure pulses in those fields cannot result in CMEs

(Hildner et al 1986). The neglect of solar magnetic fields in the early hydrodynamic calculations (e.g. Kahn 1949, Parker 1961) allowed models to provide support for the idea of expulsion of flare-heated plasma into the interplanetary medium.

A second approach to modeling CMEs assumed that magnetic reconnection occurs in the fields below an erupting prominence. Anzer & Pincman (1982) suggested that flaring loops are the lower loops rooted to the solar surface and that the upper disconnected loops provide the driving force for the CME. The driving force can occur only as the flare takes place.

These early models assumed that the CME directly overlay the associated flare and that the flare had to begin at or before the CME onset. In Sections 3.2–3.4 we review the recent observational results on the sizes, locations, timings, and energetics of flares relative to CMEs which have undermined the crucial assumptions of these models. The rejection of models linking CME propulsion to associated flares eliminates the physical connection which had long been supposed to exist between flares and interplanetary shocks.

### 2.3 Observability and Energetics of Flares and CMEs

A factor contributing to the presumption of a direct association between flares and interplanetary shocks appears to be the relative ease with which flares are observed. Worldwide H $\alpha$  patrol observations of the sun were begun about 1934, providing a large body of flare data. Optical observations must be spatially resolved to detect flares, but in the radio and X-ray ranges flare signals are frequently several orders of magnitude above their quiet solar backgrounds, so unresolved full-sun observations in both wavelength ranges are quite adequate to detect rather small flares. The white-light coronagraph, on the other hand, detects only changes in the line-of-sight brightness which correspond to the addition or subtraction of coronal material. It is sometimes necessary to subtract coronagraph images pixel by pixel (Figure 1) to detect these brightness changes (Howard et al 1985), which rarely exceed 20 to 30% of the background signal.

The occurrence of flare radiation in the radio and X-ray wavebands clearly established the presence of heated plasmas and nonthermal particles arising from the rapid release of energy. In contrast, the coronal material of CMEs observed in white-light coronagraphs is assumed not to be substantially heated above the ambient coronal temperature. In fact, coronagraph observations in the H $\alpha$  line have established that cool prominence material is often observed in the cores of CMEs (Athay & Illing 1986).

The first white-light coronagraph observations of CMEs followed the first radio and X-ray observations of flares by over 20 years, by which

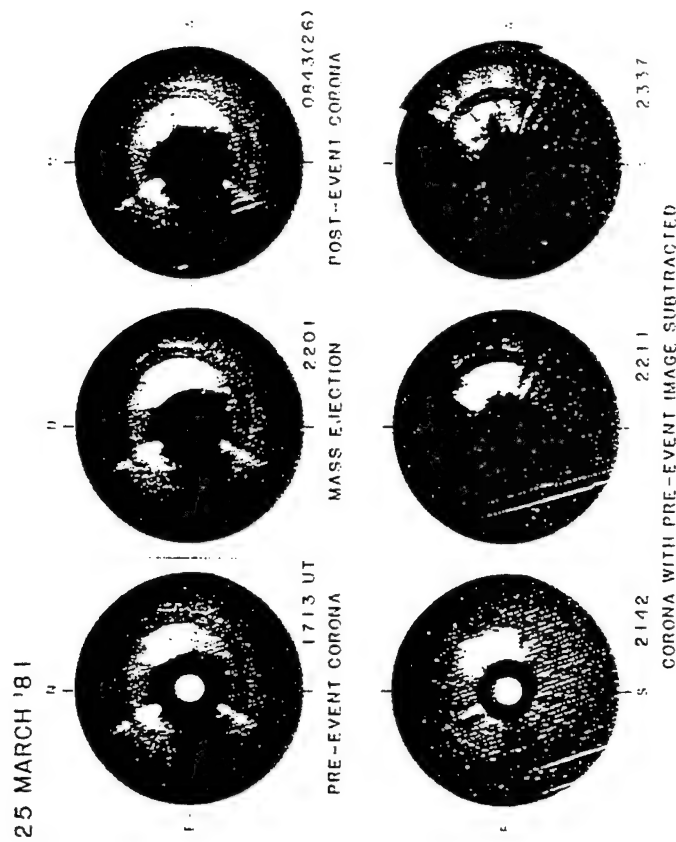


Figure 1 The CME of 25 March 1981, observed with the *Solwind* coronagraph. The top images are direct images, but the bottom images are difference images formed by subtracting a base image from the CME image. The solid white circles in the images on the left side indicate the solar disk. From N. R. Sheeley, Jr.

time the flare event itself had been firmly established as the source of SEP events and of transient high-speed wind streams causing geomagnetic storms (e.g. Smith & Smith 1963). The CME energies are due to mass motions of large-scale structures, while those of flares result from energized particles in small-scale structures. With the solar research community observationally and historically focused on flares as the sources of transient interplanetary phenomena, the concept of CMEs, rather than flares, as those sources is only now gaining credibility.

## 3. FLARE/CME RELATIONSHIPS

### 3.1 Flare/CME Statistics

The *SkyLab* mission in 1973–1974 provided the first large data base of CMEs which could be compared with other solar phenomena to look for spatial and temporal associations. The first studies were based on the EUV

and soft X-ray images of *SkyLab* flares. Sheeley et al (1975) studied spatially resolved *SkyLab* observations obtained during long-duration ( $>4.5$  hr) soft X-ray events (LDEs) seen with the *SOLRAD* spacecraft. Their observations suggested that all LDEs are accompanied by CMEs and that most LDEs were accompanied by filament eruptions. Kahler (1977) studied the X-ray structures of LDEs and found them to consist of arcades of high ( $10^5$  km) loops which he argued were the X-ray analogs of H $\alpha$  post-flare loop prominence systems. The post-flare loop prominences had been modeled earlier by Kopp & Pneuman (1976), and Kahler suggested that their model was also applicable to the LDE structures.

Pallavicini et al (1977) surveyed X-ray limb-flare images in the *SkyLab* data and concluded that all flares consist of two classes. The first class are compact flares with small volumes ( $10^{26}$ – $10^{27}$  cm $^3$ ), low heights ( $<10^4$  km), and short durations (tens of minutes). The second class consisted of large volumes ( $10^{28}$ – $10^{29}$  cm $^3$ ), great heights ( $>10^4$  km), and long time scales (hours). The second class were well associated with CMEs, but the first class were not. These results suggested that when CMEs are associated with flares, those flares are LDEs. These early results said nothing about CMEs not associated with flares.

A correlation between the average sunspot number of each longitudinal quadrant of the sun and the number of CMEs arising from that quadrant was found by Hildner et al (1976). In their view, this correlation suggested that strong magnetic fields provided the forces required to propel CMEs. Munro et al (1979) carried out the first comprehensive survey to associate CMEs with various forms of solar activity. Of those CMEs with some kind of association, about 40% were associated with flares, but more than 70% were associated with eruptive prominences or disappearing filaments. A similar result was obtained by Webb & Hundhausen (1987) for the CMEs observed on the *SMM* spacecraft at solar maximum in 1980. In addition, they found that most of the soft X-ray events associated with the *SMM* CMEs were LDEs.

The *SkyLab* studies linking LDEs to CMEs and the model of reconnecting field lines in LDE flares (Kopp & Pneuman 1976, Anzer & Pneuman 1982) led to the scheme of one class of confined, compact flares of short duration with no associated CME and a second class of eruptive flares with associated CMEs and long durations due to the reconnection of open magnetic field lines (Svestka 1986). Sheeley et al (1983) examined the durations of the soft X-ray bursts associated with CMEs observed with the *Sohwind* coronagraph. They found that the longer the duration of an X-ray event, the higher the probability of an associated CME. These probabilities ranged from 26% for the shortest durations ( $\sim 1$  hr) to 100% for the longest ( $> 6$  hr). No sharp distinction was found between short-

duration and long-duration X-ray bursts in terms of their associations with CMEs. Such a distinction would have been expected, based on the existence of the two classes of flares. The broad range of durations of X-ray flares associated with CMEs was confirmed in subsequent studies of *Sohwind* CMEs by Kahler et al (1989) and in *SMM* CMEs by Harrison (1991).

The reality of these two classes of flares has been challenged by Harrison (1991) on the grounds that no substantial difference in the range of soft X-ray durations is found between flares associated with CMEs and random samples of all flares. Kahler et al (1989) argued that the simple two-class scheme is complicated by the possibility that compact, noneruptive flares may occasionally occur as by-products of CMEs. Thus, the basic distinction between the two classes of flares still holds, but a flare of either class may be associated with a CME. Kahler et al (1989) also found a correlation between the CME angular width and the duration of the associated X-ray flare. In their view this implies a correlation between the spatial size scale of the CME and that of the associated flare, but they offer no convincing explanation of this result.

### 3.2 Flare/CME Spatial Relationships

The statistical studies of Munro et al (1979) and of Webb & Hundhausen (1987) confirmed the earlier report of Gosling et al (1974) that most CMEs were not accompanied by H $\alpha$  or X-ray flares. The first studies relating the detailed positions and timings of X-ray flares to associated CMEs were those of Harrison and colleagues. In a statistical analysis of 48 flare/CME events Harrison (1986) found a tendency for flares to lie below one leg of the CME rather than below the center of the CME. In more recent studies of *SMM* CMEs, Harrison et al (1990) and Harrison (1991) found flare locations rather broadly distributed with regard to the CME spans, matching similar results of Kahler et al (1989) using *Sohwind* CMEs. Hundhausen (1988), Kahler et al (1989), and Harrison et al (1990) have emphasized the fact that the characteristic angular sizes of CMEs exceed those of the associated H $\alpha$  flares and active regions by factors of 3 to 10. In a detailed study of four cases of flares and associated filament eruptions, Kahler et al (1988) found that the H $\alpha$  region which brightened in the impulsive phases of the flares were much smaller than the overall span of the erupting filaments. To generalize, the flare regions are much smaller and usually not centered under the erupting CMEs.

### 3.3 Flare/CME Temporal Relationships

Coronagraphs occult the inner coronal field of view in which a CME is formed. To find the time at which a CME began to leave the sun it is

necessary to plot the height of the CME as a function of time and then extrapolate the trajectory backward in time to the limb. Three unknowns (Harrison & Sime 1989) must be dealt with in this process: 1. the accelerations of CMEs at low heights (MacQueen 1985); 2. the altitude at which the CME was formed; and 3. the position, i.e. longitude and latitude, of the CME source region on the disk. One can assume a constant speed and calculate the extrapolated departure time for a CME from the solar limb. The comparison of this time relative to the onset of the associated flare can show whether the CME onset precedes or follows the flare onset. Harrison's work using this basic assumption with *SMM* CMEs has consistently shown (Harrison 1986, 1991; Harrison et al 1985, 1990) that CME onsets usually precede associated X-ray flare onsets.

If substantial acceleration occurs early in the development of a CME, it can only be observed close to the solar limb. The ground-based K-coronameter at Mauna Loa Observatory provides observations of CMEs from 1.2 to 2.0 solar radii ( $R_{\odot}$ ) from sun center. It operated during the *SMM* mission, allowing some CME trajectories to be tracked from 1.2 to 5  $R_{\odot}$  by combining the Mauna Loa and *SMM* observations (Figure 2). Hundhausen & Sime (1992) have found many CMEs from the large number observed in 1988 and 1989 in which the CME initiations are directly observed within the field of view of either the Mauna Loa or the *SMM* instrument. The launch times for such events can be determined with uncertainties of a few to ten minutes, with no need for extrapolation of observed trajectories; they once again tend to occur before the onset of associated hard or soft X-ray emissions (Figure 3).

In a related study Kahler et al (1988) examined the development of four H $\alpha$  filament eruptions during the impulsive phases of flares for evidence of how the eruptions are driven. In each case they found that the eruption began before the onset of the impulsive phase and that the eruptive motion was consistent with a smooth evolution through the impulsive phase, showing no new acceleration attributable to the impulsive phase.

### 3.4 Flare/CME Energetic Relationships

Besides the spatial and temporal relationships discussed above, we can ask whether the energetics of flares and CMEs supports the view that flares drive CMEs. MacQueen & Fisher (1983) examined the kinematic properties of 12 inner coronal (1.2–2.4  $R_{\odot}$ ) CMEs observed with the Mauna Loa K-coronameter. When the radial speeds were plotted as a function of distance from sun center, a clear difference between flare- and prominence-associated CMEs was found. Flare-associated CMEs showed generally higher speeds with little evidence of acceleration in the coronameter field of view while the prominence-associated CMEs were slower and exhibited

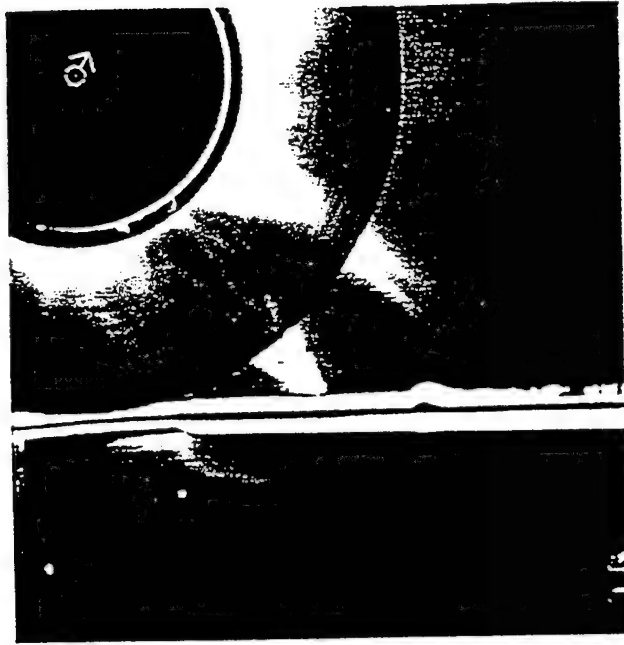


Figure 2 Composite image of a CME on 17 August 1989 observed with the Mauna Loa Observatory prominence monitor (inner field of view) and coronameter (middle field of view) and *SMM* coronagraph (outer field of view). The bright vertical structure is a detector artifact. From Hundhausen & Sime (1992).

substantial acceleration. MacQueen & Fisher suggested a fundamental difference between the two classes of CMEs, with flare-associated CMEs produced in impulsive accelerations acting over small spatial (0.2  $R_{\odot}$ ) and temporal (< 10 min) regimes. While this may be taken as evidence for flare-driven CMEs, there is some ambiguity in distinguishing between flare and prominence-associated CMEs, so an extension of their work to later periods should be carried out before their results are accepted.

In general, the estimated energies of interplanetary shocks can exceed  $10^{32}$  erg, about a factor of 10 larger than the energies of big flares (Hundhausen & Gentry 1969, Hundhausen 1972a, Lin & Hudson 1976). Hundhausen (1992) has found a poor correlation between flare X-ray intensities and associated CME energies, contrary to what is expected if CMEs are flare-driven and if X-ray intensity is a measure of the flare energy. In addition, Cane et al (1986), Heras et al (1988), and Sanahuja et al (1991) discussed 14 cases in which interplanetary shocks and SEP events arose from eruptions of filaments lying outside active regions. Despite the lack



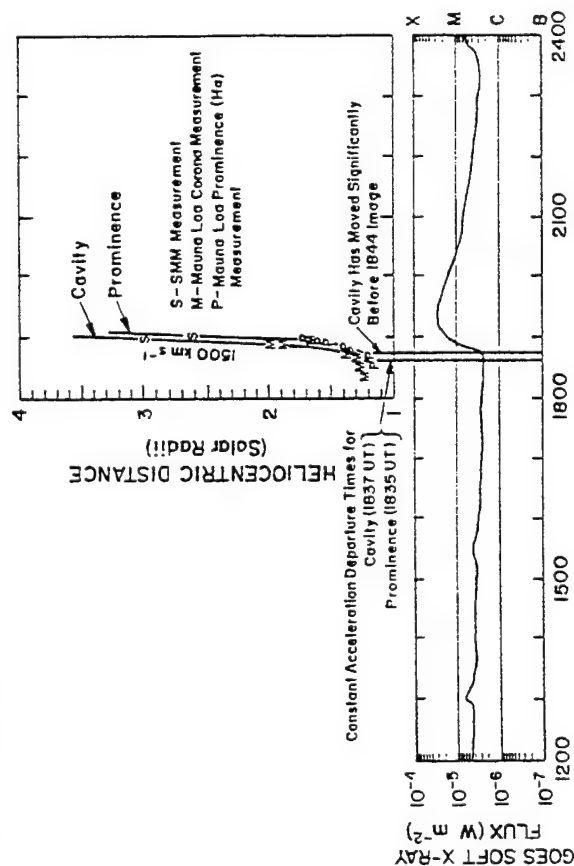


Figure 3 (Top panel) Height-time profiles of the CME cavity (the dark region behind the CME loop) and prominence. The best fits for constant acceleration give limb departure times of 1837 UT and 1835 UT for the cavity and prominence, respectively. (Bottom panel) The time profile of the GOES 1–8 Å X-ray flux. The onset of the CME components precedes the onset of the X-ray flare. From Hundhausen & Sime (1992).

of accompanying flares, these apparently innocuous solar events resulted in quite energetic interplanetary phenomena, including one case of an  $E > 50$  MeV proton event (Figure 4; Kahler et al 1986). These recent studies have shown that flare energies are poorly correlated with associated CMEs or interplanetary SEPs.

During the 1987–1989 rise in solar activity the sunspot latitudes gradually moved equatorward in the familiar butterfly pattern while the latitudes of the coronal helmet streamers moved poleward. Hundhausen (1992) found that the CME latitudes tracked the helmet streamer latitudes rather than the latitudes of sunspots, active regions, or flares. In addition, the widths and speeds of CMEs during this period showed no variation with latitude—a result suggesting that CMEs lying at active region latitudes, and possibly associated with flares, are not qualitatively different from those associated with high-latitude filament eruptions. Thus, contrary to the implications of the earlier MacQueen & Fisher (1983) result, these later

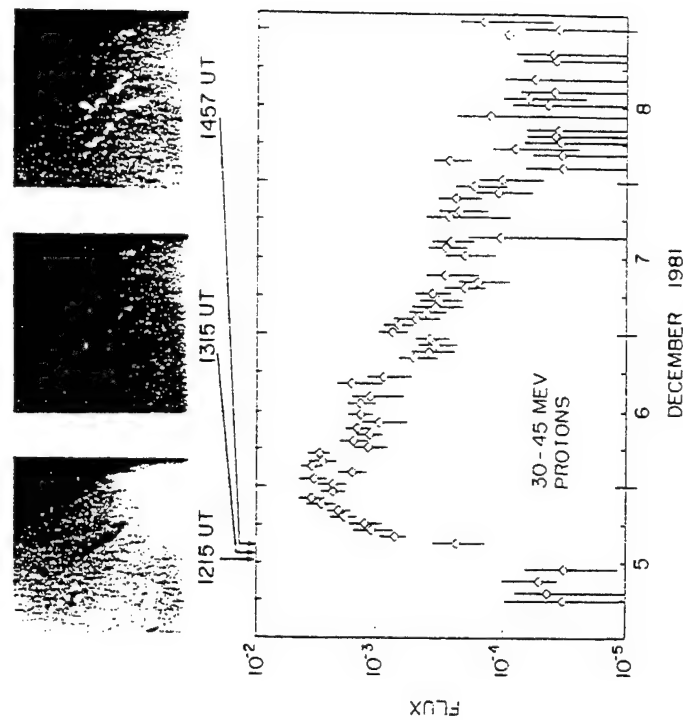


Figure 4 (Top) Ix images of the disappearing quiescent filament. The 1457 UT image shows a double-ribbon structure characteristic of active region flares, although the filament was far removed from any active region. (Bottom) The flux-time profile of 30–45 MeV protons observed at 1 AU following the filament eruption and CME. From Kahler et al (1986).

studies do not support the idea that the presence of an associated flare has some effect on the characteristics of a CME.

### 3.5 Preflare Phenomena and CMEs

If the CME involves the release of a large amount of coronal energy and begins minutes to tens of minutes before an associated flare, we might expect to find a preflare signature of the CME in the soft X-ray, microwave, or optical wavebands. It has long been known (Martin & Ramsey 1972) that distinct stages of filament activity precede the eruption of the filament itself. Since the erupting filament activity provides the bright core for many CMEs (Webb & Hundhausen 1987), the pre-eruptive filament activity provides one kind of pre-CME signal. Do we find early coronal signatures of CMEs in other wavebands? Harrison et al (1985) and Harrison (1986) found evidence for soft X-ray enhancements near the times of projected onsets of CMEs and about 20 min before the onsets of several associated flares.

In a recent study of 16 flare-associated CMEs Harrison et al (1990) found some X-ray emission preceding most of the flares, but positional information was lacking for many of those events. Tappin (1991) has also found that nearly all X-ray flares observed with the HXIS instrument on the *SAMM* spacecraft were preceded by weak soft X-ray bursts. Thus, we have an indication that weak soft X-ray emission may arise during CME onsets, but this result should be considered tentative.

### 3.6 Post-flare Phenomena and CMEs

Post-flare loop prominence systems (LPS) are magnetic loops observed to overlie the magnetic inversion line for some hours following major flares. Following the detailed description of their properties by Bruzek (1964) and the description of CMEs as eruptions of closed magnetic field lines (MacQueen et al 1974), Kopp & Pneuman (1976) proposed that an LPS forms from magnetic reconnection of oppositely directed field lines. Each newly formed loop is first observable in soft X rays (Sheeley et al 1975, Kahler 1977) and then in H $\alpha$  after it cools sufficiently. Cargill & Priest (1982) suggested that the rising neutral point trails a pair of slow MHD shocks which heat the upflowing plasma to temperatures as high as  $10^7$  K (Figure 5). The angular size of an associated CME is much larger than that of the post-flare LPS, which are observed only in active regions at flare sites. Perhaps such a reconnection scenario occurs throughout the open fields associated with the CME, and the LPS can be seen only where the fields are sufficiently strong and the reconnection sufficiently energetic to produce observable loops. Forbes et al (1989) have extended the model of Cargill & Priest (1982) to predict temperatures and maximum heights of flare loops in terms of the coronal vector field (Figure 6).

Cliver et al (1986) and Kosugi et al (1988) have found a type of post-flare event, the gradual hard X-ray burst, which is closely associated with CMEs and major flares. These events follow the occurrences of CMEs by 5 to 60 minutes and are characterized by a hardening of the  $E > 30$  keV X-ray spectrum and a high ratio of microwave to hard X-ray fluxes. They are strongly associated with type IV or continuum radio bursts and were interpreted in terms of acceleration and trapping of electrons in a post-flare LPS following a CME (Cliver et al 1986). This interpretation is supported by the observation that the bursts occur in the late phases of flares and are not accompanied by significant changes in H $\alpha$  flare brightness or area.

Another kind of coronal structure, known as a giant arch, was discovered by Svestka (1983) in images from the *SAMM* Hard X-ray Imaging Spectrometer. These large ( $> 10^5$  km) structures lie over active regions and appear to brighten in association with double-ribbon flares. Since giant

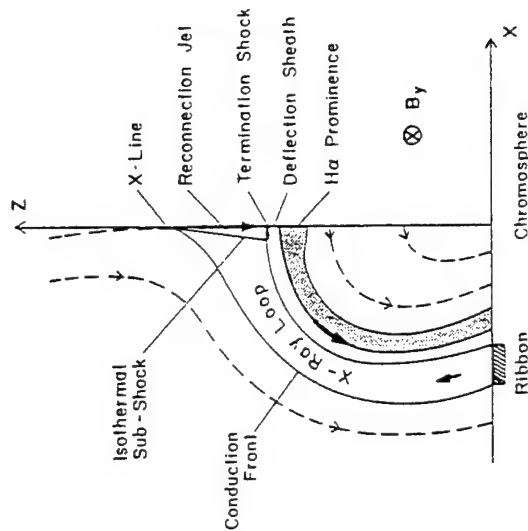


Figure 5 The flow pattern in the reconnection model of flare loops. Magnetic field reconnection at the isothermal subshocks provides the energy to heat the chromosphere. As higher field lines are reconnected, the loops grow in size. From Forbes et al (1989).

arches appear to be quasi-stationary and long-lived, it is difficult to understand how they can be associated with flares normally involved with CMEs (Svestka et al 1989). Two different interpretations of the arches have been suggested (Poletto & Svestka 1990). The first (Hick & Svestka 1987) is that there is a basic long-lived structure which is not disrupted in the double-ribbon flare. However, the reconnection process following the flare adds additional structure to the arch. This view is supported by the apparent long-lived nature of the arches and the lack of any evidence that they are disrupted during the flares. The second interpretation (Poletto & Kopp 1988) is that the arches result from the reconnection of opened field lines in a manner similar to that creating the smaller and underlying post-flare LPS. The H $\alpha$  footpoints of a series of giant arches observed in November 1980 were detected at the periphery of the active region (Martin et al 1989). Since these footpoints lay at the positions predicted by the current-free modeling of Kopp & Poletto (1990), this would appear to favor the Poletto & Kopp (1988) interpretation.

### 3.7 Type II, III, and IV Metric Radio Bursts

Type II metric radio bursts are interpreted as plasma emission from coronal shocks. The super-Alfvénic speeds ( $v > 400$  km/s) of the faster CMEs

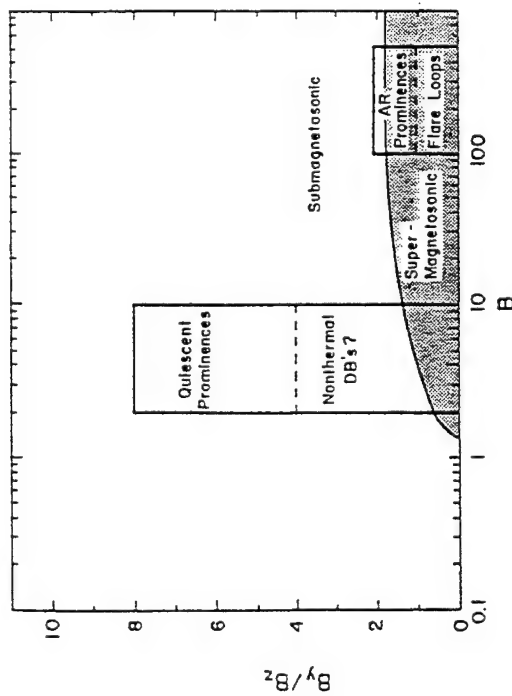


Figure 6 Ratio of  $B_{\parallel}$ , the magnetic field component along the neutral line, to  $B$ , the vertical magnetic field, versus the total field  $B$ . Shaded area indicates where the reconnection jets of Figure 5 are supermagnetosonic. In the model of Forbes et al (1989) post-flare loops can form only in regions such as active regions, which lie in the shaded area.

in the corona suggest that type II bursts are piston-driven coronal shocks. Several studies (Sheeley et al 1984, Robinson et al 1986, Kähler et al 1984b, Sawyer 1985) show that from 60% to more than 80% of all type II bursts are associated with CMEs. Sheeley et al (1984) explained the type II bursts without CMEs as blast wave shocks. Wagner & MacQueen (1983) proposed the more radical idea that all type II bursts, those with and without associated CMEs, are due to blast waves. In their view the blast wave is generated in the flare impulsive phase and then moves through and perhaps ahead of any accompanying CME. The preflare onset times of CMEs and the close association of type II bursts with flares and with impulsive phase radio bursts (Cane & Reames 1988a) supports the blast-wave case. However, the positional associations of type II bursts with filaments and streamers rather than with flares (Stewart 1984) and the fact that type II bursts are rarely associated with slow ( $v < 400$  km/s) CMEs (Kundu et al 1989) argues for piston-driven shocks. In addition, most looplike CMEs are preceded by deflections of preexisting coronal features ahead of the CME flanks, suggesting driven waves or shocks running well ahead of the CME fronts (Sime & Hundhausen 1987). Obviously, the relationship between type II shocks and CMEs remains undefined.

Type III radio bursts result from plasma emission and indicate the coronal trajectories of fast ( $v \sim 0.15c$ ) electrons (Dulk 1990). Since the electrons are guided by coronal magnetic fields, their presence may provide a diagnostic of coronal conditions during the CME/flare onset. Strong type III bursts occur preferentially with impulsive (Cane & Reames 1988a) and bright (Poquerusse & McIntosh 1990) flares and may therefore not be a good diagnostic of CMEs. However, Leblanc et al (1983) and Leblanc & Hoyos (1985) found that most type II bursts are associated with U bursts, a kind of type III burst due to electrons streaming along closed magnetic loops. When U bursts accompany type II bursts, the turning frequencies of successive U bursts drift lower, suggesting that the loops are expanding to higher altitudes. Since the expansion rates are similar to characteristic speeds of CMEs, Leblanc & Hoyos (1985) interpret these expanding loops as manifestations of CMEs.

Type IV metric radio bursts consist of broad-band emission usually seen only in conjunction with type II emission (Cane & Reames 1988b). The emission mechanism may be either gyrosynchrotron emission or plasma emission. The two broad classes of type IV bursts consist of moving type IV bursts and stationary type IV bursts, the latter sometimes called storm continuum (Pick 1986). A CME may be a necessary condition for stationary type IV bursts (Robinson et al 1986, Cane & Reames 1988a). Robinson et al (1986) found that nearly half of all CMEs with  $v > 400$  km/s were associated with type IV sources located within the CMEs, well behind the leading edge. Other observations (Kerdraon et al 1983) also find stationary type IV bursts in the bright structures at the bases of CMEs. A plausible explanation (Cliver 1983) is that the energetic electrons giving rise to the burst are produced during magnetic reconnection at neutral sheets in newly formed streamers following CMEs.

Because of their outward motion through the corona, we can expect some association between moving type IV bursts and CMEs. Gergely (1986) used several assumptions about the statistics of CMEs and type IV bursts to conclude that the mean speed of moving type IV bursts is less than that of associated CMEs and that the burst regions move behind or along with the CME leading edges. Multifrequency radioheliograph observations have shown that moving type IV bursts are confined to loops and blobs of CMEs (Kundu et al 1989, Gopalswamy & Kundu 1990). The usual association of moving type IV bursts with only fast ( $v > 400$  km/s) CMEs (Gosling et al 1976) may be a matter of detection thresholds due to the limitations of radio instrument sensitivities. Kundu et al (1989) reported the observation of a moving type IV burst associated with a slowly moving ( $v \sim 200$  km/s) CME. They suggested that a flare may not have been necessary for the production of the energetic electrons in the

type IV burst. It is possible that moving type IV bursts arise only from CMEs rather than from flares, but it is not clear that all moving type IV bursts are associated with CMEs (Gergely 1986).

## 4. INTERPLANETARY EFFECTS

### 4.1 *Shocks and Shock Driver Gas*

The composition of the interplanetary plasmas and SEPs associated with an observed eruptive solar event can provide the clues we need to distinguish between flares and ambient coronal material as the sources of the eruptions. The signature of a major interplanetary disturbance resulting from such an eruptive event consists of the arrival at the Earth of an interplanetary shock causing a geomagnetic storm and Forbush decrease. The first observations of the elemental composition of the high-speed driver-gas plasmas behind interplanetary shocks showed a He abundance enhancement (HAE) which was presumed to be flare plasma (Hirshberg et al 1972).

Borini et al (1982, 1983) analyzed the 103 forward shocks and 73 cases of solar wind HAE events ( $\text{He}/\text{H} > 10\%$  for  $> 2$  hr) observed during 1971–1978 with the Los Alamos plasma instruments on *IMP 6*, 7, and 8. They found that 44% of the HAE events followed an interplanetary shock within 2 days. Borini et al (1982, 1983) cited several observational arguments that the HAEs were interplanetary signatures of CMEs. First, the HAEs were well associated with solar type II and type IV radio bursts and varied in frequency of appearance with the solar activity cycle. Second, the high magnetic fields and low proton temperatures suggested a solar origin in strong coronal magnetic fields with closed topologies resulting in adiabatic cooling. While these arguments are certainly consistent with a solar source in CMEs, they could also be used to argue for a source in expelled flare plasma.

Another kind of solar wind He ion enrichment, that of the  $\text{He}^+$  ion relative to the normal  $\text{He}^{++}$  ion, also appears promising as a signature of the cool filamentary material known to be ejected in many CMEs (Illing & Hundhausen 1985). Enhanced  $\text{He}^+$  ion abundances have been observed in the solar wind on a number of occasions (Gosling et al 1980, Schwenn et al 1980, Bame 1983). The  $\text{He}^+/\text{He}^{++}$  ratio in these events reaches 0.1, about four orders of magnitude above that expected at coronal temperatures (Ahmad 1977). Cane et al (1986) found that at least 6 of the 15 or so reports of  $\text{He}^+$  (Bame 1983) can be associated with solar filament eruptions, suggesting that in these cases some prominence material has reached 1 AU without being raised to coronal temperatures.

The amount of cool filamentary material can be substantial. In one

CME, on 18 August 1980, Illing & Hundhausen (1986) and Athay & Illing (1986) found a prominence mass of  $\sim 10^{16}$  g, comparable to that of the rest of the CME. It should be noted, however, that most CMEs do not show the bright cores indicative of prominence plasmas (Webb & Hundhausen 1987) and that many of the features showing prominence-like structures are nearly fully ionized (Illing & Athay 1986). The lack of high instrumental sensitivity to the  $\text{He}^+$  ion may have precluded routine detection of the 1 AU passage of cool filamentary material.

Observations of high ionization states of solar-wind heavy ions have been made with electrostatic analyzers on the *Vela 5* and 6 and *ISEE-3* satellites. Bame et al (1979), Fennimore (1980), and Ipavich et al (1986) compared their heavy ion charge distributions with calculated equilibrium ionization states to deduce that some particle spectra had been heated to temperatures of  $2.5 \cdot 10 \times 10^6$  K, well above the normal solar-wind ionization temperatures. The association of these heated plasmas with post-shock flows, HAEs, and large solar flares led the authors to invoke flare-heated driver gases as the sources, as Hirshberg et al (1972) had done earlier.

What evidence do we have for flare-heated plasmas as constituents of CMEs? Before we can address that question, we have to be more specific about the term "flare-heated plasma." Three possibilities (Kahler 1988) are 1. hot ( $T > 10^7$  K) X-ray emitting flare plasma from the lower corona (Wu et al 1986); 2. coronal plasma in the CME which is radiantly heated by the lower-lying flare plasma; and 3. CME plasma which is heated to temperatures above those of the normal corona. Case 1 involves the flare source responsible for producing X-ray events observed in full-sun detectors. Case 2 corresponds to the model proposed by Mullan & Waldron (1986) in which the  $10^7$  K flare plasma heats the overlying corona to produce the high ionization states observed in solar energetic particle events. In case 3 some local heating occurs within the CME as energy is released. As discussed above, the white light coronagraph observations do not provide temperature diagnostics for coronal plasmas.

Which of the three candidate flare-heated plasmas look best? Candidate 1, part of the flare plasma itself, seems very unlikely. *Skylab* and *SMM* observations have shown these plasmas to be confined to closed loops in the lower corona. In addition, the ionization temperatures of  $\sim 2 \times 10^7$  K early in the flare are higher than what is observed in the solar wind data. Candidate 2, the plasma radiantly heated by flare X-ray emission and modeled by Mullan & Waldron (1986), seems a good choice. The ionization temperatures can differ significantly among the various solar wind ions and the enhanced temperatures should only be seen for CMEs with large X-ray flares. Both conditions are met in the few reported observations.

Candidate 3, heating within the CME, can not be ruled out, but the CME precursor observations of Harrison (1986) and the infrequent observation of moving type IV bursts and X-ray emitting blobs with CMEs suggests that the amount of heated material accompanying CMEs is small in most cases. To summarize, there is certainly evidence in the solar-wind observations for the escape of ions with high ionization temperatures, but it is only infrequently observed at 1 AU and is not likely to be escaping flare plasma.

A good statistical correlation has been found between interplanetary shocks and CMEs. Sheeley et al (1985) reported that 72% of 49 interplanetary shocks detected at the *Helios* spacecraft could be confidently associated with CMEs intersecting the ecliptic. Another 26% were possibly associated with CMEs. Only a few of the speeds of the CMEs producing shocks detected at the *Helios* spacecraft lay below 500 km/s. Cane et al (1987) studied the solar sources of interplanetary shocks fast enough to produce slow-drift kilometer type II radio bursts. They found that all 29 kilometer type II bursts with complementary *Solarwind* observations were associated with fast ( $v > 500$  km/s) and massive CMEs. A previous study by Cane et al (1986) showed that the eruptions of filaments lying outside active regions were the sources of six interplanetary shocks. Impulsive phases and metric type II bursts were absent in all six cases, showing that a rapid release of energy is not necessary for the formation of an interplanetary shock.

A very different and controversial view of the origin of interplanetary shocks was proposed by Hewish & Bravo (1986). In their study of transient events detected by interplanetary scintillation (IPS) observations at Cambridge they found that the projected solar source regions were always accompanied by coronal holes and suggested that transient activity at hole boundaries could produce interplanetary shocks. Noting the well observed association between coronal holes and high speed streams, they further argued that the 5 or 6 day duration of the high speed solar wind flow behind the shock was inconsistent with the short-lived flow expected from an explosive solar event. This view is not widely accepted for several reasons. First, the significance of the associations with holes is questioned because several holes are usually seen on the disk at any one time (Tsurutani & Gonzalez 1990). Second, the association between CMEs and IPS transients has not been established (Hewish 1990). However, assuming that CMEs are proxies for IPS events, Harrison (1990) found that active regions were far better associated with CME source regions than were coronal holes. Third, contrary to suggestions that large-scale ( $> 10^5$  km) eruptive events occur in coronal holes (Bravo et al 1991), Kahler & Moses (1990) found only small-scale ( $\sim 2 \times 10^4$  km) changes at coronal hole

boundaries. Fourth, although the long-duration high speed wind flow is inconsistent with a blast-wave model (Wu et al 1983a), as Hewish & Bravo (1986) point out, it is compatible with a piston-driven ejection corresponding to flows in newly opened coronal fields.

#### 4.2 Orientations of Flare and Interplanetary Magnetic Fields

The strongest geomagnetic storms occur when the  $B_z$  component of the interplanetary magnetic field points southward (Tsurutani et al 1990). If the transient magnetic fields behind an interplanetary shock arise solely from the eruptive magnetic fields of a flaring region, and if those fields retain their coronal orientation in interplanetary space, perhaps as a magnetic bottle (Gold 1959), then a strong geomagnetic disturbance should be preceded by an eruptive flare in which the coronal fields generally point southward. Pudovkin & Chertkov (1976) found that flares with large-scale ( $\sim 10^5$  km) southward fields were associated with intense storms, but flares with northward fields were rarely associated. This result suggested the importance of the solar flare magnetic field orientation for subsequent storm association.

Later work of Dodson et al (1982) and Lundstedt et al (1981) implied that the southward-field criterion for flares somehow selected more energetic flares which were more likely to be associated with geomagnetic storms. Although Pudovkin et al (1977) verified that daily averages of  $B_z$  observed several days after flares were rather well correlated with the flare field directions, the Dodson et al (1982) and Lundstedt et al (1981) results suggested flare energetics, rather than interplanetary  $B_z$  direction, was the dominant factor in producing geomagnetic storms.

The first contradiction to the idea that southward-field flares are significant for either flare energetics or geomagnetic storms came in a study by Wright & McNamara (1982). They examined the relationships between geomagnetic disturbances, flare energies, and flare-field directions for all large flares between 1968 and 1979. In contrast to Dodson et al (1982), no significant differences among northward, southward, and east-west flare fields in terms of average energies of flares were found. Wright & McNamara (1982) concluded that the sample of flares used by Pudovkin & Chertkov (1976) and Dodson et al (1982) was not typical. Later, Tang et al (1985, 1989) compared interplanetary events of large southward  $B_z$  values with associated flare fields and found that in three of five southward  $B_z$  events the photospheric fields had no dominant southward component.

The following problems in comparing the interplanetary  $B_z$  values with associated flare fields arose in the exchange of differences between Pudovkin & Zaitseva (1986) and Tang et al (1986): 1. uncertainties in making correct flare associations with geomagnetic storms (Neugebauer 1988); 2.



distinguishing the driver gas fields from those of the preceding compressed solar wind where  $B_z$  may also be large; and 3. differences in methodology of determining the flare field directions (Lundstedt 1982). In view of the fact that angular sizes of CMEs greatly exceed those of either flares or active regions, one might further expect that the flare fields used in these studies are not the appropriate coronal fields to use for correlation studies with interplanetary fields. The better choice of a coronal source field may be that over an erupting filament, but even that field may be only a part of the entire erupting field of the CME. A further problem is that the filament field generally lies at large angles to the overlying potential field and may be the dominant field of the CME driver. On the other hand, by the time the eruptive field reaches 1 AU, the dominant driver field of a CME may be only that from the associated active region containing most of the eruptive flux. To summarize, we don't know whether large-scale eruptive coronal fields maintain either their integrity or direction in the interplanetary medium, and if they do, we don't know the appropriate coronal source fields.

A common assumption in the preceding studies was that the solar origin of geomagnetic storms lay in flares or active regions. In a search for the solar sources of geomagnetic storms from 1976 to 1979 Joselyn & McIntosh (1981) found that many storms could be associated only with erupting filaments. Superposed epoch analyses have shown that geomagnetic (Wright & McNamara 1983) and interplanetary (Wright & Webb 1990) disturbances typically follow filament disappearances by 3 to 6 days. In view of our earlier discussion of the good correlation between filament eruptions and CMEs on the one hand and between CMEs and interplanetary shocks on the other, this association between filament eruptions and geomagnetic storms is not surprising and serves to diminish further the importance of flares as signatures of CMEs and interplanetary shocks.

### 4.3 Interplanetary SEPs

Solar energetic ( $E > 1$  MeV) particle (SEP) events have traditionally been associated with large solar flares and type II and type IV metric radio bursts (e.g. Smith & Smith 1963). SEPs have been presumed to be accelerated at the flare site, probably during the impulsive phase, after which they diffuse through the coronal and interplanetary magnetic fields on their path to the Earth. The first evidence of trouble for this simple picture of SEPs diffusing through a static corona was presented by Kahler et al (1978). Working with SEP events observed during the *SkyLab* mission, they found that nearly every SEP event could be associated with a CME or a proxy for a CME, such as an LDE X-ray event. This result was confirmed by comparisons of SEP events and CMEs observed with the *Sohrind*

coronagraph (Kahler et al 1984a, 1987) that showed a correlation between CME speed and the associated  $E > 4$  MeV peak proton flux. The comparable size scales of the CMEs and the region of fast propagation of the SEPs ( $\sim 50$ –90 degrees) suggested that the CMEs defined a dynamical coronal region over which the SEP injection occurred.

Elemental abundance measurements of SEP events have provided evidence for an ambient coronal source of the SEPs. Breneman & Stone (1985) showed that the elemental abundances of a given SEP event differ from the abundances averaged over all SEP events in a way which depends systematically on  $q/m$ , the ratio of the charge to the mass of the ions. The derived SEP source elemental abundances are essentially invariant and match the measured coronal abundances. Compared with photospheric abundances, the coronal abundances are known to be deficient in elements with a first ionization potential exceeding about 9 eV (Meyer 1985). Thus, the Breneman & Stone (1985) observations rule out a SEP source with photospheric abundances.

There is now some evidence to suggest that elemental abundances of flare plasmas more closely match the photospheric rather than the coronal abundances (Feldman & Widing 1990), perhaps because the photospheric material is the primary source of the heated flare plasma. The work of Widing & Feldman (1989) suggests a fundamental distinction in elemental abundances between closed and open magnetic structures, matching the nominal photospheric and coronal abundances, respectively. The implication is that the SEP sources lie in the open magnetic structures outside the closed-field structures of flares.

Mason et al (1984) studied the compositional variations of eight SEP events over broad ranges of heliolongitude separation angles between the optical flare sites and the footpoints of the interplanetary magnetic field at the Earth. The relative invariance of the elemental abundances with separation angles was difficult to reconcile with coronal propagation models but was more consistent with acceleration over a large volume of the corona by a shock wave.

A second kind of SEP event is that known as a  $\text{He}^3$ -rich event. These events are composed of relatively small ion fluxes, with high  $e/p$  ratios, scatter-free propagation, and enhanced abundances of  $\text{He}^3$  and heavy ions (Reames 1990b, Klecker et al 1990). These events show a correlation of heavy element abundances with flare X-ray temperatures (Reames 1988) and are apparently produced in flares (Reames et al 1988) or in impulsive coronal energy releases (Cliver & Kahler 1991). They are not associated with CMEs or type II bursts (Kahler et al 1985) and are observed only from flares in the western hemisphere of the sun which are well connected to the Earth (Reames et al 1991). Murphy et al (1991) found that the



elemental abundances they deduced for a well observed gamma-ray flare on 27 April 1981 differed significantly from those of large SEP events but resembled the abundances observed in the  $\text{He}^3$ -rich events, further suggesting a flare source for the  $\text{He}^3$ -rich events. In their survey of elemental abundances of 90 SEP events observed on *ISEE-3*, Reames et al (1990) found evidence for the two classes of events, with all the  $\text{He}^3$ -rich events having substantially higher  $\text{Fe}/\text{C}$  values than that of the corona (Figure 7).

Ionization state measurements of heavy ions in SEP events showed that the states were consistent with a source in ambient coronal temperatures of  $\sim 2 \times 10^6$  K (Gloeckler et al 1981, Luhn et al 1985). The enhanced ionization of several elements such as Mg can be explained by photoionization from flare X-ray fluxes (Mullan & Waldron 1986). The biggest challenge in the SEP ionization states is to understand why the  $\text{He}^+/ \text{He}^{++}$  is about 4 orders of magnitude larger than in the ambient corona (Hovestadt et al 1984), since this indicates a cool source of  $T \sim 10^4$  K. Contrary to the situation for the relatively small-flux  $\text{He}^3$ -rich events, in which the SEP ionization states reflect flare temperatures of  $\sim 10^7$  K (Klecker et al 1984, Luhn et al 1987), the ionization states of SEPs in large events provide further evidence for nonflare sources in the corona for those events.

More convincing evidence that the sources of SEPs lie outside flare regions would be SEP events associated either with flares lacking an impulsive phase or with a nonflare source. As examples of the former, Cliver et al (1983) discussed a number of SEP events with weak flare impulsive phases, including the GLE of 21 August 1979. They argued that in these

cases the explosive heating of the impulsive phase was not adequate to accelerate shocks to produce the SEP event and suggested that the shocks were produced by CMEs. Kahler et al (1986) discussed an example of a SEP event with both protons of  $E > 50$  MeV and relativistic electrons which was clearly associated with a fast CME and the eruption of a quiescent filament which lay well away from any active region (Figure 4). A flare-like double ribbon was observed on the disk in H $\alpha$ , but a weak interplanetary type II burst was the only radio emission detected from this event. These phenomena suggest that all the particle acceleration occurred in the high corona.

While the above results argue strongly for nonflare sources for the SEP events, there is also evidence that some SEP events may result from both flare and nonflare sources. Cliver et al (1989) examined 4–8 MeV gamma-ray line (GRL) fluences produced by  $E > 10$  MeV protons in flares. They calculated the ratios of those fluences to the peak  $\sim 10$  MeV proton fluxes in the SEP events associated with those flares. The ratios varied by over 4 orders of magnitude, but nearly every GRL flare was associated with a SEP event, suggesting that at least some of the 10 MeV protons in the flare region were escaping to interplanetary space. Reames (1990a) has discussed several examples of SEPs in which the  $\text{Fe}/\text{O}$  ratio was initially high, but then declined to values characteristic of coronal values. He suggested that the earliest part of the SEP event may have been dominated by SEPs produced in the impulsive phase of the flare, which was magnetically well connected to the Earth. Further, Cliver et al (1982) found that the onsets at 1 AU of the  $\sim 1$  BeV protons in GLE events were well associated with signatures of the flare impulsive phases.

To summarize, the abundance and ionization state measurements of SEPs strongly suggest the ambient corona, rather than a flare-heated plasma, as the primary source for these particles. The situation is complicated by the fact that a class of SEPs do originate in flare plasmas, and hybrids of the two kinds of events may occur. It is clear, however, that the classical picture of all SEPs originating in flares is no longer valid.

## 5. CONCLUSIONS

The high temperatures and rapid energy release characteristic of eruptive flares led early investigators to assume that flares were the direct causes of interplanetary SEP events and shock waves causing the most intense geomagnetic storms. Until recently, CMEs associated with flares were assumed to be a consequence rather than a cause of flares. Hudson (1987), for example, in his list of 42 discoveries that have changed our understanding of the physics of solar flares, found no place for CMEs. In this

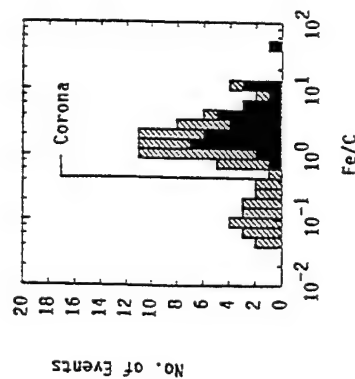


Figure 7 Distribution of  $\text{Fe}/\text{C}$  ratios of  $\sim 2$  MeV/nucleon SEP events observed at 1 AU. The blackened events indicate the  $\text{He}^3$ -rich events, which are enhanced relative to average coronal abundances (vertical line). The bimodal distribution supports the interpretation of two classes of SEP events. From Reames et al (1990).

review I have tried to show that a broad spectrum of evidence now supports a primary role for CMEs in the production of SEPs and shocks observed at 1 AU.

The recent trend in modeling CMEs is to assume a loss of equilibrium in the large-scale coronal magnetic field (Low 1990). One promising approach is to model the shear of a dipole configuration with azimuthal photospheric motions in opposite directions on each side of the magnetic neutral line (Biskamp & Welter 1989, Wu et al 1991, Steinolfson 1991). Observations of active regions have shown the importance of the shear angle for the occurrence of flares (Moore et al 1987). In addition, magnetic shear can lead to the loss of equilibrium which may also induce eruptions of prominences (Zweibel 1991), although the prominence eruption can not be the driver of the CME (Hundhausen 1988).

Despite substantial progress in understanding the relationships between flares, CMEs, and the interplanetary consequences of these phenomena, many problems remain. We still have not determined the exact boundaries of the eruptive coronal magnetic fields involved in CMEs. The development of the erupting closed fields of the CME into open fields in the interplanetary medium is not understood. The relationship of impulsive flares to CMEs (Kahler et al 1989) is still unknown, and the roles of flare-driven blast-wave shocks and CME-driven shocks have yet to be defined. Although flares appear as consequences of CMEs, it is possible that very energetic flares may still have some influence on the development of associated CMEs. In addition, source regions of SEPs and their relationships to flares and coronal shocks are only crudely known. Despite the apparent wealth of observations, some rather fundamental problems of coronal physics await solution.

#### ACKNOWLEDGMENTS

I thank E. Cliver, T. Forbes, A. Hundhausen, D. Reames, and D. Webb for their comments on this review. This work was supported at Boston College by Phillips Lab contract F19628-89-K-0033.

#### Literature Cited

- Ahmad, I. A. 1977. *Sol. Phys.* 53: 409  
 Akasofu, S.-I., Chapman, S. 1972. *Solar-Terrestrial Physics*. Oxford: Clarendon Press  
 Anzer, U., Pneuman, G. W. 1982. *Sol. Phys.* 79: 129  
 Athay, R. G., Illing, R. M. E. 1986. *J. Geophys. Res.* 91: 10,961  
 Bame, S. J. 1983. In *Solar Wind Five*, ed.
- M. Neugebauer, p. 573. Washington DC: NASA  
 Bame, S. J., Asbridge, J. R., Feldman, W. C., Fenimore, E. E., Gosling, J. T. 1979. *Sol. Phys.* 62: 179  
 Bell, B. 1961. *Smithsonian Contr. Astrophys.* 5: 69  
 Biskamp, D., Welter, H. 1989. *Sol. Phys.* 120: 49

- Borriani, G., Gosling, J. T., Bame, S. J., Feldman, W. C. 1982. *J. Geophys. Res.* 87: 7370  
 Borriani, G., Gosling, J. T., Bame, S. J., Feldman, W. C. 1983. *Sol. Phys.* 83: 367  
 Bravo, S., Mendoza, B., Perez-Enriquez, R. 1991. *J. Geophys. Res.* 96: 5387  
 Breunann, H. H., Stone, E. C. 1985. *Astrophys. J.* 299: L57  
 Bruzek, A. 1964. *Astrophys. J.* 140: 746  
 Cane, H. V., Kahler, S. W., Sheeley, N. R., Jr. 1986. *J. Geophys. Res.* 91: 13,321  
 Cane, H. V., Reames, D. V. 1988a. *Astrophys. J.* 325: 895  
 Cane, H. V., Reames, D. V. 1988b. *Astrophys. J.* 325: 901  
 Cane, H. V., Sheeley, N. R., Jr., Howard, R. A. 1987. *J. Geophys. Res.* 92: 9869  
 Cargill, P. J., Priest, E. R. 1982. *Sol. Phys.* 76: 357  
 Carrington, R. C. 1860. *MNRAS* 20: 13  
 Chapman, S. 1964. *Solar Plasma, Geomagnetism and Aurora*. New York: Gordon & Breach  
 Chapman, S., Bartels, J. 1940. *Geomagnetism*. Oxford: Clarendon  
 Chree, C., Stagg, J. M. 1927. *Philos. Trans. R. Soc. London Ser. A* 227: 21  
 Cliver, E. W. 1983. *Sol. Phys.* 84: 347  
 Cliver, E. W., Kahler, S. W., Shea, M. A., Smart, D. F. 1982. *Astrophys. J.* 260: 362  
 Cliver, E. W., Kahler, S. W., McIntosh, P. S. 1983. *Astrophys. J.* 264: 699  
 Cliver, E. W., Dennis, B. R., Kiplinger, A. L., Kane, S. R., Neidig, D. F., et al. 1986. *Astrophys. J.* 305: 920  
 Cliver, E. W., Forrest, D. J., Cane, H. V., Reames, D. V., McGuire, R. E., et al. 1989. *Astrophys. J.* 343: 953  
 Cliver, E., Kahler, S. 1991. *Astrophys. J.* 366: L91  
 Dellinger, J. H. 1936. *Phys. Rev.* 50: 1189  
 Dellinger, J. H. 1937. *Ferr. Magn. Atmos. Electr.* 42: 49  
 Dodson, H. W., Hedeman, E. R., Roelof, E. C. 1982. *Geophys. Res. Lett.* 9: 199  
 Dyer, M. 1982. *Space Sci. Rev.* 33: 233  
 Dyer, M., Wu, S. T. 1985. *J. Geophys. Res.* 90: 559  
 Dulk, G. A. 1990. *Sol. Phys.* 130: 139  
 Feldman, U., Widing, K. G. 1990. *Astrophys. J.* 363: 292  
 Fenimore, E. E. 1980. *Astrophys. J.* 235: 245  
 Feynman, J., Gu, X. Y. 1986. *Rev. Geophys.* 24: 650  
 Forbes, T. G., Muthet, J. M., Priest, E. R. 1989. *Sol. Phys.* 120: 285  
 Forbush, S. E. 1946. *Phys. Rev.* 70: 771  
 Forbush, S. E., Gill, P. S., Vallarta, M. S. 1949. *Rev. Mod. Phys.* 21: 44  
 Geigley, T. E. 1986. *Sol. Phys.* 104: 175  
 Gloeckler, G., Weiss, H., Hovestadt, D., Ipavich, F. M., Klecker, B., et al. 1981. *Proc.*
- 17th Int. Cosmic Ray Conf. 3: 136  
 Gold, T. 1959. *J. Geophys. Res.* 64: 1665  
 Gopalswamy, N., Kundu, M. R. 1990. *Sol. Phys.* 128: 377  
 Gosling, J. T., Hildner, E., MacQueen, R. M., Munro, R. H., Poland, A. I., Ross, C. L. 1974. *J. Geophys. Res.* 79: 4581  
 Gosling, J. T., Hildner, E., MacQueen, R. M., Munro, R. H., Poland, A. I., Ross, C. L. 1976. *Sol. Phys.* 48: 389  
 Gosling, J. T., Asbridge, J. R., Bame, S. J., Feldman, W. C., Zwickl, R. D. 1980. *J. Geophys. Res.* 85: 3431  
 Greaves, W. M. H., Newton, H. W. 1928a. *MNRAS* 88: 556  
 Greaves, W. M. H., Newton, H. W. 1928b. *MNRAS* 89: 84  
 Hale, G. E. 1931. *Astrophys. J.* 73: 379  
 Harrison, R. A. 1986. *Astron. Astrophys.* 162: 283  
 Harrison, R. A. 1990. *Sol. Phys.* 126: 185  
 Harrison, R. A. 1991. *Adv. Space Res.* 11: (1)25  
 Harrison, R. A., Waggett, P. W., Bentley, R. D., Phillips, K. J. H., Bruner, M. et al. 1985. *Sol. Phys.* 97: 387  
 Harrison, R. A., Sime, D. G. 1989. *Astron. Astrophys.* 208: 274  
 Harrison, R. A., Hildner, E., Hundhausen, A. J., Sime, D. G., Simnett, G. M. 1990. *J. Geophys. Res.* 95: 917  
 Heras, A. M., Sanahuja, B., Domingo, V., Joselyn, J. A. 1988. *Astron. Astrophys.* 197: 297  
 Hewish, A. 1990. *J. Geophys. Res.* 95: 12,401  
 Hewish, A., Bravo, S. 1986. *Sol. Phys.* 106: 185  
 Hick, P., Svestka, Z. 1987. *Sol. Phys.* 108: 315  
 Hildner, E., Gosling, J. T., MacQueen, R. M., Munro, R. H., Poland, A. I., Ross, C. L. 1976. *Sol. Phys.* 48: 127  
 Hildner, E., Bassi, J., Bougeret, J. L., Duncan, R. A., Gary, D. E., et al. 1986. In *Energetic Phenomena on the Sun*, ed. M. Kundu, B. Woodgate, p. 6. Washington: NASA  
 Hirschberg, J., Bame, S. J., Robbins, D. E. 1972. *Sol. Phys.* 23: 467  
 Hovestadt, D., Klecker, B., Gloeckler, G., Ipavich, F. M., Scholer, M. 1984. *Astrophys. J.* 282: L39  
 Howard, R. A., Sheeley, N. R., Jr., Koomen, M. J., Michels, D. J. 1985. *J. Geophys. Res.* 90: 8173  
 Hudson, H. S. 1987. *Sol. Phys.* 113: 1  
 Hundhausen, A. J. 1972a. *Coronal Expansion and Solar Wind*. New York: Springer-Verlag  
 Hundhausen, A. J. 1972b. In *Solar Wind*, ed. C. P. Sonett, P. J. Coleman, Jr., J. M. Wilcox, p. 393. Washington: NASA  
 Hundhausen, A. J. 1977. In *Coronal Holes*

- and *High Speed Wind Streams*, ed. J. B. Zirker, p. 225. Boulder, CO: Colo. Assoc. Univ. Press
- Hundhausen, A. J. 1988. See Pizzo et al. 1988, p. 181
- Hundhausen, A. J. 1992. *J. Geophys. Res.* Submitted
- Hundhausen, A. J., Gentry, R. A. 1969. *J. Geophys. Res.* 74: 2908
- Hundhausen, A. J., Sime, D. G. 1992. *J. Geophys. Res.*
- Hilling, R. M. E., Hundhausen, A. J. 1985. *J. Geophys. Res.* 90: 275
- Hilling, R. M. E., Hundhausen, A. J. 1986. *J. Geophys. Res.* 91: 10,951
- Hilling, R. M. E., Athay, R. G. 1986. *Sol. Phys.* 105: 173
- Ipavich, F. M., Galvin, A. B., Gloeckler, G., Hovestadt, D., Bame, S. J. et al. 1986. *J. Geophys. Res.* 91: 4133
- Joselyn, J. A., McIntosh, P. S. 1981. *J. Geophys. Res.* 86: 4555
- Kahler, S. 1977. *Astrophys. J.* 214: 891
- Kahler, S. 1988. See Pizzo et al. 1988, p. 215
- Kahler, S. W., Hildner, E., van Hollebeke, M. A. J. 1978. *Sol. Phys.* 57: 429
- Kahler, S. W., Sheeley, N. R. Jr., Howard, R. A., Koomen, M. J., Michels, D. J. 1984a. *J. Geophys. Res.* 89: 9683
- Kahler, S., Sheeley, N. R. Jr., Howard, R. A., Koomen, M. J., Michels, D. J. 1984b. *Sol. Phys.* 93: 133
- Kahler, S., Reames, D. V., Sheeley, N. R. Jr., Howard, R. A., Koomen, M. J., Michels, D. J. 1985. *Astrophys. J.* 290: 742
- Kahler, S. W., Cliver, E. W., Cane, H. V., McGuire, R. E., Stone, R. G., Sheeley, N. R. 1986. *Astrophys. J.* 302: 504
- Kahler, S. W., Cliver, E. W., Cane, H. V., McGuire, R. E., Reames, D. V., et al. 1987. *20th Int. Cosmic Ray Conf.* 3: 121
- Kahler, S. W., Moore, R. L., Kane, S. R., Zirin, H. 1988. *Astrophys. J.* 328: 824
- Kahler, S. W., Sheeley, N. R. Jr., Liggelt, K., Kahler, S. W., Moses, D. 1990. *Astrophys. J.* 362: 728
- Kahn, F. D. 1949. *MNRAS* 109: 324
- Kerdraon, A., Pick, M., Trollet, G., Sawyer, C., Illing, R., Wagner, W., House, L. 1983. *Astrophys. J.* 265: L19
- Klecker, B., Hovestadt, D., Gloeckler, G., Ipavich, F. M., Scholer, M., Fan et al. 1984. *Astrophys. J.* 281: 458
- Klecker, B., Cliver, E., Kahler, S., Cane, H. 1990. *Eos Trans. Am. Geophys. Union* 71: 1102
- Kopp, R. A., Pneuman, G. W. 1976. *Sol. Phys.* 50: 85
- Kopp, R. A., Poletto, G. 1990. *Sol. Phys.* 127: 267
- Kosugi, T., Dennis, B. R., Kai, K. 1988. *Astrophys. J.* 324: 1118
- Kundu, M. R. 1965. *Solar Radio Astronomy*. New York: Interscience
- Kundu, M., Gopalswamy, N., White, S., Cargill, P., Schmahl, E. J., Hildner, E. 1989. *Astrophys. J.* 347: 505
- Leblanc, Y., Poquerusse, M., Aubier, M. G. 1983. *Astron. Astrophys.* 123: 307
- Leblanc, Y., Itoyos, M. 1985. *Astron. Astrophys.* 143: 365
- Lin, R. P., Hudson, H. S. 1976. *Sol. Phys.* 50: 153
- Low, B. C. 1990. *Annu. Rev. Astron. Astrophys.* 28: 491
- Luhn, A., Hovestadt, D., Klecker, B., Scholer, M., Gloeckler, G., et al. 1985. *Proc. 19th Int. Cosmic Ray Conf.* 4: 241
- Luhn, A., Klecker, B., Hovestadt, D., Mobius, E. 1987. *Astrophys. J.* 317: 951
- Lundstedt, H. 1982. *Sol. Phys.* 81: 293
- Lundstedt, H., Wilcox, J. M., Scherrer, P. H. 1981. *Science* 212: 1501
- MacQueen, R. M. 1985. *Sol. Phys.* 95: 359
- MacQueen, R. M., Eddy, J. A., Gosling, J. T., Hildner, E., Munro, R. H., et al. 1974. *Astrophys. J.* 187: L85
- MacQueen, R. M., Fisher, R. R. 1983. *Sol. Phys.* 89: 89
- Martin, S. F., Ramsey, H. E. 1972. In *Solar Activity Observations and Predictions*, ed. P. S. McIntosh, M. Dryer, p. 371. Cambridge: MIT Press
- Martin, S. F., Svestka, Z. F., Bhatnagar, A. 1989. *Sol. Phys.* 124: 319
- Mason, G. M., Gloeckler, G., Hovestadt, D. 1984. *Astrophys. J.* 280: 902
- Maunder, E. W. 1904. *MNRAS* 65: 2
- Maunder, E. W. 1905. *MNRAS* 64: 205
- McLean, D. J. 1959. *Aust. J. Phys.* 12: 404
- Meyer, J.-P. 1985. *Astrophys. J. Suppl.* 57: 173
- Milne, E. A. 1926. *MNRAS* 86: 459
- Moore, R. L., Hagyard, M. J., Davis, J. M. 1987. *Sol. Phys.* 113: 347
- Mullan, D. J., Waldron, W. L. 1986. *Astrophys. J.* 308: L21
- Munro, R. H., Gosling, J. T., Hildner, E., MacQueen, R. M., Poland, A. I., Ross, C. L. 1979. *Sol. Phys.* 61: 201
- Murphy, R. J., Ramaty, R., Kozlovsky, B., Reames, D. V. 1991. *Astrophys. J.* 371: 793
- Neugebauer, M. 1988. See Pizzo et al. 1988, p. 243
- Newton, H. W. 1939. *Observatory* 62: 318
- Newton, H. W. 1943. *MNRAS* 103: 244
- Pallavicini, R., Serio, S., Vaiana, G. S. 1977. *Astrophys. J.* 216: 108
- Parker, E. N. 1961. *Astrophys. J.* 133: 1014
- Pick, M. 1986. *Sol. Phys.* 104: 19
- Pizzo, V. J., Holzer, T. E., Sime, D. G., eds. 1988. *Proceedings of the Sixth International Solar Wind Conference*. Boulder, CO: NCAR
- Poletto, G., Kopp, R. A. 1988. *Sol. Phys.* 116: 163
- Poletto, G., Svestka, Z. 1990. *Sol. Phys.* 129: 363
- Poquerusse, M., McIntosh, P. S. 1990. *Sol. Phys.* 130: 101
- Pudovkin, M. I., Chertkov, A. D. 1976. *Sol. Phys.* 50: 213
- Pudovkin, M. I., Zaitseva, S. A., Oleferenko, I. P., Chertkov, A. D. 1977. *Sol. Phys.* 54: 155
- Pudovkin, M. I., Zaitseva, S. A. 1986. *J. Geophys. Res.* 91: 13,765
- Reames, D. V. 1988. *Astrophys. J.* 325: L53
- Reames, D. V. 1990a. *Astrophys. J.* 358: L63
- Reames, D. V. 1990b. *Astrophys. J. Suppl.* 73: 235
- Reames, D. V., Dennis, B. R., Stone, R. G., Lin, R. P. 1988. *Astrophys. J.* 327: 998
- Reames, D. V., Cane, H. V., von Rosenvinge, T. T. 1990. *Astrophys. J.* 357: 259
- Reames, D. V., Kallenrode, M.-B., Stone, R. G. 1991. *Astrophys. J.* 380: 287
- Reid, G. C., Leibach, H. 1959. *J. Geophys. Res.* 64: 1801
- Robinson, R. D., Stewart, R. T., Sheeley, N. R. Jr., Howard, R. A., Koomen, J., Michels, D. J. 1986. *Sol. Phys.* 105: 149
- Sabine, E. 1852. *Philos. Trans. R. Soc. London* 142: 103
- Satohjya, B., Ileras, A. M., Domingo, V., Joselyn, J. A. 1991. *Sol. Phys.* 134: 379
- Sawyer, C. 1985. *Sol. Phys.* 98: 369
- Schwenn, R., Rosenbauer, H., Muhlihauser, K.-H. 1980. *Astrophys. Res. Lett.* 7: 201
- Sheeley, N. R. Jr., Bohlin, J. D., Brueckner, G. E., Purcell, J. D., Scherrer, V. E., et al. 1975. *Sol. Phys.* 45: 377
- Sheeley, N. R. Jr., Howard, R. A., Koomen, M. J., Michels, D. J. 1983. *Astrophys. J.* 272: 349
- Sheeley, N. R. Jr., Stewart, R. T., Robinson, R. D., Howard, R. A., Koomen, M. J., Michels, D. J. 1984. *Astrophys. J.* 279: 839
- Sheeley, N. R. Jr., Howard, R. A., Koomen, M. J., Michels, D. J., Schweini, R., et al. 1985. *J. Geophys. Res.* 90: 163
- Sime, D. G., MacQueen, R. M., Hundhausen, A. J. 1984. *J. Geophys. Res.* 89: 2113
- Sime, D. G., MacQueen, R. M., Hundhausen, A. J. 1985. *J. Geophys. Res.* 90: 563
- Sime, D. G., Hundhausen, A. J. 1987. *J. Geophys. Res.* 92: 1049
- Smith, H. J., Smith, E. v. P. 1963. *Solar Flares*. New York: MacMillan
- Steinolfson, R. S. 1991. *Astrophys. J.* 382: 677
- Stewart, R. T. 1984. *Sol. Phys.* 94: 379
- Stewart, R. T., McCabe, M. K., Koomen, M. J., Hansen, R. T., Dulk, G. A. 1974a. *Sol. Phys.* 36: 203
- Stewart, R. T., Howard, R. A., Hansen, F., Gergely, T., Kundu, M. 1974b. *Sol. Phys.* 36: 219
- Svestka, Z. 1983. *Space Sci. Rev.* 35: 259
- Svestka, Z. 1986. In *The Lower Atmospheres of Solar Flares*, ed. D. F. Neidig, p. 332. Sunspot, NM: NSO
- Svestka, Z. F., Jackson, B. V., Howard, R. A., Sheeley, N. R. Jr. 1989. *Sol. Phys.* 122: 131
- Tang, F., Akasofu, S.-I., Smith, E., Tsurutani, B. 1985. *J. Geophys. Res.* 90: 2703
- Tang, F., Akasofu, S.-I., Smith, E., Tsurutani, B. 1986. *J. Geophys. Res.* 91: 13,769
- Tang, F., Tsurutani, B. T., Gonzalez, W. D., Akasofu, S. I., Smith, E. J. 1989. *J. Geophys. Res.* 94: 3535
- Tappin, S. J. 1991. *Astron. Astrophys. Suppl. Ser.* 87: 277
- Tousey, R. 1973. In *Space Research XIII*, ed. M. J. Rycroft, S. K. Runcorn, p. 173. Berlin: Akademie-Verlag
- Tsurutani, B. T., Goldstein, H. E., Smith, E., Gonzalez, W. D., Tang, F., et al. 1990. *Planet. Space Sci.* 38: 109
- Tsurutani, B. T., Gonzalez, W. D. 1990. *J. Geophys. Res.* 95: 12,305
- Wagner, W. J., MacQueen, R. M. 1983. *Astron. Astrophys.* 120: 136
- Webb, D. F., Hundhausen, A. J. 1987. *Sol. Phys.* 108: 383
- Widing, K. G., Feldman, U. 1989. *Astrophys. J.* 344: 1046
- Wright, C. S., McNamara, L. F. 1982. *Nature* 299: 42
- Wright, C. S., McNamara, L. F. 1983. *Sol. Phys.* 87: 401
- Wright, C. S., Webb, D. F. 1990. In *Solar-Terrestrial Predictions*, ed. R. J. Thompson, D. G. Cole, P. J. Wilkinson, M. A. Shea, D. Smart, G. Heckman, p. 664. Boulder, CO: NOAA
- Wu, S. T., Dryer, M., Han, S. M. 1983a. *Sol. Phys.* 84: 395
- Wu, S. T., Wang, S., Dryer, M., Poland, A. I., Sime, D. G., et al. 1983b. *Sol. Phys.* 85: 351
- Wu, S. T., de Jager, C., Dennis, B. R., Hudson, H. S., Sinnott, G. M., et al. 1986. In *Energetic Phenomena on the Sun*, ed. M. Kundu, B. Woodgate, p. 5. Washington, DC: NASA
- Wu, S. T., Song, M. T., Martens, P. C. H., Dryer, M. 1991. *Sol. Phys.* 134: 353
- Zweibel, E. G. 1991. *Astrophys. J.* 376: 761

# Multiple Heliospheric Current Sheets and Coronal Streamer Belt Dynamics

N. U. CROOKER,<sup>1</sup> G. L. SISCOE,<sup>1</sup> S. SHODHAN,<sup>2</sup> D. F. WEBB,<sup>3</sup>

J. T. GOSLING,<sup>4</sup> AND E. J. SMITH<sup>5</sup>

The occurrence of multiple directional discontinuities in the coronal streamer belt at sector boundary crossings in the heliosphere, often ascribed to waves or kinks in the heliospheric current sheet, may alternatively be attributed to a network of extended current sheets from multiple helmet streamers with a hierarchy of sizes at the base of the corona. Frequent transient outflows from these helmets can account for a variety of signatures observed at sector boundaries, including ordered field rotations, planar magnetic structure, and sandwichlike plasma structure.

## 1. INTRODUCTION

Throughout most of the solar cycle, the coronal streamer belt extends into interplanetary space from an arcade of helmet streamers encircling the Sun [e.g., *Hundhausen*, 1977]. As the solar wind draws the solar magnetic field outward, the coronal streamer belt becomes the boundary between the regions of northern and southern solar polarity and thus the location of the heliospheric current sheet, or sector boundary [e.g., *Schulz*, 1973; *Svalgaard et al.*, 1975; *Saito*, 1975; *Alfven*, 1977; *Smith et al.*, 1978; *Thomas and Smith*, 1981].

A number of papers published mainly in the early eighties present detailed studies of spacecraft data across the streamer belt. The present paper offers a new interpretation of their results. Section 2 reviews the published streamer belt properties, section 3 describes the new conceptual model that organizes them, section 4 presents a case study of a typical sector boundary crossing in terms of the new model, and section 5 summarizes the model's features and implications.

## 2. STREAMER BELT PROPERTIES

The concept of the coronal streamer belt as a sheath surrounding the heliospheric current sheet in interplanetary space received substantial support from studies of the plasma characteristics near sector boundary crossings. Although the plasma is usually highly structured on a time scale of hours, on the scale of a solar rotation it has low-speed, high-density, low-temperature, low-helium abundance, and high-oxygen freezing-in temperatures [*Borini et al.*, 1981; *Feldman et al.*, 1981; *Gosling et al.*, 1981], consistent with streamer characteristics. The density structure contains a high incidence of noncompressive density enhancements, also consistent with streamer origin [*Gosling et al.*, 1977; *Feldman et al.*, 1981].

The magnetic field across the coronal streamer belt is also highly structured most of the time, with many directional discontinuities occurring on a hierarchy of time scales [e.g., *Klein and Burlaga*, 1980; *Behannon et al.*, 1981]. Efforts to determine the orientation of the imbedded heliospheric current sheet with minimum variance analysis are thwarted by the variability of boundary normal directions from one discontinuity to the next and by the problem of deciding which discontinuities are heliospheric current sheet crossings. Implicit in the statement of the latter problem is the assumption that although current sheets associated with limited structures are common in the solar wind, the heliospheric current sheet is special because it forms a single surface that is continuous on a global scale. This paper offers an alternative view.

Several approaches have been taken to overcome the difficulties of analyzing heliospheric current sheet structure. For example, *Klein and Burlaga* [1980] treat the sheet as the entire region between periods of stable, opposite polarity. Thus, according to their definition, the current sheet can be thick. To determine the orientation of a particular sheet, they apply minimum variance analysis across the entire transition region. *Villante and Bruno* [1982] restrict their study to well-defined, thin heliospheric current sheet crossings and also use minimum variance analysis. *Eselevich and Filippov* [1988] plot hourly averages of magnetic field longitude  $\Phi$  against latitude  $\Theta$  across thick current sheets and obtain their orientations by treating the traces as latitude circles on a sphere with an axis of arbitrary orientation. *Behannon et al.* [1981] analyze all of the discontinuities with angular changes greater than  $120^\circ$  in the sector boundary region and suggest that each is a heliospheric current sheet crossing. They demonstrate that most discontinuities within the region have large angular changes, unlike the angular changes in a random selection of discontinuities.

Two major findings from these studies highlight gaps in our understanding of heliospheric current sheet structure. The first concerns the orientations of the normals to the numerous discontinuity surfaces in each sector boundary region. The global current sheet orientations obtained by *Klein and Burlaga* [1980] with minimum variance analysis across the entire region of multiple discontinuities in thick current sheets tend to be aligned with the Parker spiral and inclined like the neutral line on coronal field maps. Yet the individual discontinuity orientations within each region display considerable scatter about the global orientation. *Behannon et al.* [1981] show that a histogram of the latitude angle  $\theta_N$  of 105 discontinuity normals across 13 sec-

<sup>1</sup>Department of Atmospheric Sciences, University of California, Los Angeles.

<sup>2</sup>Center for Space Physics, Boston University, Boston, Massachusetts.

<sup>3</sup>Institute for Space Research, Boston College, Newton Center, Boston, Massachusetts.

<sup>4</sup>Los Alamos National Laboratory, University of California, Los Alamos, New Mexico.

<sup>5</sup>Jet Propulsion Laboratory, California Institute of Technology, Pasadena.

tor boundary regions is essentially flat when normalized by solid angle. The histogram of their longitude angles  $\phi_N$  peaks between the ortho-Parker-spiral and radial directions. Except in a few cases, successive discontinuities show no coherence suggesting waves. Of course, partial immersions of the spacecraft into a wavy current sheet preclude wave analysis. However, even to fit waves to the normals in the few coherent cases, one must assume large wave amplitudes and short wavelengths. Behannon et al. mention that the variability in normal orientations could be caused by small-scale flux tube structures, an argument pursued in this paper, but they favor instead an interpretation of small-scale fluctuations of a single boundary surface. Klein and Burlaga [1980, p. 2269] agree with the results of earlier studies that the internal structure of sector boundaries is very complex, and they find "no uniform way to describe it."

The second major finding points to ambiguity regarding the interpretation of magnetic field rotations through the heliospheric current sheet. In analyses across both thick and thin sector boundaries, Klein and Burlaga [1980], Villante and Bruno [1982], and Eselevich and Filippov [1988] commonly found smooth field rotations with constant field magnitude in the plane of the current sheet. Eselevich and Filippov [1988] propose that the rotations result from magnetic field skewing in the coronal streamer belt. Klein and Burlaga [1982], 2 years after their first paper, reclassified three of their seven thick sector boundary crossings with pronounced field rotations as magnetic clouds preceding stream interaction regions. Magnetic clouds are usually interpreted as flux ropes in coronal mass ejections (CMEs) [e.g., Goldstein, 1983; Marubashi, 1986; Burlaga, 1988; Gosling, 1990]. Minimum variance analysis through clouds yields normals with  $\phi_N$  ranging from the radial to the ortho-Parker-spiral direction [Klein and Burlaga, 1982], like those for the discontinuity normals in sector boundaries. For a flux rope, the normal points perpendicular to the rope axis [Goldstein, 1983].

Schwenn [1990] notes that the idea of magnetic clouds at sector boundaries is in essence what Rosenberg and Coleman [1980] proposed in a draft of their paper to explain observations of field rotations there. They suggested that magnetic loops form by reconnection between the antiparallel fields across the heliospheric current sheet. However, the published version offers an alternative explanation in terms of a pure, stream-interaction-region effect. It is difficult to separate field rotations caused by interaction regions from those of solar origin in the coronal streamer belt because of their close proximity.

Another type of field rotation that lacks a full explanation is planar magnetic structure [Nakagawa et al., 1989], identified by a sine wave signature on a  $\Phi$ - $\Theta$  plot of high time resolution data. Nakagawa [1993] reports on a class of recurrent planar magnetic structures located near sector boundaries, where the great circle outlined by the magnetic field vectors often lies in the plane of the heliospheric current sheet, consistent with the streamer belt signatures found by Eselevich and Filippov [1988] with hourly averages. However, planar magnetic structures differ in a fundamental way from the rotations documented by Klein and Burlaga [1980] and Villante and Bruno [1982]. The sine waves on the  $\Phi$ - $\Theta$  plots form not by a gradual change in magnetic field orientation across the sector boundary region but rather by a random series of discontinuous changes in field orienta-

tion within the plane of the current sheet. Nakagawa et al. [1989] interpret planar magnetic structure as a series of small, parallel magnetic tongues and/or loops that close on themselves. Neugebauer et al. [1993] disagree with this interpretation because their observations of planar magnetic structure show no bidirectional streaming of suprathermal electrons thought to be characteristic of closed field configurations [e.g., Gosling, 1990]. Neugebauer et al. [1993] find that planar magnetic structures commonly precede coronal mass ejections and ascribe them to draping of disordered fields about the ejections. Minimum variance analysis across the discontinuities in planar magnetic structure yields normals with  $\phi_N$  ranging from the radial to the ortho-Parker-spiral direction [Nakagawa, 1993; Neugebauer et al., 1993], the same as for sector boundary discontinuities and magnetic clouds.

This paper proposes a model of the coronal streamer belt that helps to integrate the many views and order the complex observational results discussed above.

### 3. A MODEL OF THE CORONAL STREAMER BELT

#### 3.1. Multiple Current Sheets

Eddy [1973] notes that a coronal ray in a 1922 eclipse photograph extends outward from a twin-arch helmet streamer associated with two distinct chromospheric active regions. Eddy [1973, p. 393] interprets it as a current sheet viewed edge-on and concludes that

a single large helmet streamer can be formed by the confluence of open field lines from two widely separate bipolar magnetic regions, each of which forms its own system of high, closed-field arches....As the surface of the Sun displays a hierarchy of granules and super-granules, so apparently does the corona consist of both simple and conglomerate streamers. Helmet streamers are often noted to extend over ranges of 50° or more in heliocentric latitude, and it may be that more of these than are first apparent are twin-arch streamers which tie together smaller magnetic substructures of streamer size.

A magnetic topology for a twin-arch helmet streamer is sketched in Figure 1a. The central current sheet, aligned with the coronal ray in Eddy's [1973] case, is flanked by two additional current sheets, one from each helmet dome. These were not visible in Eddy's case, presumably because of lower density or temperature at their base, but they are required by the antiparallel fields on either side. Figure 1b generalizes the special configuration of Figure 1a to a broad region of multiple helmet streamers covering a wide range of latitude. It represents the third state in a progression from a single helmet spanning the closed field line region of the Sun, as in the Pneuman and Kopp [1971] model, to the double helmet in Figure 1a, to Figure 1b. Thus it represents a progression from a single heliospheric current sheet, to a triple current sheet, to multiple current sheets. The two helmets at the highest latitudes are larger, as expected for traditional helmet streamers overlying quiescent prominences, while the smaller helmets (we use the term indiscriminately) span the active regions at lower latitudes.

With Figure 1b as a model, we propose that in some cases what appear as multiple crossings of a single, fluctuating current sheet [e.g., Villante et al., 1979; Behannon et al., 1981; Gosling et al., 1981] are instead crossings of multiple current sheets originating from small-scale helmet structures on the sun. If the multiple helmets are small in the direction normal to the plane of Figure 1b as well, the distribution of the elevation angles  $\theta_N$  of the normals to the current sheets



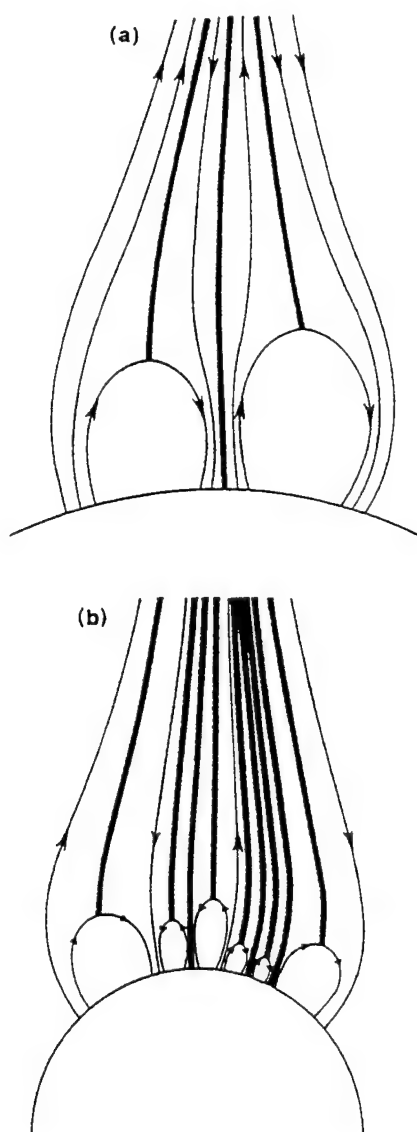


Fig. 1. Multiple current sheets (heavy lines) in the streamer belt required by magnetic topologies with more than one helmet streamer at the base: (a) double helmets, after Eddy [1973]; (b) multiple small helmets covering a large belt of active regions bordered by larger helmets over high-latitude filaments.

will be broad, as observed. In this view, the coronal streamer belt consists of bundles of flux tubes of opposite polarity separated by current sheets of finite latitudinal and longitudinal extent. Applying Eddy's [1973] arguments, most likely the bundles have a broad hierarchy of sizes.

### 3.2. Field Rotations

To explain the observations on field rotations in the coronal streamer belt, we add time dependence to the steady state picture in Figure 1b. The best documented, time-dependent structure that rises out of the streamer belt is the coronal mass ejection. CMEs are large-scale structures that appear to have a lower limit on their spatial scale [Hundhausen, 1993]. To form a CME, one of the small helmets in Figure 1b may expand to fill the streamer belt base and then lift off, as in a case reported by Hundhausen [1988]. The magnetic configuration within the rising helmet, as it

travels outward along the sector boundary, can cause large-scale field rotations in the following way.

Figure 2a illustrates a likely magnetic topology for a helmet streamer [e.g., Hundhausen, 1988]. The outer contour is an arcade of helmet arches, viewed nearly at right angles from the views in Figure 1. The arcade overlies the elongated arch of a prominence (filament) field, and the transition in field orientation from the arcade to the prominence occurs gradually with a series of concentric arcades of decreasing height and increasing skew. (The figure linearizes the transition, ignoring the fact that most of the skew occurs low in the corona, close to the prominence.)

If the structure in Figure 2a expands into the heliosphere as a CME, it will create three different rotational signatures, depending upon how a spacecraft passes through it and whether reconnection changes the magnetic topology. To discuss the geometry, we let  $x$  be the radially outward direction and  $y$  be the direction of corotation. If the structure expands radially outward and passes over a spacecraft with speed  $V_x$ , the spacecraft will observe a field rotation of  $90^\circ$ , from the top of the outermost helmet arcade orientation in the negative  $y$  direction to the prominence orientation in the  $z$  direction, as pictured by the solid arc in the hodogram in Figure 2b. Minimum variance analysis would give a radial normal ( $x$ -directed). To obtain the full  $180^\circ$  rotation completed by the dashed arc in Figure 2b, as is usually observed in magnetic clouds [e.g., Klein and Burlaga, 1982],

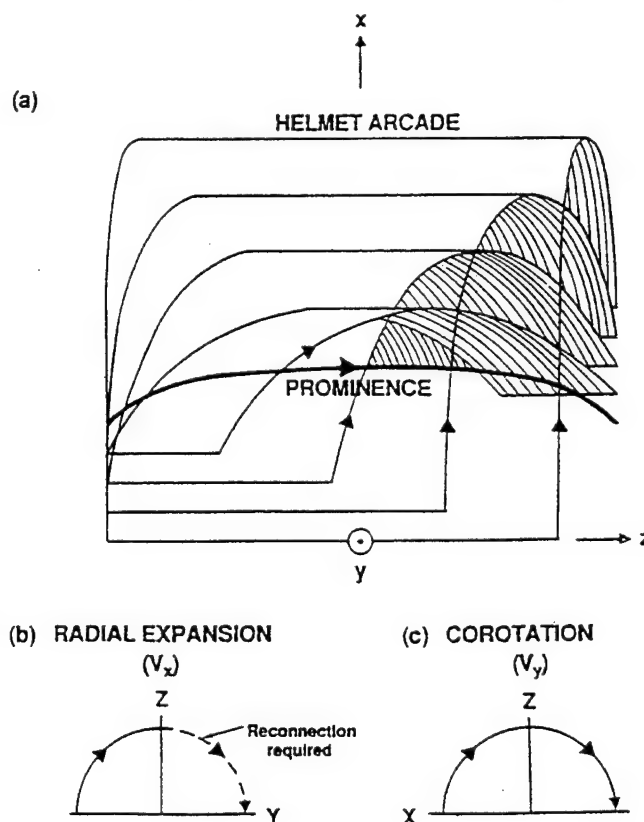


Fig. 2. (a) Diagram of sheared magnetic structure of a helmet streamer. Nested, arched field lines are progressively shifted in orientation by a total of  $90^\circ$ , from the core field of the prominence (filament) to the overlying helmet arcade. Hodograms of magnetic field variations for (b) radial expansion and (c) corotation of the structure past a spacecraft are shown below. In Figure 2b, rotation by  $180^\circ$  is achieved only if reconnection sunward of the prominence field occurs, to form a flux rope.



one must invoke reconnection sunward of the prominence field to form a flux rope with positive  $y$  fields on the back side [e.g., Crooker et al., 1990; Gosling, 1990].

Alternatively, if the streamer belt ( $x$ - $z$ ) plane is highly inclined so that the ecliptic plane is the  $x$ - $y$  plane, and the leading edge of the structure of Figure 2a passes beyond the heliocentric distance of a spacecraft before encounter, the structure will corotate past the spacecraft with speed  $V_y$ . As Figure 2c illustrates, corotation yields a  $180^\circ$  rotation without reconnection. The field rotates in the plane of the streamer belt, from one side of the outermost helmet arcade in the  $x$  direction, to the  $z$ -directed prominence field, to the other side of the outermost arcade in the negative  $x$  direction. Minimum variance analysis along this trajectory gives a normal in the  $y$  direction, perpendicular to the plane of the streamer belt.

With the magnetic structure in Figure 2a moving outward through the coronal streamer belt as a CME, one can explain all of the large-scale rotational features described in section 2. In terms of the findings by Klein and Burlaga [1982], Figure 2b (with reconnection) applies to CME- and shock-associated magnetic clouds, which have radially aligned normals, and Figure 2c to clouds preceding interaction regions, which have normals perpendicular to the Parker spiral. Figure 2 implies that the former expanded radially over the spacecraft while the latter corotated past it. Thus we associate all cloud categories with CMEs. Figure 2c also applies to the many reports of smooth rotations across sector boundaries. The further the leading edge of the structure passes beyond the spacecraft orbit at the time of corotation past it, the less skew there will be, until all that remains are the legs of the CME with antiparallel fields. This range of possibilities provides a continuum of signatures from a smooth rotation to an abrupt change in polarity.

The multiple current sheet topology in Figure 1b offers two, possibly interrelated interpretations for planar magnetic structure. First, it may arise from ejection of the multiple helmet loops. If these loops lie not in the plane of the figure but have alternating inward and outward field components of various intensities at each foot, forming simple skewed loops, and all are ejected into the solar wind beyond the orbit of some spacecraft, then corotation of the loops past the spacecraft will yield planar magnetic structure. The field in each leg of each helmet will lie roughly parallel to the plane of the coronal streamer belt but will retain some degree of skew, placing the vector tip at a random point along the great circle of field rotation in the streamer belt plane. Eventually, of course, the skew will disappear as the flux loops continue to stretch outward, ultimately becoming radially directed at their bases.

Alternatively, if one of the helmets in Figure 1b expands to form a CME, it will push aside the multiple current sheets as it travels outward along the sector boundary. Those current sheets on the side that forms its leading edge will drape around the CME, tipping their discontinuity normals toward the radial direction. The multiple current sheet region will form planar magnetic structure in the CME sheath, as observed by Neugebauer et al. [1993], providing that the fields between the current sheets have random orientations in the draping plane. These may arise either from small-scale ejections on closed loops, as described above, or from turbulence on open lines. Multiple current sheets on the opposite side of the CME will corotate with the trailing leg, with discon-

tinuity normals perpendicular to the Parker spiral, and may form planar magnetic structure there in the same way. This interpretation accounts for the range of observed normal directions.

Some planar magnetic structure may be the signature of prominence fields trailing behind CMEs. Erupting prominences appear highly disordered in coronagraph observations [e.g., Hundhausen, 1988], yielding the required multiple discontinuities for planar magnetic structure. The planar order may be a reflection of their order on the Sun, where they delineate neutral lines which tend to lie parallel to the global neutral line in source surface maps of coronal fields [Hoeksema and Scherrer, 1986]. Hence, on a global scale, erupting prominence fields, like the erupting small-scale helmet fields described above, may tend to lie parallel to the coronal streamer belt plane, forming planar magnetic structure with normals roughly perpendicular to the Parker spiral.

### 3.3. Streamer Activity

White light observations of streamers near the Sun suggest that streamer outflow is frequently unsteady. For example, MacQueen and Poland [1977] show that streamer structure can vary not only during periods of CME activity but also during quiet periods. They report quiet-time brightness variations between limb passages by as much as a factor of 2. Poland [1978] shows that a particularly persistent streamer overlying a group of active regions and filaments underwent significant evolution between some limb passages. Its mass varied by as much as 50%, its longitudinal extent decreased, and its position migrated in latitude. Mass changes over time scales as short as hours were also observed during individual limb passages. None of these changes were observed to be directly associated with typical, large-scale CMEs. Such changes might be caused in part by frequent mass outflow from ejections on closed tongues from small helmets over both active regions and filaments.

Webb [1986] describes SMM observations of the evolution of a large helmet streamer observed prior to the eruption of a huge CME (analyzed by A. Hundhausen, private communication, 1985) as a slow ejection of bright shells of material, like the peeling of an onion. Although such large, slowly evolving events are not common, they demonstrate what might occur much more frequently on smaller, less easily observed size scales—the frequent release of small amounts of mass from the sun on closed loops. Consistent with this view, Jackson [1993] finds that the number of CMEs per unit mass increases exponentially with decreasing mass, implying a high-frequency rate for small CMEs. That CMEs can be spatially small is inconsistent with the findings of Hundhausen [1993], mentioned earlier. Since this point is still controversial [e.g., Kahler, 1987], we shall reserve the term “CME” for the large-scale phenomenon and treat small-scale ejections as a separate category.

Two objections to the proposed, frequent outflow of small-scale tongues concern their magnetically closed structure. The first is the sparsity of bidirectional particle streaming events observed in the solar wind. If bidirectional streaming necessarily occurs in all closed structures [e.g., Gosling, 1990], then the proposed outflow implies that it should commonly occur in the streamer belt, contrary to observations. The second objection, faced by all papers on CMEs, concerns flux buildup in the heliosphere [Gosling, 1975; Mac-

Queen, 1980]. As discussed by *McComas et al.* [1992], reconnection must occur somewhere in the heliosphere to prevent continuous buildup, but its likely signatures, heat flux dropouts, seem insufficient to balance the known CME flux, let alone flux from frequent, small-scale tongue outflow. It may be that detectable signatures of reconnection in small-scale tongues take other forms, such as ion jets [*Feldman et al.*, 1993]. These issues of magnetic topology remain open questions.

### 3.4. Global View

The picture of the streamer belt that emerges here is a disk of variable thickness, depending upon the number and size of the helmet structures at its base. Those regions extending from multiple helmets have discontinuities corresponding to multiple current sheets with normals primarily orthogonal to the Parker spiral but with a wide variety of elevations reflecting the tubular shapes of either open flux tubes or the legs of magnetic tongues. This view of the streamer belt consistently orders the observations described in section 2. It implies that the heliospheric current sheet is a not a single surface but a constantly changing layer with a varying number of current sheets of finite extent filling the finite thickness of the coronal streamer belt.

From this global point of view, the streamer belt extends from the closed field line regions of the Sun and forms a conduit for CME outflow. It could well be the source of all of the slow solar wind [cf. *Feldman et al.*, 1981; *Schwenn*, 1990] and the source of all CMEs. The latter conclusion is consistent with the findings of *Hundhausen* [1993] based on coronagraph observations of CMEs mapped to white light synoptic maps of coronal brightness. He shows that CMEs nearly always originate in the bright band that outlines the coronal streamer belt near the Sun.

Figure 3 illustrates most of the proposed coronal streamer belt features in a three-dimensional view. It shows a tilted, warped disk with thickness dependent not only upon the width of the closed field line region beneath but also the volume of local outflow. The outflow can be (a) quiet, (b) slowly expanding as small-scale ejections from multiple helmets, or (c) erupting as large-scale CMEs, possibly with flux rope structure. Thus sector boundary passage at Earth can produce (a) geomagnetic calm by sluggish flow in a quiet streamer belt, (b) moderate activity by small-scale mass ejection, or (c) large geomagnetic storms by CMEs. With appropriate changes in inclination and shape, this view of the coronal streamer belt should be valid for most of the solar cycle, as argued in section 4.

## 4. A CASE STUDY OF CORONAL STREAMER BELT DYNAMICS

The purpose of this section is to present observations of a single event that demonstrate that what would usually be interpreted as a typical crossing of a steady state, corotating coronal streamer belt is, instead, a crossing of a rapidly changing structure, consistent with our hypothesis that the streamer belt evolves dynamically. In addition, the case study provides an example of how the reinterpretation of discontinuities across sector boundaries in terms of multiple current sheets solves a geometrical problem inherent in the wave interpretation.

The left panel of Figure 4 gives the results of the superposed epoch analysis of *Borini et al.* [1981] for a set of

sector boundary crossings followed by high-speed streams. The density peaks sharply and the velocity and proton temperature dip before rising rapidly. These patterns are nearly identical to the data in the right panel, from the ISEE 3 sector boundary crossing on April 21, 1979. We choose this crossing for our case study because it is so typical of the coronal streamer belt at 1 AU, almost irrespective of solar cycle phase. It occurs during the ascending phase of the solar cycle, close to solar maximum, yet contains the sector and stream structure commonly associated with the descending phase and approach to minimum, from which many of the superposed epoch analysis events were drawn.

In the left panel of Figure 5, hourly averages of the ISEE 3 velocity  $V$ , and density  $n$  are replotted from Figure 4 along with the magnetic longitude angle  $\Phi$ . Here the time interval is shorter and  $n$  is plotted on a linear rather than logarithmic scale. The  $\Phi$  plot reveals multiple current sheet crossings as the spacecraft passed from an away to a toward sector. The density peak spans the crossings, while the speed reaches a shallow minimum before rising. The right panel of Figure 5 shows measurements of the same streamer belt four days earlier when it passed Helios 2 at 0.5 AU. Helios 2 was located in the ecliptic plane  $\sim 15^\circ$  behind Earth in solar longitude, so the 4-day delay is consistent with one day for corotation and three days for radial flow at  $\sim 300$  km/s. The density scale is contracted by a factor of 4 to account for the  $1/r^2$  variation in the Parker model, where  $r$  is solar distance. Thus, if the streamer belt were a steady, corotating structure with little time-dependent outflow—a commonly held view—then the plots would be roughly identical. This is nearly true for all three parameters through the first half, but major differences in the density plots appear thereafter. Helios 2 shows a large spike where the ISEE 3 density is nearly flat. *Webb and Jackson* [1990] identify the spike with passage through the bright portions of a CME viewed remotely by the white light photometers on Helios 2. Clearly, this coronal streamer belt crossing, taken as typical because of its similarity to the superposed epoch results at 1 AU, is not a steady state structure.

Figures 6 and 7 show that the streamer belt crossing at ISEE 3 in Figure 5 typifies the thick or complicated sector boundaries described in section 2. Twenty-four hours of high time resolution magnetic field data in Figure 6 span the heart of the streamer belt, centered on the three changes in  $\Phi$  in Figure 5. The data show multiple directional discontinuities, identified in the bottom panel by the ratio of

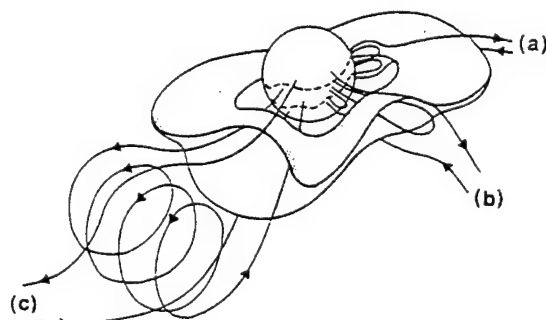


Fig. 3. The coronal streamer belt as a conduit for outflow from (a) steady state helmet streamers, (b) small-scale ejections, and (c) large-scale CMEs (with or without flux rope structure [cf. *Gosling*, 1990]).

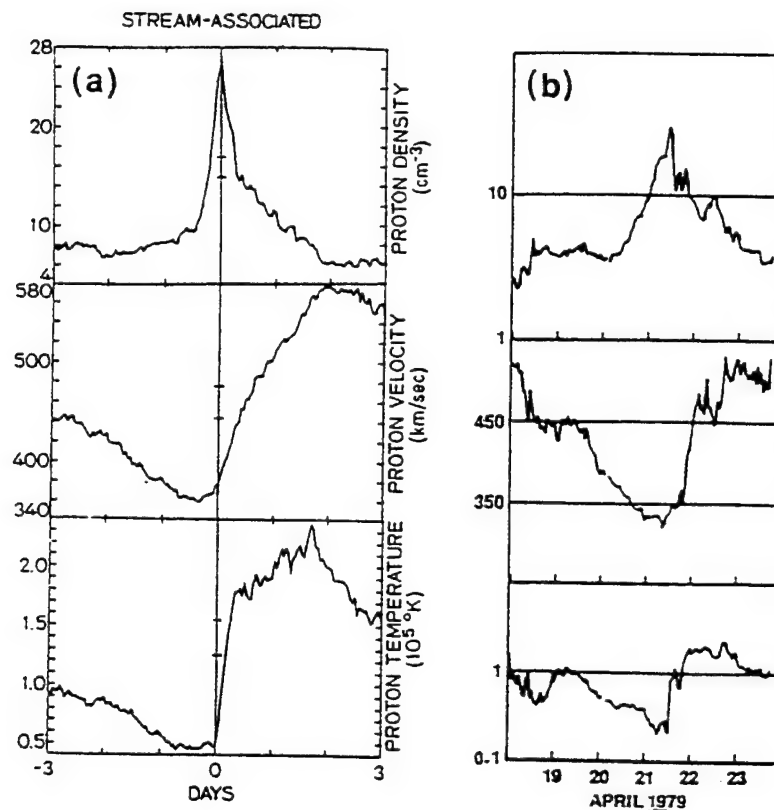


Fig. 4. Solar wind plasma parameters across the coronal streamer belt. The left panel shows the results of a superposed epoch analysis centered on sector boundary crossings, from *Borini et al.* [1981], and the right panel shows data from *King* [1986] of an individual crossing that nearly replicates the superposed epoch patterns.

the square of the maximum to minimum eigenvalues  $\lambda_1/\lambda_3$ , from minimum variance analysis with a sliding window of eleven 1-min averages. This identification method picks out most but not all of the discontinuities. For example, the discontinuity that effects the polarity change near hour 15 has no max/min peak because it occurs over more than eleven minutes and because its field vectors do not rotate in a well-defined plane.

Figure 7 shows histograms of the longitude angle  $\phi_N$  and the absolute value of the latitude angle  $\theta_N$  of the normal to each of the 21 discontinuity surfaces for which  $(\lambda_1/\lambda_3)^2 > 300$ . The ratio of the intermediate to minimum eigenvalues  $\lambda_2/\lambda_3$  is a measure of how well the normal is determined. A value greater than two is considered acceptable [Lepping and Behannon, 1980]. All chosen discontinuities meet this criterion except one, which has a ratio of 1.8. Minimum variance analysis across the entire day, following the *Klein and Burlaga* [1980] analysis method for thick sector boundaries, yields  $\phi_N = 224^\circ$ , orthogonal to the Parker spiral, and  $\theta_N = -12^\circ$ , both marked with arrows. Figure 7 agrees with previous findings that  $\phi_N$  tends to point toward the radial side of the direction orthogonal to the Parker spiral, and that  $\theta_N$  takes on a wide range of values but peaks near the thick boundary value of  $12^\circ$ .

High time resolution data from Helios 2 (not shown, data kindly provided by K.-H. Glassmeier and F. Neubauer) show similar complexity, with multiple discontinuities, only a few of which can be paired with ISEE 3 discontinuities, namely the major changes in  $\Phi$  apparent in the hourly averages in Figure 5. The main result of the comparison is that the fine structure of the streamer belt has evolved significantly

between 0.5 and 1 AU, consistent with dynamic activity in the streamer belt.

The 1-min averages at 1 AU of magnetic field longitude  $\Phi$  and latitude  $\Theta$  from Figure 6, plotted against each other in Figure 8, show a noisy but unmistakable sine wave signature of planar magnetic structure. The encircled cross marks the position of the thick sector boundary normal. Its central

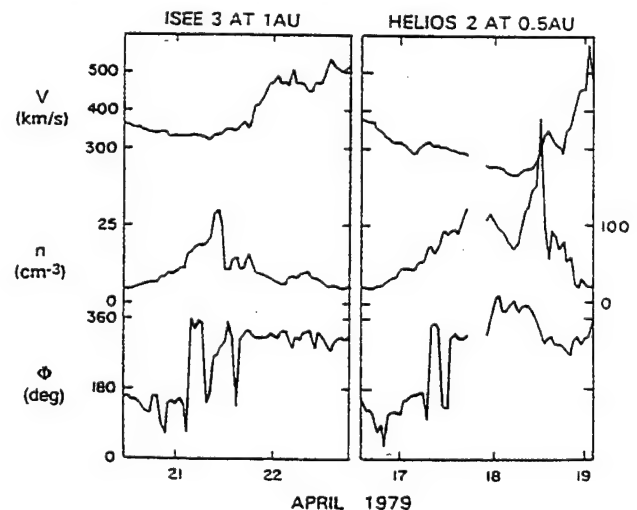


Fig. 5. Hourly averages of solar wind speed  $V$ , density  $n$ , and magnetic field longitude angle  $\Phi$  (GSE coordinates) across the same coronal streamer belt observed at ISEE 3 at 1 AU and at Helios 2 at 0.5 AU (see, also, Figure 5b from *Webb and Jackson* [1990]). The density scales are proportional to  $1/r^2$ , where  $r$  is distance from the Sun.

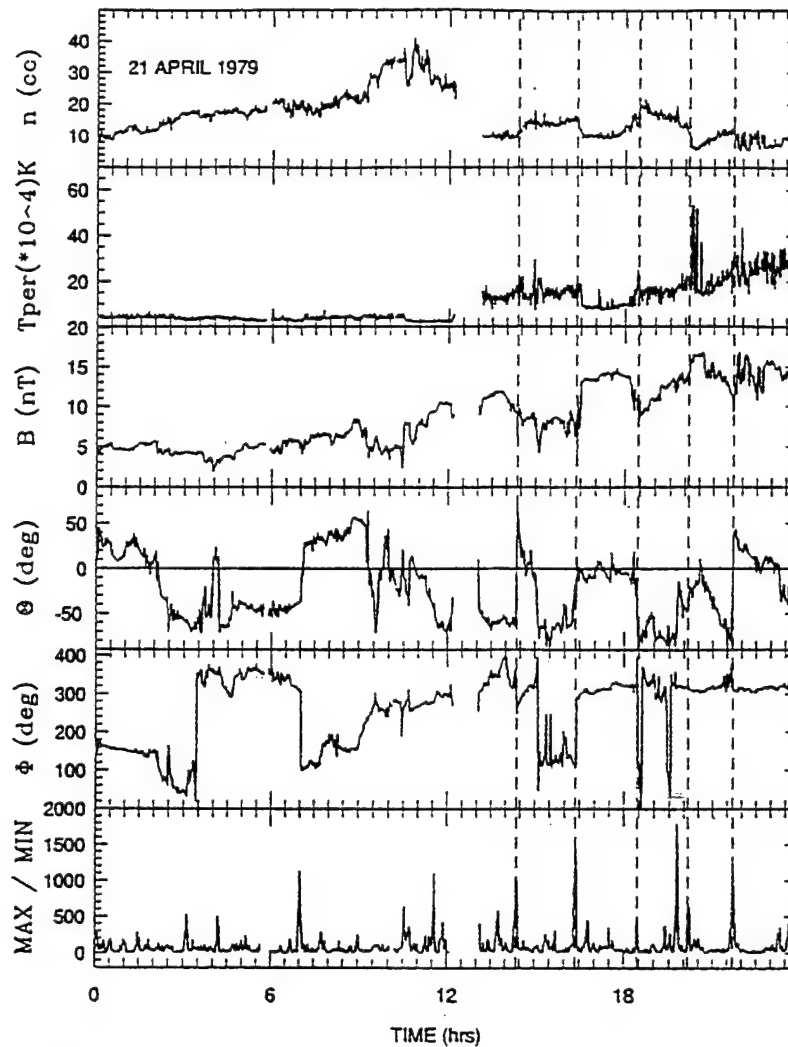


Fig. 6. High time resolution (1 min) plots of ISEE 3 coronal streamer belt density  $n$ , proton temperature  $T_{per}$  in the direction perpendicular to  $B$ , magnetic field strength  $B$ , magnetic field latitude  $\Theta$  and longitude  $\Phi$  (GSE coordinates), and the max/min eigenvalue ratio  $(\lambda_1/\lambda_3)^2$  from minimum variance analysis indicating directional discontinuity location. The dashed, vertical lines divide sandwiches of different plasma regimes.

location indicates that the magnetic vectors trace out a great circle lying in the plane of the streamer belt. In accord with section 3.2, the planar magnetic structure at ISEE 3 may be prominence material trailing the CME seen at Helios 2 or multiple current sheets bordering its trailing leg. Planar magnetic structure is not present in the Helios 2 data across the sector boundary, suggesting that these regions reached the Helios 2 orbit at a longitude east of the spacecraft. By the time the CME reached ISEE 3, the leading edge, moving radially, must have been past 1 AU, so that ISEE 3 entered its flank. The lack of the sharp density peak at ISEE 3, seen earlier at Helios 2, is consistent with this view.

Additional evidence that the ISEE 3 data show the aftermath of the Helios 2 CME comes from the sandwich-like nature of the high time resolution plasma parameters in Figure 6. These are prominent during the second half of the day, where the ISEE 3 and Helios 2 parameters do not match, and where the CME was detected at Helios 2. Sandwichlike field strength variations pervade the examples of planar magnetic structure given by Nakagawa *et al.* [1989], and it has been noted at sector boundaries by Behannon *et al.* [1981]. The field strength tends to plateau at a different level in each layer. Between layers it often drops sharply,

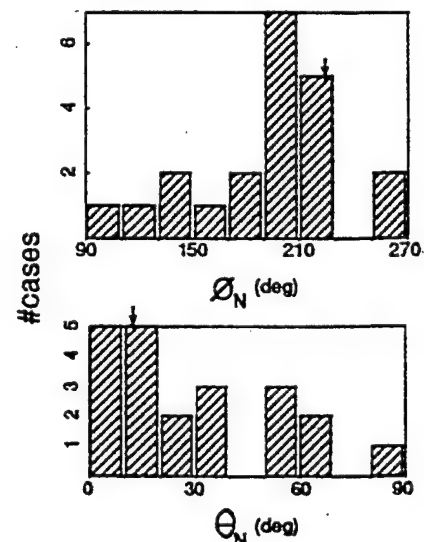


Fig. 7. Histograms of the longitude angle  $\Phi_N$  and the latitude angle  $\Theta_N$  of the normal to each of the 21 discontinuities in Figure 6 for which  $(\lambda_1/\lambda_3)^2 > 300$ . The dots in the  $\Theta_N$  histogram mark values normalized by solid angle.

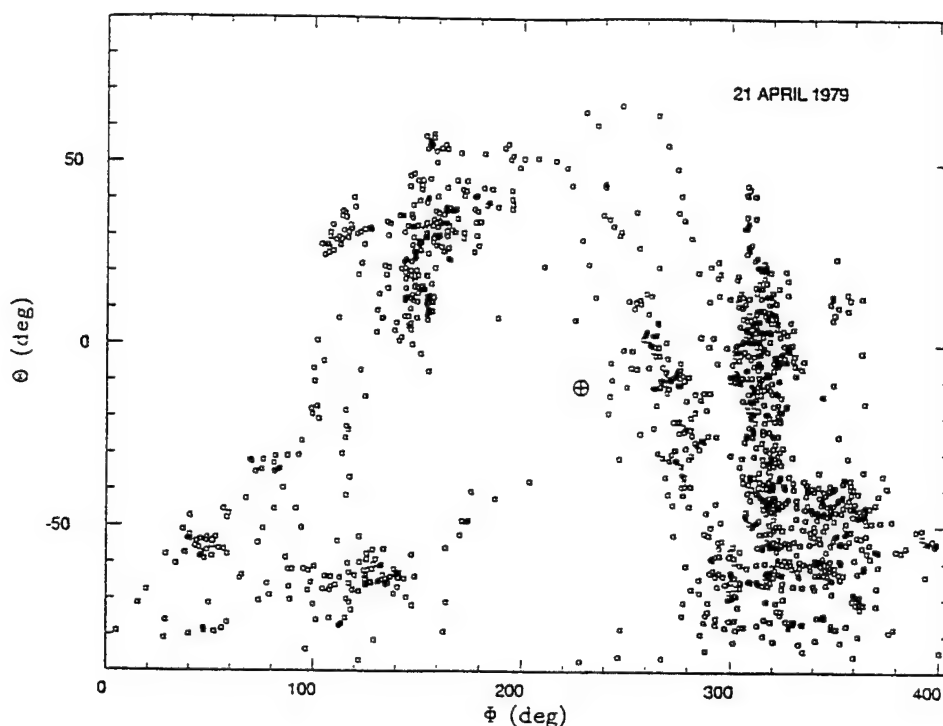


Fig. 8. Magnetic field longitude  $\Phi$  plotted against latitude  $\Theta$  (GSE coordinates) for the 1-min averages of ISEE 3 data in Figure 6. The sinusoidal pattern is the signature of planar magnetic structure. The encircled cross marks the position of the normal to the plane of the coronal streamer belt, determined from minimum variance analysis across the entire belt. Its central location in the sine wave indicates that the magnetic vectors tend to lie in the streamer belt plane.

forming magnetic holes [Turner *et al.*, 1977], although none occur in the data in Figure 6. Klein and Burlaga [1980] report a high incidence of magnetic holes at sector boundaries, consistent with sandwich structure there. Figure 6 shows that the density roughly anticorrelates with field strength, having high plateaus when  $B$  has low plateaus, consistent with pressure balance. The temperature also has sandwich-like changes, somewhat correlated with  $n$ , often with sharp spikes between plateaus. Five vertical dashed lines in Figure 6 mark the clearest sandwich structure. They drop to peaks in the  $(\lambda_1/\lambda_3)^2$  panel at the bottom, indicating directional discontinuities between the plateaus. We note, however, that not all discontinuities mark changes in plasma characteristics. This is especially true during the first half of the day, where the streamer belt has been stable between Helios 2 and ISEE 3.

What leads us to propose that the sandwich structure occurs in the aftermath of CMEs is that the same structure is often present in observations of typical CME passage in the solar wind. Pronounced examples are shown by Crooker *et al.* [1990] both before and after a large magnetic cloud within a fast CME. Burlaga *et al.* [1981] describe a single, outstanding example after another large cloud, which has since been identified in the Helios 2 photometers as a CME. Both studies interpret the pattern as a signature of filamentary solar material. Here we propose that filamentary streamers of solar material associated with prominences and/or multiple current sheets trailing CMEs, each contained in a flux tube with its own set of plasma parameters different from its neighbor's, account for the sandwichlike patterns at sector boundaries. Although these flux tubes may be small-scale ejections on closed tongues, their plasma parameters should be different from the strong magnetic fields and low tem-

peratures associated with the closed tongues or flux ropes of large-scale CMEs in the solar wind. The latter probably map back only to the dark cavity portion of the CME observed in coronagraphs [Hundhausen, 1988], while the sandwich structure would map back to bright regions.

A sketch of sandwiched flux tubes in cross section across the streamer belt, consistent with the ISEE 3 observations, is shown in Figure 9. Heavy line segments intersecting the ecliptic plane indicate the location and inclination of those discontinuities with  $\phi_N$  falling within the two most populated bins in Figure 7, which are those nearest the direction orthogonal to the Parker spiral. Use of only these cases allows a two-dimensional representation of the current sheet

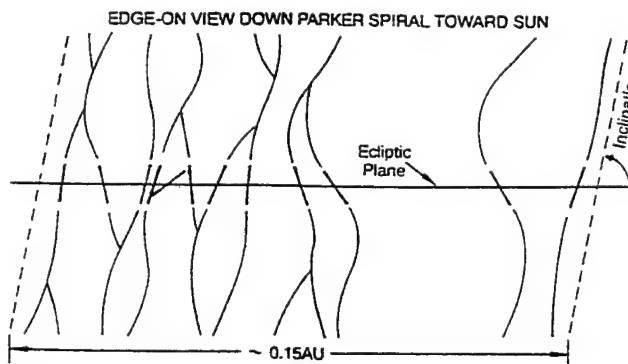


Fig. 9. Cross section of the streamer belt with schematic multiple current sheets. The heavy line segments intersecting the ecliptic plane indicate current sheet locations and orientations determined from the data in Figure 6 for those discontinuities with  $\phi_N$  nearest the Parker spiral. The dashed lines delineate the streamer belt and indicate its inclination, determined by minimum variance analysis across the entire sector boundary.



inclinations in a plane perpendicular to the Parker spiral. Schematic curves extend the tilted lines into a network of current sheets bounding flux tubes. Traced back to the Sun, the sheets may extend from helmet loops, as in Figure 1b, which, for this case, represents the ecliptic plane. If the helmets in Figure 1b formed infinitely long arcades, the current sheets in Figure 9 would be parallel. That they form a network, instead, reflects the assumption of arcades of finite length. In most cases the magnetic fields in adjacent flux tubes do not have opposite polarity, according to  $\Phi$  in Figure 6, but do have different directions. Thus, in three dimensions, the flux tubes must be braided together in a pattern that changes continually with time. Discontinuities not taken into account in Figure 9 imply even more complicated structures. Many of the braided tubes may be connected, forming masses of outflowing loops. Although the structures may passively convect outward with the solar wind, in this view their time dependence reflects dynamic coronal processes.

The solar origin view of sandwich structure described above is an alternative to a prevailing view that pressure balance structures and directional discontinuities can arise entirely from solar wind turbulence [e.g., Zank and Matthaeus, 1992; Roberts et al., 1992]. Our analysis does not preclude turbulence as a viable option. However, a synthesis of both views may ultimately apply. For example, in their AGU abstract, Roberts and Goldstein [1992] propose that high-density structures of solar origin near the current sheet in the inner heliosphere evolve with distance from the Sun owing to increasing effects of solar wind turbulence. Turbulence undoubtedly contributes to the complexity of the time variations in Figure 6, but to what extent remains to be determined.

The dashed lines bounding the current sheet network in Figure 9 delineate a highly inclined streamer belt, consistent with the value  $\theta_N = -12^\circ$  derived from minimum variance analysis across the thick sector boundary. This value is exactly orthogonal to the sector boundary on the corresponding coronal magnetic field map derived from source surface calculations by Hoeksema and Scherrer [1986], confirming with surprising accuracy the high inclination of the streamer belt.

An attempt to fit the discontinuities in Figure 9 with a wavy current sheet rather than a multiple current sheet meets with several problems. First, as discussed by Behannon et al. [1981], the high inclinations and incoherence of the discontinuity surfaces require large amplitude, irregular waves. But a more serious problem is that a wavy current sheet must have a global inclination angle that is low because the sheet must pass through the ecliptic plane many times across the width of the sector boundary. The orientation of a wavy current sheet fit is roughly orthogonal to a multiple current sheet fit. Studies at solar minimum [e.g., Behannon et al., 1981; Villante et al., 1979] do not face this problem because then the global current sheet inclination is low. For this case, however, a low-inclination current sheet would be inconsistent with both the streamer belt plane normal obtained by minimum variance analysis across the entire structure and with the neutral line inclination on the coronal field map.

In a sense the network of current sheets pictured in Figure 9 provides a synthesis of the concepts of wavy single and parallel multiple current sheets. Although the overall

structure has high inclination, it is conceivably possible to trace along current sheets from one side of the streamer belt to the other, parallel to the ecliptic plane on average, by passing up and down around flux tubes, thus tracing out a pattern resembling an irregular wave with large amplitude.

The concept of multiple current sheets and braided flux tubes proposed in this paper has been illustrated using data from a high-inclination sector boundary crossing near solar maximum. S. Shodhan et al. (manuscript in preparation, 1993) predict that sector boundaries at 1 AU should be highly inclined most of the time, based on a histogram of neutral line inclinations at the ecliptic plane on source surface maps [Hoeksema and Scherrer, 1986], which peaks in the  $80^\circ$ - $90^\circ$  bin. Even near solar minimum, when the latitudinal excursions of the neutral line are small, inclinations at the ecliptic plane can be large because of kinks in the neutral line [e.g., Villante and Bruno, 1982]. Thus the geometrical argument in favor of the proposed streamer belt structure for high inclinations may apply to most of the solar cycle. For low inclinations, either the wavy or multiple current sheet interpretation is viable. A spacecraft passing through the Figure 9 pattern held at right angles, representing low inclination, can still encounter multiple current sheets with high inclinations, as observed at solar minimum [e.g., Behannon et al., 1981], especially if the flux tube cross sections are less elongated.

## 5. SUMMARY

Based on the results of published observational studies, we propose a new view of the heliospheric current sheet and the coronal streamer belt that has the following two coronal features: (1) Multiple current sheets stemming from multiple helmet arcades of finite length, and (2) frequent ejections of mass from the helmet arcades.

Feature 1 extends into interplanetary space as the coronal streamer belt filled with braided flux tubes with cross sections elongated parallel to the streamer belt plane, and feature 2 constantly changes the flux tube pattern. Thus the streamer belt becomes a compound heliospheric current disk of variable thickness that serves as a conduit for frequent mass ejection. The new view can be used to explain poorly understood properties of sector boundary crossings as follows:

1. While the global orientation of the coronal streamer belt plane at any spacecraft crossing may be found by minimum variance analysis through the thickness of the whole structure, the same procedure applied to the many directional discontinuities within the structure give highly variable orientations. These can be ascribed to the multiple current sheets surrounding flux tubes and/or magnetic tongues. A single wavy current sheet interpretation fails for multiple discontinuities across highly inclined sector boundaries.

2. Ejections of progressively skewed, helmet streamer arcades threaded by prominence fields can account for the large-scale rotational structures at sector boundaries, including magnetic clouds. The signature of a magnetic cloud, usually ascribed to radial passage of a flux rope, can also be produced by corotation of a skewed helmet structure past a spacecraft.

3. Planar magnetic structure observed in the sheath preceding CMEs may arise from the multiple current sheet structure pushed aside as the CME bulge passes outward



along the streamer belt corridor. Planar magnetic structure may also occur in the trailing portions of CMEs, where prominence loops lie roughly parallel to the plane of the coronal streamer belt.

4. Plasma in the streamer belt, especially in the aftermath of CME passage, often displays a sandwichlike pattern, with discontinuities and, sometimes, magnetic holes between layers, consistent with layered flux tubes, each with its own solar source of plasma.

The above view is offered as an alternative interpretation of existing observations. Whether or not it is valid remains to be determined with new studies designed to test its specific propositions. Such studies are currently underway.

**Acknowledgments.** We thank E. W. Cliver for alerting us to the relevance of the work by Eddy [1973], J. A. Joselyn for providing an extensive bibliography on sector boundaries, and S. W. Kahler and T. Nakagawa for valuable comments on the manuscript. This research was supported in part by AFOSR's University Resident Research Program, by NASA under subcontracts UC884C27 (LANL to UCLA), 958922 (JPL to BU), and 959485 (JPL to UCLA), and by the Phillips Laboratory under contract AF19628-90-K0006 to BC. Work at Los Alamos was performed under the auspices of the U.S. Department of Energy, with partial support from NASA.

The Editor thanks L. W. Klein and R. Schwenn for their assistance in evaluating this paper.

#### REFERENCES

- Alfven, H., Electric currents in cosmic plasmas, *Rev. Geophys.*, **15**, 271-284, 1977.
- Behannon, K. W., F. M. Neubauer, and H. Barnstorf, Fine-scale characteristics of interplanetary sector boundaries, *J. Geophys. Res.*, **86**, 3273-3287, 1981.
- Borini, G., J. T. Gosling, S. J. Bame, W. C. Feldman, and J. M. Wilcox, Solar wind helium and hydrogen structure near the heliospheric current sheet: A signal of coronal streamers at 1 AU, *J. Geophys. Res.*, **86**, 4565-4573, 1981.
- Burlaga, L. F., Magnetic clouds and force-free fields with constant alpha, *J. Geophys. Res.*, **93**, 7217-7224, 1988.
- Burlaga, L., E. Sittler, F. Mariani, and R. Schwenn, Magnetic loop behind an interplanetary shock: Voyager, Helios, and IMP 8 observations, *J. Geophys. Res.*, **86**, 6673-6684, 1981.
- Crooker, N. U., J. T. Gosling, E. J. Smith, and C. T. Russell, A bubblelike coronal mass ejection flux rope in the solar wind, in *Physics of Magnetic Flux Ropes*, *Geophys. Monogr. Ser.*, vol. 58, edited by C. T. Russell, E. R. Priest, and L. C. Lee, pp. 365-371, AGU, Washington, D. C., 1990.
- Eddy, J. A., Observation of a possible neutral sheet in the corona, *Solar Phys.*, **30**, 385-394, 1973.
- Eselevich, V. G., and M. A. Filippov, An investigation of the heliospheric current sheet (HCS) structure, *Planet. Space Sci.*, **36**, 105-115, 1988.
- Feldman, W. C., J. R. Asbridge, S. J. Bame, E. E. Fenimore, and J. T. Gosling, The solar origins of solar wind interstream flows: Near-equatorial coronal streamers, *J. Geophys. Res.*, **86**, 5408-5416, 1981.
- Feldman, W. C., J. T. Gosling, D. J. McComas, and J. L. Phillips, Evidence for ion jets in the high-speed solar wind, *J. Geophys. Res.*, **98**, 5593-5605, 1993.
- Goldstein, H., On the field configuration in magnetic clouds, in *Solar Wind Five*, edited by M. Neugebauer, *NASA Conf. Publ.*, CP-2280, 731-733, 1983.
- Gosling, J. T., Large-scale inhomogeneities in the solar wind of solar origin, *Rev. Geophys.*, **13**, 1053-1058, 1975.
- Gosling, J. T., Coronal mass ejections and magnetic flux ropes in interplanetary space, in *Physics of Magnetic Flux Ropes*, *Geophys. Monogr. Ser.*, vol. 58, edited by C. T. Russell, E. R. Priest, and L. C. Lee, pp. 343-364, AGU, Washington, D. C., 1990.
- Gosling, J. T., E. Hildner, J. R. Asbridge, S. J. Bame, and W. C. Feldman, Noncompressive density enhancements, *J. Geophys. Res.*, **82**, 5005-5010, 1977.
- Gosling, J. T., G. Borini, J. R. Asbridge, S. J. Bame, W. C. Feldman, and R. T. Hansen, Coronal streamers in the solar wind at 1 AU, *J. Geophys. Res.*, **86**, 5438-5448, 1981.
- Hoeksema, J. T., and P. H. Scherrer, The solar magnetic field—1976 through 1985, *Rep. UAG-94*, World Data Cent. A for Sol. Terr. Phys., Boulder, Colo., 1986.
- Hundhausen, A. J., An interplanetary view of coronal holes, in *Coronal Holes and High Speed Wind Streams*, edited by J. B. Zirker, pp. 225-329, Colorado Associated University, Boulder, 1977.
- Hundhausen, A. J., The origin and propagation of coronal mass ejections, in *Proceedings of the Sixth International Solar Wind Conference*, edited by V. J. Pizzo, T. E. Holzer, and D. G. Sime, pp. 181-214, Rep. NCAR/TN-306+Proc, National Center for Atmospheric Research, Boulder, Colo., 1988.
- Hundhausen, A. J., The sizes and locations of coronal mass ejections: SMM observations from 1980 and 1984-1989, *J. Geophys. Res.*, in press, 1993.
- Jackson, B. V., Remote sensing observations of mass ejections and shocks in interplanetary space, in *Eruptive Solar Flares*, edited by Z. Svestka, B. Jackson, and M. Machado, Springer-Verlag, Heidelberg, in press, 1993.
- Kahler, S., Coronal mass ejections, *Rev. Geophys.*, **25**, 663-675, 1987.
- King, J. H., Interplanetary medium data book—Supplement 3, 1977-1985, *Rep. NSSDC 86-04*, NASA, Goddard Space Flight Cent., Greenbelt, Md., 1986.
- Klein, L. and L. F. Burlaga, Interplanetary sector boundaries 1971-1973, *J. Geophys. Res.*, **85**, 2269-2276, 1980.
- Klein, L. W., and L. F. Burlaga, Interplanetary magnetic clouds at 1 AU, *J. Geophys. Res.*, **87**, 613-624, 1982.
- Lepping, R. P., and K. W. Behannon, Magnetic field directional discontinuities, I, Minimum variance errors, *J. Geophys. Res.*, **85**, 4695-4703, 1980.
- MacQueen, R. M., Coronal transients: A summary, *Philos. Trans. R. Soc. London, Ser. A*, **297**, 605, 1980.
- MacQueen, R. M., and A. I. Poland, Temporal evolution of the equatorial K-corona, *Sol. Phys.*, **55**, 143-159, 1977.
- Marubashi, K., Structure of the interplanetary magnetic clouds and their solar origins, *Adv. Space Res.*, **6**, 335-338, 1986.
- McComas, D. J., J. T. Gosling, and J. L. Phillips, Interplanetary magnetic flux: Measurement and balance, *J. Geophys. Res.*, **97**, 171-177, 1992.
- Nakagawa, T., A. Nishida, and T. Saito, Planar magnetic structures in the solar wind, *J. Geophys. Res.*, **94**, 11761-11775, 1989.
- Nakagawa, T., The solar source of interplanetary planar magnetic structures, *Solar Phys.*, in press, 1993.
- Neugebauer, M., D. R. Clay, and J. T. Gosling, The origins of planar magnetic structures in the solar wind, *J. Geophys. Res.*, in press, 1993.
- Pneuman, G. W., and R. A. Kopp, Gas-magnetic field interactions in the corona, *Sol. Phys.*, **18**, 258-270, 1971.
- Poland, A. I., Motions and mass changes of a persistent coronal streamer, *Sol. Phys.*, **57**, 141-153, 1978.
- Roberts, D. A., and M. L. Goldstein, Striated structure of the plasma sheet near the heliospheric current sheet (abstract), *Eos Trans. AGU*, **73**, 431, 1992.
- Roberts, D. A., M. L. Goldstein, W. H. Matthaeus, and S. Ghosh, Velocity shear generation of solar wind turbulence, *J. Geophys. Res.*, **97**, 17,115-17,130, 1992.
- Rosenberg, R. L., and P. J. Coleman, Jr., Solar cycle-dependent north-south field configurations observed in solar wind interaction regions, *J. Geophys. Res.*, **85**, 3021-3032, 1980.
- Saito, T., Two-hemisphere model on the three-dimensional magnetic structure of the interplanetary space, *Sci. Rep. Tohoku Univ.*, **Ser. 5, Geophys.**, **23**, 37-54, 1975.
- Schulz, M., Interplanetary structure and the heliomagnetic equator, *Astrophys. Space Sci.*, **24**, 371, 1973.
- Schwenn, R., Large-scale structure of the interplanetary medium, in *Physics of the Inner Heliosphere I*, edited by R. Schwenn and E. Marsch, pp. 99-181, Springer-Verlag, New York, 1990.
- Smith, E. J., B. T. Tsurutani, and R. L. Rosenberg, Observations of the interplanetary sector structure up to heliographic latitudes of 16°: Pioneer 11, *J. Geophys. Res.*, **83**, 717-724, 1978.
- Svalgaard, L., J. M. Wilcox, P. H. Scherrer, and R. Howard, The Sun's magnetic sector structure, *Sol. Phys.*, **45**, 83, 1975.
- Thomas, B. T., and E. J. Smith, The structure and dynamics

- of the heliospheric current sheet, *J. Geophys. Res.*, **86**, 11,105-11,110, 1981.
- Turner, J. M., L. F. Burlaga, N. F. Ness, and J. F. Lemaire, Magnetic holes in the solar wind, *J. Geophys. Res.*, **82**, 1921-1924, 1977.
- Villante, U., R. Bruno, F. Mariani, L. F. Burlaga, and N. F. Ness, The shape and location of the sector boundary surface in the inner solar system, *J. Geophys. Res.*, **84**, 6641-6648, 1979.
- Villante, U., and R. Bruno, Structure of current sheets in the sector boundaries: Helios 2 observations during early 1976, *J. Geophys. Res.*, **87**, 607-612, 1982.
- Webb, D. F., The origin and kinematics of coronal mass ejections, in *Solar Terrestrial Physics, Proceedings of Second Indo-US Workshop on Solar-Terrestrial Physics*, edited by M. R. Kundu, B. Biswas, B. M. Reddy, and S. Ramadurai, pp. 283-302, National Physical Laboratory, New Delhi, India, 1986.
- Webb, D. F., and B. V. Jackson, The identification and characteristics of solar mass ejections observed in the heliosphere by the Helios 2 photometers, *J. Geophys. Res.*, **95**, 20,641-20,661, 1990.
- Zank, G. P., and W. H. Matthaeus, Waves and turbulence in the solar wind, *J. Geophys. Res.*, **97**, 17,189-17,194, 1992.
- 
- N. U. Crooker and G. L. Siscoe, Department of Atmospheric Sciences, University of California, Los Angeles, CA 90024-1565.
- J. T. Gosling, Los Alamos National Laboratory, MS D438, Los Alamos, NM 87545.
- S. Shodhan, Center for Space Physics, Boston University, 725 Commonwealth Avenue, Boston, MA 02215.
- E. J. Smith, Jet Propulsion Laboratory, MS 169-506, 4800 Oak Grove Drive, Pasadena, CA 91109.
- D. F. Webb, Phillips Laboratory/GPSG, Hanscom Air Force Base, MA 01731.
- (Received July 16, 1992;  
revised February 19, 1993;  
accepted February 22, 1993.)

## Relativistic Solar Proton Database for the Ground Level Enhancements During Solar Cycle 22

LOUISE C. GENTILE

*Boston College Institute for Space Research, Newton, Massachusetts*

A new software application called GLEINFO has been established to enable scientists who have remote networking capability to examine the computerized database of relativistic solar proton data for the ground level enhancements during Solar Cycle 22. This database was compiled in cooperation with principal investigators of the international network of neutron monitors to provide a consistent data set for detailed analysis of the processes involved in solar proton acceleration and propagation.

### INTRODUCTION

For almost 40 years the international network of neutron monitors has recorded relativistic solar proton events detected at the Earth. These ground level enhancements (GLEs) are marked by the observation of secondary particles generated by high-energy protons ( $> 450\text{ MeV}$ ) interacting at the top of the atmosphere [Shea and Smart, 1990]. More than 50 such events have been observed since the neutron monitor network was activated for the International Geophysical Year. These cosmic ray sensors have been described by Simpson [1957] and Carmichael [1968].

The GLEs of Solar Cycle 22 have been quite remarkable and renewed interest in relativistic solar particle events and their effects on the Earth's environment and modern technology. Eleven events occurred between July 1989 and May 1990, an unprecedented sequence of events within so short a time span. The increase recorded on September 29, 1989, was the largest measured since February 23, 1956, with a relative increase greater than 400% above the background cosmic ray intensity recorded at Calgary, Canada (altitude 1128 m, effective vertical cutoff rigidity 1.1 GV, calculated using the 1980 International Geomagnetic Reference Field [Shea et al., 1983]). This GLE was also recorded by an underground muon telescope at a depth of 35 m water equivalent (mwe) with a threshold rigidity of 19 GV [Swinson and Shea, 1990] and by a cosmic radiation environment monitor on a supersonic aircraft [Dyer et al., 1990].

Three GLEs were observed within a 6-day period in October 1989, all with significant increases and long durations. Their total solar proton fluence was greater than that measured at the Earth during the entire previous solar cycle [Shea and Smart, 1993]. Four events were observed in May 1990 within a span of 8 days, including the event on May 24, 1990, when for the first time direct solar neutrons were reported in association with a relativistic solar proton event [Shea et al., 1991]. Two additional GLEs were recorded during a period of intense solar activity in June 1991 [Smart et al., 1993].

In October 1989 the principal investigators of the neutron monitors were encouraged to send data for the September 29, 1989, event in a standard format described by Shea et al. [1987] to the Geophysics Directorate of Phillips Laboratory at Hanscom Air Force Base with the understanding

that all of the data received would be distributed to those who contributed. The objective of this cooperative effort was to expedite analysis of this unusual event by providing a comprehensive computerized database from neutron monitors throughout the world.

Plots of preliminary data from more than 30 stations were distributed to principal investigators at the GLE Highlight session at the 21st International Cosmic Ray Conference (ICRC) in Adelaide, Australia, in January 1990. Despite difficulties with network communications, the majority of the data for the September 29, 1989, event were distributed shortly after the ICRC, primarily via electronic mail. Compilation and distribution of such a substantial, computerized database so soon after a GLE represents a significant advance. Previously, data were exchanged primarily in printed form in station-specific formats requiring substantial modifications before analysis [Gentile et al., 1990].

Participants in the Solar-Terrestrial Workshop at the 21st ICRC requested that data be compiled for all the events of Solar Cycle 22. With the continued cooperation of the principal investigators, this has been done, and the database is updated regularly. Table 1 lists the number of data files currently available for each event.

Principal investigators are responsible for data quality and preparation. Although data preparation techniques vary from station to station, all data in the database are in a standard format which includes station information, hourly and small-time uncorrected and corrected data, and barometric pressure measurements [Shea et al., 1987]. Verified data are clearly marked in the comment section of the file, which also includes the name of the person who provided the data. Data that are not marked as verified are considered preliminary. All files are screened before they are added to the database.

### DISCUSSION

A menu-driven software application called GLEINFO has been established at the Geophysics Directorate to provide access to the GLE Database for Solar Cycle 22 for anyone who has remote networking capability. The database resides on a Digital Equipment Corporation VAX 7620 currently running OpenVMS version 6.0. The VAX is connected to both NSI/DECnet and the Internet. International network addresses are given in Table 2.

### LOGIN PROCEDURE

Connect to the PL VAX via NSI/DECnet or the Internet, enter GLEINFO at both the USERNAME and PASS-

TABLE 1. Status of Ground Level Enhancement Database for Solar Cycle 22

Event	Date	Neutron Monitor Data Files
40	July 25, 1989	34
41	August 16, 1989	31
42	September 29, 1989	48 <sup>a</sup>
43	October 19, 1989	38
44	October 22, 1989	37
45	October 24, 1989	39 <sup>b</sup>
46	November 15, 1989	30
47	May 21, 1990	19
48	May 24, 1990	28 <sup>c</sup>
49	May 26, 1990	21
50	May 28, 1990	17
51	June 11, 1991	32
52	June 15, 1991	36
53	June 25, 1992	23
54	November 02, 1992	08

Number of files currently in the database for each GLE observed during Solar Cycle 22. Events are numbered beginning with the first GLE reported in 1942.

<sup>a</sup>Plus 18 files from muon telescope or ionization chamber.

<sup>b</sup>Plus 3 files from muon telescope.

<sup>c</sup>Plus 2 partial files from muon telescope.

WORD prompts, then enter your own remote username. For NSI/DECnet users, the command to establish remote network connection is generally SET HOST; for those on the Internet, the command is TELNET. Since the procedures for establishing remote network connections depend upon the local operating system and network software, users who are not familiar with remote login procedures should contact their system managers for the specific system commands.

The Main Menu includes options to list the files in each event subdirectory, to examine individual data files, or to view event dates and times. An expanded help section, including a description of each Main Menu option and a full explanation of each command, is available via option 1. Event dates, baseline times, the time intervals selected for hourly and small-time data, the flare associations for each event, station names, and the complete GLE standard format description are available via options 2 and 3. Data are accessible via option 3.

Data are organized in subdirectories by event. Data file names are in the form C##NAME.DAT, where C indicates a Counts Per Second/Percentage Increase file, ## represents event number, and NAME is a four-letter abbreviation for the station name. A full list of station names is available via option 2.

Each event subdirectory contains a file GLE##.LIS which briefly summarizes the available event data, including the information reported in Solar Geophysical Data for the associated flare and preliminary estimates of the onset time and maximum relative increase observed at each station. The station latitude, longitude, altitude, type of instrument, and effective vertical cutoff rigidity are also included.

Once you are logged in, select an option from the Main

TABLE 2. International Network Addresses for VAX at Geophysics Directorate, Phillips Laboratory, Hanscom Air Force Base, Massachusetts

Network	Nodename	Address
NSI/DECnet	ZIRCON	61457
Internet	PLH.AF.MIL	146.153.100.5

Menu and enter the option number at the user prompt. The available commands are then displayed on screen along with a user prompt.

Enter a command to select a specific event subdirectory, to read data files, return to the Main Menu to select another option, or to logout. If a particular command has optional parameters or requires additional information, the user is prompted further. An invalid entry results in an error message and a redisplay of the available commands and user prompt.

When finished, logout of the application, and terminate the remote network connection.

### GLE APPLICATION FOR COPYING DATA

The GLE database is also accessible via a separate application which provides authorized users the additional capability of copying data to the user's remote node [Gentile, 1991, 1993]. Authorized users may also transfer files from the GLE database using either direct DECnet copy or the TCP/IP FTP protocol. GLEINFO users who have examined the data and are interested in obtaining access to the GLE database for copying data files should send their name, address, and electronic mail address to the author. The access information will be sent upon request.

Please contact the author at AFGLSC::GENTILE or GENTILE@PLH.AF.MIL if any difficulties are encountered or if there are suggestions for modifications or improvements.

### SUMMARY

The GLEs of Solar Cycle 22 have renewed interest in the effects of relativistic solar proton events. The GLEINFO software application permits examination of a comprehensive computerized database for analysis of these events to enhance understanding of the processes involved in the acceleration and propagation of relativistic solar protons. The complete GLE Database for Solar Cycle 22 will eventually be archived at World Data Center-A for Solar-Terrestrial Physics.

**Acknowledgments.** The research at Boston College was supported by the Geophysics Directorate (U.S. Air Force Materiel Command) contract F19628-90-K-0006. The author wishes to thank the principal investigators of the international network of neutron monitors who provided data for the database, to acknowledge technical assistance and support from Kathleen Berry, Nancy Mooradian, and Michael O'Brien of Digital Equipment Corporation and Susan C. Bredezen of the Geophysics Directorate of Phillips Laboratory Hanscom AFB, and to thank those who have reviewed this manuscript and tested the application. The author also gratefully acknowledges the work of John M. Campbell who cataloged the GLE data for Solar Cycle 22 and maintains a complete catalog for the full GLE database.

The Editor thanks M. Dryer, R. J. Walker, and J. L. Green for their assistance in evaluating this paper.

### REFERENCES

- Carmichael, H., Cosmic rays (instruments), *Ann. IQSY*, 1, 178-197, 1968.
- Dyer, C. S., A. J. Sims, J. Farren, and J. Stephen, Measurements of solar flare enhancements to the single event upset environment in the upper atmosphere, *IEEE Trans. Nucl. Sci.*, 37, 1929-1937, 1990.
- Gentile, L. C., Accessing the computerized database of solar relativistic proton data for the ground-level enhancements of solar cycle 22, *Proc. Int. Conf. Cosmic Rays*, 22nd, 3, 149-152, 1991.
- Gentile, L. C., Ground-level enhancement database for solar cycle

- 22: An update, *Proc. Int. Conf. Cosmic Rays*, 23rd, 3, 63-66, 1993.
- Gentile, L. C., M. A. Shea, and D. F. Smart, Problems associated with the cataloging of neutron monitor data for ground-level solar cosmic ray events, *Proc. Int. Conf. Cosmic Rays*, 21st, 5, 148-151, 1990.
- Shea, M. A., and D. F. Smart, A summary of major solar proton events, *Sol. Phys.*, 127, 297-320, 1990.
- Shea, M. A. and D. F. Smart, Significant proton events of solar cycle 22 and a comparison with events of previous solar cycles, *Adv. Space Res.*, in press, 1993.
- Shea, M. A., D. F. Smart, and L. C. Gentile, Vertical cutoff rigidities for selected cosmic ray stations for epoch 1980.0, *Proc. Int. Conf. Cosmic Rays*, 18th, 3, 411-414, 1983.
- Shea, M. A., D. F. Smart, J. E. Humble, E. O. Flückiger, L. C. Gentile, and M. R. Nichol, A revised standard format for cosmic ray ground-level event data, *Proc. Int. Conf. Cosmic Rays*, 20th, 3, 171-174, 1987.
- Shea, M. A., D. F. Smart, and K. R. Pyle, Direct solar neutrons detected by neutron monitors on 24 May 1990, *Geophys. Res. Lett.*, 18, 1655-1658, 1991.
- Simpson, J. A., Cosmic-radiation neutron intensity monitor, *Ann. IGY*, 4, 351-373, 1957.
- Smart, D. F., M. A. Shea, and L. C. Gentile, The relativistic solar proton ground-level enhancements associated with the solar neutron events of 11 June and 15 June 1991, *Proc. Conf. High Energy Phys. Sol. Flares*, in press, 1993.
- Swinson, D. B., and M. A. Shea, The September 29, 1989 ground-level event observed at high rigidity, *Geophys. Res. Lett.*, 17, 1073-1075, 1990.
- L. C. Gentile, Boston College Institute for Space Research, 885 Centre Street, Newton, MA 02159
- (Received March 11, 1993;  
revised June 20, 1993;  
accepted July 28, 1993.)

**X-CLASS SOFT X-RAY BURSTS AND MAJOR PROTON EVENTS  
DURING SOLAR CYCLE 22 (1987-1991)**

**L. C. Gentile and J. M. Campbell**  
Boston College Institute for Space Research  
885 Centre Street  
Newton, MA 02159 USA

**E. W. Cliver**  
Geophysics Directorate  
Phillips Laboratory (USAF)  
Hanscom AFB, MA 01731 USA

**H. V. Cane**  
Physics Department  
University of Tasmania  
Hobart, Tasmania, 2001 AUSTRALIA

**ABSTRACT**

We compiled a list of all major solar proton events ( $J(> 10 \text{ MeV}) \geq 10 \text{ pr cm}^{-2} \text{ s}^{-1} \text{ sr}^{-1}$ ) observed during the first half of Solar Cycle 22 (January 1987 - September 1991) and their flare associations. We also tabulated all X-class soft X-ray bursts observed during this period and studied the intersection of the two data sets. In particular we examined the usefulness of the e-folding decay time of intense soft X-ray bursts as an indicator, for forecasting purposes, of the likelihood of ensuing significant proton events at 1 AU. This study is an update of work covering Solar Cycle 21 (1976-1986) presented at the Leura Predictions Workshop. Results presented here are in general agreement with those of the earlier study. Impulsive X-class soft X-ray bursts are only infrequently ( $< 10\%$  of the time) associated with major  $> 10 \text{ MeV}$  proton events.

**1. INTRODUCTION**

Cliver and Cane (1990) studied the e-folding decay time ( $\tau$ ) of the X-class soft X-ray bursts of Solar Cycle 21 as a forecast tool for major proton events. They found that although  $\sim 40\%$  (61 out of 162) of the X-class soft X-ray bursts were impulsive, ( $\tau \leq 10$  minutes), only  $\sim 3\%$  (2 / 61) of the impulsive X-class X-ray bursts were associated with significant solar proton events. Approximately  $30\%$  (30 / 101) of the gradual ( $\tau > 10$  minutes) X-class soft X-ray bursts were associated with proton events. They also found that all C- and M-class flares which gave rise to major proton events and for which  $\tau$  could be determined (31 / 31) were gradual soft X-ray bursts. Cliver and Cane concluded that these results suggest that null-proton-event forecasts can be made following impulsive X-class X-ray bursts.



### 1.1. X-RAY BURSTS

We followed the procedure described by Cliver and Cane (1990), first compiling a list of X-class 1-8 Å bursts which occurred between January 1987 and September 1991 from the plots in Solar Geophysical Data (SGD) and the Energetic Event Summaries in the Preliminary Report and Forecast of Solar Geophysical Data (Pre-SGD), published weekly by the NOAA Space Environment Services Center.

We had microfilm plots of the soft X-ray data from at least one of the GOES satellites for January 1987 through May 1991. If there were gaps in the microfilm data for the time period of a burst, or if the event occurred during June-September 1991, we calculated the  $\tau$  value from enlargements of the GOES X-ray plots in SGD. From the plots we obtained the e-folding decay time of the soft X-ray emission measured from the peak of the event as described by Cliver and Cane (1990). Events with a  $\tau \leq 10$  were classified as impulsive events, those with  $\tau > 10$  were classified as gradual events. Figure 1 illustrates this technique for a representative event of each type.

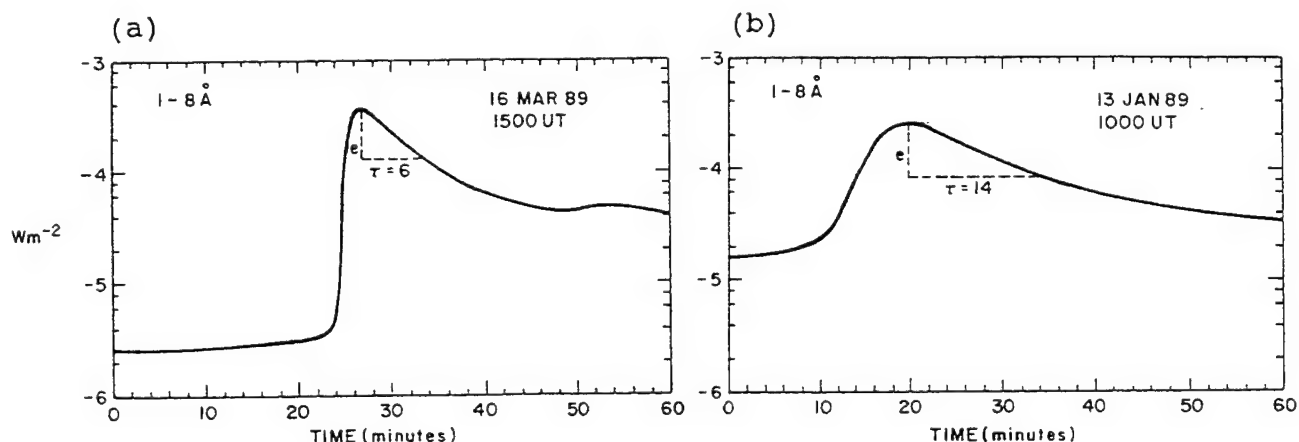


**Figure 1.** Example of (a) impulsive and (b) gradual X-class soft X-ray bursts illustrating the calculation of  $\tau$  value.

Of the 130 X-class events in our data set, we had microfilm plots for 106 of them. For 6 events before and the 16 events after May 1991,  $\tau$  was calculated from enlarged SGD plots. For two events no data were available from which to calculate  $\tau$ . Uncertainties in  $\tau$  for events for which we had microfilm data are estimated to be  $\pm 1$  minute for  $\tau \leq 15$  minutes and  $\pm 5$  minutes for  $\tau > 60$  minutes. When  $\tau$  was determined from enlarged SGD plots, uncertainties are estimated to be five minutes or more for events of all durations.

The flare associations for each event were determined from the H $\alpha$  observations published in SGD. The X-class bursts were approximately evenly divided between solar hemispheres, with 69 events originating in eastern hemisphere flares and 61 from flares in the west. Four X-class bursts were associated with flares behind the east limb and three with flares behind the west limb.

Two considerations affecting the determination of  $\tau$  should be mentioned. For the seven behind-the-limb flares, it is possible that the more impulsive sources of X-ray emission were partially blocked because of the flare location. These events would then appear to be more gradual. Despite such possible occultation effects, three of the seven behind-the-limb flares (11 May 1990, 4 March 1991, and 31 March 1991) gave rise to impulsive soft X-ray events. The second consideration concerns eight events (6 March 1989, 16 August 1989, 19 October 1989, and 1, 4, 6, 11, and 15 June 1991) for which the 1-8 Å detector was saturated; for these events the  $\tau$  value obtained represents an upper limit. All eight were gradual bursts.

Of the 128 events for which we could determine a  $\tau$  value, 56 or 44 % were impulsive, 72 (56 %) were gradual. Figure 2 is a histogram of the  $\tau$  values calculated for these events. Of the impulsive events, 35 were associated with eastern hemisphere flares, 21 with western hemisphere flares. The gradual events were more evenly divided between solar hemispheres, with 39 associated with western hemisphere flares, and 33 with eastern hemisphere flares.

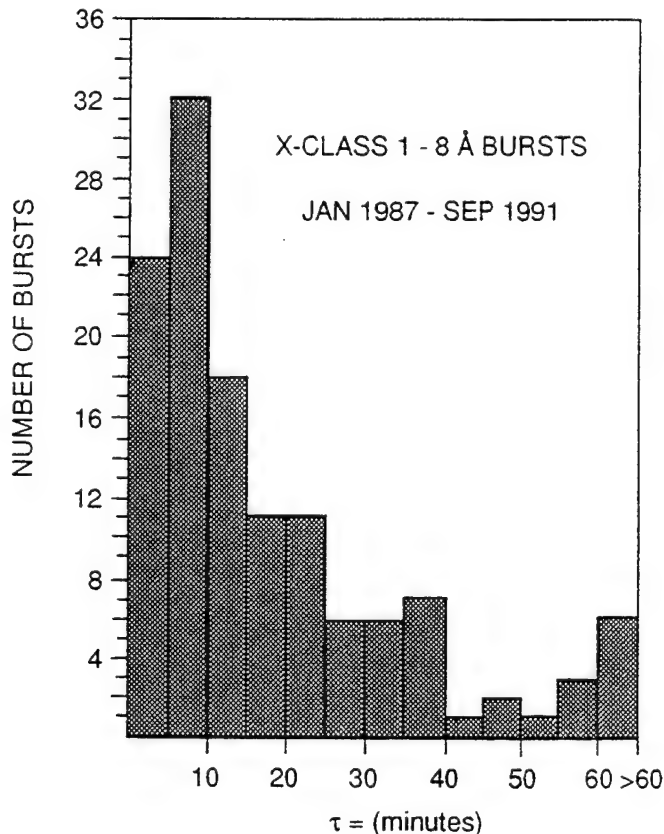


**Figure 2.** A histogram of  $\tau$  values for X-class 1-8 Å bursts occurring during the first half of Solar Cycle 22 (January 1987 to September 1991).

## 1.2. PROTON EVENTS

From the 11 February 1992 Preliminary Report and Forecast of Solar Geophysical Data, and the plots published weekly, we compiled a list

of 67 major ( $J(> 10 \text{ MeV}) \geq 10 \text{ pr cm}^{-2} \text{ s}^{-1} \text{ sr}^{-1}$ ) proton events for the time period of this study (January 1987–September 1991). Flare associations were determined from data in SGD and Pre-SGD. In general, we used a Big Flare Syndrome (Kahler, 1982) approach to making associations, taking the largest flare near particle onset and also considering metric type II data. In most cases we were able to attribute the proton event to a single flare, but for seven cases we identified two flares as contributors to the proton event. In events with long rise and/or decay profiles, it is often difficult to distinguish between fresh injections of particles and interplanetary modulation of previously accelerated protons. We judged that approximately 10 of the 67 events in our sample resulted from such modulation. For a few other cases, there was no good candidate source flare.

We were able to associate 54 of the 67 major proton events with visible disk or near-limb flares and obtained a  $\tau$  value for all but two of these 54 events. Our associations are in general agreement with those published in Pre-SGD. Table 1 lists the proton events, the associated flares, and the  $\tau$  values calculated for the associated X-ray bursts. A histogram of the  $\tau$  values of soft X-ray bursts associated with major proton events is given in Figure 3 for comparison with the histogram of  $\tau$  values of all X-class soft X-ray bursts given in Figure 2.

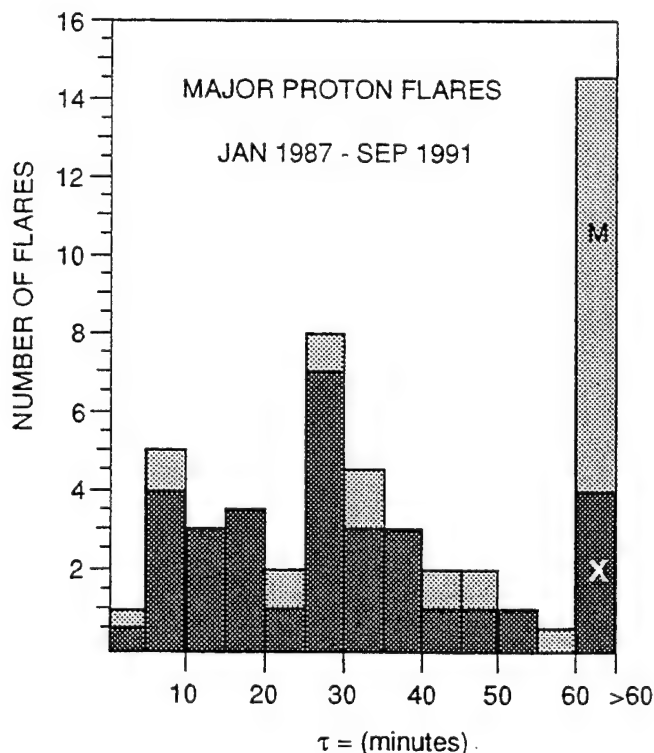


**Figure 3.** A histogram of  $\tau$  for major proton flares from the first half of Solar Cycle 22 (January 1987 to September 1991). Dark shading denotes X-class soft X-ray bursts; light shading denotes M-class and C-class flares.

**Table 1.** Major Proton Events and Associated Flares for the First Half of Solar Cycle 22 (January 1987 to September 1991)

PROTON EVENT			FLARE				
Onset Date	Peak 10 MeV Flux*	Date	Location	1-8 Å			
				Peak Time	Class	$\tau$ (min)	
1	Nov-08-87	110	Nov-07-87	N30 W105	2014	M 1	75
2	Jan-02-88	92	Jan-02-88	S35 W18	2135	X 1	40
3	Mar-25-88	58	Mar-25-88	N20 W100	2154	C 4	18
4	Jun-30-88	21	Jun-30-88	S16 E23	0906	M 9	06
5	Aug-26-88	42	Aug-23-88	N24 E90	1804	M 2	114
6	Oct-12-88	12	Oct-12-88	S21 W68	0511	X 2	16
7	Nov-08-88	13	Nov-08-88	N17 W07	1252	C 3	95
8	Nov-14-88	13	Nov-13-88	S24 W27	2311	M 3	28
9	Dec-17-88	29	Dec-16-88	N27 E33	0846	X 4	26
10	Jan-04-89	28	Jan-04-89	S20 W59	1805	M 4	48
11	Mar-08-89	250	Mar-06-89	N33 E71	1405	X15	32
12	Mar 10 89	3500	Mar-10-89	N32 E22	1922	X 4	65
13	Mar-17-89	2000	Mar-17-89	N33 W61	1744	X 6	26
14	Mar-23-89	53	Mar-23-89	N18 W28	1959	X 1	40
15	Apr-11-89	450	Apr-09-89	N35 E28	0105	X 3	16
		and ?	Apr-10-89	N40 W08	2323	M 1	396
16	May-05-89	110	May-05-89	N30 E04	0737	X 2	24
17	Jun-18-89	18	? Jun-18-89	N12 W30	1448	C 3	??
18	Jun-30-89	17	Jun-29-89	N30 W41	2127	M 3	43
19	Jul-01-89	17	Jun-30-89	S17 E88	0616	M 3	33
		and/or	Jun-30-89	S14 E77	0750	M 2	60
20	Jul-25-89	54	Jul-25-89	N26 W85	0844	X 2	06
21	Aug-12-89	<9200	Aug-12-89	S16 W38	1427	X 2	30
22	Aug 16 89	2000	Aug-16-89	S15 W85	0118	X20	33
23	Sep-04-89	44	Sep-03-89	S17 E19	1432	X 1	06
24	Sep-12-89	57	Sep-12-89	N17 E15	1012	M 7	266
		or	Sep 12-89	S17 W100	0814	M 5	212
25	Sep-29-89	4800	Sep-29-89	S27 W100	1133	X 9	33
26	Oct-19-89	40000	Oct-19-89	S25 E09	1258	X13	44
27	Oct-22-89	8000	Oct-22-89	S27 W32	1805	X 2	37
28	Oct-24-89	4100	Oct-24-89	S29 W57	1831	X 5	66
29	Oct 29 89	40	Oct-29-89	S27 W120	2155	M 4	62
30	Nov-15-89	71	Nov-15-89	N11 W28	0659	X 3	16
31	Nov 27 89	380	Nov-25-89	N29 E07	2355	X 1	66
		and/or	Nov-26-89	N25 W03	1941	M 4	79
32	Nov-30-89	7300	Nov-30-89	N25 W52	1229	X 2	49
33	Mar-19-90	950	Mar-19-90	N33 W39	0508	X 1	28
34	Mar 28 90	16	Mar-28-90	S05 W35	0750	M 4	>39
35	Apr-17-90	12	Apr-15-90	N32 E54	0302	X 1	66
		and/or	Apr-16-90	S12 E46	0634	X 2	06
36	May-21-90	410	May-21-90	N34 W37	2219	X 5	11
37	May-24-90	177	May-24-90	N36 W76	2051	X 9	06
38	May 26 90	89	May-26-90	N35 W100	2058	X 1	14
39	May-28-90	45	May-28-90	N35 W120	0433	C 1	??

Table 1. (continued)

PROTON EVENT			FLARE					
Onset Date	Peak 10 MeV Flux*		Date	Location	Peak Time	1-8 Å τ		
						Class	(min)	
40	Jun-12-90	79	Jun-12-90	N10 W32	0541	M 6	24	
41	Jul-26-90	21	Jul-25-90	S14 E56	2335	M 2	87	
42	Aug-01-90	230	Jul-30-90	N18 E42	0736	M 4	64	
43	Jan-31-91	240	Jan-31-91	S17 W35	0230	X 1	64	
44	Feb-25-91	13	Feb-25-91	S15 W82	0819	X 1	27	
45	Mar-23-91	43000	Mar-22-91	S26 E28	2247	X 9	08	
	and/or		Mar-23-91	S17 E06	0429	M 6	179	
46	Apr-03-91	52	Apr-02-91	N15 E02	2327	M 6	33	
47	May-13-91	350	May-13-91	S10 W100	0144	M 8	66	
48	May-31-91	22	? May-29-91	N06 E36	2345	X 1	05	
	and/or		? May-30-91	N07 E30	0941	M 8	05	
49	Jun-04-91	220	Jun-04-91	N34 E75	0352	X12	26	
50	Jun-11-91	3000	Jun-11-91	N32 W15	0209	X12	12	
51	Jun-15-91	1400	Jun-15-91	N36 W70	0821	X12	17	
52	Jun-29-91	110	Jun-28-91	N30 E115	0626	M 6	68	
53	Jul-07-91	2300	Jul-07-91	N28 E00	0223	X 1	26	
54	Aug-25-91	240	Aug-25-91	N23 E76	0115	X 2	51	

\* pr cm<sup>-2</sup> s<sup>-1</sup> sr<sup>-1</sup>

? flare association uncertain

?? τ indeterminant

## 2. ANALYSIS

We associated 30 of the proton events with X-class soft X-ray bursts (two such bursts in one case), 16 with M-class bursts (two such bursts in two cases), 4 with single C-class flares, and 4 with both an M-class and an X-class burst. Thus a total of 61 soft X-ray bursts were associated with the 54 proton events with identified sources. Of these 61 bursts, we were able to calculate a  $\tau$  value for 59. Eight of the 59 bursts were impulsive (6 X-class and 2 M-class), the remainder were gradual. Of the eight impulsive X-ray bursts associated with major proton events, two (17 April 1990 and 23 March 1991) are listed as co-contributors with gradual soft X-ray flares. In the accompanying histograms and statistical tables we credited each flare of the seven dual-associated proton events in Table 1 with half of an association. Thus we find that ~ 12 % (6 / 52;  $\tau$  undetermined for 2 events) of the major proton events during the peak of Solar Cycle 22 were associated with impulsive flares, a significant increase from the 3 % (2 / 61) value found by Cliver and Cane (1990) for Solar Cycle 21. A contingency matrix showing the relationship of gradual and impulsive X-class soft X-ray bursts to large proton events is given in Table 2. Yates'  $\chi^2$  test shows that the probability of this distribution arising by random chance is  $< 2 \times 10^{-3}$ .

**Table 2.** Contingency Matrix Showing Relationship Between X-Class Gradual and Impulsive Flares and Significant ( $> 10$  MeV) Proton Events

		<u>Protons*</u>	
		<u>Yes</u>	<u>No</u>
<u>X-Class</u>	<u>Gradual</u>	27.5	44.5
	<u>Impulsive</u>	4.5	51.5

\*  $J(> 10 \text{ MeV}) \geq 10 \text{ pr cm}^{-2} \text{ s}^{-1} \text{ sr}^{-1}$ .

Cliver and Cane (1990) also observed that X-class flares associated with significant proton events tended to be uniformly distributed in longitude. Figure 4 is a histogram of flare longitudes for the X-ray bursts associated with the major proton events for the first half of Solar Cycle 22. For both the X-class and smaller flares, there is a preference toward the western hemisphere in contrast to the results of the Cliver and Cane study for Solar Cycle 21.-

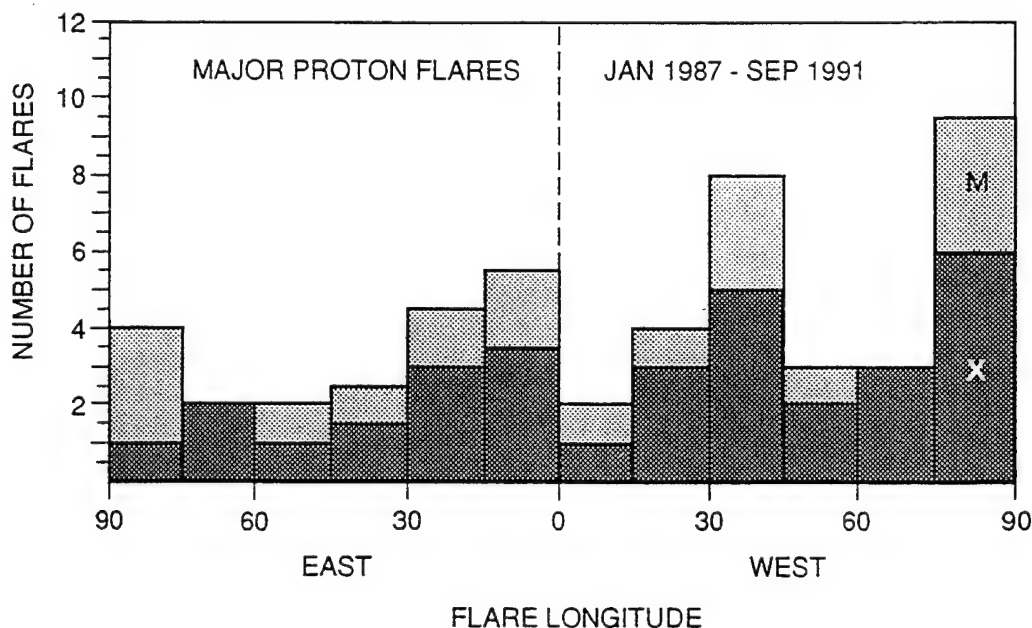


**Figure 4.** The longitude distribution of solar flares associated with major proton flares ( $J(> 10 \text{ MeV}) \geq 10 \text{ cm}^{-2} \text{ s}^{-1} \text{ sr}^{-1}$ ) from the first half of Solar Cycle 22 (January 1987 to September 1991). Dark shading indicates X-class soft X-ray bursts; light shading denotes M-class and C-class flares. Limb ( $> 90^\circ$ ) flares are included in  $75\text{--}90^\circ$  bin.



### 3. SUMMARY

Our results for the first half of Solar Cycle 22 are in general agreement with those of Cliver and Cane (1990) for Solar Cycle 21. Of the 128 X-class soft X-ray bursts (with  $\tau$  values) observed from January 1987 to September 1991, 32 (25 %) were associated with major solar proton events. Approximately 44 % (56 / 128) of the soft X-ray bursts were impulsive, and only 8 % (4.5 / 56) of these were associated with a significant solar proton event. Two of the proton events associated with impulsive flares (25 July 1989 and 24 May 1990) were Ground-Level Enhancements indicating that  $> 500$  MeV protons were present (Kahler et al., 1991).

Approximately 38 % (27.5 / 72) of the gradual X-class soft X-ray bursts were associated with solar proton events. The 32 proton events associated with X-class X-ray bursts (27.5 gradual and 4.5 impulsive) comprise 60 % (32 / 54) of the proton events with identified sources observed through September 1991 in Solar Cycle 22. The remaining 22 major proton events from this period were associated with M-class or C-class X-ray bursts, all but two of which were gradual ( $\tau$  indeterminate for two events).

The higher frequency (38 % vs. 8 %) with which gradual X-class soft X-ray bursts are followed by major proton events in comparison with impulsive X-class bursts indicates that  $\tau$  can be used to support null forecasts of proton events following intense impulsive flares. The corresponding figures reported by Cliver and Cane (1990) for the percentages of gradual and impulsive X-class bursts during Solar Cycle 21 that were followed by major proton events were 30 % and 3 %, respectively, in general agreement with results for the peak of Solar Cycle 22.

### 4. ACKNOWLEDGMENTS

The research at Boston College was supported by the Phillips Laboratory Geophysics Directorate (USAF) contract F19628-90-K-0006.

### 5. REFERENCES

- Cliver, E.W. and H.V. Cane, X-Class Soft X-Ray Bursts and Major Proton Events During Solar Cycle 21, Proceedings of the Solar-Terrestrial Predictions Workshop, Leura, Australia, edited by R. J. Thompson, D.G. Cole, P.J. Wilkinson, M.A. Shea, D. Smart, and G. Heckman, 1, 359, 1990.
- Kahler, S.W., The Role of the Big Flare Syndrome in Correlations of Solar Energetic Proton Fluxes and Associated Microwave Burst Parameters, J. Geophys. Res., 87, 3439, 1982.
- Kahler, S.W., M.A. Shea, D.F. Smart, and E.W. Cliver, Ground-Level Events from Impulsive Flares, Proceedings of the 22nd International Cosmic Ray Conference, 3, 21, 1991.
- Solar-Geophysical Data, National Geophysical Data Center, U.S.

Department of Commerce, NOAA, Boulder, Colorado, No. 515-571, July  
1987 - March 1992.

# The solar cycle variation of coronal mass ejections and the solar wind mass flux

David F. Webb

Institute for Space Research, Boston College, Newton Center, Massachusetts

Russell A. Howard

Naval Research Laboratory, Washington, D.C.

**Abstract.** Coronal mass ejections (CMEs) are an important aspect of coronal physics and a potentially significant contributor to perturbations of the solar wind, such as its mass flux. Sufficient data on CMEs are now available to permit study of their longer-term occurrence patterns. Here we present the results of a study of CME occurrence rates over more than a complete 11-year solar sunspot cycle and a comparison of these rates with those of other activity related to CMEs and with the solar wind particle flux at 1 AU. The study includes an evaluation of corrections to the CME rates, which include instrument duty cycles, visibility functions, mass detection thresholds, and geometrical considerations. The main results are as follows: (1) The frequency of occurrence of CMEs tends to track the solar activity cycle in both amplitude and phase; (2) the CME rates from different instruments, when corrected for both duty cycles and visibility functions, are reasonably consistent; (3) considering only longer-term averages, no one class of solar activity is better correlated with CME rate than any other; (4) the ratio of the annualized CME to solar wind mass flux tends to track the solar cycle; and (5) near solar maximum, CMEs can provide a significant fraction (i.e.,  $\approx 15\%$ ) of the average mass flux to the near-ecliptic solar wind.

## 1. Introduction

Coronal mass ejections (CMEs) are now known to be important for understanding the physics of the solar corona. CMEs are also important to our understanding of heliospheric disturbances and even the background solar wind because they involve the injection of significant amounts of mass and energy into large volumes of the interplanetary medium. CMEs may also provide the key link between geomagnetic activity and supposedly independent classes of "geoeffective" solar activity. Therefore, depending on the distributions of the rates and masses of CMEs directed into the ecliptic, CMEs might significantly contribute to the mass flux of the solar wind as measured at 1 AU.

The characteristics of CMEs near the Sun have been extensively studied by white light coronagraphs since their discovery in the early 1970s (see recent reviews by Kahler [1987, 1992]; Harrison [1991]; Hundhausen [1988]; and Webb [1992]). Transient interplanetary shocks and the CME/driver gas which often accompanies them have also been studied for over two decades

by a variety of techniques from spacecraft and from the ground [e.g., Klein and Burlaga, 1982; Watanabe and Kakinuma, 1984; Cane, 1985; Jackson, 1992; Webb and Jackson, 1990, 1993]. However, despite significant progress in studies of mass ejecta during this time, CMEs are still a relatively poorly understood phenomenon. Fundamental questions remain, such as how they are initiated, what is their basic geometry, and what is their signature in and their effects on the interplanetary medium.

The number of observations of CMEs has increased greatly over the last 15 years so that now we effectively can study their longer-term occurrence patterns. In this paper we present the results of a study of CME occurrence rates over more than a complete 11-year sunspot cycle and a comparison of these rates with the solar wind particle flux at 1 AU.

Previous event by event and statistical studies have consistently shown a better association between CMEs and certain classes of solar activity, such as erupting prominences, than others, such as  $H\alpha$  flares (for a recent review see Webb [1992]). If these associations are physically relevant to the initiation and/or propagation of CMEs, then this differentiation by activity class should be maintained over long time intervals. Therefore, we might expect different average longer-term correlations between CMEs and other related classes of solar activity.

Thus, our goals were (1) to examine the longer-term variation in the rate of CMEs over more than a complete sunspot activity cycle, from 1973 to 1989, using data from Earth-orbiting coronagraphs and the Helios photometers; (2) to study the annual variations of other activity related to CMEs and, using statistical correlation analyses, to compare the rates of CMEs with those of other activity related to CMEs; and (3) to estimate the near-ecliptic contribution of CMEs to the solar wind mass flux at 1 AU and determine its variation. These studies are described in sections 2, 3, and 4, respectively, and the conclusions are discussed in section 5. Webb [1991] presented an earlier preliminary summary of the work discussed in sections 2 and 3.

## 2. The Solar Cycle Variation of the Occurrence Rate of CMEs

CMEs are most directly detected by white light emission arising from Thomson scattering from free electrons. CMEs were first detected by a coronagraph on the OSO 7 satellite in 1971–1973, and large numbers of CMEs have been observed by orbiting coronagraphs on Skylab in 1973–1974, on P78-1 in 1979–1985, and on SMM in 1980 and 1984–1989. In addition, the Helios zodiacal light photometers have been used to detect CMEs in the interplanetary medium [e.g., Jackson, 1985a] and to estimate their occurrence frequency from 1975 to 1982, a period which includes a gap in coronagraph coverage [Webb and Jackson, 1990, 1993]. These observations form the basic database for our study.

To properly utilize CME rate data, the observed frequencies of occurrence must be corrected for both instrument-dependent effects and effects due to the mass and geometrical distributions of CMEs. For a given coronagraph the instrumental effects include the observational duty cycle, the visibility function or the detectability of CMEs away from the plane of the sky, and the detection threshold for events in the skyplane.

### 2.1. Corrections for Instrumental Duty Cycles

Only duty cycle corrections of observed CME rates have been published by the groups operating orbital coronagraphs over extended periods of time. Corrections to the CME rate using the duty cycles of the High Altitude Observatory's (HAO) Skylab and 1980 SMM coronagraphs were described by Hundhausen *et al.* [1984], and the annual observing efficiencies over the lifetime of the SMM instrument were discussed recently by MacQueen and St. Cyr [1991]. The annual observed SMM CME counting rates were provided by A. Hundhausen (private communication, 1992). We then corrected them for the instrument duty cycle in the following way. First, we found the annual number of effective days of SMM coronagraph operation by multiplying the number of effective days of operation by the observing efficiency (a measure of the frequency with which complete coverage of the corona during each orbit was obtained). These latter values are tabulated by Hund-

hausen *et al.* [1984] for 1980 and by MacQueen and St. Cyr [1991] for 1984–1989. The duty cycle correction was then applied by dividing the observed annual CME count rate by the effective days of operation for that year to get a daily corrected rate.

Corrections to the CME rate using the duty cycles of the Naval Research Laboratory's (NRL) Solwind coronagraph were discussed for 1979–1981 by Howard *et al.* [1985] and for 1984 and 1985 by Howard *et al.* [1986]. For the Helios photometer data we used the daily CME occurrence rates corrected for the spacecraft and instrument duty cycles for 1975 to 1982 as discussed by Webb and Jackson [1990, 1993].

### 2.2. Corrections for Instrumental Visibility

Coronagraphs have their maximum sensitivity to events in the plane of the sky, so they will miss or less efficiently detect CMEs which do not originate at the solar limb. Although the reduction in sensitivity away from this plane due to Thomson scattering and vignetting is well understood [e.g., Hundhausen, 1993], there is no direct way of measuring the overall detection sensitivity (or visibility function) of a given coronagraph.

Webb [1986] first made preliminary estimates of visibility corrections for these coronagraphs, which tended to reduce the discrepancies in CME rates. In this study we extend that work by using the most recent CME rate data corrected for both duty cycles and visibility functions, and including CME rates for 1975–1982 as determined with the Helios photometers. Because of the different results reported in the literature and the importance of determining the long-term variation of CME occurrence, we detail in this section our method of determining coronagraph visibility functions and correcting the observed CME rates and the use of the Helios photometer data for detecting and counting CMEs in the interplanetary medium. We emphasize that by correcting for visibility, we are estimating the actual number of CMEs distributed globally around the Sun, i.e., over  $360^\circ$  in longitude.

Metric type II bursts identified with H $\alpha$  flares form a useful database for indirectly evaluating the visibility function of a coronagraph. The association between type II bursts and CMEs has been shown to be high for source regions near the limb [Munro *et al.*, 1979; Kahler *et al.*, 1984; Sawyer, 1985; Webb and Cliver, 1988]. In most cases the timing of type II bursts permits accurate identification with their parent H $\alpha$  flares. Since the longitude distribution of type II bursts associated with H $\alpha$  flares in general, and those of Importance  $\geq 1$  in particular, is relatively uniform [Wright, 1980], their associations with or without CMEs can be used as a measure of the detection efficiency of a coronagraph.

**2.2.1. Solwind visibility function.** Kahler *et al.* [1984] performed such an analysis of the longitude distribution of Solwind CMEs and type II flares over  $3\frac{1}{2}$  years around the activity maximum of solar cycle 21, from March 1979 to August 1982. They compared a

comprehensive list of type II bursts associated with H $\alpha$  flares with the Solwind CMEs and generated lists of the flares associated and not associated with CMEs. Figure 1a shows their result, the longitude distribution of these two classes of type II flares. Consideration of this result led Kahler *et al.* [1984] to conclude that about 60% of all type II flares were associated with Solwind CMEs, and that Solwind detected about two thirds of all CMEs within 30° of Sun center.

We updated Kahler *et al.*'s result, comparing Solwind CMEs with all type II flares through the end of 1982. The Solwind coronagraph operated nearly continuously from March 1979 to September 1985. However, the operational duty cycle decreased significantly in 1984 and 1985. In addition, beginning in early 1983, the level and distribution of instrumental stray light varied intermittently. At its worst level, the east limb of the Sun was obscured, and observations of CMEs were seriously degraded. Therefore we made no attempt to determine Solwind visibility functions for years beyond 1982, and have used the function determined by the type II method from the data for 1979–1982 for all the years of operation.

From these data we determined the visibility correction as follows. First, we assume that the coronagraph is most sensitive to events near the limb such that its efficiency for detecting CMEs (and therefore CMEs associated with type II flares) is maximized between 60°

and the limb. In this band, 62% of all type II flares were associated with Solwind CMEs. We then multiplied the total number of type II flares in the bins from 0 to 60° by this fraction to find the number of CMEs that should have been observed. Comparison of this number with that actually observed from 0 to 60° indicates that Solwind detected about 77% of all CMEs. This visibility function was then applied by multiplying the Solwind duty cycle corrected occurrence rates of CMEs by a factor of 1.3. Note that normalizing the type II/CME distribution in this way avoids such problems as whether and how the fraction of CMEs associated with type IIs might vary over the solar cycle, for instance, because of a variation in the speeds of CMEs.

### 2.2.2. SMM coronagraph visibility functions.

We performed a similar analysis for the SMM coronagraph using the lists of observed CMEs compiled by Burkepile and St. Cyr [1993]; also see Webb [1986]. We compared the longitude distribution of these SMM CMEs with an updated version of Kahler's list of type II flares (S. Kahler, private communication). This distribution for 1980 indicates that the SMM coronagraph detected significantly fewer CMEs within 45° of Sun center. Thus, its detection efficiency decreased from the limb inward. The 1980 data yielded a multiplicative visibility correction for the SMM CME rate of 1.7, significantly higher than that for Solwind. However, we

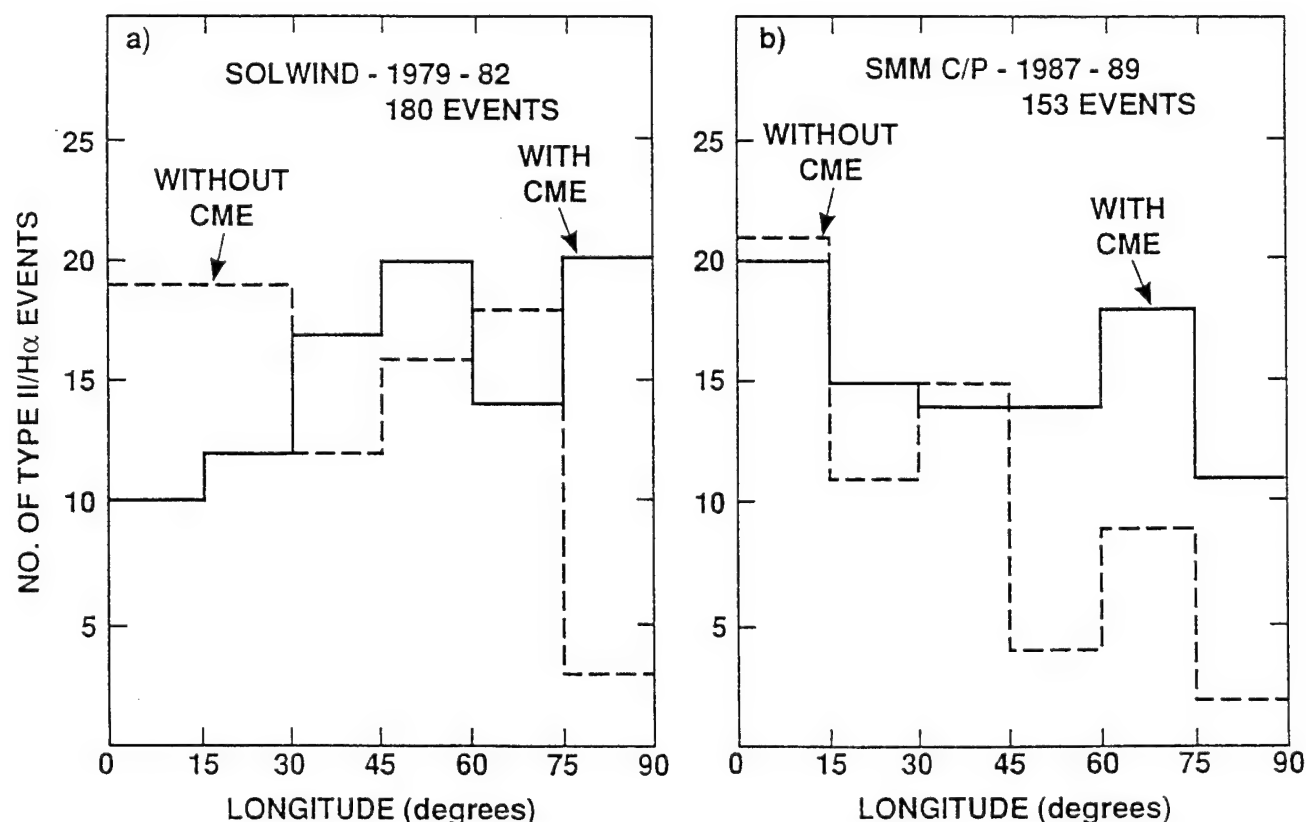


Figure 1. Heliolongitude distributions of metric type II bursts with H $\alpha$ -associated flares with and without (a) Solwind and (b) SMM CMEs during solar maximum. The data are summed in 15° longitude bins. Also see Kahler *et al.* [1984].

did not use this value for the 1980 data because we believe that data were statistically marginal and the east and west limbs were not sampled in a consistent manner.

The SMM satellite failed late in 1980, then was repaired by shuttle astronauts in April 1984. The SMM coronagraph then operated nearly continuously, acquiring data at a regular cadence of one complete view of the corona per spacecraft orbit, or every 90 min, from June 1984 to November 1989 [Burkepile and St. Cyr, 1993]. Since the main electronics box of the instrument was replaced and the operational philosophy changed beginning in 1984, we reanalyzed the visibility function of the coronagraph using all identified type II flares during the coronagraph operating period through 1989. The numbers of reported type II bursts/flares during solar minimum in 1984–1986 were too sparse for an adequate statistical test of the visibility function in those years. However, the numbers were robust for the 1987–1989 period and resulted in 153 type II flares to compare with the CME data. These distributions are plotted in Figure 1b. We found that the coronagraph visibility function for these years was identical to that of Solwind in 1979–1982 (i.e., yielding a correction of 1.3). Kahler *et al.* [1984] also found a similar result for the Skylab CMEs. The weighted average of the type II/CME data for SMM in 1980 and 1987–1989 gave a visibility correction of 1.4. We decided to apply this single correction to all of the Skylab and SMM CME rates.

**2.2.3. Helios photometer visibility function.** Jackson and Leinert [1985] and Jackson [1985a] have described the use of the Helios zodiacal light photometers as a means of detecting and studying CMEs in the interplanetary medium. Webb and Jackson [1990, 1993] have used the photometer data to count and estimate the frequency of occurrence of CMEs from 1975 through 1982, thereby filling a long gap in the Earth-based coronagraph coverage. In the Helios data, CMEs are identified as electron plasma clouds moving radially outward from the Sun. Event studies have found the Helios CMEs to be well associated with Solwind and SMM CMEs observed earlier near the Sun (e.g., Jackson and Leinert [1985]; Jackson *et al.* [1985]; Jackson [1985b]; McCabe *et al.* [1986]; Webb and Jackson [1990]). Webb and Jackson also found that during the period of overlapping coverage in 1979, the occurrence rates, speeds, and size scales of Helios and Solwind CMEs were comparable indicating that the Helios photometers detected most CMEs directed through their fields of view.

In this study we used the daily CME occurrence rates for Helios for 1975–1982 corrected for spacecraft and instrument duty cycles and instrument visibility function as determined by Webb and Jackson [1993]. Because of the heliospheric perspective from Helios, Webb and Jackson could not use the aforementioned type II/flare technique to determine a visibility correction for Helios. Instead, they made a single, coarse correction for the global (360°) azimuthal distribution of CMEs by multiplying the duty cycle rates by a factor of 8. This correction is based on the assumptions that the longitu-

dinal distribution of CMEs is uniform and that the average longitudinal width of a CME is equal to the average CME latitudinal span of 45° [e.g., Kahler, 1987]. Therefore, in ecliptic longitude Helios should have intersected only approximately  $\frac{1}{8}$  of all CMEs. This correction is appropriate because, although the Helios photometers could remotely view a wide range of longitude, Webb and Jackson [1993] selected only those CMEs which were directed toward the spacecraft.

### 2.3. Corrected CME Occurrence Rate

In Table 1 we list long-term occurrence rates of the CMEs and of other activity related to CMEs. These data span a period of 18 years, or about  $1\frac{1}{2}$  solar cycles, from 1972, one year before the start of the Skylab mission in June 1973, to the demise of SMM in November 1989. Annual values of the non-CME data from 1972 through 1989 are included for completeness and will be discussed in section 3. The CME data cover 17 years, with only 1974 lacking any significant amount of CME data. Included are the data discussed above from the spaceborne coronagraphs on Skylab from 1973 to 1974, P78-1 (Solwind) from 1979 to 1985, and SMM in 1980 and from 1984 to 1989, and from the Helios photometers from 1975 to 1982. For now we restrict our attention to the first five columns of Table 1. Column 1 lists the year and instrumental source of the CME data. Columns 3–5 include the following occurrence rates: the uncorrected observed rate, the duty cycle corrected rate, and our rate corrected for the instrument visibility function, respectively. The units of the rates are CME per day averaged over the number of months within each year when the CME data were obtained with each instrument (column 2). Daily CME rates are used for consistency with current convention.

For each year of its operation two Solwind rates are given, one for all observed CMEs and a lower one for only “major” CMEs (those designated Y + Q). The importance categorization was discussed by Howard *et al.* [1985], who separated the observed CMEs into one of three categories, Y, Q, or N, based on their subjective impression as to whether or not the CME event was considered major. If agreement could not be reached or if the CME was not well observed, then it was placed in the Q category. In general, the brighter and/or larger CMEs were Y class and the fainter and/or narrower CMEs were N class.

The daily CME rates from column 5 of Table 1, corrected for duty cycles and visibility functions, are plotted in Figure 2a. Continuous stretches of data from a single experiment have been connected by lines to guide the eye. We conclude the following from the CME rate data: (1) The CME rates tend to track that of the solar activity cycle, as usually traced by sunspot number, with minima in 1976 and 1985 and maxima in 1980–1981 and 1989. (2) After corrections for duty cycles and visibility functions (but not detection thresholds), the annual CME rates from different instruments are in reasonable agreement. (3) The Helios and Solwind CME rates in 1979 overlap. The near-equality of the



Table 1. Frequencies of Occurrence of CMEs and Related Classes of Activity

Year/ Instrument	CMEs, counts/day <sup>a</sup>				Related Activity, counts/month <sup>b</sup>									
	Observation		D-C		Visibility	Sunspot Number	H $\alpha$ Flares		Type II Bursts	IP Shocks <sup>d</sup>		DFs	EPLs	GRFs
	Period	Rate	Rate	Rate			Imp. $\geq 1$	$\geq 1$ hr		S/C	SCs			
1972	1 year	—	—	—	—	67	—	—	7.0	1.0	2.1	—	—	2.75
1973	1 year	—	—	—	—	39	—	—	5.9	0.6	1.2	—	—	2.25
1973-1974 Skylab	8 months	—	0.55	0.76	0.76	34	—	—	4.9	(0.6)	0.75	—	—	1.1
			0.34-0.74	0.48-1.04										
1974	1 year	—	—	—	—	32	—	—	3.3	1.3	1.0	—	—	1.4
1975	1 year	—	—	—	—	18	3.7	1.9	1.7	1.2	0.75	—	—	0.25
Helios	11 months	0.05	0.06	0.46	0.46	18	3.8	2.1	1.8	1.3	0.6	—	—	0.3
1976/Helios	1 year	0.02	0.03	0.27	0.27	13	1.75	1.25	1.2	0.5	0.9	12.2	0.9	0.5
1977/Helios	1 year	0.07	0.09	0.73	0.73	32	9.25	6.2	3.2	1.7	1.5	12.8	5.5	0.1
1978	1 year	—	—	—	—	91	37	21	13.6	4.1	3.3	31.4	5.5	3.6
Helios	9 months	0.10	0.18	1.45	1.45	87.4	37	20	16.4	3.2	5.0	30.9	4.7	3.0
1979	1 year	—	—	—	—	149	61.5	42	11.1	2.9	3.1	30.5	8.4	4.0
Helios	6 months	0.10	0.23	1.84	1.84	154	61	40	9.8	2.2	2.3	28.5	8.0	3.5
Solwind	9 months	1.34	1.64	2.13	2.13	157	62	42	11.2	1.8	2.4	30.0	8.0	4.1
Solwind-Y+Q	9 months	0.65	0.80	1.04	1.04									
1980/Solwind	1 year	1.05	1.80	2.34	2.34	155	72	40	15.1	3.9	3.5	30.3	13.2	5.75
Solwind-Y+Q	1 year	0.67	1.14	1.48	1.48									
SMM	6 months	0.46	2.22	3.11	3.11	156	66	32	15.3	4.7	3.7	29.0	13.2	7.0
Helios	5 months	0.08	0.22	1.75	1.75	152	82	45	16.2	2.8	5.4	30.8	9.9	3.2
1981/Solwind	1 year	1.31	1.95	2.54	2.54	141	54.5	46	12.8	4.6	4.2	27.25	6.9	6.25
Solwind-Y+Q	1 year	0.73	1.08	1.40	1.40									
Helios	4 months	0.09	0.31	2.48	2.48	140	42	38.5	8.25	3.0	3.25	26.5	5.3	2.25
1982/Solwind	1 year	0.89	1.24	1.61	1.61	116	88	40	14.3	3.0	2.9	26.2	4.9	5.6
Solwind-Y+Q	1 year	0.56	0.79	1.03	1.03									
Helios	3 months	0.04	0.23	1.85	1.85	123	113	48	18	3.7	6.3	29.0	7.9	4.3

Table 1. (continued)

Year/ Instrument	CMEs, counts/day <sup>a</sup>				Related Activity, counts/month <sup>b</sup>									
	Observation		D-C		Visibility	Sunspot	H $\alpha$ Flares		Type II		IP Shocks <sup>d</sup>		EPLs	GRFs
	Period	Rate	Rate	Rate	Rate <sup>c</sup>	Number	Imp. $\geq 1$	$\geq 1$ hr	Bursts	S/C	SCs	DFs		
1983/Solwind	1 year	0.48	0.72	0.94		75	34	16.5	5.4	—	1.6	21.8	3.5	2.3
Solwind-Y+Q	1 year	0.29	0.45	0.585										
1984/Solwind	1 year	0.36	0.59	0.77		42	24	14.75	3.25	—	0.8	18.8	3.2	1.6
Solwind-Y+Q	1 year	0.19	0.31	0.40										
SMM	7 months	0.17	0.35	0.49		34	10	6.6	1.4	—	0.6	17.9	2.4	0.3
1985/Solwind	8 months	0.18	0.515	0.67		18	8.6	6.9	1.5	—	1.1	11.4	1.4	0.4
Solwind-Y+Q	8 months	0.09	0.27	0.35										
SMM	1 year	0.16	0.19	0.26		18	7.7	5.4	1.7	—	1.2	11.2	1.25	0.4
1986	1 year	—	—	—		14	6.6	2.7	1.7	—	1.2	9.1	1.3	0.3
SMM	11 months	0.16	0.22	0.31		14	7.1	2.8	1.7	—	1.3	9.4	1.1	0.4
1987	1 year	—	—	—		32	15	6.25	4.2	—	1.3	16.2	3.2	1.2
SMM	9 months	0.32	0.49	0.685		36	19	7.9	5.1	—	1.5	18.2	3.9	1.6
1988/SMM	1 year	1.04	1.2	1.74		98.5	47	16	10.5	—	2.3	21.4	4.3	1.8
1989	1 year	—	—	—		154	93	37	17.3	—	3.8	27.1	10.8	3.1
SMM	10.5 months	1.39	2.0	2.83		154	96	38	18.4	—	3.9	27.0	11.1	3.2

<sup>a</sup>The CME rates are counts per day averaged over the specified observing period in column 2. Skylab and SMM coronagraph duty cycle (D-C) corrected rates are from *Hundhausen et al.* [1984] and courtesy A. Hundhausen (private communication, 1992), respectively. For Skylab a best determined value and a range are given. Two Solwind rates are given for each year. The first row is the rate for all observed CMEs, and the second row is for only "major" CMEs (Y + Q).

<sup>b</sup>Related activity rates are counts per month averaged over the annual or CME observing period. SS, sunspot; DFs, disappearing filaments; EPLs, erupting prominences at the limb; GRFs, gradual rise and fall bursts.

<sup>c</sup>CME visibility rate is the duty cycle rate (column 4) corrected for the instrument visibility function. The visibility functions we applied were 1.4 for the Skylab and SMM coronagraphs, 1.3 for the Solwind coronagraph, and 8.0 for the Helios photometers. See text for details.

<sup>d</sup>Counts per month of interplanetary shock waves. S/C (spacecraft) gives the shocks detected in situ by the IMP spacecraft from 1972 to 1974 and by the Helios 1 spacecraft from 1975 to 1982. The value used for the Skylab period is the annual IMP rate in 1973, since no shocks were actually observed during Skylab. There were no Helios 1 data after 1982. Also given are the number of sudden commencements (SCs) at Earth counted on the yearly graph of planetary Kp indices in the Solar Geophysical Data Bulletin (SGD).

Helios rate with that of major Solwind CMEs and the association of individual Helios CMEs with major Solwind CMEs [Webb and Jackson, 1990] suggest that only the larger, more energetic CMEs significantly influence the interplanetary medium. (4) Given result 1, we can predict that there should be a good correlation between the occurrence rates of CMEs and those of other activity related to CMEs. As shown in section 3, this expectation is, in general, obtained.

### 3. The Solar Cycle Variation of the Rates of Activity Related to CMEs

Both individual event and statistical studies have consistently shown different degrees of association between CMEs and certain classes of solar activity. For example, activity such as erupting prominences and soft X-ray long decay events (LDEs) are better associated with the location and onset times of CMEs than are H $\alpha$  flares [Munro *et al.*, 1979; Sheeley *et al.*, 1983; Webb and Hundhausen, 1987; Kahler, 1987, 1992]. Coronal shock waves, as evidenced by metric type II emission, are well correlated with faster CMEs ( $> 400$  km/s) [Gosling *et al.*, 1976; Sheeley *et al.*, 1984]. Transient interplanetary shocks, which may evolve from coronal shocks and can be tracked outward by kilometric type II radiation, are also well associated with fast CMEs [Sheeley *et al.*, 1985; Cane *et al.*, 1987]. Such studies lead us to expect different average longer-term correlations between CMEs and other related classes of solar activity. It is our purpose in this section to examine the statistical strength of these relationships over solar cycle time periods.

To this end we collated the occurrence rates, in units of counts per month, of the following classes of activity during the interval 1972–1989 for comparison with the CME occurrence rate data: smoothed sunspot numbers, H $\alpha$  flares, metric type II bursts (coronal shocks), interplanetary shocks, long-duration 10.7-cm gradual rise and fall bursts (GRFs), disappearing filaments (DFs), and erupting prominences at the limb (EPLs). All of these classes of activity have been considered in previous CME association studies [e.g., Webb, 1992]. In contrast to the CME analysis, we did not attempt to derive absolute occurrence rates of these parameters but only to assure that each activity data set was internally consistent. In other words, our approach was to make the data sets comparable with each other in a relative sense and, in particular, with the CME rate data.

Tabulations of the rates of these classes of activity, averaged on an annual basis over the appropriate CME observing period, are presented in columns 6–13 of Table 1. The annual numbers of the activity classes are plotted in Figures 2 and 3. In Figure 2b we show plots of smoothed sunspot numbers and metric type II bursts from 1972 to 1989. The sunspot numbers were taken from the Solar-Geophysical Data (SGD) Bulletin tables of smoothed monthly sunspot numbers, a commonly used tracer of solar activity.

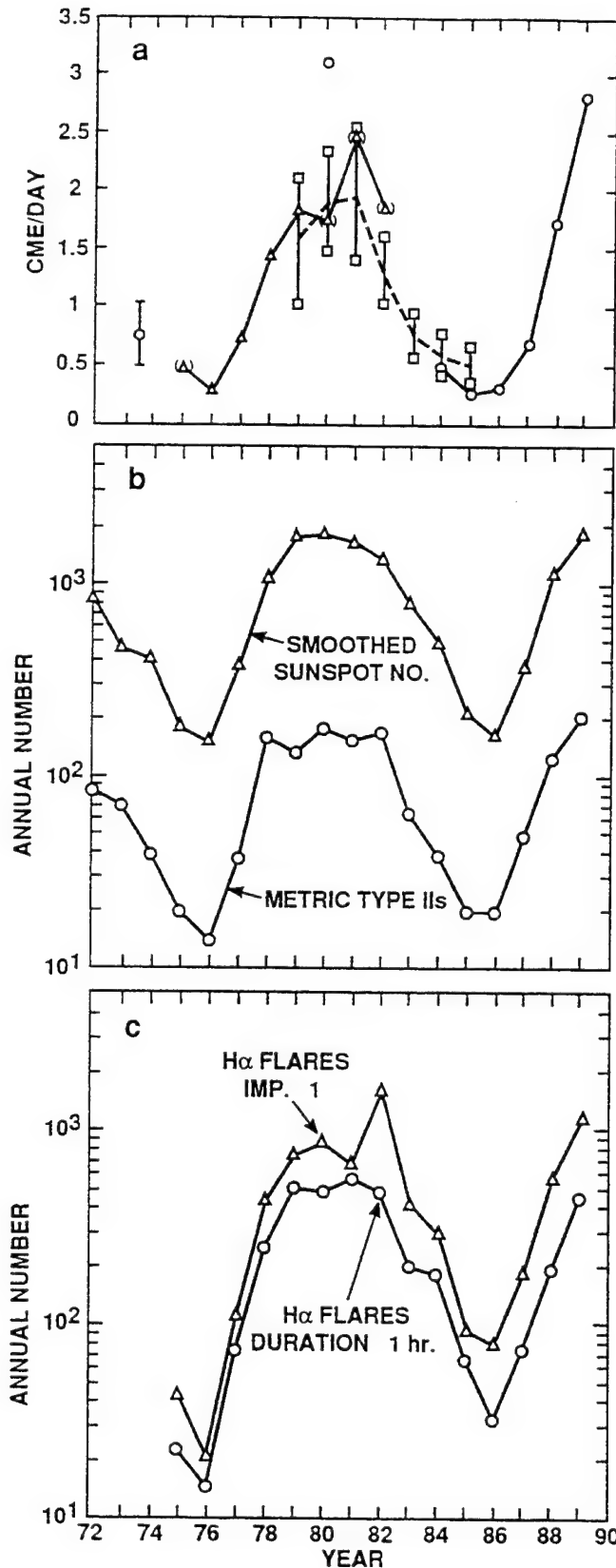
The metric type II burst data include all such bursts listed in the SGD tables of "Solar Radio Emission Spectral Observations". Additional events were included from catalogs of type II bursts compiled by Dodge [1974], Krivsky and Lukac [1980], and S. Kahler (private communication). Like many of the solar synoptic databases, the number of observatories reporting type II bursts varied over this period. But the reports from Culgoora Observatory in Australia are consistently available and dominate the type II burst data; on average Culgoora reported about half of all type II bursts. An annualized plot of Culgoora type II bursts mimics that of all type II bursts.

Figure 2c shows plots of two classes of solar H $\alpha$  flares for the period 1975–1989. The first class consists of all grouped H $\alpha$  flares of Importance  $\geq 1$ . This class of larger flares is more likely to be associated with CMEs than subflares [e.g., Munro *et al.*, 1979]. The second class consists of all grouped H $\alpha$  flares of duration  $\geq 1$  hour. Long-duration flares are also known to be better associated with CMEs.

Figure 3a shows the annual variation of the occurrence rate of two samples of interplanetary shock waves. At the top is plotted the annual variation of sudden commencement (SC) geomagnetic storms at Earth from the annual planetary Kp indices in SGD. The solar cycle variation of these SCs was first discussed by Cane [1988]. Although there are problems with the systematic identification and recording of SCs, it is accepted that most well-observed SCs are accompanied by interplanetary shocks recorded by spacecraft at 1 AU [Smith 1983]. Plotted at the bottom are shocks identified in the Los Alamos plasma experiments data on IMP 6, 7, and 8 in Earth orbit from 1972 to 1978 [Borriani *et al.*, 1982], and from the Max Planck plasma and magnetic field experiments on the Helios 1 spacecraft orbiting the Sun from 1975 to 1982 (R. Schwenn, private communication, 1986).

Figure 3b is a plot of the annual variation of the occurrence rate of microwave 10.7 cm GRF bursts of duration  $\geq 4$  hours. These data are from the monthly lists of outstanding events at the Canadian radio observatories at Ottawa, Ontario (2800 MHz), and at Penticton, British Columbia (2700 MHz), operated by the Herzberg Institute of Astrophysics. They were collected through 1985 and were discussed by Kahler and Cliver [1988]. For this study we extended the database through 1989. Kahler and Cliver consider the long-duration GRFs to be a good proxy for X-ray LDEs, which are themselves well associated with CMEs [e.g., Kahler, 1977; Sheeley *et al.*, 1983].

Figure 3c shows the annual variation of the occurrence rate of DFs on the solar disk from 1972 to 1989, and of EPLs from 1976 to 1989. The data on DFs are from catalogs of DFs collected by J. Joselyn (private communication, 1993) from 1976 to 1989 and by Wright [1991] from 1965 to 1980. The DFs in both data sets were counted systematically using daily H $\alpha$  full-disk photographs. No attempt was made to include DFs within active regions where most flares occur, so these



**Figure 2.** (a) Rate of occurrence of CMEs over the solar cycle. Data are corrected for instrumental duty cycles and visibility functions as discussed in text and are tabulated in Table 1. The data are from coronagraphs on Skylab and SMM (circles) and P78-1 (squares) satellites, and from the Helios 1 and 2 photometers (triangles). Two Solwind rates are given, one for all CMEs

are representative of DF events which are independent of flares.

Also plotted in Figure 3c are the annual counts of EPLs. We compiled these data from the individual observatory reports of active prominences and filaments that are sent to the World Data Center A (WDC-A) in Boulder, Colorado. The reports before 1985 were provided to us courtesy of J. Joselyn and H. Coffey and after February 1984 were taken directly from the SGD listings. These data are probably the least reliable of all of our databases; the reporting of EPLs is inconsistent from one observatory to the next, and the number of observatories reporting EPLs varies widely from year to year. The longest enduring and most consistent fraction of reports was from the observatories at Catania, Italy and Culgoora, Australia. The annual EPL count is the sum of all EPLs reported by all observatories reporting for every month of each year. From 1984 to 1989 we listed only reports of separate EPLs. Before 1984 we normalized the total number of reports to account for multiple reports of the same EPL.

These activity data sets show similar annual trends, with minima in 1976–1977 and 1985–1986 and maxima about 1980 and 1989. Not surprisingly, the curves of sunspot numbers and H $\alpha$  flares are very similar. (We cannot explain the peak in 1982 in the curve of flares of Importance  $\geq 1$ .) The rates of type II bursts and long-duration flares generally followed the sunspot cycle but with sharp rises in 1978 to flat-topped maxima extending through 1982, followed by rapid declines. These sharp rises in 1978, only 2 years after sunspot minimum, also were reflected in the rates of interplanetary shocks, GRFs and DFs; in addition, the GRF rate fell rapidly after 1982.

We can now compare the corrected occurrence rates of CMEs with the rates of each activity class averaged only over those months when the CME observations were obtained (Table 1), and calculate the linear correlation functions. As an example, in Figure 4 we present the plot of the daily CME rates versus equivalent average monthly sunspot numbers. The linear regression line is shown, and the correlation parameters are given in Table 2. The symbols refer to the same CME data as in Figure 2a.

and a lower one for only “major” (Y + Q) CMEs. (b) Annual numbers of smoothed sunspot numbers (triangles) and metric type II bursts (circles) from 1972 to 1989. The sunspot numbers are from the Solar-Geophysical Data (SGD) Bulletins tables of smoothed monthly sunspot numbers. The metric type II burst data are from the SGD tables of “Solar Radio Emission Spectral Observations”, and from catalogs by S. Kahler (private communication) and *Krivsky and Lukac* [1980]. (c) Annual numbers of two classes of H $\alpha$  flares from 1975 to 1989. The flare data are for “grouped” flares and were provided courtesy of J. McKinnon of the National Geophysical Data Center. The two classes are flares of Importance  $\geq 1$  (triangles) and flares of duration  $\geq 1$  hour (circles).

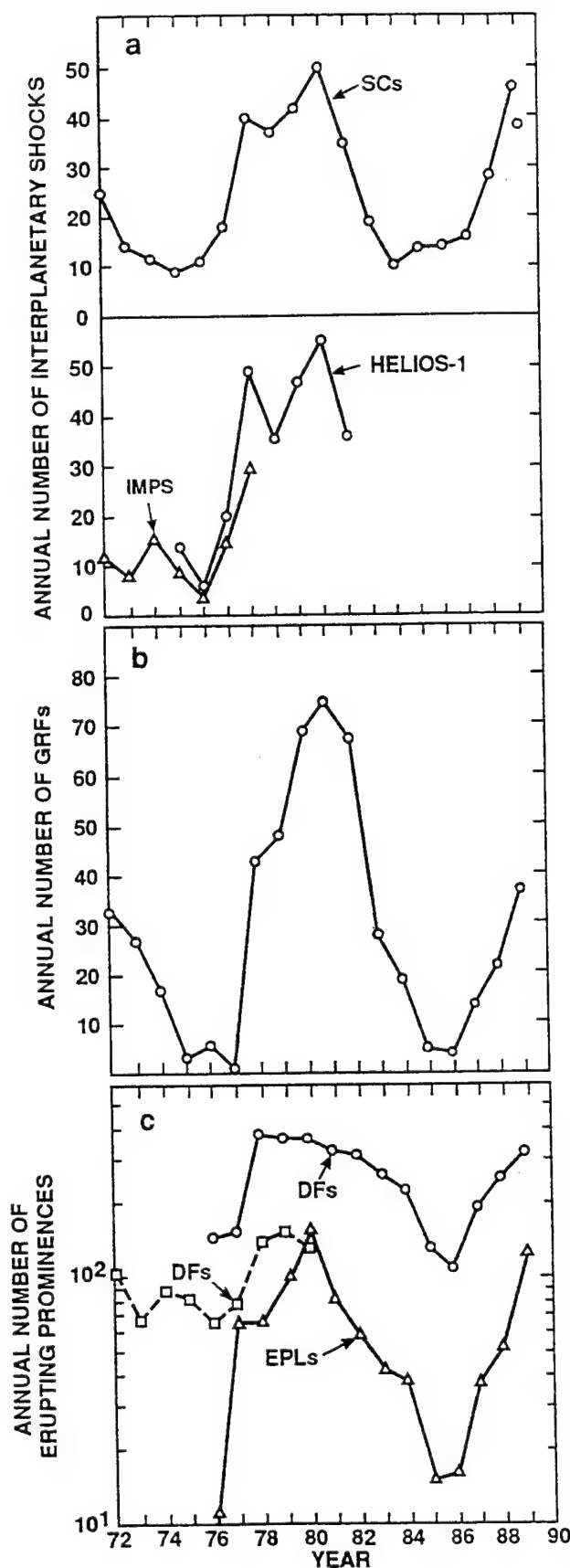


Figure 3. (a) Annual numbers of two sets of interplanetary shock waves. (top) Sudden commencement (SC) geomagnetic storms at Earth from the annual planetary magnetic 3-hour-range indices of  $K_p$  published

All of the correlation data reveal similar trends. The greatest scatter about the mean is for the years around maximum activity. The 1980 and 1989 SMM points lie farthest above and the Helios data lie farthest below the linear regression line.

Table 2 summarizes the results of the statistical comparison between the occurrence rates of CMEs and those of the related activity classes. The activity classes are listed in descending order of the linear correlation coefficients  $r$  of their fits to the CME rates. The quantity  $r$  basically measures the degree of scatter in the fits. The third column shows the number of degrees of freedom (the number of CME intervals from Table 2 having that particular kind of related activity) in each data set. Although all of the activity classes are correlated with the CME rate at >95% confidence level, the best fit is with sunspot numbers. We note that there is a large discrepancy between the fits of CMEs and SCs as an interplanetary shock proxy, and of CMEs and spacecraft-observed shocks. We do not know why this is, except that the poor fit with the spacecraft data may be related to problems with single-point spacecraft measurements and inadequate duty cycle corrections.

The amplitudes of the cyclical variations of each class, shown as the ratio of the rates at solar maximum to those at minimum, are given in Table 2 for cycles 21 (1980/1976) and 22 (1989/1986). The CME amplitudes were derived from the SMM and Helios rates as indicated in Table 2.

The correlations in Table 2 are all surprisingly high considering the varying quality and methods of acquisition of the data sets. Given this variation, these results lead us to the following conclusions: (1) Over the long term, no one class of solar activity is better correlated with CME rate than any other, and (2) the CME rate

in SGD. Also see Cane [1988]. (bottom) Data from the Los Alamos plasma experiments on IMP 6, 7, and 8 from 1972 to 1978 [Borrini et al., 1982], and from the Max Planck experiment on the Helios 1 spacecraft from 1975 to 1982 (R. Schwenn, private communication, 1986). (b) Annual numbers of microwave 10.7-cm gradual rise and fall bursts (GRFs) of duration 4 hours or greater. From the monthly lists of outstanding events at the radio observatories at Ottawa (2800 MHz) and at Penticton (2700 MHz) operated by the Herzberg Institute of Astrophysics. Also see Kahler and Cliver [1988]. (c) Annual numbers of disappearing filaments (DFs) on the solar disk from 1972 to 1989, and erupting filaments at the limb (EPLs) from 1976 to 1989. The circles are DFs from an unpublished catalog of J. Joselyn (NOAA Space Environment Laboratory, private communication, 1993), the squares are DFs from the catalog of Wright [1991], and the triangles are EPLs from the SGD lists of active prominences and filaments and by courtesy of H. Coffey of the National Geophysical Data Center. The DFs were counted systematically on daily  $H\alpha$  full-disk photographs. J. Joselyn used primarily photographs taken at Boulder and Wright used photographs from Culgoora, Australia.

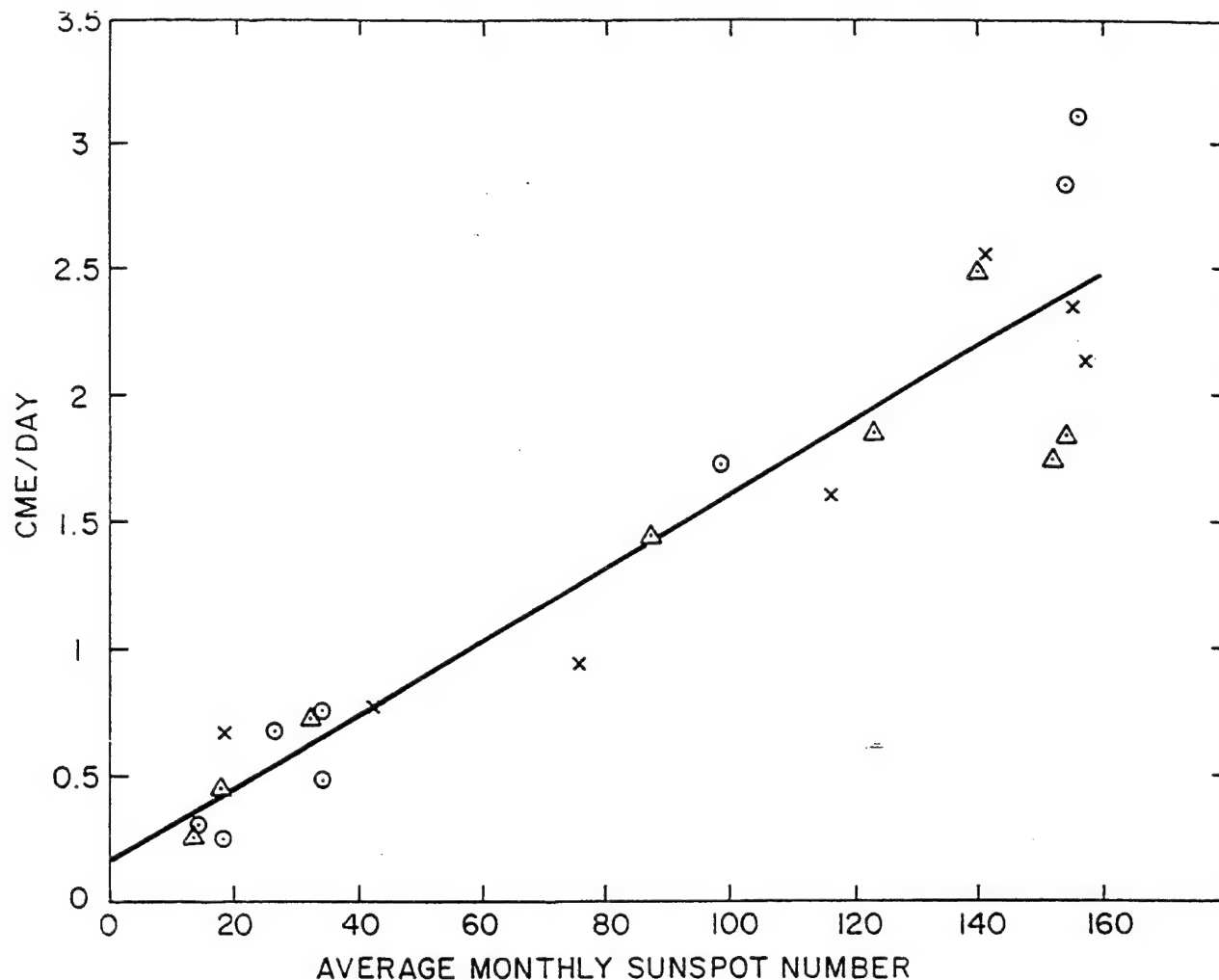


Figure 4. Comparison of the occurrence rates of CMEs and monthly sunspot numbers averaged over the appropriate CME observing period. The line is the linear regression fit, and the correlation parameters are given in Table 2. The symbols refer to the same CME data as in Figure 2a, except crosses instead of squares. Only the total Solwind CME points are shown and used in the statistical analysis.

varies over the cycle by about an order of magnitude, a range similar to that of the other activity classes. (However, the variations of the rates of DFs and SCs are significantly lower and of flares higher than this range.)

#### 4. The Contribution of CMEs to the Solar Wind Mass Flux

Since typical CMEs are massive and, at least near solar maximum, relatively frequent, they might contribute significant amounts of mass to the solar wind. In section 2 we evaluated the variation of the CME occurrence frequency over the solar cycle by performing corrections for the duty cycle and visibility function of each instrument. In this section we use these results to estimate the contribution of CMEs to the solar wind mass flux measured at 1 AU. First, in section 4.1 we calculate the annual average CME mass flux into the ecliptic over the solar cycle, making appropriate corrections for the lati-

tude variations and mass distributions of CMEs. Then in section 4.2 we discuss the available data on annual averages of the solar wind particle flux normalized to 1 AU, and, finally, in section 4.3 we estimate the annual percentage contributions of CMEs to this mass flux.

##### 4.1. The Near-Ecliptic CME Mass Flux

To more accurately evaluate the contribution of CMEs to the solar wind mass flux, further corrections should be made to the occurrence rate of CMEs to account for characteristics such as their mass and latitude and longitude distributions, all as functions of time. A fundamental parameter for deducing the CME mass flux is knowledge of the true CME mass distribution and how it varies with time. This parameter is poorly known because the detection threshold, or sensitivity function of a given coronagraph for CMEs in the plane of the sky is not known, and the derivation of excess mass for any event is a time-consuming process yielding results with large uncertainties.



Table 2. Comparison of the Long-Term Occurrence Rates of CMEs With Related Solar Activity

Activity Class	Linear Correlation		Cycle 21	Cycle 22
	r	N <sup>a</sup>	Amplitude	Amplitude
CMEs	—	—	11.5; 9 <sup>b</sup>	11 <sup>c</sup>
Sunspot number	0.94	23	12	11
Interplanetary shocks: SCs	0.91	23	3.8	3.3
EPLs	0.86	21	14	8
H $\alpha$ flares $\geq$ 1 hour	0.86	22	32	14
10.7-cm GRF bursts	0.85	23	11.5	9
Type II bursts	0.84	23	13	10
Disappearing filaments	0.84	21	2.5	3
H $\alpha$ flares $\geq$ Importance 1	0.79	22	41	14
Interplanetary shocks: spacecraft	0.64	14	7.8	—

<sup>a</sup>Parentheses indicate the number of degrees of freedom.

<sup>b</sup>The CME ratios are for SMM 1980/HELIOS 1976 and HELIOS 1981/HELIOS 1976, respectively.

<sup>c</sup>For SMM 1989/SMM 1985.

Observationally, the measurable mass of a CME is the amount of excess material in the field of view of a coronagraph at a given time when compared to the amount present at an earlier time when the CME was not present. The mass of a CME is usually derived by integrating over contours of excess columnar density, which are proportional to brightness changes [Stewart *et al.*, 1974; Jackson and Hildner, 1978; Illing and Hundhausen, 1986; Karpen and Howard, 1987]. The excess mass attributed to a given event is usually computed using only one or a few images at a time when the bright leading edge of the CME is within the field of view of the coronagraph. At later times after the leading edge has moved out of the field of view, mass presumably continues to flow upward from below the occulting disk but is not accounted for. That such mass calculations result in underestimates is suggested by estimates of CME masses in the interplanetary medium [Jackson, 1985a], ejected toward Earth [Howard *et al.*, 1982], and in possible flows beneath the leading edge [Anzer and Poland, 1979]. These results imply that typical coronagraph estimates of mass in the plane of the sky may be underestimated by factors of 2 or 3.

Excess mass calculations of 24 Skylab CMEs observed in 1973 to 1974 gave a mass distribution narrowly peaked at  $1\text{--}5 \times 10^{15}\text{g}$  with a lower cutoff of  $8 \times 10^{14}\text{g}$  [Rust and Hildner *et al.*, 1980]. CME mass calculations using SMM data have been limited because of photometric calibration problems, but early estimates of some 1980 CME masses yielded values similar to those of Skylab CMEs [e.g., Illing and Hundhausen, 1985]. We will adopt the average value of Skylab CME masses of  $\approx 5 \times 10^{15}\text{g}$  for the average mass of both Skylab and SMM CMEs in 1980 for our subsequent mass flux calculations.

The detailed properties of Solwind CMEs have been published by Howard *et al.* [1985, 1986]. In Figure 5 we present histograms of the annual distributions of four of these properties which are important for estimating

the contribution of CMEs to the solar wind mass flux. These are the angular span or width, the apparent central latitude, masses and mass per degree of latitude. We have also determined the annual averages of these properties for comparison with the CME rate data.

The Solwind mass distributions shown in Figure 5b were estimated indirectly as follows [see Howard *et al.*, 1985]. First, mass/degree factors were estimated for three brightness classes of CMEs as calibrated with 15 well-observed Solwind CMEs. Then the angular span of a given CME was multiplied by its appropriate mass/degree factor to yield the total mass. The Solwind mass distributions are fairly broad and similar for each year, except that they shift toward lower values as one goes from activity maximum to minimum. The average CME mass in 1979–1981 was  $4.0 \times 10^{15}\text{g}$ , in general agreement with the Skylab results.

Several factors must be noted in comparing the CME mass distributions calculated for the Skylab and Solwind data. The Skylab measurements were biased toward larger, brighter events, and that sample is well calibrated but small. No attempt was made to calculate the masses of a representative sample of all CMEs observed by Skylab and therefore the sensitivity function of the coronagraph. However, Jackson and Howard [1993] have estimated that Skylab CMEs with masses  $\geq 3 \times 10^{14}\text{g}$  would have been detected by the method Jackson and Hildner [1978] used to find Skylab forerunners. On the other hand, although the Solwind calculations are indirect, the sample of events is large with over 1600 CMEs observed over the life of the instrument. The mass distribution curve of Solwind CMEs gradually turns over toward the low end (Figure 5b), suggesting a lower mass limit of  $1\text{--}2 \times 10^{14}\text{g}$  (see also Jackson and Howard [1993]). The Solwind field of view is also larger than that of either the Skylab or SMM coronagraphs, an effect which should on average yield larger CME masses.

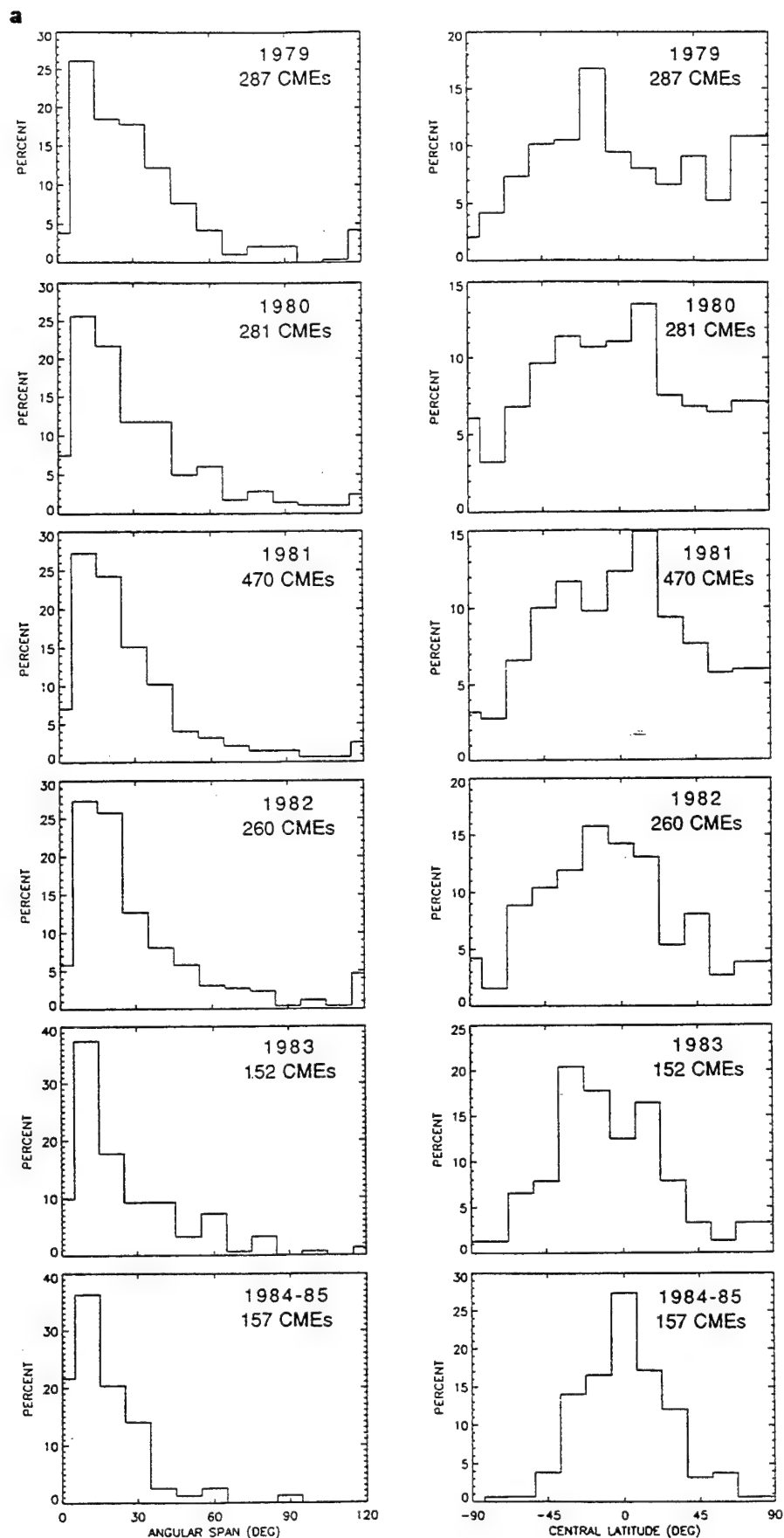


**Figure 5.** Stacked histograms showing the annual variations of four parameters of Solwind CMEs from 1979 to 1985. The plots show the fraction in percent attributed to each bin. The years 1984 and 1985 have been combined to improve the statistics. The total number of CMEs measured in each year are shown on each panel. The four parameters are (a) angular span or width (left) and apparent central latitude (right), and (b) mass (left) and mass per degree of latitude (right). Also see *Howard et al.* [1985].

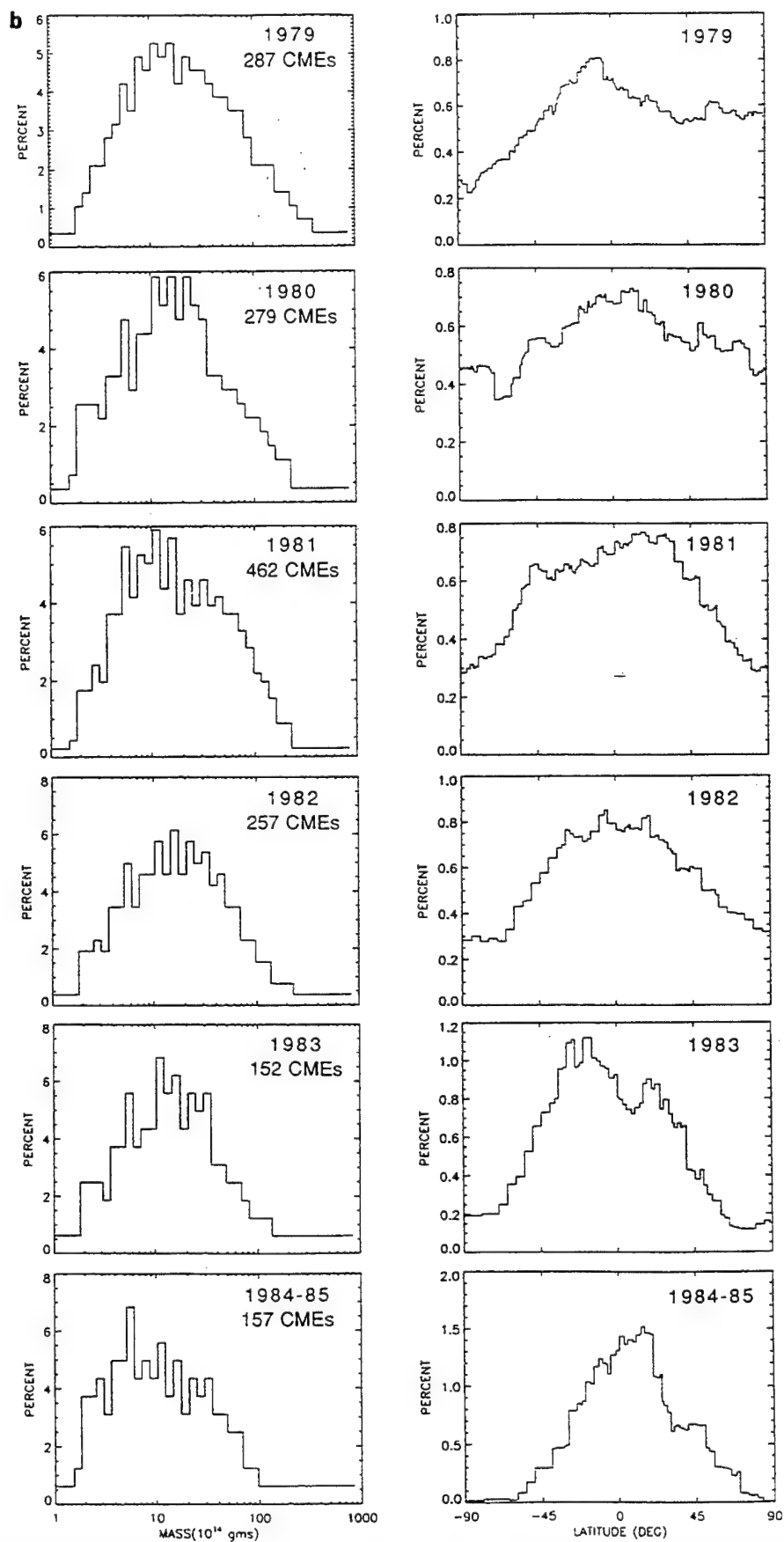


Fig.5 (continued)

Knowledge of the heliolatitude distributions of CMEs and their shapes and trajectories is important for determining the influence of CMEs on the near-ecliptic solar wind. The heliolatitude distribution of CMEs is well determined. The annual distributions of the central latitudes of CMEs are shown in Figure 5a for Solwind CMEs and in Figure 6 for SMM CMEs. These demonstrate the solar cycle variation of this parameter. During the solar maxima in 1980 and 1989, CMEs were more uniformly distributed in latitude than during the Skylab epoch or the recent solar minimum in 1985–1986 [Hundhausen *et al.*, 1984; Howard *et al.*, 1985, 1986; Hundhausen, 1993].

Although the geometrical shapes of CMEs are not well understood, their angular spans, or widths, and trajectories projected onto the plane of the sky are well determined. The temporal variation of the average inclinations of CME trajectories from the local vertical (radial) direction appears to be a small effect which we will ignore [MacQueen *et al.*, 1986]. Histograms of the angular spans of CMEs measured with the coronagraphs are shown in Figure 5a for Solwind CMEs and in Figure 6 for SMM CMEs. These annual averages are summarized in Table 3. The Skylab and SMM CME distributions remain fairly uniform with time, with an average span of about  $45^\circ$ . However, the distributions of the angular spans of Solwind CMEs differ from those of Skylab and SMM. Although the overall average of all Solwind CME spans is similar to that of Skylab and SMM, the Solwind distribution narrows and the annual average span decreases sharply from activity maximum to minimum. This cyclical variation is apparent in both samples of all Solwind CMEs and of major (Y + Q) CMEs.

Taken together, these data indicate that on average at any phase of the cycle the central axis of a CME must lie within  $15$  to  $20^\circ$  of the solar equator to have much influence on the ecliptic solar wind. (We have neglected any effects due to the changing solar tilt angle. This is justified because our yearly averages smooth over such effects, and any related uncertainties should be small compared with the large errors in the CME mass estimates.) This assumption is supported by results suggesting that CMEs are, to first order, three-dimensional spherical objects [e.g., Webb, 1988] and that they propagate with little dispersion into the interplanetary medium [e.g., Jackson, 1992]. For the Skylab and SMM data, combining the latitude distributions, as in Figure 6, within  $20^\circ$  of the equator with the corrected CME rates in Table 1 yields estimates of the rates of those CMEs directed into the ecliptic. We will return to the calculation of the ecliptic mass flux of Skylab and SMM CMEs later.

We use the method first discussed by Howard *et al.* [1985] to calculate the annual values of the near-ecliptic mass flux at 1 AU attributable to Solwind CMEs. In Figure 5b we show the annual histograms of the CME mass ejected into each degree of latitude. These plots were computed from consideration of the mass, central latitude and angular span distributions [see Howard *et*

*al.*, 1985]. From the ejected mass data we can determine the mass rate ejected into any latitude segment desired. In Table 4, column 3 we have listed the annual values of the CME mass per day ejected into an equatorial latitude bin  $1^\circ$  high and corrected for the Solwind visibility function. We will assume that this mass flux is distributed uniformly between the east and west limbs and ejected into  $90^\circ$ -wide longitude sectors at each limb. The choice of  $90^\circ$ -wide sectors is arbitrary but reasonable in that the more energetic CMEs likely to have the most effect on the interplanetary medium tend to have large spans [e.g., Webb and Jackson, 1990]. The Solwind mass fluxes at each limb have been summed together and thus represent the total flux ejected into a hemisphere of  $180^\circ$ . We will represent this area as a lune, a crescent-shaped  $180^\circ$  segment of a sphere, which provides a more accurate correction for the latitudinal projection of CMEs onto the skyplane [see Jackson and Howard, 1993].

The average equatorial mass flux ejected through this hemispherical segment at 1 AU is then calculated as in the following example. In 1979 the corrected mass flux per degree at the equator  $F$  is  $6.8 \times 10^{13}$  g deg  $d^{-1}$ . The area of a  $180^\circ$  crescent-shaped segment  $1^\circ$  wide at the equator at 1 AU is  $2R^2\theta$ , where  $R$  is 1 AU and  $\theta$  is  $1^\circ$ . So,

$$A = 2 \times (1.5 \times 10^{13} \text{ cm})^2 \times 0.0175 \text{ rad/deg}$$

$$A = 7.85 \times 10^{24} \text{ cm}^2/\text{deg}.$$

The equatorial CME mass flux at 1 AU then is  $F/A = 1.0 \times 10^{-16}$  g/cm $^2$  s. Equivalently, if we assume that helium constitutes 10% of this mass, we derive an average particle flux at 1 AU due to CMEs in 1979 of  $4.3 \times 10^7$  protons/cm $^2$  s. The estimated Solwind particle fluxes for 1979 to 1985 are listed in column 4 of Table 4.

Table 4 also lists the derived particle fluxes from the CME data for Skylab in 1973–1974 and SMM in 1980. The Skylab and 1980 SMM ejected masses were estimated as follows. We multiplied the average CME mass of  $5 \times 10^{15}$  g by the near-ecliptic CME rates discussed earlier and divided by  $40^\circ$  to get the mass/degree ejected into the ecliptic. These values may be upper limits because the average CME mass is likely overestimated and is not distributed uniformly in latitude. The CME mass and particle fluxes were then calculated as above. Note the near equality of the SMM and Solwind fluxes in 1980, which lends confidence that our overall results are reasonable.

#### 4.2. The Variation of the Solar Wind Particle Flux

Previous estimates of the CME contribution to the solar mass flux have been based on IMP spacecraft observations of proton flux densities at 1 AU in the early seventies. Feldman *et al.* [1977, 1978] presented plots of 27-day averages of the particle flux for 1971–1976. The average flux was  $3.4 \times 10^8$  ions/cm $^2$  s before Au-

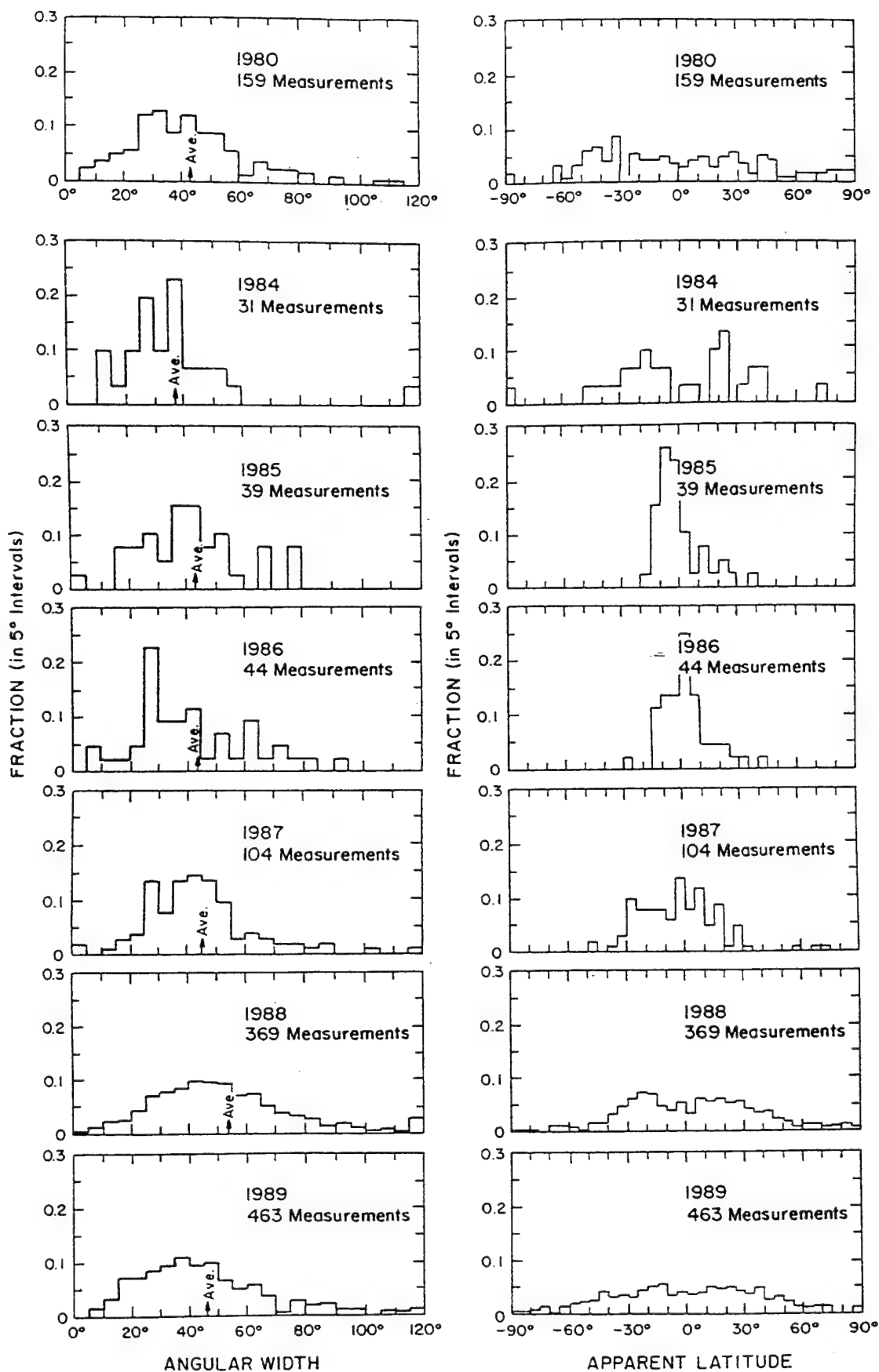


**Figure 6.** Similar stacked histograms showing the annual variations of the angular spans or widths and apparent central latitudes of SMM CMEs for 1980 and 1984 to 1989. The plots give the fraction in percent attributed to each 5° bin. The total number of CMEs measured in each year are shown on each panel. The arrows indicate the average of the CME spans for each year, which are also given in Table 3. Courtesy of A. Hundhausen of NCAR High Altitude Observatory. Also see *Hundhausen [1993]*.

Table 3. Annual Average Spans of CMEs

	Skylab/SMM <sup>a</sup>	Solwind	Solwind
		All	Y + Q
1973/1974	42	—	—
1979	—	52.9	75.1
1980	42.8	41.7	55.3
1981	—	40.7	58.2
1982	—	45.5	59.1
1983	—	36.5	49.3
1984	37.3	24.3	33.2
1985	42.8	21.4	31.1
1984-1985	—	23.6	32.7
1986	43.1	—	—
1987	45.0	—	—
1988	54.1	—	—
1989	46.0	—	—
Overall mean, deg	44.1	41.8	57.2

Spans are given in degrees.

<sup>a</sup>From *Hundhausen* [1993]

gust 1972, after which it jumped to an average of  $4.0 \times 10^8$  between 1972 and 1976. These values remained relatively constant and appeared to show little correlation with solar wind speed or sunspot number variation during this declining portion of cycle 20.

*Schwenn* [1983] presented Helios in situ data for the period 1975–1982. Intercalibration of the IMP and Helios data during the period of overlap in 1975–1976 revealed similar trends in the data sets. R. Schwenn (private communication, 1986) has provided us with yearly averages of the Helios particle flux data through 1984. We calculated the annual averages of the IMP 6, 7, and 8 data from *Feldman et al.* [1978] for the period 1972–1976. These two data sets, normalized to 1 AU, are plotted in Figure 7. The Helios points in 1974 and 1984 are less certain because they average only a small amount of data. We do not know the reason for the displacement of about  $1 \times 10^8$  ions/cm<sup>2</sup> s between the IMP and Helios data sets in 1975 and 1976; *Schwenn* [1983] did not discuss his intercalibration procedures. However, as he noted, the two sets do show a similar rising trend during this period.

Over these 13 years the trend of the solar wind particle flux is out of phase with solar activity, reaching a minimum near the cycle maximum in 1980 and vice versa. However, in agreement with most bulk solar wind parameters [e.g., *Schwenn*, 1983], the average flux variations were small, about 15–20%. As is evident by comparing Figures 7 and 2a, the CME rate, which follows the activity cycle, is poorly correlated with the solar wind mass flux. Should we expect a good long-term correlation between these parameters? The answer is probably not. *Schwenn* showed that the average particle flux is inversely correlated with the wind speed, and *Feldman et al.* [1978] showed that the peak particle flux showed the same tendency. Since the particle flux  $n_p v_p$  is a function of wind speed and mass, its bulk flow is likely influenced by the dominance of high-speed streams during the years around cycle minimum and by solar activity near maximum. The combination of these effects tends to flatten the long-term variation.

#### 4.3. The Variation of the Contribution of CMEs to the Solar Wind Mass Flux

We can now directly compare the average near-ecliptic mass fluxes of CMEs with the average solar wind particle fluxes at 1 AU on an annual basis over the solar cycle. For this purpose we again averaged the particle fluxes only during the monthly periods when CME observations were obtained; these values are listed in column 5 of Table 4. The resulting annual fractional contribution of the ecliptic CME mass flux to the solar wind particle flux at 1 AU is listed in the last column of Table 4. We used the IMP particle fluxes, which as noted above are higher than from Helios, for the Skylab period and the Helios fluxes for the other periods. The Helios flux in 1984 is more uncertain; that value was also used to compare with the 1985 Solwind CME flux.

How do our results compare to previous studies and what do they tell us about the importance of CMEs to the interplanetary mass flux? *Hildner* [1977] estimated a contribution from Skylab CMEs of only 3%. But he did not account for the latitude variation of CMEs, instead comparing the global CME flux with the parti-

Table 4. CME Mass Fluxes and Their Contribution to the Solar Wind Mass Flux

Year	Instrument	Equatorial CME MF	CME MF at 1 AU	SW MF at 1 AU	CME/SW Mass Flux
		$10^{13} \text{ g deg}^{-1} \text{ d}^{-1}$	$10^7 \text{ prot. cm}^{-2} \text{ s}^{-1}$	$10^7 \text{ prot. cm}^{-2} \text{ s}^{-1}$	%
1973/1974	Skylab	$\leq 9.1$	5.7	40	$\leq 14.3$
1979	Solwind	6.8	4.3	29	14.8
1980	Solwind	6.0	3.8	29	13.0
1980	SMM	$\leq 6.4$	4.0	30	$\leq 13.4$
1981	Solwind	5.85	3.7	33	11.3
1982	Solwind	4.55	2.9	38.5	7.45
1983	Solwind	1.8	1.1	37	3.1
1984	Solwind	1.6	1.0	37	$\sim 2.7$
1985	Solwind	2.6	1.6	37	(4.4)

MF, mass flux; SW, solar wind.



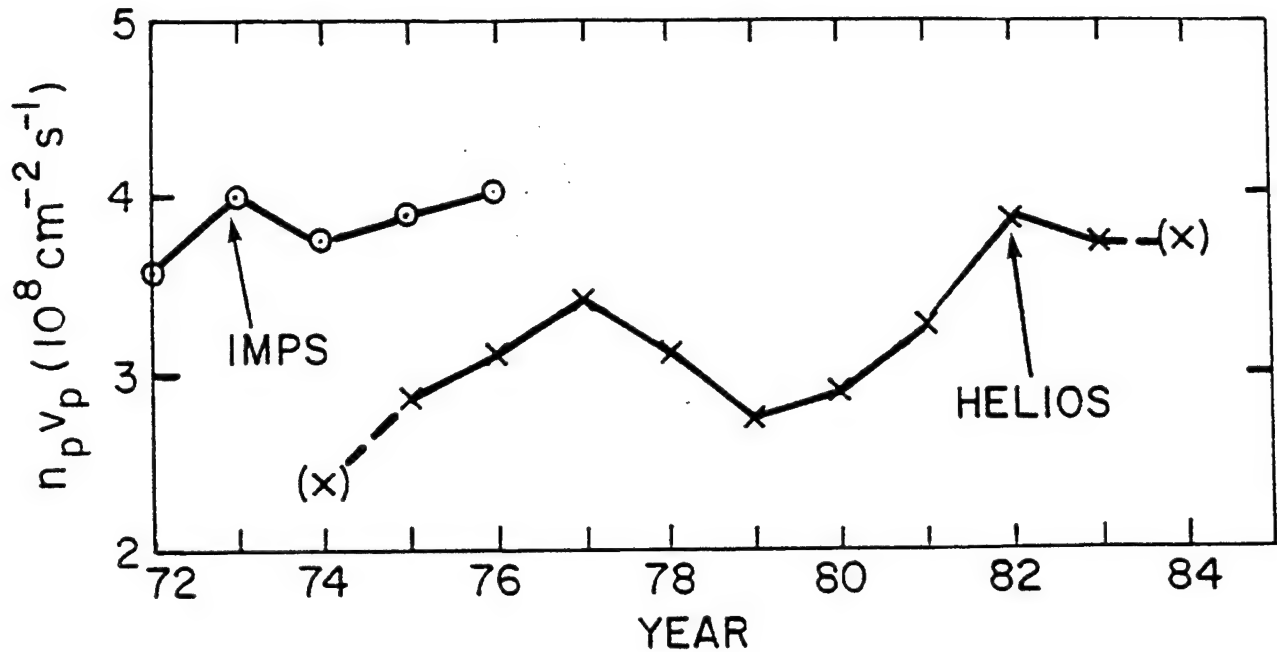


Figure 7. Annual rates of occurrence of the solar wind proton flux from 1972 to 1984. The circled data for 1972 to 1976 are annual means of the 27-day averages of IMP 6, 7, and 8 data from Feldman *et al.* [1978]. The Helios data, denoted by crosses, cover the period 1974 to 1984. These have been normalized to 1 AU for comparison with the IMP data. The 1974 and 1984 averages include only a small amount of data at the end and beginning, respectively, of each of those years. The Helios data were provided courtesy of R. Schwenn of Max-Planck- Institut/Lindau.

cle flux at 1 AU extrapolated into  $4\pi$  sr. However, he did apply a crude visibility correction, assuming a rate of one CME per day. Proper correction for the latitude variation of CMEs during Skylab yields an ecliptic contribution from Skylab CMEs of about 10%. On the basis of the Skylab results and the assumption of a continuing good correlation of CME rate with sunspot number, Hildner *et al.* [1976] and Hildner [1977] predicted a CME contribution of 16% at solar maximum.

From Table 4 we see that our results agree well with Hildner's estimates for Skylab corrected for the CME latitude distribution. Our value during solar maximum in 1980 is slightly less than his prediction, possibly because the CME latitude distribution was much broader at maximum. However, Howard *et al.* [1985] calculated a CME contribution of only 5% for the 1979 to 1981 era using the Solwind data and an average of the IMP data. Our estimates of the contribution due to Solwind CMEs are nearly 3 times greater than Howard *et al.*'s because we have included corrections for the visibility function, have used an improved calculation for the geometrical area into which the CME flux is spread, and have used Helios solar wind particle flux data for the appropriate periods. Recently, Jackson and Howard [1993] calculated that the global Solwind CME mass during 1979 to 1981 was  $\approx 16\%$  of the Helios solar wind mass, based on an exponential integration of the Solwind CME mass curve. The rather close agreement of these independent results at solar maximum is rather remarkable considering that the data came from three different instruments and that the calculations were relatively simplistic.

Our results (Table 4) together with those mentioned above, indicate that the general trend was for the fractional CME contribution to the particle flux to decline between solar maximum in 1979 to 1980 and minimum in 1985 by a factor of about 5. This decline is likely due to a combination of factors, such as the very low ecliptic CME rates and lower average CME masses in 1984 and 1985.

From this section we conclude the following: (1) Although CME occurrence rates are not well correlated with the solar wind particle flux over the solar cycle, the estimated fractional contribution of CMEs to the particle flux does generally track the activity cycle; (2) this variation has an amplitude of about 5; and (3) the estimated contribution of CMEs of about 15% at solar maximum is potentially significant. We emphasize that this is a bulk long-term average value; during specific shorter term periods (days to weeks) the influence of localized CME activity on the interplanetary medium is certainly greater.

## 5. Discussion and Conclusion

### 5.1. Discussion

These results provide new information about CMEs, some of which differs from previous concepts about mass ejections and their relationships to other forms of solar activity. Previous studies concerning the origin or initiation of CMEs have shown better associations between CMEs and certain classes of solar activity than others.

Our results do not support such a differentiation by activity class over the long term.

As one example, since CMEs often do not overlie active regions and are not commonly associated with flares, the phase of their occurrence rate might differ from that of the sunspot cycle. Originally, *Hildner et al.* [1976] found a good correlation between Skylab CME rate and sunspot number. Because of the good latitude correlation with active regions, *Hildner* [1977] predicted that the CME rate at solar maximum would follow the sunspot number and thus be a factor of 3–4 greater than during Skylab. However, *Hundhausen et al.* [1984] and *Sime*, [1986] compared CME rates and latitude and longitude distributions between the HAO coronagraphs on Skylab in 1973–1974 and SMM in 1980 and concluded that contrary to *Hildner's* prediction, there was no simple relation between sunspot number and CME rate. On the other hand, *Howard et al.* [1985, 1986] found that the average annual sunspot number was well correlated with the Solwind CME rate, in agreement with *Hildner*. However, they found a poor correlation with short-term (7 and 27 day) averages of CME rates and sunspot numbers, suggesting that the relation between these parameters is not straightforward.

With the CME data now available and presented herein, it is clear that the average CME rate is well correlated with the sunspot cycle. This in turn suggests that in a very general sense, CME activity, like most other forms of solar activity, is controlled by the emergence and evolution of the global solar magnetic field. However, close examination of other details of this relationship, such as the spatial distributions as a function of time of the different classes of activity [e.g., *Sime*, 1989; *Hundhausen*, 1993] are needed to better understand the causes of CMEs.

We find reasonably consistent results for the CME rates from different coronagraphs, when corrected for visibility functions, during overlapping observation periods. This conclusion differs from that made previously by some researchers who found discrepancies between CME data sets, such as occurrence rates, that, until now, have only included corrections for duty cycles [*Hundhausen et al.*, 1984; *Kahler*, 1987]. For example, for many years the NRL Solwind data had consistently yielded higher duty cycle corrected CME rates than those for SMM [*Hundhausen et al.*, 1984; *Howard et al.*, 1985, 1986]. However, with the completion of the SMM mission, the HAO group has recently revised upward the number of CMEs counted in 1980 and in 1984–1986 [*Burkepile and St. Cyr*, 1993], bringing the SMM and Solwind rates for those years into closer agreement. We believe that our data demonstrate that such discrepancies are mainly instrumental and statistical and do not depend strongly on methodology and selection effects.

We made estimates of the potential contribution over the solar cycle of CMEs to the solar wind mass flux at 1 AU. Since typical CMEs are massive and, at least near solar maximum, relatively frequent, they might contribute significant amounts of mass to the solar wind. With appropriate corrections for instrumental effects and for the latitude variations and mass distributions of

CMEs, we estimated the annual average CME flux into the ecliptic over the solar cycle and compared it with the solar wind particle flux at 1 AU. We found that the fractional contribution of CMEs to the solar wind mass flux tracks the solar cycle and that at solar maximum CMEs can provide a significant average mass flux to the near-ecliptic solar wind. This result is consistent with our recent improved understanding of the importance of CMEs to such transient heliospheric phenomena as geomagnetic storms, IP shocks, energetic proton acceleration and transport, and cosmic ray modulation.

In this study we have attempted to determine realistic global CME rates and mass fluxes using the most reliable data and analytical results presently available. However, we note that the mass flux estimates, in particular, are dependent on certain CME parameters which are as yet not well determined. These include the true mass distribution of CMEs and how it varies over the long term and the shape and overall geometry of CMEs. Retrospective analyses of existing data sets could enhance our understanding of the mass distribution and geometry of CMEs. Some related projects which are underway include the following: Improved calibrations of the SMM coronagraph are being made which will permit the determination of relative masses and energies for many of the SMM CMEs (*A. Hundhausen*, private communication, 1992), leading to an estimate of that coronagraph's mass sensitivity function. The Helios photometer data are being used to determine the global mass distribution and energies of CMEs in the inner heliosphere [*Webb and Jackson*, 1993]. Although having crude spatial resolution, the Helios data are well suited for determining the total mass flow and overall geometry of CMEs. Finally, because of its excellent photometric quality, we believe it would be very worthwhile to measure the masses of all of the Skylab CMEs so as to determine their mass distribution and the Skylab coronagraph's sensitivity function.

In the near future, improved observations of CMEs should be available from the Solar and Heliospheric Observatory spacecraft, and may be possible from several proposed ground-based and Earth-orbiting instruments, such as the Solar Mass Ejection Imager.

## 5.2. Summary

A summary of the main results of this study is as follows:

1. The frequency of occurrence of CMEs tends to track the solar activity cycle in both amplitude and phase.
2. The CME rates determined from data from different instruments, when corrected for both duty cycles and visibility functions, are reasonably consistent.
3. Considering longer-term averages, no one class of solar activity is better correlated with CME rate than any other.
4. The fractional contribution of the annualized CME to solar wind mass flux tends to track the solar cycle.
5. Near solar maximum, CMEs can provide a significant average mass flux (i.e.,  $\approx 15\%$ ) to the near-ecliptic solar wind.

**Acknowledgments.** We thank the following researchers who have contributed data for this study: A. Hundhausen and J. Burkepile of NCAR High Altitude Observatory, J. Joselyn of NOAA Space Environment Laboratory, H. Coffey and J. McKinnon of WDC-A, Boulder, C. St. Cyr of ATSC NASA GSFC, S. Kahler of the Air Force Phillips Lab/GPS, and R. Schwenn of the Max Planck Institut/Lindau. We are grateful to S. Kahler and E. Cliver of the Air Force Phillips Lab/GPS, N. Sheeley of the Naval Research Laboratory, and B. Jackson of UCSD for helpful comments. D. Webb acknowledges support for this study from HAO NCAR where he was a visiting scientist in 1985. NCAR is sponsored by the National Science Foundation. Work by D. Webb was also supported by NASA contract NAS5-28727 and by the AF Phillips Lab/GPS under contracts AF19628-87-K-0033 and AF19628-90-K-0006.

The editor thanks H. V. Cane and J. A. Joselyn for their assistance in evaluating this paper.

## References

- Anser, U., and A.I. Poland, Mass flow in loop-type coronal transients, *Sol. Phys.*, **61**, 95, 1979.
- Burkepile, J.T., and O.C. St. Cyr, A revised and expanded catalog of mass ejections observed by the Solar Maximum Mission coronagraph, *NCAR/TN-369+STR*, Natl. Center for Atmospheric Research, Boulder, Jan. 1993.
- Borrini, G., J.T. Gosling, S.J. Bame, and W.C. Feldman, An analysis of shock wave disturbances observed at 1 AU from 1971 through 1978, *J. Geophys. Res.*, **87**, 4365, 1982.
- Cane, H.V., The evolution of interplanetary shocks, *J. Geophys. Res.*, **90**, 191, 1985.
- Cane, H.V., The large-scale structure of flare-associated interplanetary shocks, *J. Geophys. Res.*, **93**, 1, 1988.
- Cane, H.V., N.R. Sheeley, Jr. and R.A. Howard, Energetic interplanetary shocks, radio emission and coronal mass ejections, *J. Geophys. Res.*, **92**, 9869, 1987.
- Dodge, J.C., *Rep. SN-5*, Radio Astron. Obs. of the Univ. of Colo., Boulder, 1974.
- Feldman, W.C., J.R. Asbridge, S.J. Bame, and J.T. Gosling, Plasma and magnetic fields from the Sun, in *The Solar Output and Its Variation*, p. 351, Colorado Associated University Press, Boulder, 1977.
- Feldman, W.C., J.R. Asbridge, S.J. Bame, and J.T. Gosling, Long-term variations of selected solar wind properties: IMP 6, 7, and 8 results, *J. Geophys. Res.*, **83**, 2177, 1978.
- Gosling, J.T., E. Hildner, R.M. MacQueen, R.H. Munro, A.I. Poland, and C.L. Ross, The speeds of coronal mass ejection events, *Sol. Phys.*, **48**, 389, 1976.
- Harrison, R.A., Coronal mass ejection, *Philos. Trans. R. Soc. London, Ser. A*, **336**, 401, 1991.
- Hildner, E., Mass ejections from the corona into interplanetary space, in *Study of Travelling Interplanetary Phenomena*, edited by M.A. Shea et al., p. 3, D. Reidel, Dordrecht, Holland, 1977.
- Hildner, E., J.T. Gosling, R.M. MacQueen, R.H. Munro, A.I. Poland, and C.L. Ross, Frequency of coronal transients and solar activity, *Sol. Phys.*, **48**, 127, 1976.
- Howard, R.A., D.J. Michels, N.R. Sheeley, Jr. and M.J. Koomen, The observation of a coronal transient directed at earth, *Astrophys. J.*, **203**, L101, 1982.
- Howard, R.A., N.R. Sheeley, Jr., M.J. Koomen, and D.J. Michels, Coronal mass ejections: 1979-1981, *J. Geophys. Res.*, **90**, 8173, 1985.
- Howard, R.A., N.R. Sheeley, Jr., D.J. Michels, and M.J. Koomen, The solar cycle dependence of coronal mass ejections, in *The Sun and the Heliosphere in Three Dimensions*, edited by R.G. Marsden, p. 107, D. Reidel, Dordrecht, Holland, 1986.
- Hundhausen, A.J., The origin and propagation of coronal mass ejections, in *Proceedings of the Sixth International Solar Wind Conference*, edited by V.J. Pizzo, T.E. Holzer, and D.G. Sime, *NCAR/TN-306+Proc*, p. 181, Natl. Center for Atmospheric Research, Boulder, 1988.
- Hundhausen, A.J., Sizes and locations of coronal mass ejections: SMM observations from 1980 and 1984-1989, *J. Geophys. Res.*, **98**, 13,177, 1993.
- Hundhausen, A.J., C. Sawyer, L. House, R.M.E. Illing, and W.J. Wagner, Coronal mass ejections observed during the Solar Maximum Mission: Latitude distribution and rate of occurrence, *J. Geophys. Res.*, **89**, 2639, 1984.
- Illing, R.M.E., and A.J. Hundhausen, Observation of a coronal transient from 1.2 to 6 solar radii, *J. Geophys. Res.*, **90**, 275, 1985.
- Illing, R.M.E., and A.J. Hundhausen, Disruption of a coronal streamer by an eruptive prominence and coronal mass ejection, *J. Geophys. Res.*, **91**, 10,951, 1986.
- Jackson, B.V., Imaging of coronal mass ejections by the Helios spacecraft, *Sol. Phys.*, **100**, 563, 1985a.
- Jackson, B.V., Helios observations of the earthward-directed mass ejection of 22 November 1979, *Sol. Phys.*, **95**, 363, 1985b.
- Jackson, B.V., Solar-generated disturbances in the heliosphere, in *Solar Wind Seven*, edited by E. Marsch and R. Schwenn, p. 623, Pergamon, New York, 1992.
- Jackson, B.V., and E. Hildner, Forerunners: Outer rims of solar coronal transients, *Sol. Phys.*, **60**, 155, 1978.
- Jackson, B.V., and R.A. Howard, A CME mass distribution derived from Solwind coronagraph observations, *Sol. Phys.*, **148**, 359, 1993.
- Jackson, B.V., and C. Leinert, Helios images of solar mass ejections, *J. Geophys. Res.*, **90**, 10,759, 1985.
- Jackson, B.V., R.A. Howard, N.R. Sheeley, Jr., D.J. Michels, M.J. Koomen, and R.M.E. Illing, Helios spacecraft and Earth perspective observations of three looplike solar mass ejection transients, *J. Geophys. Res.*, **90**, 5075, 1985.
- Kahler, S., The morphological and statistical properties of solar X-ray events with long decay times, *Astrophys. J.*, **214**, 891, 1977.
- Kahler, S., Coronal mass ejections, *Rev. Geophys.*, **25**, 663, 1987.
- Kahler, S.W., Solar flares and coronal mass ejections, *Annu. Rev. Astron. Astrophys.*, **30**, 113, 1992.
- Kahler, S., and E.W. Cliver, Solar cycle variation of long duration 10.7 cm and soft X-ray bursts, *Sol. Phys.*, **115**, 385, 1988.
- Kahler, S., N.R. Sheeley, Jr., R.A. Howard, M.J. Koomen, and D.J. Michels, Characteristics of flares producing metric type II bursts and coronal mass ejections, *Sol. Phys.*, **93**, 133, 1984.
- Karpen, J.T., and R.A. Howard, A search for forerunner activity associated with coronal mass ejections, *J. Geophys. Res.*, **92**, 7227, 1987.
- Klein, L., and L. Burlaga, Interplanetary magnetic clouds at 1 AU, *J. Geophys. Res.*, **87**, 613, 1982.
- Krivsky, L., and B. Lukac, Catalog of solar type II bursts and their source flares for cycle no. 20 (1966-1976), *Astron. Obs.*, Hurbanovo, Czech Republic, 1980.
- MacQueen, R.M., and O.C. St. Cyr, Sungrazing comets observed by the Solar Maximum Mission coronagraph, *Icarus*, **90**, 96, 1991.
- MacQueen, R.M., A.J. Hundhausen, and C.W. Conover, The propagation of coronal mass ejection transients, *J. Geophys. Res.*, **91**, 31, 1986.
- McCabe, M.K., Z.F. Svestka, R.A. Howard, B.V. Jackson, and N.R. Sheeley, Jr., Coronal mass ejection associated

- with the stationary post-flare arch of 21–22 May 1980, *Sol. Phys.*, **103**, 399, 1986.
- Munro, R.H., J.T. Gosling, E. Hildner, R.M. MacQueen, A.I. Poland, and C.L. Ross, The association of coronal mass ejection transients with other forms of solar activity, *Sol. Phys.*, **61**, 201, 1979.
- Rust, D.M. and E. Hildner et al., Mass ejections, in *Solar Flares*, edited by P.A. Sturrock, p. 273, Colorado Associated University Press, Boulder, 1980.
- Sawyer, C., Visibility and rate of coronal mass ejections, *Sol. Phys.*, **98**, 369, 1985.
- Schwenn, R., The "average" solar wind in the inner heliosphere: Structure and slow variations, in *Solar Wind Five*, *NASA Conf. Publ.-2280*, 489, 1983.
- Sheeley, N.R., Jr., R.A. Howard, M.J. Koomen, and D.J. Michels, Associations between coronal mass ejections and soft X-ray events, *Astrophys. J.*, **272**, 349, 1983.
- Sheeley, N.R., Jr., R.T. Stewart, R.D. Robinson, R.A. Howard, M.J. Koomen, and D.J. Michels, Associations between coronal mass ejections and metric type II bursts, *Astrophys. J.*, **279**, 839, 1984.
- Sheeley, N.R., Jr., R.A., Howard, M.J., Koomen, R. Schwenn, K.H. Muhlauser, and H. Rosenbauer, Coronal mass ejections and interplanetary shocks, *J. Geophys. Res.*, **90**, 163, 1985.
- Sime, D.G., Coronal transients at high heliographic latitudes, in *The Sun and the Heliosphere in Three Dimensions*, edited by R.G. Marsden, p. 101, D. Reidel, Dordrecht, Holland, 1986.
- Sime, D.G., Coronal mass ejection rate and the evolution of the large-scale K-coronal density distribution, *J. Geophys. Res.*, **94**, 151, 1989.
- Smith, E.J., Observations of interplanetary shocks: Recent progress, *Space Sci. Rev.*, **34**, 101, 1983.
- Stewart, R.T., M.K. McCabe, M.J. Koomen, R.T. Hansen, and G.A. Dulk, Observations of coronal disturbances from 1 to 9 Ro, *Sol. Phys.*, **36**, 203, 1974.
- Watanabe, T., and T. Kakinuma, Radio scintillation observations of interplanetary disturbances, *Adv. Space Res.*, **4**(7), 331, 1984.
- Webb, D.F., The origin and kinematics of coronal mass ejections, in *Solar-Terrestrial Physics: Proceedings of Second Indo-US Workshop on Solar-Terrestrial Physics*, edited by M.R. Kundu et al., p. 283, National Physical Laboratory, New Delhi, India, 1986.
- Webb, D.F., Erupting prominences and the geometry of coronal mass ejections, *J. Geophys. Res.*, **93**, 1749, 1988.
- Webb, D.F., The solar cycle variation of the rates of CMEs and related activity, *Adv. Space Res.*, **11**(1), 37, 1991.
- Webb, D.F., The solar sources of coronal mass ejections, in *Eruptive Solar Flares*, edited by Z. Svestka, B. Jackson and M. Machado, p. 234, Springer-Verlag, New York, 1992.
- Webb, D.F., and E.W. Cliver, Are all metric type II bursts piston driven by CMEs?, *Bull. Am. Astron. Soc.*, **20**, 745, 1988.
- Webb, D.F., and A.J. Hundhausen, Activity associated with the solar origin of coronal mass ejections, *Sol. Phys.*, **108**, 383, 1987.
- Webb, D.F., and B.V. Jackson, The identification and characteristics of solar mass ejections observed in the heliosphere by the Helios-2 photometers, *J. Geophys. Res.*, **95**, 20641, 1990.
- Webb, D.F., and B.V. Jackson, Characteristics of CMEs observed in the heliosphere using Helios photometer and in-situ data, in *Solar-Terrestrial Predictions - IV*, edited by J. Hruska et al., Vol. 2, pp. 381–388, Natl. Oceanic and Atmospheric Administration, Boulder, 1993.
- Wright, C.S., On the longitudinal distribution of solar type II bursts, *Proc. Astron. Soc. Aust.*, **4**, 59, 1980.
- Wright, C.S., Catalogue of solar filament disappearances, 1964–1980, *Rep. UAG 100*, World Data Cent. A, WDC-A, Natl. Geophys. Data Cent., Boulder, 1991.
- D. F. Webb, Phillips Laboratory/GPSG, 29 Randolph Road, Hanscom AFB, MA 01731-3010. (e-mail: webb@plh.af.mil)
- R. A. Howard, Naval Research Laboratory, Code 7666, Washington, D.C. 20375.

(Received April 4, 1993; revised September 1, 1993; accepted September 21, 1993.)

## Coronal mass ejections: The key to major interplanetary and geomagnetic disturbances

David F. Webb<sup>1</sup>

Institute for Space Research, Boston College, Newton Center, MA

The U.S. Government is authorized to reproduce and sell this report. Permission for further reproduction by others must be obtained from the copyright owner.

### Introduction

For years it was thought that solar flares were responsible for major interplanetary (IP) particle events and geomagnetic storms. However, recently we have seen an important paradigm shift such that now coronal mass ejections (CMEs), not flares, are considered the key causal link with solar activity. CMEs are vast structures of plasma and magnetic fields that are expelled from the sun into the heliosphere. We now know that CMEs drive all large geomagnetic storms and their attendant effects, such as auroral displays. Fast CMEs produce transient IP shocks which cause sudden commencements at Earth. The CME-related shocks also accelerate the solar energetic particle (SEP) events associated with major IP disturbances and with radiation hazards at Earth. This new paradigm has important implications for prioritizing the development of instruments and techniques to predict IP disturbances and geomagnetic activity.

CMEs are best viewed in white light from space-borne coronagraphs; these reveal that, even near the sun, the CME can dwarf the solar disk [see Figure 1]. The onset of CMEs can be associated with both flares and filament eruptions [e.g., Webb, 1992; Feynman and Hundhausen, 1994]. However, most of the energy is associated with the ejected mass and shock wave, not the flare, even in the most energetic cases. Many CMEs cannot be associated with any surface activity. Most flares occur independently of CMEs and even those accompanying CMEs are now considered a secondary consequence rather than a cause of CMEs [Kahler, 1992; Gosling, 1993]. Indeed, the basic physics of the two phenomena may be quite different.

The following sections review the evidence supporting the new paradigm in terms of the development and evolution of CMEs near the sun, the signatures of their passage through the interplanetary medium, and how and why CMEs are geoeffective. (Geoeffective means that an agent can significantly perturb Earth's environment.) Finally, we discuss implications of this paradigm for forecasting IP disturbances and geomagnetic activity.

This is not meant as a comprehensive review but rather a portrayal of recent work in the light of this new concept. For further details about CMEs see the following review papers by U.S. authors: Steinolfson [1991; 1992b], Kahler [1992], Webb [1992; 1993], Gosling [1993], Low [1993], Dryer [1994] and Hundhausen [1995].

### CMEs Near the Sun

Significant new results on white light CMEs derived from analyses of images from the Solar Maximum Mission (SMM) orbiting coronagraph, the Mauna Loa Solar Observatory (MLSO) K-coronameter, and the zodiacal light photometers on the Helios spacecraft have been published. These results add to earlier studies of data from the coronagraphs on Skylab and on the P78-1 spacecraft (called SOLWIND). It is now clear that there is a large range in the basic properties of CMEs. Their speeds, accelerations, masses and energies range over 2-3 orders of magnitude. The masses and kinetic energies of SOLWIND CMEs extend from  $10^{11}$  to  $5 \times 10^{13}$  kg and  $10^{22}$  to  $6 \times 10^{24}$  J, respectively [Howard et al., 1985], and some SMM CMEs exceed these values [Hundhausen, 1994]. CME occurrence rates vary by an order of magnitude over the solar cycle [Webb and Howard, 1994]. CME widths range from 10 to  $\approx 120^\circ$ , exceeding by factors of 3-10 the sizes of flares and active regions.

In white light images CMEs often appear to have a bright leading looplike structure followed by a dark cavity and a bright core of denser material, suggesting the eruption of a preexisting prominence, its overlying coronal cavity, and the ambient corona. However, the frequency of occurrence of these structures differs from one coronagraph to another; for example, the fraction of looplike CMEs ranged from 1% of SOLWIND CMEs to nearly half of the SMM CMEs. Two-thirds of the SMM CMEs also contained bright cores. It is not obvious that these differences can be explained merely by solar cycle effects. The leading CME structures are likely the sky-plane projections of three-dimensional structures such as arcades [Steinolfson, 1992a] or shells [Hundhausen, 1994].

From what kind of structures do CMEs emanate? Recent studies confirm that CMEs arise from large-scale, closed structures, most of which ( $\approx 75\%$ ) are preexisting coronal streamers [Hundhausen, 1993; Webb et al., 1994]. This is not consistent with the suggestion of Hewish and coworkers [e.g., Hewish and Bravo, 1986] that CMEs arise in open field regions (coronal holes)

<sup>1</sup> Also at Geophysics Directorate, Phillips Laboratory/GPSG, Hanscom AFB, Massachusetts.



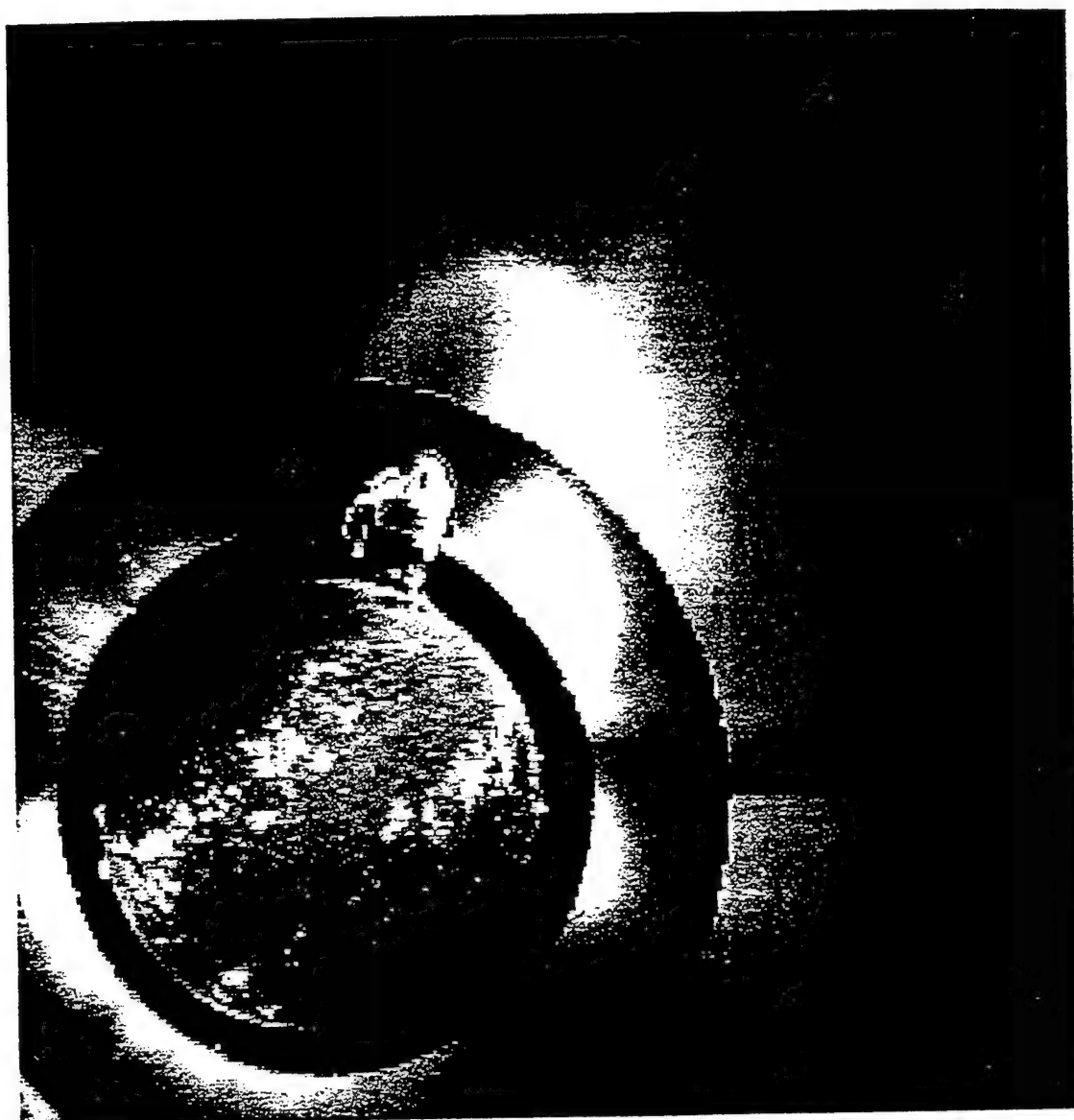


Figure 1. A CME and prominence eruption on October 5, 1989. Superposition of SMM coronagraph images of outer corona, MLSO images of inner corona in white light, and of photosphere, chromosphere and corona in hydrogen  $\alpha$  emission. [A. Hundhausen, *Coronal Diagnostics*; notes from lectures at Intl. School of Space Science, L'Aquila, Italy, 1993].

[Harrison, 1990; Hundhausen, 1993]. The temporal and latitudinal distributions of CMEs are similar to those of streamers and prominences, being confined to low latitudes about the current sheet near cycle minimum and becoming distributed over all latitudes near maximum [Hundhausen, 1993]. This evolution is very different from that of active regions, flares or sunspots. Many energetic CMEs are actually the disruption of a preexisting streamer, which increases in brightness and size for days before erupting as a CME. Afterwards the streamer and CME are gone giving the appearance of a "bugle" on white light synoptic maps [Hundhausen, 1993]. Often a thin ray appears in the location of the streamer, and may be a current sheet rising from a newly reformed streamer. Feynman and Martin [1995] find that major erupting filaments are strongly associ-

ated with emerging magnetic flux oriented so as to favor reconnection of field lines. Since filament eruptions are associated with CMEs and streamers, this suggests that streamers can be destabilized by emerging flux. SMM CMEs have also been found to be associated with large-scale evolving patterns of existing surface flux, delineated by polarity inversion lines [Webb *et al.*, 1994].

What are the kinematical properties of CMEs? The speeds of the leading loops of SMM CMEs ranged from 20 to 1100 km/s [Hundhausen *et al.*, 1994]. The average speeds of SOLWIND CMEs were much higher near solar maximum than minimum [Howard *et al.*, 1986], but SMM CME speeds were not solar-cycle dependent. Significant progress has been made in simulating the coronal response to the passage of a CME [reviewed by Steinolfson, 1992b and Hundhausen, 1994]. Fast



magnetohydrodynamic shocks apparently driven by fast CMEs are the most common type in the inner heliosphere. However, in the lower corona the speeds of typical CME outer loops are higher than the sound speed but less than the Alfvén speed (for SMM averaging 445 km/s) and the trajectories are consistent with constant speed. Numerical simulations of the disruption of model streamers indicates that slow, intermediate and fast mode shocks should form ahead of CMEs with speeds of 200–300, 300–900, and  $\geq 900$  km/s, respectively. Thus, slow and intermediate mode shocks might be associated with most CMEs, and some CMEs do exhibit the predicted flattened fronts. The existence of fast mode shocks in the corona is strongly supported by the observation of rapidly drifting radio bursts and their association with fast ( $\geq 400$  km/s) CMEs [e.g., *Kahler*, 1992]. However, it is unclear whether they compress sufficient material to be detected optically as bow waves in front of CMEs.

In previous years much theoretical work on CMEs was focussed on reconnection of the magnetic fields which close after the CME has erupted. The recent models of this process describe the late phase reasonably well [cf., *Svestka and Cliver*, 1992; *Webb et al.*, 1994]. In such models field lines stretched open during the eruption of a prominence and CME reconnect near the surface to form a magnetic loop system, the long-duration/ two-ribbon flare. New observational results generally support this concept. *Kahler and Hundhausen* [1992] found that the bright structures following many SMM CMEs are streamers probably newly-formed by reconnection. Observations from the Japanese Yohkoh spacecraft and from MLSO of the reformation of a giant helmet streamer also provide strong evidence of reconnection following CMEs [*Hiei et al.*, 1993]. Another Yohkoh observation suggests rapid reconnection following the ejection of a plasmoid associated with a two-ribbon flare [see *Webb et al.*, 1994]. This observed structure was found to be in excellent agreement with field lines derived from a circuit model, lending further support for the two-ribbon flare scenario.

Most of the models intended to describe the origin and propulsion of CMEs are not sufficiently developed to compare with observations. Most such models involve force-free equilibria which cannot realistically describe the complex evolution of the pressure, magnetic and gravitational forces acting on a magnetically closed coronal structure [e.g., *Hundhausen*, 1994]. The class of models which require a thermal or pressure pulse (i.e., flare) as driver no longer seem viable [cf., *Dryer*, 1994; *Webb et al.*, 1994]. For instance, such models are not consistent with CMEs which exhibit significant accelerations over large distances. Recently there has been intensive work on the origin of CMEs based on the slow evolution of particular coronal structures through metastable states or sequences of stable equilibria until the stability or equilibrium breaks down, resulting in the mass ejection and opening of the field. *Steinolfson* [1991], *Low* [1993] and *Dryer* [1994] review such analytic models and numerical simulations. Causes of the evolution of these coronal structures, especially streamer

configurations, include the emergence of magnetic flux [*Steinolfson*, 1992a], the dynamical evolution of arcades [*Steinolfson*, 1991; *Mikic and Linker*, 1994], and the shear of field lines across inversion lines [*Steinolfson*, 1991; *Wolfson and Low*, 1992; *Mikic and Linker*, 1994]. However, no strong consensus has yet emerged.

## CMEs in the Heliosphere

CMEs carry large amounts of plasma and magnetic fields into the heliosphere. This material is detected by remote sensing and in-situ spacecraft observations. Remote sensing of CME plasma has been primarily with the Helios 1 and 2 white light photometers and by measurements of IP scintillation of galactic radio sources from the ground [e.g., *Hewish and Bravo*, 1986]. The Helios photometers were analogous to heliospheric coronagraphs and viewed  $\approx 200$  CMEs over a period of 9 years [*Jackson et al.*, 1994]. The occurrence rates, spans and speeds of these CMEs are consistent with measurements made by coronagraphs near the sun [*Webb and Howard*, 1994]. The appearance of the expanding CMEs is also similar, often with two brighter "legs" behind a tenuous leading front. However, derived masses tend to be higher than those determined by coronagraphs [*Jackson and Webb*, 1995]. The IP scintillation technique detects transient disturbances as enhanced scintillation along the line of sight to a distant steady source. However, there are problems with the accuracy and reliability of this technique for detecting CME plasma.

A variety of in-situ signatures have been proposed as proxies for the passage of CME ejecta past spacecraft. These include shocks, density changes, decreased temperatures, flows with enhanced helium abundances [He(A)], and magnetic field structures consistent with looplike topologies [cf., *Gosling*, 1993; *Webb*, 1993]. Recent efforts have focussed on signatures considered to be indicative of the topology of the ejected magnetic fields [see *McComas*, 1995]. Most such studies involve observations and modeling of magnetic clouds and bidirectionally streaming particle flows. Magnetic clouds are long-lived solar wind flows having enhanced field strengths which exhibit smooth, coherent rotations [*Burlaga* 1991].

*Wilson and Hildner* [1986], *Bothmer and Schwenn* [1994], *Rust* [1994] and others have associated some magnetic clouds with solar filament disappearances. Solar filaments consist of dense plasma embedded in helical, horizontal magnetic fields. The close association of CMEs with filament eruptions and shearing fields near the surface has led to the modeling of CMEs as flux ropes. *Gosling*, [1993] describes a process wherein the interior fields of a rising, sheared CME reconnect, resulting in an ejected flux rope and new, closed coronal loops. He suggests that  $\approx \frac{1}{3}$  of all bidirectional electron events and magnetic clouds, i.e., CMEs, in the heliosphere have the characteristics of flux ropes. *Bothmer and Schwenn* [1994] found in 4 of 5 cases that Helios magnetic flux ropes (clouds) had the same orientation and polarity as associated erupting filaments at the sun.

Furthermore S. Martin [1994, private communication] finds that high latitude filaments always have twist in the same sense in a given hemisphere, regardless of the cycle number. These results suggest that the sign of the helicity of the erupted fields can be predicted assuming one can associate a given flux rope with a high-latitude filament eruption. Rust [1994] did so for a list of magnetic clouds modeled as force-free structures at 1 AU and claimed good agreement. Thus, filament eruptions and CMEs may be important ways that the sun sheds helicity or twist.

Bidirectional flows of electrons have been interpreted as evidence that the associated transient field lines are entirely or partially closed and, thus, are a good proxy for CMEs [e.g., Gosling, 1993]. Bidirectional proton flows have also been detected in the solar wind, often but not always in association with shocks and ejecta flows [e.g., Richardson and Reames, 1993]. Although magnetic clouds and bidirectional flows are usually considered proxies for closed structures and CMEs, the observational evidence is not sufficient to differentiate between the partially closed (flux rope), entirely closed (bottle or plasmoid), or even entirely open field configurations [e.g., Kahler and Reames, 1991; Suess, 1993].

Recently, a number of bidirectional events were observed as Ulysses moved to higher southern heliographic latitudes [Gosling *et al.*, 1994]. The speeds of these events (740 km/s on average) are much higher than those observed in the ecliptic plane and comparable to the high speed of the surrounding solar wind flow. This suggests that CMEs in general are affected by the same forces as the surrounding solar wind. Since the typical speeds of CMEs observed in the field of view of coronagraphs ( $\leq 10$  solar radii) is  $\sim 400$  km/s, much of this acceleration must occur beyond this point.

Solar energetic particle (SEP) events are commonly associated with IP shocks and can arrive at Earth within minutes following onset of a flare [see Reames, 1995]. They are of concern because of their deleterious effects on communications systems, satellites, astronauts and high flying aircraft. In the new paradigm, CMEs are important to the production of the SEP particles because the bulk of the particles are not accelerated at the low flare site or during its impulsive phase, but relatively high in the corona and for prolonged periods of time by the shock driven ahead of the CME. The key supporting observational results are: large, prompt SEP events are nearly always associated with fast CMEs, they are not well correlated with the amplitude of a flare's impulsive phase, their abundances and ionization states are typical of ambient coronal rather than flare-heated plasma, and isolated erupting filaments can also produce SEPs [e.g., Kahler, 1992].

As mentioned earlier, CMEs tend to arise in coronal streamers which form a belt that encircles the sun and is the base of the heliospheric current sheet (HCS). The HCS is the separatrix between the oppositely-directed fields on either side of the streamer belt and, in projection, is the heliomagnetic equator of the sun. A new model by Crooker *et al.* [1993] suggests that the base

of the HCS may often be broad, encompassing multiple helmet streamers tens of degrees across with associated multiple current sheets. Most CMEs might then be spatially associated with the HCS. In this view the HCS is more dynamic than previously thought, and acts as a conduit for a range of activity from slowly evolving streamers to large CMEs. This activity also acts to compress, amplify and align preexisting magnetic discontinuities in the HCS and at the leading edge of high speed streams [Neugebauer *et al.*, 1993]. These factors enhance the geoeffectiveness of CMEs as discussed next.

## The Geoeffectiveness of CMES

The geomagnetic indices used to quantify the magnitude of geomagnetic storms are highly correlated with solar wind speed and the strength of the southward component ( $B_s$ ) of the IP magnetic field. These parameters are in general enhanced during the passage of IP CMEs. We next summarize the studies that demonstrate the new paradigm linking CMEs with IP and geomagnetic disturbances [e.g., Kahler, 1992; Gosling, 1993].

Geomagnetic storms are often preceded by abrupt increases in the northward component of the earth's field, called sudden commencements, which are well correlated with IP shocks. Since these shocks are driven by fast CMEs, we infer that it is the CME that causes the sudden commencement storms. Gosling *et al.* [1991] demonstrated this statistically using bidirectional events observed by the International Sun-Earth Explorer-3 (ISEE-3) spacecraft as proxies for CMEs. They found that all but one of the largest storms from 1978–1982 was associated with the passage of bidirectional electron events and/or shocks. Such storms are most geoeffective when both a fast CME and its shock pass over the earth; in this case the disturbance is encountered head-on where the flow parameters are maximized. However, Gosling *et al.* note that the association between the bidirectional events and storms is much reduced for the more frequent smaller storms. In a related study Zhao *et al.* [1993] identified all ISEE-3 periods which had strong  $B_s$  fields  $\geq 10^{-9}$  T for durations  $\geq 3$  hr, and found that 78% of these periods were associated with one or more CME proxies.

Compression and draping of magnetic field lines in the leading edge of the CME and of the ambient IP field are prime causes of strong southward fields [e.g., Tsurutani *et al.*, 1992; Gosling, 1993]. Draping alone can enhance  $B_s$  over the ecliptic field components. If, in addition, the strong field in the leading edge of the CME is southward, a severe storm at the earth can ensue. Crooker *et al.* [1992] emphasize that the semiannual effect, caused by the periodic interaction between the earth's dipole and IP magnetic fields, will also enhance  $B_s$  fields due to compression and draping of the shock sheath fields in the ecliptic.

Good associations have been found between storms and other IP proxies of CMEs [cf., Webb, 1993]. Strong correlations were found between geomagnetic distur-

bances and large, sustained values of  $B_s$  in magnetic clouds at 1 AU. Compound streams, which are formed by faster streams overtaking slower ones, often involve magnetic clouds and can be associated with storms. Burlaga *et al.* [1987] found that more than half of the 17 largest storms were associated with a compound stream or magnetic cloud or both.

He(A) events, considered a good CME proxy, observed by the Interplanetary Monitoring Platform (IMP) spacecraft were well correlated with geomagnetic storms [Borrini *et al.*, 1982]. Since the main phase storm intensity was much greater for shocks with He(A) than for shocks without He(A), we again infer that it is CMEs that influence storm development. Finally, isolated filament disappearances are associated with sudden commencements and storms [Joselyn and McIntosh, 1981; Wright, 1990]. Wright [1990] compared IP disturbances associated with disappearing filaments with geomagnetic parameters, and found that filament-related disturbances led to significant increases in sudden commencements, geomagnetic indices, and occurrences of large  $B_s$ , with delays from onset of 2.5–5 days.

### Implications of the New Paradigm

The old concept that solar flares and, more recently, isolated filament eruptions cause major transient interplanetary disturbances and geomagnetic storms is being challenged. Many researchers embrace a new paradigm that the CME, a subset of which are associated with both flares and filament eruptions, is the crucial link between solar activity and transient disturbances at Earth. Much of this misconception arose because CMEs are eruptions of coronal, not lower atmospheric material. To earlier researchers the corona was mostly invisible, whereas flare effects in the lower solar atmosphere were easily viewed in the optical regime. The development of spaceborne imaging instruments allowed us to study the corona and eventually correct our understanding of solar-terrestrial linkages. The concept that CMEs are the key geoeffective solar phenomenon has important implications for prioritizing the development of instruments and techniques for the observation of signatures at the sun and in the vicinity of the earth used to predict transient IP disturbances and geomagnetic storms.

CMEs arise in large-scale structures lying near the base of the solar corona. Most of the ejected material originally consisted of hot, highly ionized gas imbedded in closed loop structures. Most CMEs are associated with coronal streamers, many of which are in the streamer belt that is the base of the HCS. Thus, CMEs may be an integral part of dynamical phenomena occurring in the HCS. Two important implications of this are that the transient disturbances related to CMEs will tend to occur more frequently near sector boundary crossings, and that the stronger recurrent storms, usually thought to be caused by high speed streams between sector crossings, may actually be associated with compression of CME flows in stream interaction regions

near the boundaries [Crooker and Cliver, 1994]. Therefore, determining the time of sector boundary crossings at the earth, based on the location and degree of activity in the streamer belt at the sun, should improve storm forecasts.

The largest storms are caused by fast CMEs and strong shocks which often have associated energetic flares at the sun, but most storms are of moderate to small size. The disturbances that cause these storms have few clear observables at the sun, partly because we don't directly observe against the disk the coronal plasma and magnetic fields participating in the CME. In the optical regime disappearing filaments should be the best predictor of CMEs, but they are not well observed or routinely reported. In general, predictions should be based not on the occurrence of a large flare, but whether the observed activity is indicative of a CME.

Therefore, high priority should be given to the development of instrumentation to detect the onset of CMEs at the sun and their propagation through the corona and the heliosphere. Some older techniques have proven vital to our present understanding of coronal and IP mass ejecta, and should be considered in future planning. These include X-ray imagers, white light coronagraphs and metric radio telescopes for observations near the sun. Near-Earth coronagraphs, of course, best observe material above the solar limb and not CMEs directed at the earth. Observations of ejecta in the IP medium and the vicinity of the earth have been made by heliospheric white light imagers, detectors observing IP radio scintillation, kilometric radio telescopes and spacecraft instruments measuring the in-situ solar wind.

In addition to careful application of these known technologies, we need to develop new methods to study CMEs and forecast their arrival at Earth. Some promising missions involve directly imaging dense plasma within the inner heliosphere. These include white light imagers placed in Earth orbit, one or more coronagraphs placed at the Lagrangian points at  $60^\circ$  or at about  $90^\circ$  leading or trailing the earth in its orbit, and instruments designed to image IP shock waves. These methods are intended to provide 1-3 days advance warning of a disturbance headed toward the earth.

**Acknowledgments.** I thank E. Cliver of AF Phillips Laboratory/GPS for useful discussions, and G. Siscoe and the referees for helpful comments on the manuscript. The work of DFW was supported at Boston College by the Geophysics Directorate of Phillips Lab under contract AF19628-90-K-0006.

### References

- Borrini, G., J. T. Gosling, S. J. Bame, and W. C. Feldman, Helium abundance enhancements in the solar wind, *J. Geophys. Res.*, **87**, 7370, 1982.
- Bothmer, V. and R. Schwenn, Eruptive prominences as sources of magnetic clouds in the solar wind, in *Mass Supply and Flows in the Solar Corona*, edited by B. Fleck, G. Noci and G. Poletto, p. 215, Kluwer, Norwell, MA, 1994.
- Burlaga, L.F.E., Magnetic Clouds, in *Physics of the Inner*

- Heliosphere*, edited by R. Schwenn and E. Marsch, p. 1, Springer-Verlag, Berlin-Heidelberg, Vol. 2, 1991.
- Burlaga, L.F., K.W. Behannon, and L.W. Klein, Compound Streams, Magnetic Clouds, and Major Geomagnetic Storms, *J. Geophys. Res.*, **92**, 5725, 1987.
- Crooker, N.U., and E.W. Cliver, A postmodern view of M-regions, *J. Geophys. Res.*, **99**, 23,383, 1994.
- Crooker, N.U., E.W. Cliver, and B.T. Tsurutani, The semi-annual variation of great geomagnetic storms and the postshock Russell-McPherron effect preceding coronal mass ejections, *Geophys. Res. Lett.*, **19**, 429, 1992.
- Crooker, N.U., G.L. Siscoe, S. Shodan, D.F. Webb, J.T. Gosling, and E.J. Smith, Multiple heliospheric current sheets and coronal streamer belt dynamics, *J. Geophys. Res.*, **98**, 9371, 1993.
- Dryer, M., Interplanetary studies: propagation of disturbances between the sun and the magnetosphere, *Space Sci. Rev.*, **67**, 363, 1994.
- Feynman, J., and A. J. Hundhausen, Coronal mass ejections and major solar flares: The great active center of March 1989, *J. Geophys. Res.*, **99**, 8451, 1994.
- Feynman, J., and S. F. Martin, On the initiation of coronal mass ejections by newly emerging magnetic flux, *J. Geophys. Res.*, in press, 1995.
- Gosling, J.T., The solar flare myth, *J. Geophys. Res.*, **98**, 18,937, 1993.
- Gosling, J.T., D.J. McComas, J.L. Phillips, and S.J. Bame, Geomagnetic activity associated with earth passage of interplanetary shock disturbances and coronal mass ejections, *J. Geophys. Res.*, **96**, 731, 1991.
- Gosling, J.T., S.J. Bame, D.J. McComas, J.L. Phillips, B.E. Goldstein, and M. Neugebauer, The speeds of coronal mass ejections in the solar wind at mid heliographic latitudes: Ulysses, *Geophys. Res. Lett.*, **21**, 1109, 1994.
- Harrison, R.A., The source regions of solar coronal mass ejections, *Solar Phys.*, **126**, 185, 1990.
- Hewish, A. and S. Bravo, The sources of large-scale heliospheric disturbances, *Sol. Phys.*, **106**, 185, 1986.
- Hiei, E., A.J. Hundhausen, and D.G. Sime, Reformation of a coronal helmet streamer by magnetic reconnection after a coronal mass ejection, *Geophys. Res. Lett.*, **20**, 2785, 1993.
- Howard, R.A., Sheeley, N.R. Jr., Koomen, M.J. and Michels, D.J., Coronal mass ejections: 1979-1981, *J. Geophys. Res.*, **90**, 8173, 1985.
- Howard, R.A., Sheeley, N.R. Jr., Michels, D.J. and Koomen, M.J., The solar cycle dependence of coronal mass ejections, *The Sun and the Heliosphere in Three Dimensions*, edited by R. G. Marsden, p. 107, 1986.
- Hundhausen, A.J., Sizes and locations of coronal mass ejections: SMM observations from 1980 and 1984-1989, *J. Geophys. Res.*, **98**, 13,177, 1993.
- Hundhausen, A.J., Coronal mass ejections: a summary of SMM observations from 1980 and 1984-1989, in *The Many Faces of the Sun*, edited by K. Strong, J. Saba, and B. Haisch, to be published, 1995.
- Hundhausen, A.J., Burkepile, J.T. and St. Cyr, O.C., Speeds of coronal mass ejections: SMM observations from 1980 and 1984-1989, *J. Geophys. Res.*, **99**, 6543, 1994.
- Jackson, B.V., and D.F. Webb, The masses of CMEs measured in the inner heliosphere, *Proceedings of the Third SOHO Workshop*, edited by A. Poland, in press, 1995.
- Jackson, B.V., D.F. Webb, P.L. Hick, and J.L. Nelson, *Catalog of Helios 90° photometer events*, PL-TR-94-2040, Phillips Laboratory, Hanscom AFB, MA, 1994.
- Joselyn, J.A. and P.S. McIntosh, Disappearing solar filaments: a useful predictor of geomagnetic activity, *J. Geophys. Res.*, **86**, 4555, 1981.
- Kahler, S.W., Solar flares and coronal mass ejections, *Annu. Rev. Astron. Astrophys.*, **30**, 113, 1992.
- Kahler, S.W., and A.J. Hundhausen, The magnetic topology of solar coronal structures following mass ejections, *J. Geophys. Res.*, **97**, 1619, 1992.
- Kahler, S.W., and D.V. Reames, Probing the magnetic topologies of magnetic clouds by means of solar energetic particles, *J. Geophys. Res.*, **96**, 9419, 1991.
- Low, B.C., Mass acceleration processes: the case of the coronal mass ejection, *Adv. Space Res.*, **13**(9), 63, 1993.
- McComas, D.J., in *U.S. Natl. Report to the IUGG, 1991-1994*, AGU, in press, 1995.
- Mikic, Z. and Linker, J.A., Disruption of coronal magnetic field arcades, *Astrophys. J.*, **430**, 898, 1994.
- Neugebauer, D.R. Clay, and J.T. Gosling, The origins of planar magnetic structures in the solar wind, *J. Geophys. Res.*, **98**, 9383, 1993.
- Reames, D.V., Solar energetic particles: a paradigm shift, in *U.S. Natl. Report to the IUGG, 1991-1994*, AGU, in press, 1995.
- Richardson, I.G., and D.V. Reames, Bidirectional 1 MeV  $\text{amu}^{-1}$  ion intervals in 1973-1991 observed by the Goddard Space Flight Center instruments on IMP 8 and ISEE 3/ICE, *Astrophys. J. Suppl.*, **85**, 411, 1993.
- Rust, D.M., Spawning and shedding helical magnetic fields in the solar atmosphere, *Geophys. Res. Lett.*, **21**, 241, 1994.
- Steinolfson, R.S., Models of material ejection, in *Dynamics of Solar Flares*, edited by B. Schmieder and E. Priest, p. 171, Observatoire de Paris, DASOP, 1991.
- Steinolfson, R.S., Three-dimensional structure of coronal mass ejections, *J. Geophys. Res.*, **97**, 10,811, 1992a.
- Steinolfson, R.S., Coronal shock waves, in *Proceedings of the 26th ESLAB Symposium*, p. 51, ESA SP-346, 1992b.
- Suess, S.T., The relationship between coronal and interplanetary magnetic fields, *Adv. Space Res.*, **13**(9), 31, 1993.
- Svestka, Z. and E. W. Cliver, History and basic characteristics of eruptive flares, in *Eruptive Solar Flares*, edited by Z. Svestka, B. Jackson and M. Machado, p. 1, Springer-Verlag, New York, 1992.
- Tsurutani, B. T., W. D. Gonzalez, F. Tang, and Y. T. Lee, Great magnetic storms, *Geophys. Res. Lett.*, **19**, 73, 1992.
- Webb, D.F., The solar sources of coronal mass ejections, in *Eruptive Solar Flares*, edited by Z. Svestka, B. Jackson and M. Machado, p. 234, Springer-Verlag, New York, 1992.
- Webb, D.F., The heliospheric manifestations and geoeffectiveness of solar mass ejections, in *Solar-Terrestrial Predictions Workshop-IV*, edited by A. Hruska et al., p. 71, Natl. Oceanic and Atmospheric Administration, Boulder, Vol. 2, 1993.
- Webb, D.F., and R.A. Howard, The solar cycle variation of coronal mass ejections and the solar wind mass flux, *J. Geophys. Res.*, **99**, 4201, 1994.
- Webb, D.F., T.G. Forbes, H. Aurass, J. Chen, P. Martens, B. Rumpolt, V. Rusin, S.F. Martin, and V. Gaizauskas, Material ejection, *Solar Phys.*, **153**, 73, 1994.
- Wilson, R.M. and E. Hildner, On the Association of Magnetic Clouds With Disappearing Filaments, *J. Geophys. Res.*, **91**, 5867, 1986.
- Wolfson, R. and Low, B.C., Energy buildup in sheared force-free magnetic fields, *Astrophys. J.*, **391**, 353, 1992.
- Wright, C.S., A Comparison of the Signatures of Disappearing Filaments and Flares in the Interplanetary Medium at 1 AU, and Their Relationships to Geomagnetic Disturbances, in *Solar-Terrestrial Predictions*, edited by R.J. Thompson et al., p. 658, Natl. Oceanic and Atmospheric Administration, Boulder, Vol. 1, 1990.

Zhao, X.P., J.T. Hoeksema, J.T. Gosling, and J.L. Phillips, Statistics of IMF Bz Events, in *Solar-Terrestrial Predictions Workshop-IV*, edited by J. Hruska et al., p. 712, Natl. Oceanic and Atmospheric Administration, Boulder, Vol. 2, 1993.

D. F. Webb, Geophysics Directorate, Phillips Laboratory/GPSG, 29 Randolph Road, Hanscom AFB, MA 01731-3010. (e-mail: webb@plh.af.mil)

(Received June 17, 1994; revised December 30, 1994; accepted January 18, 1995.)



The U.S. Government is authorized to reproduce and sell this report.  
Permission for further reproduction by others must be obtained from  
the copyright owner.

## Correlator measurements of megahertz wave-particle interactions during electron beam operations on STS

M. P. Gough,<sup>1</sup> D. A. Hardy,<sup>2</sup> M. R. Oberhardt,<sup>2</sup> W. J. Burke,<sup>2</sup> L. C. Gentile,<sup>3</sup> B. McNeil,<sup>4</sup> K. Bounar,<sup>4</sup> D. C. Thompson,<sup>5</sup> and W. J. Raitt<sup>5</sup>

**Abstract.** We report on the analysis of megahertz modulation of electrons as measured by the Shuttle Potential and Return Electron Experiment (SPREE) during dc firing of the shuttle electrodynamic tether system (SETS) fast pulsed electron generator (FPEG). The SPREE and FPEG were flown aboard the space shuttle Atlantis flight STS 46 as part of the Tethered Satellite System (TSS 1) mission. The principal data reported here are from the SPREE multiangular electrostatic analyzers (ESAs) and Space Particle Correlator Experiment (SPACE). The ESAs, mounted on rotary tables, measured electrons and ions in the energy range from 10 eV to 10 keV over a solid angle of  $2\pi$  sr. The SPACE is a signal processing system that analyzes the pulse stream from the SPREE ESAs to identify bunching of the electrons and ions produced by coherent wave-particle interactions (WPIs). The SPACE detects modulations in the electron fluxes in frequency range 0- to 10-MHz. This paper concerns 2- to 4-MHz modulations of the electron flux detected by the SPACE when the FPEG was firing in a dc mode at pitch angles close to  $90^\circ$ . During such operations, FPEG emitted a current of 100 mA at an energy of 1 keV. For these times, electrons with energies from 10 to 1850 eV were measured by the SPREE. For energies between  $\sim 10$  and 100 eV the electron flux is basically isotropic. At higher energies the flux increases for pitch angles near  $90^\circ$ . The electron distribution functions generally decrease monotonically with increasing energy up to 100 eV. At energies  $> 100$  eV the distributions either monotonically decrease or exhibit a peak or plateau at energies near the beam emission energy. Megahertz modulations were observed for electrons with energies from 10 to 1180 eV, on both positive and negative slopes in the distribution function and throughout the  $2\pi$  sr sampled by the ESAs. The occurrence and strength of the modulations exhibit no clear dependence on the pitch angle at which the electrons are measured. However, they appear to be limited to low parallel velocities ( $< 3 \times 10^6$  m s<sup>-1</sup>) where beam-generated waves are in resonance with suprathermal electrons.

## Introduction

The injection of electron beams into the ionosphere produces prompt changes in the plasma environment. These include the creation of a broad energy/angle spectrum of returning electrons and a high level of heating

of the ambient thermal electrons [Hardy *et al.*, 1995]. Since previous observations have shown that Coulomb scattering is a minor contributor to the interaction of the beam with the ambient environment [Wilhelm *et al.*, 1985], wave-particle interactions (WPIs) with fast growth rates must contribute significantly to the production of these effects. In this paper we report evidence for strong WPIs in the form of megahertz modulations of electrons observed in the energy range from 10 eV to 1.2 keV.

During previous beam-emission experiments wave sensors have detected both megahertz and kilohertz frequency signals. During Spacelab 1, Mourenas *et al.* [1989] reported strong waves at the harmonic of the electron gyrofrequency,  $n f_{ce}$ , closest to the upper hybrid frequency  $f_{uhr}$ . The Echo 7 sounding rocket measured beam-induced wave activity near  $f_{uhr}$  at  $\sim 4.2$  MHz [Ginet and Ernstmeier, 1991] with a few broadband flashes extending up to 20 MHz [Winckler *et al.*,

<sup>1</sup>Space Science Centre, University of Sussex, Brighton, England, United Kingdom

<sup>2</sup>Phillips Laboratory, Hanscom Air Force Base, Massachusetts.

<sup>3</sup>Boston College Institute for Space Research, Newton, Massachusetts.

<sup>4</sup>Radex Inc., Bedford, Massachusetts.

<sup>5</sup>Center for Atmospheric and Space Science, Utah State University, Logan, Utah.



1989]. Abe *et al.* [1988] observed waves both close to the proton gyrofrequency,  $f_{H^+}$  of 800 Hz, and the hybrid frequency of  $H^+$  and  $He^+$ , as well as around the lower hybrid frequency  $f_{lhr} \sim 8.5$  kHz on sounding rocket Echo 6. A broad peak was frequently observed near  $f_{lhr}$  during beam emissions from the Echo 7 rocket [Ginet and Ernstmeier, 1991] and Spacelab 2 [Cairns and Gurnett, 1991]. Also on Spacelab 2, finite antenna-length effects led to interference patterns across the broad frequency range 0–10 kHz that were interpreted as obliquely propagating ion acoustic or high-order,  $O^+$  ion cyclotron waves [Feng *et al.*, 1992].

Three-dimensional, electrostatic simulations show that when beam electrons are injected into the ionosphere at oblique angles to the magnetic field they form hollow cylinders [Pritchett, 1991]. With time, these cylinders become increasingly filled in by particles. The transverse wave spectrum for this case is dominated by a peak close to  $f_{lhr}$  inside the cylinder, and by broadband, low-frequency waves up to the ion plasma frequency outside the cylinder. This prediction is consistent with measurements taken during the Spacelab 2 mission. When the plasma diagnostic package (PDP) subsatellite was flying close to the guiding center field line of beam electrons, its electric field sensor detected strong emissions near  $f_{lhr}$  [Gurnett *et al.*, 1988].

Particle correlation measurements of the natural electron beams over auroral arcs reveal the presence of similar megahertz particle modulations at  $f_{lhr}$ . The electron autocorrelators flown on the E2B sounding rocket detected 2.8-MHz oscillations on a 4.5-keV auroral beam at 230 km [Gough and Urban, 1983]. On the CAESAR 2 rocket, 1.4-MHz oscillations were measured on a 9-keV auroral beam at 690 km [Gough *et al.*, 1990]. In both cases, the frequency of modulation was primarily governed by the local value of  $f_{lhr}$ . Both rockets flew over quiet auroral arcs where predominantly field-aligned electron beams had evolved adiabatically to cover a range of pitch angles with shell-shaped velocity distributions. Maggs and Lotko [1981] and Lotko and Maggs [1981] have considered the stability of shell distributions to the growth of electrostatic waves. They concluded that the Landau resonance ( $n = 0$ ) dominates over a large range of altitudes with wave growth strongest for propagation parallel to the magnetic field. At low altitudes the shell feature extends adiabatically to large pitch angles and the Doppler-shifted cyclotron resonance ( $n = +1$ ) can become important. The necessary condition for the  $n = +1$  resonance is for the existence of a positive value for  $df/dv_{\perp}$  at the resonant parallel velocity. Gough *et al.* [1990] showed that the auroral beam distribution at low altitudes could support both the  $n = 0$  and  $n = +1$  resonant conditions. The  $n = +1$  resonance requires oblique wave propagation at angles  $> 85^\circ$ .

Kellogg and Monson [1979, 1984] and more recently Weatherwax *et al.* [1994] reported receiving megahertz radio signals from aurora. Frequencies observed are near harmonics of the local ionospheric electron gyrofrequency. One of the sounding rockets detected auroral-

electron modulations close to  $f_{lhr} = 2f_{ce}$ , a frequency-matching condition predicted by Kaufmann [1980] as leading to strong electrostatic wave growth. Gough and Urban [1983] suggested that a few percent of the electrostatic wave power generated on the modulated auroral beam they had observed could convert into electromagnetic radiation. This value was based on GEOS satellite measurements of electrostatic to electromagnetic wave-power conversion at sources of continuum emissions in the magnetosphere. Radio wave power observed at the ground was compatible with a modulated primary auroral beam source if ionospheric absorption limited transmission to about 1%.

This paper reports on the direct measurement of WPIs by the Shuttle Potential and Return Electron Experiment (SPREE) aboard the STS 46. The detection of electrons modulated at megahertz frequencies was accomplished by SPREE's Space Particle Correlator Experiment (SPACE). These modulations were observed in four intervals during which the fast pulsed electron generator (FPEG) was emitting a 100-mA beam of 1-keV electrons at pitch angles near  $90^\circ$ . In the following section we describe the measuring capabilities of SPREE and SPACE. We then present detailed analyses of two modulation events. The final section discusses relationships between these measurements and results reported from previous shuttle and sounding rocket flights. We also comment on their significance for understanding high-frequency WPIs in beam-emission environments.

## SPREE and SPACE Instrument Capabilities

STS 46 offered an opportunity to study beam plasma interactions in space under controlled conditions with advanced particle detectors, offering high-resolution in energy/angle, and fast-time response. All results discussed here were obtained while the tethered satellite was stowed in the payload bay.

A detailed description of SPREE is given by Oberhardt *et al.* [1994]. Briefly, its core elements are two nested, triquadrangular, electrostatic analyzers (ESAs) that simultaneously measure fluxes of electrons and ions with energies between 10 eV and 10 keV over a  $100^\circ \times 8.5^\circ$  angular fan. The resolution for electron energy channels is  $\Delta E/E \approx 7\%$ . Spectra were compiled at rates of either 1 or 8  $s^{-1}$  in 32 logarithmically spaced energy channels. The active detection elements of the ESAs are strips of microchannel plates (MCP). The  $100^\circ$  dimension of the angular fan is divided in 10 zones of  $10^\circ$  width, designated 0 to 9. Zone 0 has its lower edge  $5^\circ$  below parallel to the base of the ESA unit while zone 9 looks  $5^\circ$  beyond shuttle's zenith.

Each ESA was mounted on a rotary table that was either parked or turned through  $180^\circ$  every 30 s. The two analyzers and rotary tables, designated ESA A and B, were mounted back to back with a constant phase angle in their detection fans of  $180^\circ$ , such that both the elec-

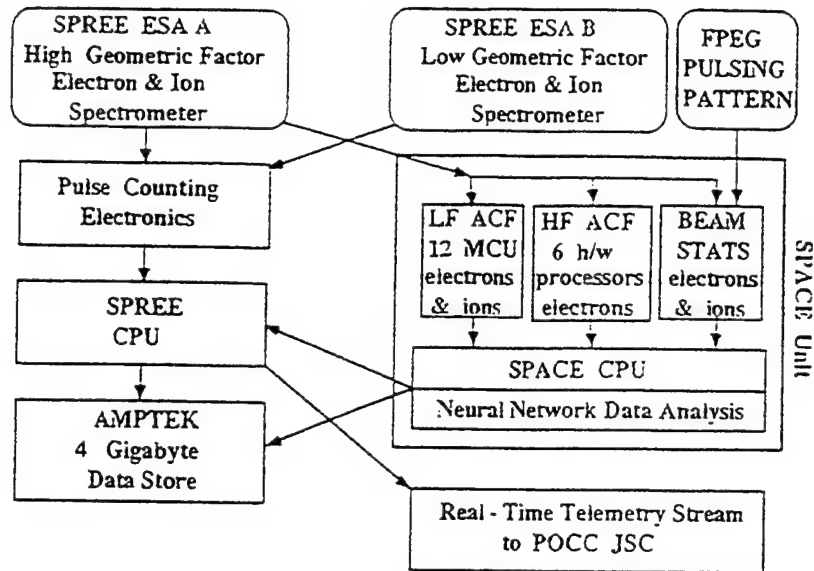


Figure 1. Block diagram providing an overview of the SPREE-SPACE sensor on STS 46.

tron and ion spectra were sampled over a solid angle of  $2\pi$  sr every 30 s. In the text that follows we use a standard shuttle coordinate system with the  $X$ ,  $Y$  and  $Z$  in the directions of shuttle's nose, starboard and nadir, respectively. Also we make reference to the azimuth angle of the rotary table for ESA A. Rotary angles of  $0^\circ$ ,  $90^\circ$ , and  $180^\circ$  reference times when the aperture of ESA A faced toward shuttle's left wing ( $-Y$ ), bow ( $X$ ), and right wing ( $Y$ ), respectively. To assure unsaturated measurements in both the ambient and disturbed environments expected during the mission, the geometric factors of ESA B were  $\sim 100$  times smaller than those of ESA A.

Figure 1 is a diagram of the SPREE/SPACE combination. In parallel with the normal counting, SPACE processes data streams from selected zones of ESA A and ESA B. For the selected zones, particle correlations are made using 19 parallel processing elements. Groups of these units independently determine low-frequency autocorrelation functions (LF ACF), high-frequency autocorrelation functions (HF ACF) and beam correlations. All LF ACF and HF ACF units have their selected input zones changed every 30 s (once per rotation of the sensors) and their frequency range stepped every 90 s, with full sensor-frequency coverage taking 540 s since there are three frequency ranges for each ACF type. Data from the LF and HF units were initially processed in real time for ground experimenters by an on board neural network [Gough, 1994]. Here results come from the full data set, stored on SPREE data recorder for post-flight analysis. The LF ACF units cover the frequency range 0 – 10 kHz. The beam units specify on/off fluence differences for selected ion and electron data streams taken while FPEG was being pulsed at frequencies  $>1$  Hz. In this paper we are only concerned with high-frequency modulations detected while FPEG operated in its dc mode. The details of the HF ACF processing are given below.

Megahertz range autocorrelation functions are made by six separate, hard-wired processing elements on six electron detection streams (three each from electron detectors A and B). The technique here is similar to that used on previous space flights [Gough, 1980, 1985; Gough et al., 1990]. Times between electron arrivals are measured in units of counts of a clock running at twice the maximum frequency to be studied. Histograms of occurrence of time separations are generated as a function of electron energy. A histogram is generated for each of the 32 energy levels sampled by the SPREE ESAs. For each arrival of an electron that is separated in time from the previous electron by a count  $C$  of the clock, a bin in the histogram is incremented by 1:

$$H(E, C) = H(E, C) + 1, \quad 1 < C < 64$$

At each energy a 64-point histogram is accumulated over all periods in which channels were sampled. With SPREE operating in the slow mode, HF ACFs are summed over 3 s with each energy channel being sampled 3 times for a total of 31.2 ms. With SPREE operating in the fast mode, HF ACFs are summed over 12 s and each energy channel is sampled 96 times each time for 3.91 ms. This gives total accumulation times of 93.7 and 375 ms for slow and fast modes, respectively. At the end of these accumulation periods the whole block of 2048 values (32 energies  $\times$  64 lags) is read by the SPACE CPU into the SPREE recorder for telemetry, and these values are then reset to zero to begin the next accumulation period.

These histograms are equivalent to the summation of many one-bit autocorrelations where only two bits are set in each group of samples being correlated. This technique is much less computationally intensive than calculating the equivalent autocorrelation functions. Usually, there is little loss in performance over full autocorrelation since the probability of receiving more than two

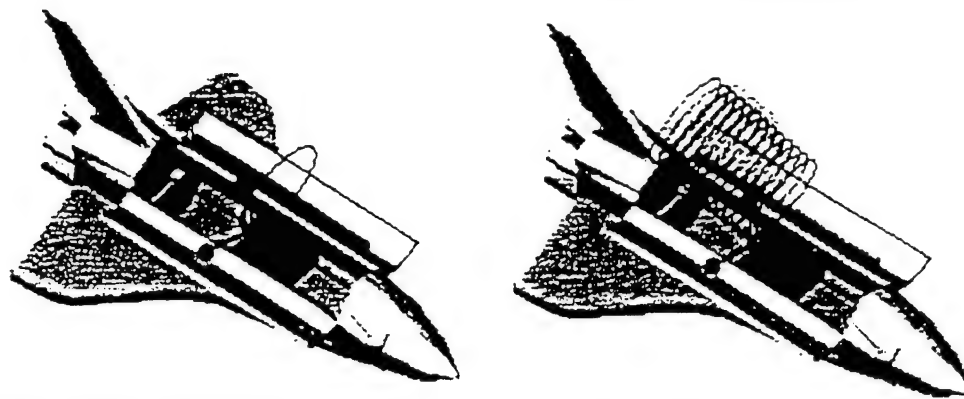


Figure 2. To-scale representations of unperturbed trajectories for electrons emitted at the center of the FPEG beam on August 3, 1992 at 2008:29 (left) and 2009:45 UT (right).

electrons in 64 cycles of a 20-MHz clock is very low for typical count rates of  $10^5$  counts  $s^{-1}$ . The main advantage of this buncher-histogram technique is that it allows the study of modulated frequencies that are a few orders of magnitude higher than the average count rate, providing that the phenomena are sufficiently stable over summation times. The main disadvantage is its extreme sensitivity to modulation depth. The measured

histogram, fractional-counts modulation varies as the square of the fraction of modulated electrons. If only 50% of electrons are wave modulated, then only 1 in 4 of the histogram counts correspond to measurements between modulated electrons, and only 25% contribute to the measured modulation.

HF ACF units employ field programmable gate arrays with local random access memories to accumu-

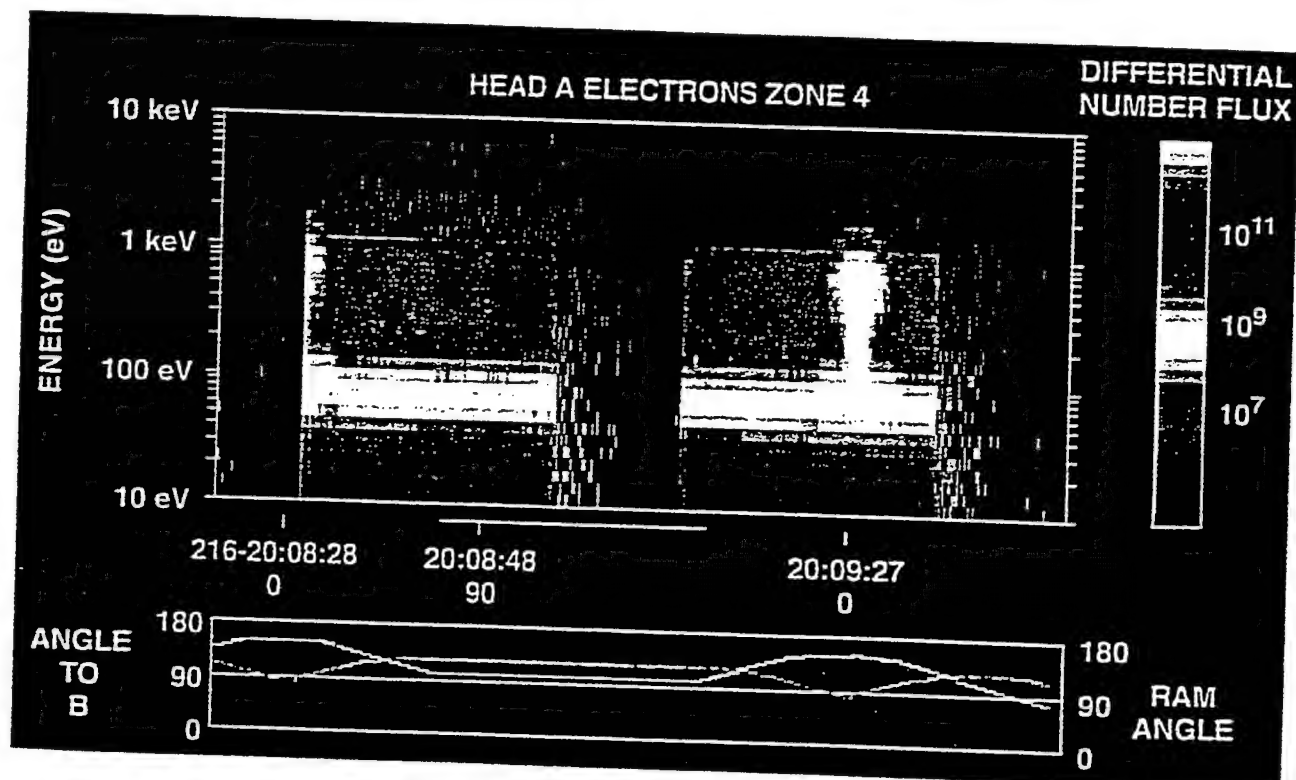


Plate 1. Directional differential fluxes of electrons with energies between 10 eV and 10 keV measured in ESA A, zone 4 in an energy-versus-time spectrogram format. The tic marks on the horizontal axis indicate UT and the rotary look angle of ESA A's aperture. Here the sensor rotated from  $0^\circ$ , looking over the left wing, to  $90^\circ$ , looking toward the shuttle's nose. After parking for 27 s, as indicated by the solid line, it rotated back toward  $0^\circ$ . The scale on the right side gives the flux intensity in  $(cm^2 s sr eV)^{-1}$ . Traces in the bottom panel indicate the pitch angle (red) of electrons entering the aperture and direction with respect to the shuttle ram velocity (green).

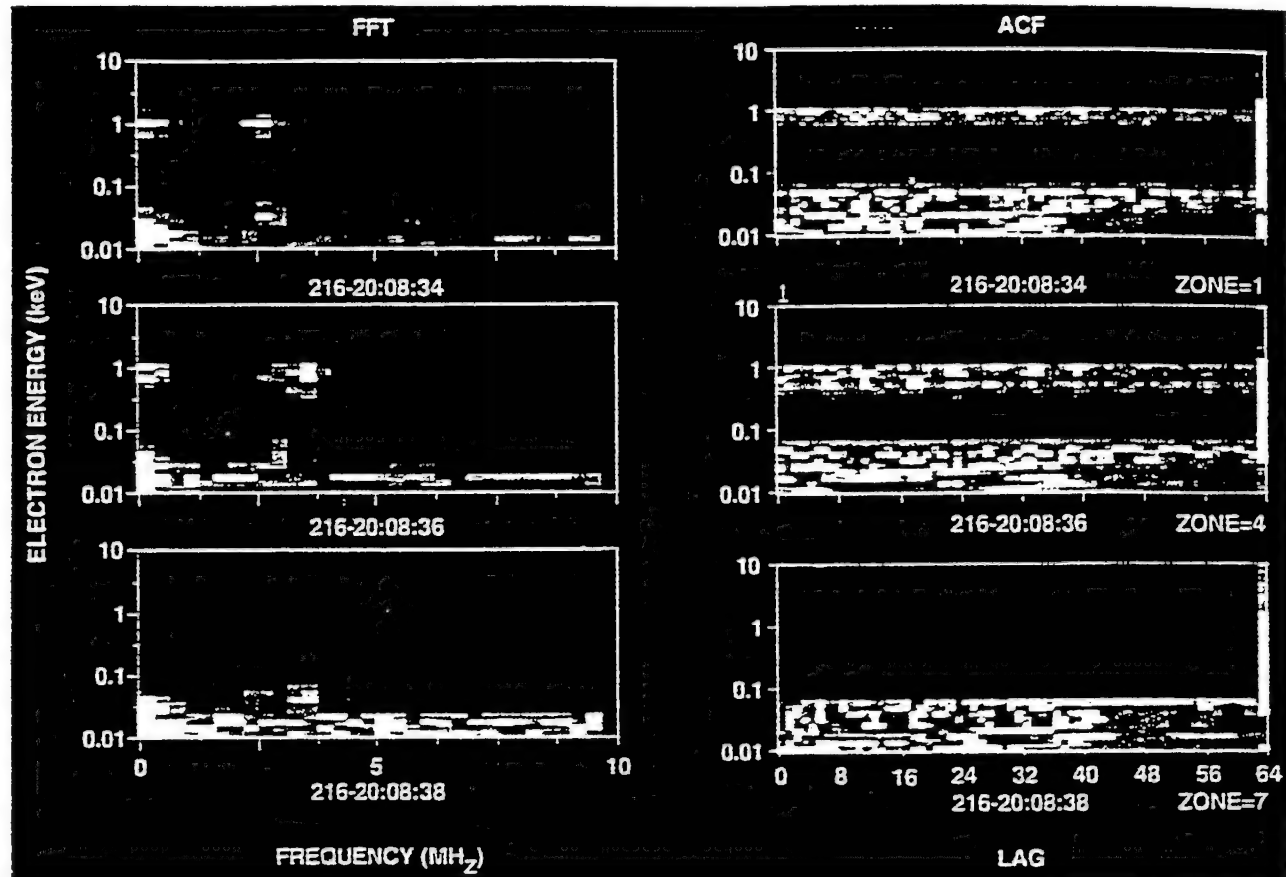


Plate 2. ACFs and FFTs of electron modulations observed in zones (top) 1, (middle) 4, and (bottom) 7 at  $\sim 2008:34$  UT on Julian day 216 during the first dc firing of FPEG shown in Plate 1. The ordinates indicate electron energy between 10 eV and 10 keV. The ACF abscissa gives lags 1 to 64 with lag increments of 50 ns. The FFT abscissa is frequency 1 to 10 MHz.

late two-dimensional (energy and time lag) histograms. Each unit was directly accessed by the SPACE CPU bus for read out at the end of the summation periods of 3 or 12 s. HF ACF units were cycled over the frequency ranges: 0 - 10 MHz, 0 - 2.5 MHz, and 0 - 0.625 MHz. All of the results presented here were obtained from the 0 to 10 MHz frequency range with histogram time lags of 50 ns. Because of the dead times of the electronics, the first HF ACF bin for this frequency range is for 650 ns electron separations and the last bin is for 3.85- $\mu$ s separations. In the lower-frequency ranges, for the events studied, no significant modulations were detected. Besides any real electron modulation, data accumulated in the lower-frequency ranges also included a strong background shape corresponding to that expected from the Poisson statistics of time separation measurements for random-count events.

Ground computer fast Fourier transform (FFT) processing of the 64-point histograms yields a 32-point frequency spectrum for each of the 32 energies for each accumulation period. Frequency resolution is thus  $\frac{1}{32}$  of the maximum frequency: 312 kHz in the 10-MHz frequency range. As a result of the electronics dead time, the first histogram bin corresponds to a time of 13 lags, and the histogram cannot be reflected about zero lag before Fourier transformation.

## High-Frequency Electron Modulations

This paper discusses SPACE and SPREE measurements acquired during the only four periods of the STS 46 mission when FPEG was emitting a continuous beam at nearly  $90^\circ$  to the magnetic field and SPACE was operating in its 0- to 10-MHz mode. In each instance it detected electron fluxes that were strongly modulated at megahertz frequencies. We found numerous examples of FPEG emitting at pitch angles far from  $90^\circ$ , in which SPACE detected kilohertz, but not megahertz, modulations of electrons reaching SPREE. The first and strongest modulations at the high frequency were detected between 2008:29 and 2009:36 UT on August 3, 1992 (Julian day 216). The last three occurred on August 4, 1992 (Julian day 217) during the intervals 0620:02-0620:45, 0651:00-0651:35, and 0732:30-0732:45 UT. The first and third (second and fourth) modulation events occurred while shuttle was in darkness (sunlight). In the following paragraphs we focus on measurements taken during the first two events.

### First High-Frequency Modulation Event

During the first modulation event shuttle was in darkness over South Africa with the magnetic field di-

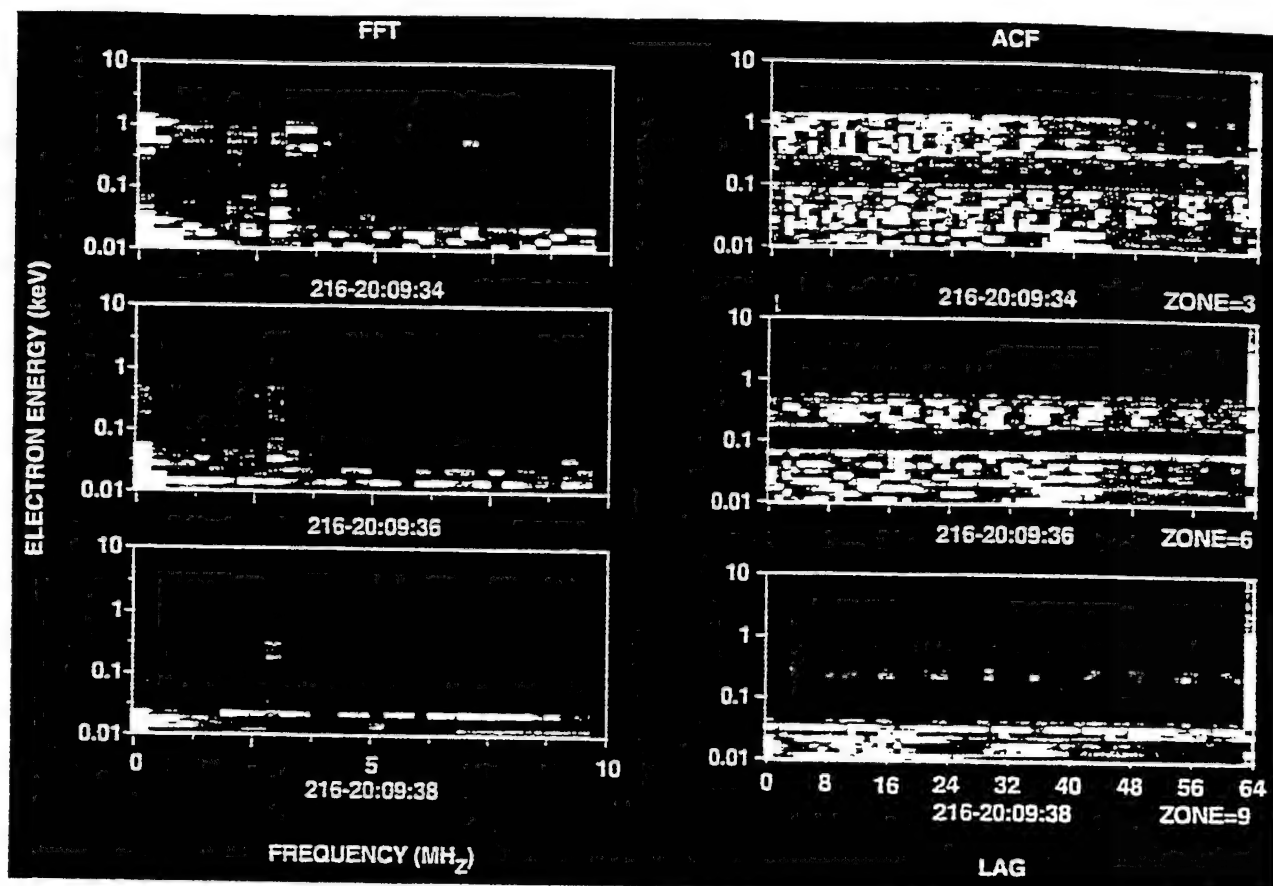


Plate 3. ACFs and FFTs of electron modulations observed in zones 3 (top), 6 (middle), and 9 (bottom) at  $\sim 2009:36$  UT on Julian day 216 in the same format as Plate 2.

rection approximately along the long axis ( $X$ ) of the payload bay. Figure 2 shows two unperturbed trajectories for electrons at the center of the FPEG beam with geometrically accurate representations of the shuttle and the TSS 1 payload. The magnetic field at 2008:29 UT should have forced electrons at the center of FPEG's emission cone to impact the shuttle's remote manipulator arm close to SPREE in less than one Larmor period ( $\sim 1.25 \mu\text{s}$ ). The magnetic field strength and orientation changed slowly so that by 2009:45 UT central-angle electrons should have completed ten gyrations before hitting the shuttle's tail. Within this period of megahertz modulations, the SPREE encountered intense fluxes of electrons with energies at and near 1 keV, whenever its detectors faced toward the shuttle's left wing and sampled pitch angles close to  $90^\circ$ . Hardy *et al.* [1995] interpreted the electrons with energies near 1 keV as FPEG-emitted electrons directly returning to the shuttle.

Plate 1 is an energy-versus-time, color spectrogram of SPREE electron measurements from ESA A during this period. Directional differential number fluxes are plotted in units of electrons  $(\text{cm}^2 \text{ s sr eV})^{-1}$ , as designated by a color code displayed to the right of the spectrogram. The horizontal axis is annotated with time and the azimuth angle of the rotary table. These data

are from SPREE zone 4 which is located near the center of the detection fan. Line plots below the spectrogram give the pitch angle and the angle to ram at the center of the zone. During this period, SPREE was operating in its fast mode. FPEG was emitting a dc current, using a 30 s on, 15 s off cycle. Plate 1 illustrates several relevant points. First, there are two periods when intense fluxes of electrons were observed, coinciding with the times when FPEG was turned on. The spectrogram shows the fluxes extending from SPREE's lower limit up to and beyond the FPEG beam energy. These electron fluxes were detected at all azimuth angles for the rotary table and in all of SPREE's zones. Periods with FPEG turned off show no electrons being detected within the energy range and sensitivity of SPREE. Second, at rotary-table angles of  $\sim 0^\circ$  and a pitch angle of  $\sim 90^\circ$  the electron flux was enhanced at all energies with an intense peak around 1 keV. Electrons were measured to energies as high as  $\sim 1850$  eV. Hardy *et al.* [1995] showed that the 1-keV electrons directly return from the FPEG after they have traveled almost one full gyroperiod. Third, at all other rotary-table angles the electron spectra, in general, decrease monotonically with at most a weak peak at energies above 500 eV. This electron population is nearly isotropic with a calculated number density, within SPREE's energy range.



of  $1$  to  $5 \times 10^4$  electrons  $\text{cm}^{-3}$ .

A total of six HF ACFs of 12-s duration were taken during the period between 2008:29 and 2009:36 UT. Significant HF modulations were observed in every zone sampled during all six intervals, corresponding to the range of rotary table angles from  $0^\circ$  to  $90^\circ$ . In the first three 12-s intervals, HF ACFs were taken for SPREE data from ESA A zones 1, 4, 7 (Plate 2). For the last three intervals, SPREE data were from zones 3, 6, and 9 (Plate 3).

Plates 2 and 3 display color spectrograms in which ACF data are plotted in the three right panels, and the corresponding FFTs of the ACF are plotted in the three left panels. In the ACF plots the horizontal axis is the lag from 1 to 64, the vertical axis is the energy of the SPREE channel being sampled, and color represents the accumulated counts at each lag. For the FFTs the horizontal axis gives frequency from 0 to 10 MHz; the vertical axis is SPREE energy. Colors represent the FFT amplitudes. The FFTs were calculated without detrending or windowing the data. This level of processing was sufficient for the purpose of surveying the data to identify periods of HF modulation. Each panel is annotated with the end time of the 12-s period over which the ACFs and FFTs were determined.

In Plate 2 and 3 there are clear periodicities in the HF ACFs in each of the three zones. In the FFTs these translate to strong amplitude peaks in a frequency band between 3.0 and 3.9 MHz. Within this band, megahertz modulations are seen over two separate ranges in energy. In all three zones the modulation occurs at energies from approximately 20 to 60 eV. For zones 1 and 4 the modulation is also seen between 600 and 1180 eV and between 400 and 1180 eV, respectively. At the center time of the HF ACF accumulation interval in Plate 2, zones 1, 4, and 7 were sampling electron fluxes at pitch angles near  $96^\circ$ ,  $86^\circ$ , and  $80^\circ$ , respectively.

In Figure 3 we show in more detail two specific HF

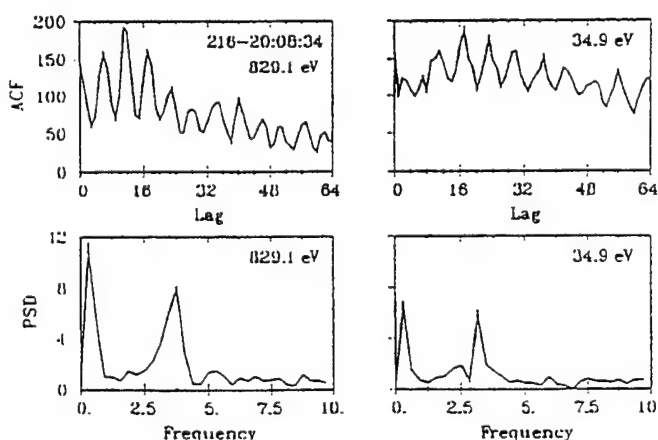


Figure 3. Detailed FFTs and ACFs for ESA A energy channels at 829 eV (left) and 34.9 eV (right) taken at 2008:34 UT on Julian day 216.

ACFs and FFTs for this interval. These are for zone 4 for energy channels centered at 829 and 34.9 eV. There are two points of note. First, both ACFs show a strong depth of modulation. In both cases the percentage of the ACF corresponding to modulated counts is in the range of 25 to 30%, indicating that more than half of the electrons in this energy range are modulated by the wave. Second, there is a real difference in the frequency of the modulation at different zones at different energies. In the 829-eV case (left panel), the FFT peaks at the channel with a central frequency of 3.90-MHz while in the 34.9-eV case (right panel) the FFT peaks for the 3.28-MHz channel. This difference in the FFT reflects a real difference in the periodicity of the ACFs. For the ACF at higher energy 12 peaks are seen within the 64 lags, while for the low-energy channel only 11 peaks are observed.

Figure 4 contains plots of representative electron distribution functions from ESA A, zone 4 acquired during the accumulation interval of the HF ACFs and FFTs in Plate 2. The three spectra (A, B, and C) illustrate the range in the shapes of the distribution function during this interval. Spectra from ESA A, zone 4 were chosen because the detector was unsaturated except in the first or second lowest-energy channels. Saturation results when there are high levels of particle flux to the MCP within an ESA. Electrons that have been energy analyzed by the ESA impact the MCP. There each electron unleashes an electron cascade that results in a pulse of sufficient size to trigger the electronics, thus producing a count. At high levels of particle flux to the MCP, the average size of the pulses decreases so that some fraction is no longer sufficiently large to trigger the electronics. At these flux levels the measured count rate is no longer linearly related to the incident flux. The higher the flux above some definable threshold level, the greater the fraction of impacting electrons that are not counted. At some point the count rate actually decreases with increasing flux. In zone 1, near the FPEG beam energy, the flux was so high that the instrument saturated in this way. For comparison the bottom right panel of Figure 4 contains the distribution of electrons measured in ESA B, zone 0 while facing in the direction of beam return [Hardy et al., 1995]. Since the geometric factor of ESA B was 100 times smaller than that of ESA A, it was never in saturation.

The spectra from ESA A, zone 4 illustrate several important points. First, the distribution measured at energies above 500 eV at 2008:29 UT is the highest of the three from ESA A. Comparing Figure 4 and Plate 2, one can see that phase space densities, enhanced by 2 orders of magnitude, only occurred at the beginning of the 12-s interval during which the HF ACFs and FFTs were accumulated. Since high fluxes are needed to produce the high count rates required for meaningful HF ACFs, we conclude that the spectrum as measured at 2008:29 UT must be the one in which modulations, seen in the energy range from 300 to 1180 eV, occurred. One notes that this spectrum  $df/dv \approx 0$  over



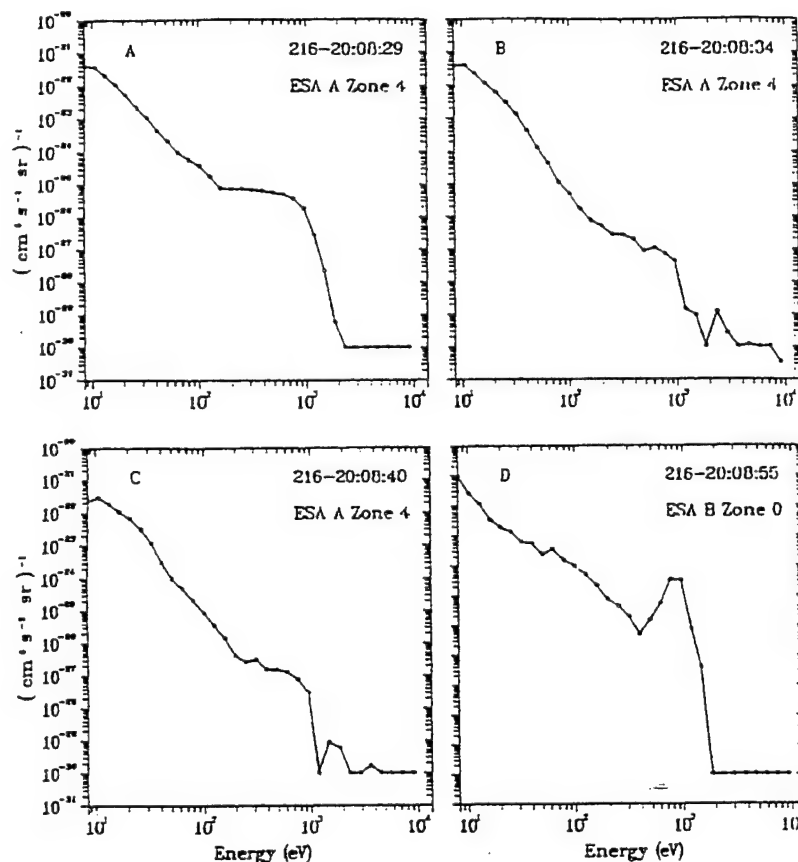


Figure 4. Electron distribution functions measured by ESA A in zone 4 while facing (a) the shuttle's left wing toward returning FPEG electron beam, and (b, c) in the shuttle's forward direction. (d) The electron distribution function measured by ESA B, zones 0 while facing in the direction of the returning FPEG beam.

the energy range 195 to 600 eV. The distribution function has a strong negative slope at higher energies up to 1850 eV. The megahertz modulations are seen for electrons on both the flat and negative-slope parts of the distribution function in this energy range with no measurable difference in the frequency of the modulation. The distribution function has a thermal shape at energies above the peak. Linear, least squares fits to plots in this energy range of the logarithm of the distribution function versus energy on a linear scale give temperatures of 100 eV. Second, at the lower energies of electrons where megahertz modulations are observed,  $df/dv$  is again strongly negative. In general, the spectra monotonically decrease for energies up to  $\sim 250$  eV. The spectral turnover in the lowest-energy channels results from saturation as discussed previously. There is nothing in the shape of the distribution function that suggests why the modulation is seen only in a limited range at low energies. Since, for energies up to  $\sim 200$  eV, the count rate sharply decreases with increasing energy, the high-energy cutoff may merely mark the point where the count rate dropped to a level that is too low for modulations to be detectable. This conjecture does not explain the lack of modulation at lower energies where the count rate is significantly higher than in the channels where modulation is observed.

Megahertz modulations are seen primarily at low energies during the next three of the six intervals when HF ACFs were measured. Strong modulations in the higher-energy channels are observed starting in the interval 2009:10 to 2009:26 UT. The strongest modulations were measured in the second interval from 2009:22 to 2009:34 UT, as shown in Plate 3. The key observation from this interval is that in zone 3, significant HF modulations actually occur at all energies between 16 and 1180 eV. This statement appears to be contrary to the spectrogram in Plate 3 in which a wave power minimum occurs from 100 to 300 eV. To demonstrate that significant modulations occurred at all energies requires more detailed processing of the ACFs as shown in Figure 5. In this figure, we have plotted for electrons measured at 200 eV the raw ACF and its FFT. The FFT shows a significant peak at a frequency of  $\sim 3$  MHz even though the FFT color spectrogram shows no clear peak. For the zone 3 measurements, the electron ACFs were processed in this way to determine the channels in which HF modulation occurred. We also note that compared to the first interval, the FFTs for the interval 2009:22 to 2009:34 UT are taken over a longer period of increased flux at energies above a few hundred eV. As such, the wider energy range for the megahertz modulation may reflect simply higher count rate statis-

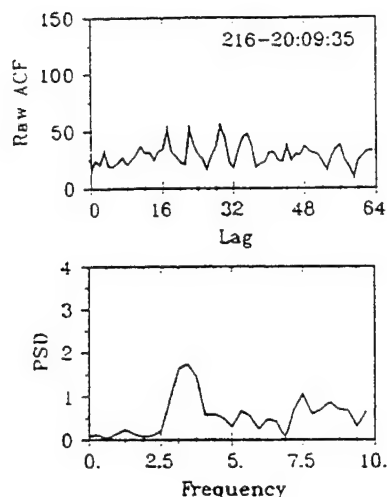


Figure 5. (top) Raw ACF and (bottom) FFT for ESA A's channel at 200 eV, taken at 2009:35 UT.

tics. A second point of note in the FFTs is that again there is a difference in the modulation frequency at different energies. For zone 3, for energies near the FPEG beam energy, the FFTs have a peak at a frequency of 3.90 MHz, while at lower energies the peak is  $\sim 0.6$  MHz lower in frequency. Modulations at lower energies are also seen in zones 5 and 9. The electron distribution functions have almost the same shapes as those shown in the first interval.

### Second High-Frequency Modulation Event

We next consider megahertz modulations observed on Julian day 217 between 0620:00 and 0620:50 UT while the shuttle was in sunlight over Australia. The magnetic field was directed out of the shuttle bay, approximately orthogonal to its bottom. Over this interval, the central pitch angle of the FPEG beam varied smoothly from  $73^\circ$  to  $90^\circ$  as the shuttle executed a  $20^\circ$  roll. FPEG emitted a dc pulse from 0620:01 to 0620:52 UT. Figure 6 plots the trajectories of central-angle, beam electrons from 0620:01 to 0620:31 UT, and illustrates two points. First, the gyromotion of the electrons initially deflects them toward the front of the shuttle and the stowed TSS 1 satellite. These central-angle electrons hit neither the satellite nor its support structure. Second, SPREE detectors are located just outside of the cylinder defined by the gyromotion of these FPEG electrons. The detection fan of ESA A points toward the cylinder when the rotary table azimuth angle is  $90^\circ$ . Since the FPEG electrons have a component of velocity along the magnetic field line, few of them should return to the shuttle.

During this period, SPREE was operating in its slow sweep mode. This has the advantage that the HF ACFs are accumulated over 3 instead of 12 s. As such, the ACFs can be more precisely related to specific electron spectra. Plate 4 is a color spectrogram of the differential number flux for zone 2 between 0619:45 and 0621:15 UT. Throughout the period of dc emissions, electrons were measured from the lowest-energy threshold of the

SPREE ESA to above the FPEG emission energy. The spectrum again generally decreases monotonically with increasing energy. There is an occasional weak peak at energies of  $\sim 800$  eV. Unlike the first event there is no evidence of a direct return of FPEG emitted electrons to SPREE.

Plate 5 presents color spectrograms of FFTs from the two consecutive intervals, 0620:03 to 0620:06 and 0620:06 to 0620:10 UT. The three panels from top to bottom give FFTs from zones 2, 5, and 8, respectively. For these two intervals and three zones, ESA A was measuring electrons with pitch angles near  $70^\circ$ ,  $41^\circ$ , and  $14^\circ$ , respectively. These figures illustrate four important points. First, as in the previous example, a strong peak in the FFT amplitude is seen in the range from 2 to 3 MHz that extends over a range in electron energies. The modulation is seen over the widest energy range in zone 2, while in zones 5 and 8 the modulation is confined to low-energy channels between 11 and 18 eV. Second, at low energies the modulations in zones 5 and 8 are stronger than those in zone 2. This is shown in Figure 7 where the ACFs and FFTs are plotted for the 11.4-eV energy channels for each of the three zones. The strongest modulation near 3 MHz was in zone 5 with no measurable modulation in zone 2, and an intermediate level in zone 8. This difference in level of modulation cannot be attributed to a difference in count rate. For this example, the three count rates were between 300 and 500 kilocounts  $s^{-1}$  with the highest counts in zone 2 where no modulations were detected. Third, in zone 2, at energies of a few hundred eV, the strength of the modulation decreased sharply from the first to the second interval. Again, we checked to see if this could be attributed to a change in the count rate. Examining the spectra at the center of the two intervals, we determined that at energies from 57 to 218 eV where the strong modulations are seen in the first interval, the count rate actually increased during the second interval. Fourth, the modulation extended over a wider energy range in zone 2 at a larger pitch angle than for the other two zones.

This is a general characteristic of the phenomenon that seems to indicate a pitch angle variation in the energy range over which the electrons are modulated.

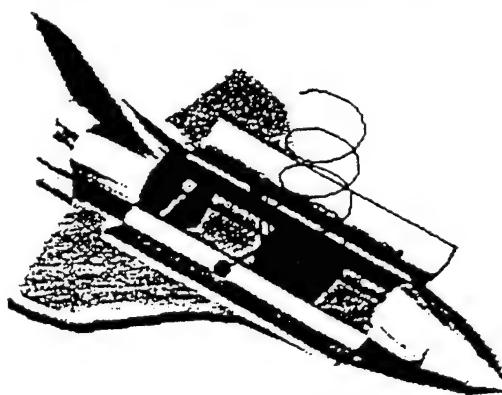


Figure 6. To-scale representation of trajectories for electrons emitted at the center of the FPEG beam on August 4, 1992, at 0620 UT.

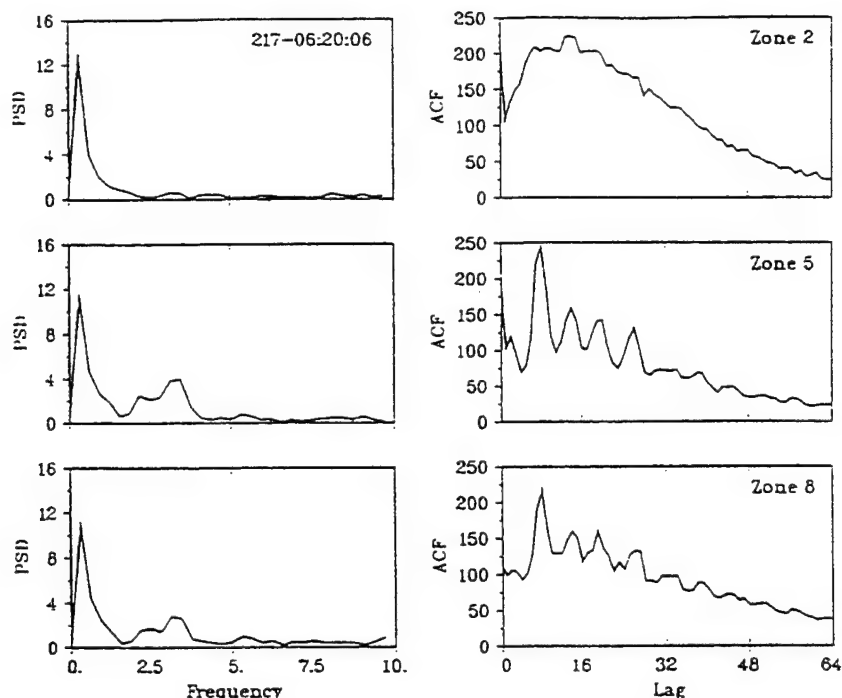


Figure 7. Detailed ACFs and FFTs for ESA A's 11.4 eV channel in zones 2, 5, and 8 acquired near 0620:06 UT on Julian day 217.

Care must be exercised in drawing conclusions from this fact since this trend also follows a variation in the count rate with pitch angle for energies above 100 eV.

The last point is illustrated in Figure 8 where we have plotted the differential number flux for the central time of the first interval for each of the three zones. One can see that the flux level in zone 2, at energies above 60 eV, is generally more than an order of magnitude larger than that for the other two spectra. In all four analyzed intervals the count rate at energies above ~100 eV increases with pitch angles toward 90°. We were able to find no cases where the variation in the energy range with pitch angle did not follow the variation in count rate with pitch angle. Despite this, it is also clear that the observation of the modulation is

not purely a matter of count rate. As we have shown, the modulation is generally not observed in the lowest-energy channels of SPREE even when the count rate in these channels is higher than for channels at higher energies where the modulation is observed. Similarly, within the same event, modulations of equal intensity and at the same energy can be seen for quite different count-rate levels. This is illustrated in Figure 9 where the electron spectra are plotted at 06:20:05 and 06:20:044 UT in zone 2 as well as the ACFs and FFTs at 55 eV. The two ACFs are seen to be comparable in their depth of modulation and in the amplitude of the FFTs. The level of the differential number flux, however, and hence the count rates are seen to be significantly lower for the later interval.

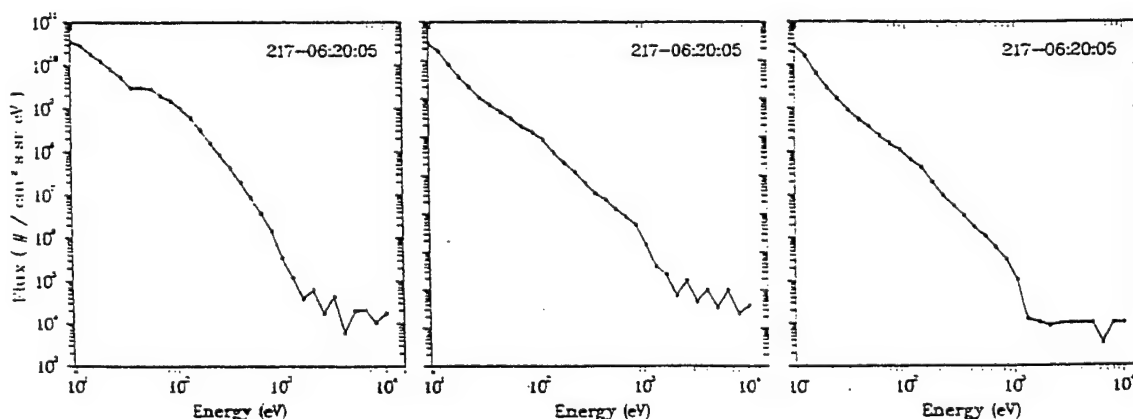


Figure 8. Directional differential fluxes measured in ESA A zones 2, 5, and 8 (left to right) at 0620:05 UT on Julian day 217.

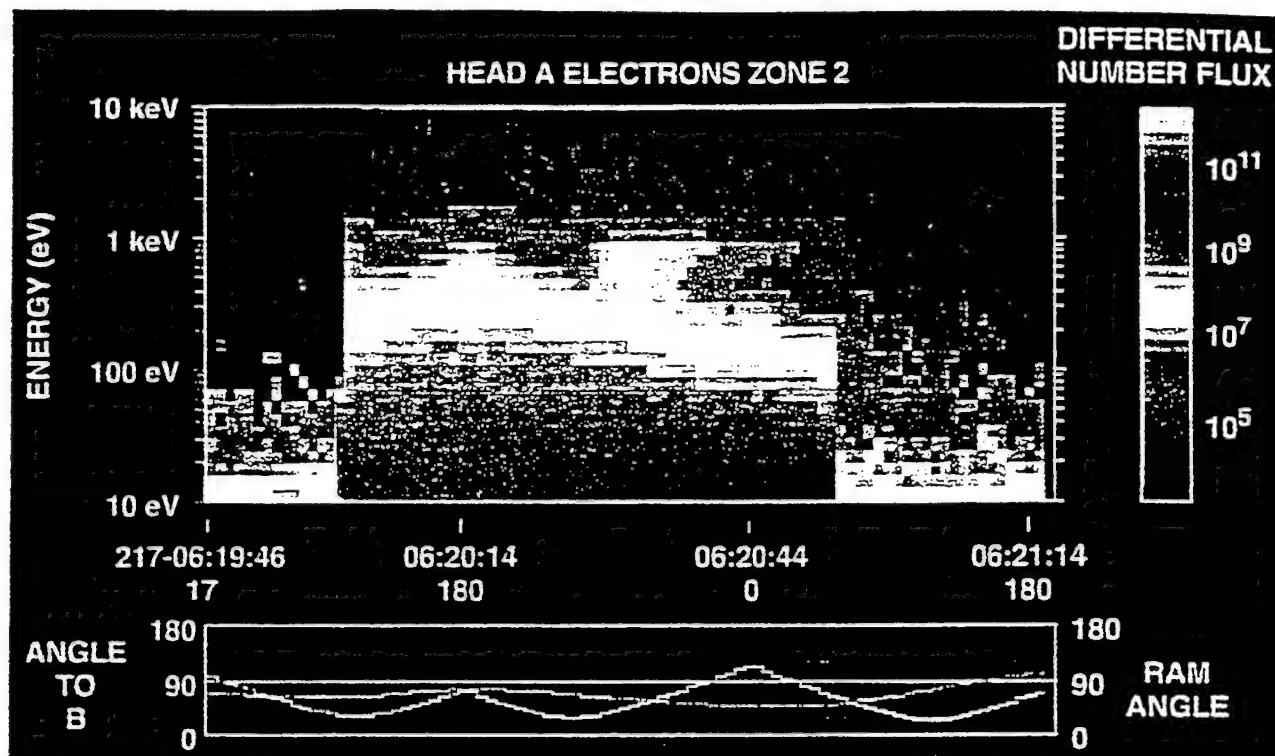


Plate 4. Directional differential fluxes of electrons with energies between 10 eV and 10 keV measured in zone 2. The rotary angle, pitch angle, and ram angle information are in the same format as Plate 1.

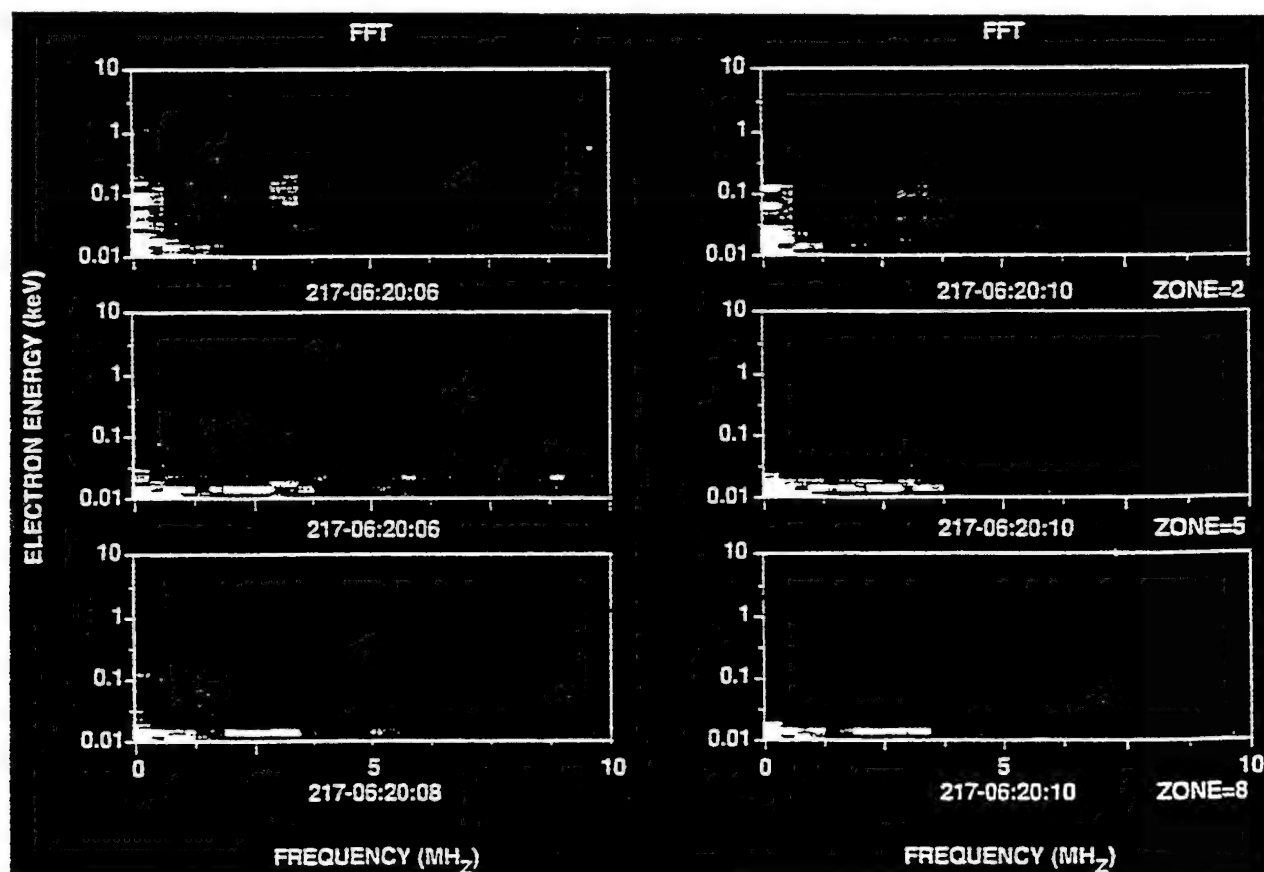


Plate 5. FFTs measured by ESA A zones (top) 2, (middle) 5, and (bottom) 8, near (left) 0620:06 and (right) 0620:10 UT, in the same format as Plate 2.

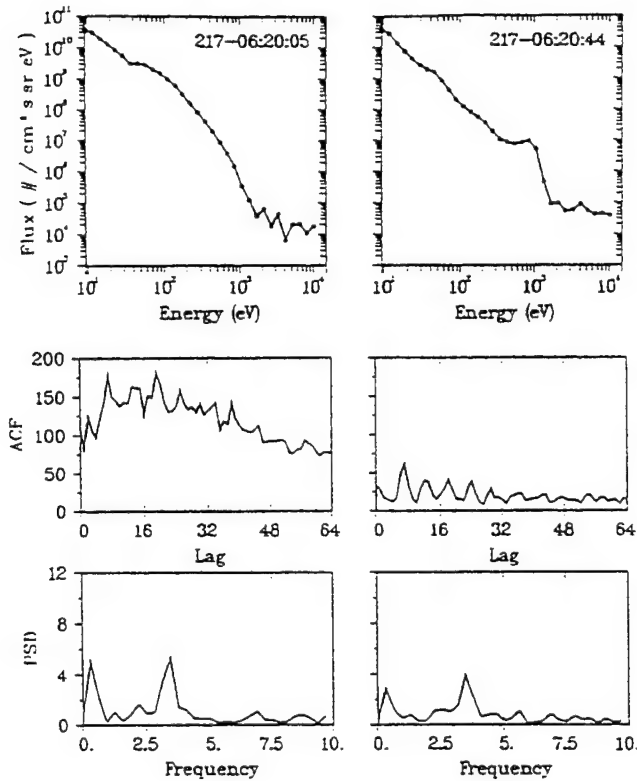


Figure 9. Directional differential flux (top panel) measured in ESA A zone 2, at 0620:05 and 0620:44 UT on Julian day 217. The bottom panels contain ACFs and FFTs for the 55-eV channel.

## Summary and Discussion

A survey of HF measurements during the TSS 1 mission identified four intervals of FPEG emissions during which SPACE detected electron fluxes that were modulated at megahertz frequencies. Two occurred with the shuttle in sunlight, two in darkness. All happened while FPEG emitted beam electrons at pitch angles close to  $90^\circ$ . When FPEG emitted electrons at pitch angles significantly different from  $90^\circ$ , HF modulations were not observed. This is consistent with the simulation results of Pritchett [1991] showing upper hybrid waves inside of the beam cylinder and broadband low frequency waves outside of it. During the Spacelab 2 mission wave sensors on the remote flying plasma diagnostics payload detected upper hybrid emissions only when they were close to the guiding center field line of beam electrons emitted from shuttle [Gurnett *et al.*, 1988].

In the first event (day 216, 2008:29 – 2009:36 UT) the magnetic field was nearly parallel to the shuttle's long axis ( $-X$  direction). At times of FPEG turn-on, SPREE detected enhanced fluxes of beam related electrons. At energies  $<200$  eV, electron distribution functions monotonically decreased with increasing energy or peaked at energies  $<50$  eV. When either ESA looked out over the shuttle's left wing, returning beam electrons were observed.

Wave activity was sampled in zones 1, 4, and 7 near 2008:34 UT and in zones 3, 6, and 9 one minute later.

Electrons reaching any of SPREE's zones while the detector looked over the left wing had pitch angles near  $90^\circ$ . In the lower numbered zones (1, 3, 4), SPACE measurements indicate that electron fluxes in the 400- to 1180-eV range were modulated at frequencies of  $\sim 3$  and 3.9 MHz. When detected at lower energies, modulations were generally at  $\sim 3.3$  MHz. In the higher-numbered zones, SPACE detected modulations only in low-energy electron channels.

During the second event (day 217, 0620:02 – 0620:45 UT) the magnetic field was nearly perpendicular to the payload bay floor. SPREE generally detected monotonically decreasing electron fluxes over the 10 eV to 1.5 keV range. The range of pitch angles sampled by SPACE in zones 2, 5, and 8 extended from  $70^\circ$  to  $14^\circ$ . In all three zones the most intense modulations were at frequencies of  $\sim 3$  MHz. In zone 2, with pitch angles of  $70^\circ$ , the modulations were detected in channels sampling electrons with energies of a few hundred eV. In zones 5 and 8 (pitch angles of  $41^\circ$  and  $14^\circ$ ) electron flux modulations were confined to the 11 – 18 eV channels. At low energies the modulations were observed at frequencies down to 2 MHz.

In general, wave-particle interactions in a plasma fall into the categories of resonant and nonresonant. In resonant interactions the phase between the electric field of the wave and the particle motion is stationary. For magnetized electrons the resonance condition is expressed

$$\omega - k_{\parallel} v_{\parallel} + n \Omega_{ce} = 0 \quad (1)$$

where  $\omega$  and  $\Omega_{ce}$  are the angular wave frequency and the electron gyrofrequency,  $k_{\parallel}$  and  $v_{\parallel}$  represent the components of the wave vector and the electron velocity along the magnetic field, and  $n$  is an integer, harmonic number. The case  $n = 0$  represents the Landau resonance. Electrons that satisfy a resonance condition tend to become bunched as they entrain in a propagating wave. SPACE only detects bunched electrons. Nonresonant interactions do not satisfy (1), and any small-amplitude bunchings they produce fall below the SPACE's level of sensitivity. There are two classes of resonant electron distributions, those that amplify and those that damp a given wave mode. Amplifying electron distributions have free energy that can be transferred to the wave. Damping electron distributions extract kinetic energy at the expense of the wave fields. To see how these general principles apply to the SPREE/SPACE measurements, it is useful to consider the physical circumstances under which the measurements were made.

Hardy *et al.* [1995] analyzed electron distributions measured by SPREE during the period of FPEG emissions shown in Plate 1. While facing toward the shuttle's left wing ( $-Y$  direction), ESA B observed intense fluxes of beam electrons that propagated to SPREE in less than a gyroperiod. Beam spreading and scattering, perhaps by a virtual cathode near FPEG's aperture, are required for these electrons to reach the location of SPREE [Hardy *et al.*, 1995]. The most intense fluxes of beam electrons were detected in zone 0. Fluxes decreased rapidly with increasing zone number. In its low-

numbered zones, ESA B measured electron distribution functions that had strong positive slopes ( $\partial f/\partial v_{\perp} > 0$ ) in the energy range from several hundred eV to 1 keV (Figure 4d). For ESA A, saturation effects only allow measurements of electron distribution functions near beam energy in ESA A zones 4 and above. The top panel of Figure 4 shows that when looking in the direction of beam return, the distribution function in zone 4 had a broad plateau ( $\partial f/\partial v_{\perp} \approx 0$ ) from  $\sim 200$  eV to 1 keV. In this energy range SPACE detected electron flux modulations at  $\sim 3.9$  MHz. The critical, empirical point is that there exists a region in the vicinity of shuttle in which electron distribution functions have positive slopes and are the most likely source for waves detected by SPACE.

Within a small fraction of a second after beam turn on, a population of warm (10–200 eV) electrons appear at SPREE. Beam-generated ionization and locally enhanced heating of ionospheric plasma are the probable sources. Assessing the relative contributions to electron heating during beam emissions by lower hybrid waves [McBride *et al.*, 1972; Papadopoulos, 1984] and by the HF waves reported here, lies beyond the scope of this observational report. Suffice it to say that all electron distributions measured by SPREE in this energy range had negative slopes. Thus this part of the distribution is responsible for wave damping.

At the times of the two examples presented above,  $f_{ce} \approx 0.81$  and 0.77 MHz. Electrons with energies in the zero-slope part of the distribution function were modulated at  $\sim 3.9$  MHz. Beam electrons with pitch angles near  $90^\circ$  may be sources of upper hybrid or electron cyclotron harmonic (ECH) emissions [Tataronis and Crawford, 1970a, b]. The absence of low-harmonic ECH modulations may preclude the latter interpretation. It is possible that an electric field sensor on shuttle would have detected such beam-generated waves. This would indicate that resonant parts of the electron distribution function were too narrowly spread in energy to be detected by SPREE/SPACE. In the case at hand, if 3.9 MHz is the upper-hybrid frequency, then the plasma frequency is 3.78 MHz and the local plasma density is  $1.75 \times 10^5$ . For low-energy electrons to appear as bunched, they must see the upper hybrid waves that are Doppler shifted to some harmonic of  $f_{ce}$ . The observed modulations of 3.3 MHz are close to the fourth ( $n = -4$ ) cyclotron harmonic. Producing such a frequency downshift requires that  $k_{\parallel}$  and  $v_{\parallel}$  be in the same direction with the wave overtaking the electrons.

Although other scenarios are theoretically possible, and require further constraining analyses, we present one that kinematically describes our observations. If the central pitch angle of the FPEG beam is near  $90^\circ$ , beam electrons may move in both directions (Figure 2) or one (Figure 6) direction along the magnetic field, depending on its orientation with respect to shuttle. Upper hybrid modulations of beam electrons are seen when they directly impact SPREE. Waves generated by nonimpacting beam electrons propagate in the warm plasma both away from and back toward the shuttle.

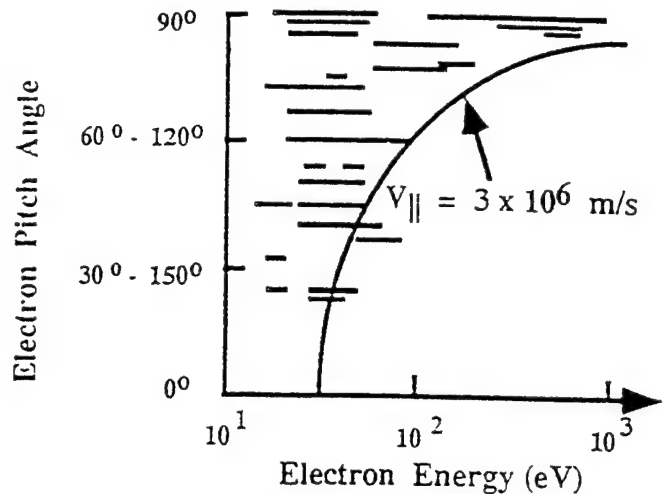


Figure 10. Summary of all 3–4 MHz modulations with electron energy plotted against pitch angle. Modulated electrons are generally those with parallel velocity components  $< 3 \times 10^6 \text{ m s}^{-1}$ .

Electrons with resonant  $v_{\parallel}$  are overtaken by the back propagating waves, Doppler shifting them down to the nearest cyclotron harmonic. Resonant electrons reaching SPREE/SPACE appear to be bunched at this frequency. Since the slope of the distribution is negative, the resultant wave-particle interaction damps the wave and increases the thermal energy of the warm electron population. Thus, if this part of the electron distribution had been measured further from the upper-hybrid wave source, the population would appear warmer and the ECH resonance amplitude weaker.

In the megahertz electron modulations reported here there is clear evidence of modulations just below or close to the beam energy as well as over a wide range of lower energies. The frequency of modulation observed is close to that observed previously with artificial beams, both to the strong waves reported during Spacelab 1 by Mourenas *et al.* [1989] at the harmonics of the electron gyrofrequency,  $nf_{ce}$ , nearest to  $f_{uhr}$ , and also to the beam induced wave activity observed on Echo 7 near  $f_{uhr}$  at around 4.2 MHz [Ginet and Ernstmeier, 1991].

Of particular note is the strong confinement of our modulations to cases where the FPEG beam has a pitch angle within a few degrees of  $90^\circ$ . Figure 10 shows a summary of all megahertz modulations plotted as a function of electron energy and pitch angle. Most of the measurements have maximum energies defined by the curve in Figure 10 corresponding to a maximum parallel velocity of  $3 \times 10^6 \text{ m s}^{-1}$ . At these times the parallel velocity component of the beam is very low and waves that can resonate with the beam electrons will also couple well with lower-energy electrons, with the wave frequency and electron parallel velocity satisfying equation 1 both near to the beam and at lower energies. Figure 11 illustrates this expected scenario. Both the electron beam and the lower-energy thermal electrons are within the same shaded region of Figure 11, corresponding to parallel velocity components:



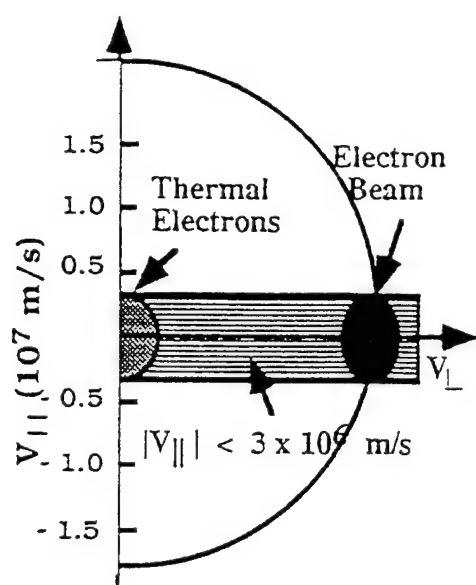


Figure 11. Schematic showing how the electron beam at 90° pitch angle shares the same narrow range of parallel velocities as the bulk of the thermal electrons.

$$|v_{||}| < 3 \times 10^6 \text{ m s}^{-1} \quad (2)$$

Figure 11 illustrates how beam electrons with ~90° pitch angles share the same narrow range of parallel velocities as the bulk of the thermal electrons.

The megahertz electron modulations reported here are also close to the frequencies observed to be modulating the natural auroral electron beam over auroral arcs [Gough and Urban, 1983; Gough et al., 1990] and to the frequency of the associated ground based radio wave measurements [Kellogg and Monson, 1979, 1984; Weatherwax et al., 1994]. This suggests that artificial electron beams mimic some of the features observed in the natural auroral electron beams after they evolved adiabatically for sufficient positive  $df(v)/dv_{\perp}$  to develop [Gough et al., 1990]. A reflight of TSS is presently planned as a 14 day mission. There should be sufficient time after the deployment phase to have an extended period devoted to 90° FPEG operations. We thus propose that ground-based radio measurements should be made in conjunction with this reflight mission when the beam is well defined and its modulation accurately measured. It is clear from the results presented here that beam pitch angles of ~90° and dc firing sequences should be scheduled for overflights of any ground sites. These should occur preferably at night when ionospheric absorption would be at a minimum. Although the FPEG emits only a 100-mA beam, its geometry leads to narrow-band modulations that should be observable on the ground.

**Acknowledgments.** This work was supported in part by the Particle Physics and Astronomy Research Council of the UK, by the U.S. Air Force Office of Scientific Research task 2311PL05 and by Air Force contract F19628-92-K-0006 with Boston College.

The Editor thanks I. H. Cairns and another referee for their assistance in evaluating this paper.

## References

- Abe Y., K. N. Erickson, and J. R. Winckler, ELF electric turbulence near an electron beam-emitting rocket in the auroral ionosphere: ECHO 6, *Planet. Space Sci.*, **36**, 235, 1988.
- Cairns I. H., and D. A. Gurnett, Plasma waves observed in the vicinity of the space shuttle, *J. Geophys. Res.*, **96**, 13913, 1991.
- Feng W., D. A. Gurnett, and I. H. Cairns, Interference patterns in the spacelab 2 plasma wave data: Oblique electrostatic waves generated by the electron beam, *J. Geophys. Res.*, **97**, 17005, 1992.
- Ginet G. P., and J. Ernstmeier, VLF plasma waves generated by an electron beam, in *Space, Physics of Space Plasmas*, **11**, edited by T. Chang, G. W. Crew, and J. R. Jasperse, Scientific Publishers, p. 209, Cambridge, Mass., 1991.
- Gough, M. P., A technique for rocket borne detection of electron bunching at megahertz frequencies, *Nucl. Instrum. Methods*, **177**, 581, 1980.
- Gough, M. P., Space particle correlator for AMPTE UKS spacecraft, *IEEE Geophys. Remote Sens.*, **GE23**, 305, 1985.
- Gough, M. P., Space instrument neural network for real-time data analysis, *IEEE Trans. Geosci. and Rem. Sens.*, **31**, 1264, 1994.
- Gough, M. P., and A. Urban, Auroral beam plasma interaction observed directly, *Planet. Space Sci.*, **31**, 875, 1983.
- Gough, M. P., P. J. Christiansen, and K. Wilhelm, Auroral beam-plasma interactions: Particle correlator investigations, *J. Geophys. Res.*, **95**, 12287, 1990.
- Gurnett, D. A., W. S. Kurth, J. T. Steinberg and S. D. Shawhan, Plasma wave turbulence around the shuttle: Results from the Spacelab 2 flight, *Geophys. Res. Lett.*, **15**, 760-763, 1988.
- Hardy, D. A., M. R. Oberhardt, W. J. Burke, D. C. Thompson, W. J. Raitt, and L. C. Gentile, Observations of electron beam propagation perpendicular to the Earth's magnetic field during the TSS 1 mission, *J. Geophys. Res.*, (in press), 1995.
- Kaufmann, R. L., Electrostatic wave growth: Secondary peaks in a measured auroral electron distribution function, *J. Geophys. Res.*, **85**, 1713, 1980.
- Kellogg, P. J., and S. J. Monson, Radio emissions from the aurora, *Geophys. Res. Lett.*, **6**, 297, 1979.
- Kellogg, P. J., and S. J. Monson, Further studies of auroral roar, *Radio Sci.*, **19**, 551, 1984.
- Lotko, W., and J. E. Maggs, Amplification of ES noise in cyclotron resonance with adiabatic auroral beam, *J. Geophys. Res.*, **86**, 3499, 1981.
- Maggs J. E., and W. Lotko, Altitude dependent model of the auroral beam and beam generated ES noise, *J. Geophys. Res.*, **86**, 3439, 1981.
- McBride, J. B., E. Ott, J. P. Boris, and J. H. Orens, Theory and simulation of turbulent heating by the modified two-stream instability, *Phys. Fluids*, **15**, 2367, 1972.
- Mourenas D., C. Beghin, and J. P. Lebreton, Electron cyclotron and upper hybrid harmonics produced by electron beam injection on Spacelab 1, *Ann. Geophys.*, **7**, 519, 1989.
- Oberhardt, M. R., D. A. Hardy, W. E. Slutter, J. O. McGarity, D. J. Sperry, A. W. Everest, A. C. Huber, J. A. Pantazis, and M. P. Gough, The shuttle potential and return electron experiment (SPREE), *Nuovo Cimento*, **17**, 67, 1994.
- Oberhardt, M. R., D. A. Hardy, D. C. Thompson, W. J. Raitt, E. Melchioni, C. Bonifazi, M. P. Gough, Positive spacecraft charging as measured by the Shuttle Potential

- and Return Electron Experiment, *IEEE Trans. Nucl. Sci.*, 40, 1532, 1993.
- Papadopoulos, K., On the shuttle glow (the plasma alternative), *Radio Sci.*, 19, 571-577, 1984.
- Pritchett P. L., A three-dimensional simulation model for electron beam injection experiments in space, *J. Geophys. Res.*, 96, 13,781, 1991.
- Tataronis, J. A., and F. W. Crawford, Cyclotron harmonic wave propagation and instabilities, 1, Perpendicular propagation, *J. Plasma Phys.*, 4, 231-248, 1970a.
- Tataronis, J. A., and F. W. Crawford, Cyclotron harmonic wave propagation and instabilities, 2, Oblique propagation, *J. Plasma Phys.*, 4, 249-264, 1970b.
- Weatherwax, A. T., J. LaBelle, M. L. Trimpi, and R. Brittain, Ground based observations of radio emissions near  $2f_{ce}$  and  $3f_{ce}$  in the auroral zone, *J. Geophys. Res.*, 99, 2109, 1994.
- Wilhelm K., W. Studemann, and W. Riedler, Observations of the electron spectrometer and magnetometer on board Spacelab 1 in response to electron accelerator operations, *Earth-Orient. Applic. Space Technol.*, 5, 47, 1985.
- Winckler J. R., et al., An electron beam experiment in the magnetosphere, *EOS Trans. Amer. Geophys. U.*, 70, 657, 1989.
- K. Bounar and B. McNeil, Radex Inc., Bedford, MA, 01730.
- W. J. Burke, D. A. Hardy, and M. R. Oberhardt, Phillips Laboratory, Hanscom AFB, MA, 01731.
- L. C. Gentile, Boston College Institute for Space Research, Newton, MA, 02159.
- M. P. Gough, Space Science Centre, University of Sussex, Brighton, England, BN1 9QT, United Kingdom.
- W. J. Raitt and D. C. Thompson, Center for Atmospheric and Space Sciences, Utah State University, Logan, UT, 84322.

(Received August 9, 1994; revised February 21, 1995;  
accepted February 21, 1995.)

# Observations of electron beam propagation perpendicular to the Earth's magnetic field during the TSS 1 mission

David A. Hardy, Marilyn R. Oberhardt, and William J. Burke

Phillips Laboratory, Hanscom Air Force Base, Massachusetts

Donald C. Thompson and William J. Raitt

Center for Atmospheric and Space Sciences, Utah State University, Logan

Louise C. Gentile

Boston College Institute for Space Research, Newton, Massachusetts

**Abstract.** We report on measurements by the Shuttle Potential and Return Electron Experiment (SPREE), acquired during a period of the Electrodynamic Tethered Satellite mission when the fast pulsed electron generator (FPEG) injected a 1-keV electron beam nearly perpendicular to the Earth's magnetic field. Using multiangular electrostatic analyzers mounted on rotary tables, SPREE was capable of determining the flux of electrons and ions in the energy range from 10 eV to 10 keV and over a solid angle of  $2\pi$  sr. SPREE was located in the shuttle bay where it could observe beam electrons after they had completed  $\sim 1$  gyrocycle when fired nearly perpendicular to the local magnetic field. For the case presented here, the beam's intensity decreased from  $\sim 100$  mA cm $^{-2}$  at FPEG's aperture to  $\sim 0.18$  nA cm $^{-2}$  at the location of SPREE. The spectrum of the return electrons displays a sharp peak at the beam energy with an intensity at the peak of approximately  $2 \times 10^{10}$  electrons cm $^{-2}$  s $^{-1}$  sr $^{-1}$ . The distribution of the electrons around the peak has a half width of several hundred eV, with observed energies as high as 1850 eV. For energies between 10 and a few hundred eV, intense fluxes of electrons are seen at all look angles. For angles where the beam is observed the spectrum in this energy range has a power law shape. At angles away from the direction of beam return, the spectrum in this energy range can display a more thermal shape with a peak at energies up to 50 eV. In general, the flux intensity in the lower-energy portion of the spectrum is isotropic with an average integral flux of  $0.5$  to  $2 \times 10^{12}$  electrons cm $^{-2}$  s $^{-1}$  sr $^{-1}$ . Integrating over energy and pitch angle gives number densities of  $\sim 5 \times 10^4$  electrons cm $^{-3}$ . The return current density of  $0.5$  to  $2 \mu\text{A cm}^{-2}$  s $^{-1}$  sr $^{-1}$  carried by this isotropic component is sufficient to balance that emitted by FPEG and keep the shuttle at a low potential. We find that both scattering and spreading of the beam near FPEG are necessary for primary electrons to reach the locations of the SPREE detectors.

## Introduction

A large body of literature deals with beam emissions from spacecraft in the ionosphere and with the special characteristics of the shuttle's environment. This paper considers some effects of electron beam emissions from shuttle. Recent electron beam-related studies divide conveniently into two broad categories, emphasizing either observations or simulations of beam interactions with the space environment, with the host vehi-

cle, and with itself. The generation of waves [Gurnett *et al.*, 1988; Bush *et al.*, 1987; Abe *et al.*, 1988; Farrell *et al.*, 1988; Winckler *et al.*, 1989; Reeves *et al.*, 1988, 1990], the heating of ambient plasmas [Arnoldy and Pollock, 1985; Winckler and Erickson, 1990], the creation of secondary ionization [Sasaki *et al.*, 1985; Myers *et al.*, 1989; Gülchrist *et al.*, 1990; Burke *et al.*, 1990], and the stimulation of optical emissions [Hess *et al.*, 1971; Halinan *et al.*, 1978; Banks and Raitt, 1988; Winckler *et al.*, 1989] are the major observed environmental effects. Spacecraft charging [Maehlum *et al.*, 1988], sheath generation [Denig *et al.*, 1991], and occasional damage to system components [Burke *et al.*, 1990] are observed beam effects on host vehicles. There are few observations of beam self-interactions. Observations of primary

beam fluxes at large distances from the point of emission [Winckler, 1992; Frank et al., 1989] indicate beams maintain some coherence over long distances.

Computer simulations provide insight into the physics of beam self-interactions, especially in the immediate vicinity of the emission aperture. As computing power has increased, these simulations have evolved from one [Winglee and Pritchett, 1987; Borovsky, 1988] to two [Okuda and Berchem, 1988; Winglee and Pritchett, 1988] and three [Pritchett, 1991] dimensions in configuration space. In all simulations, electrons upon emission initially slow as they approach a stagnation region. In the stagnation region some electrons are reflected toward the host vehicle, while the rest are accelerated away from it. The fraction of particles that escape depends on the ratio of the beam density to the background plasma density. In the simulations the estimated constraints on beam escape relax as the simulations grow in sophistication [Pritchett, 1991]. As simulated timescales and volumes increase and as effects of wave-plasma interactions are included, direct comparisons between simulation predictions and spacecraft observations will become more conclusive. Previous simulations were limited to a few centimeters of the emission aperture.

The immediate environment of the shuttle differs significantly from that of the unperturbed ionosphere through which it moves. Owing to outgassing, the shuttle can carry its own atmosphere [Narcisi et al., 1983]. Charge exchange between coorbiting shuttle-generated neutrals and ambient ions creates a relatively energetic (several eV) ion population [Stone et al., 1983; Hunton and Calo, 1985]. Through modified two-stream interactions these ions generate lower hybrid waves [Cairns, 1990; Cairns and Gurnett, 1991a, b], which in turn heat ambient electrons [Tanaka and Papadopoulos, 1983] in the vicinity of shuttle [McMahon et al., 1983]. This complex environment is sporadically modified by large quantities of neutral gas introduced during thruster firings to control the shuttle's attitude [Wulf and von Zahn, 1986; Machuzak et al., 1993].

This paper presents detailed measurements of primary beam electrons detected in close proximity to their emission aperture. In the present case, beam electrons were emitted nearly perpendicular to the Earth's magnetic field with an energy of  $\sim 1$  keV. The beam was emitted from the fast pulsed electron generator (FPEG) during the tethered satellite shuttle (TSS) mission and detected after less than a full gyrotorn by the Shuttle Potential and Return Electron Experiment (SPREE). All data were acquired while the tethered satellite was stowed in the shuttle's payload bay. The remainder of the paper is divided into three parts in which we describe the instrumentation, present two examples of single-turn beam measurements, and discuss their implications for understanding nearby effects of beam emissions.

## Instrumentation

The SPREE was an integral part of the TSS 1 flown in the payload bay of the shuttle Atlantis during the

forty-sixth flight of the Space Transportation System (STS 46). TSS 1 was a cooperative mission of the National Aeronautics and Space Administration (NASA) and the Italian Space Agency (ASI), with sensors also supplied by the United States Air Force. Atlantis flew (July 31 through August 7, 1992) in a  $28.5^\circ$  inclination orbit at an altitude of  $\sim 300$  km. The scientific objective of the mission was to specify the electrodynamic effects of deploying and retrieving an electrically conducting satellite connected to the shuttle by a conducting tether. Owing to the orbital motion of the combined system across the Earth's magnetic field a significant potential drop between the satellite and the shuttle was anticipated. A suite of instruments to monitor and control this potential difference and the current flowing in the tether, called the shuttle electrodynamic tether system (SETS), was flown in the payload bay [Banks et al., 1981; Aguero et al., 1994]. In this paper we are only concerned with the FPEG component of SETS.

Oberhardt et al. [1993, 1994] presented a detailed description of SPREE. Briefly, its core elements are two nested, triquadraspherical electrostatic analyzers (ESAs) that simultaneously measure fluxes of electrons and ions with energies between 10 eV and 10 keV over a  $100^\circ \times 8.5^\circ$  angular fan. The particle spectra were measured at rates of either 1 or  $8 \text{ s}^{-1}$  in 32 channels, logarithmically spaced in energy. In parallel with its normal counting, SPREE also monitored the differences in arrival times of individual electrons in selected zones to identify particle bunching signifying resonant wave-particle interactions. Results of correlation measurements during FPEG firings are discussed by Gough et al. [1995]. The  $100^\circ$  dimension of the angular fan was divided into 10 zones of  $10^\circ$  width, designated 0 through 9. Ion and electron spectra are measured independently in each zone. Zone 0 has its lower edge  $5^\circ$  below parallel to the base of the ESA units, while zone 9 looks  $5^\circ$  beyond shuttle zenith. Each ESA was mounted on a rotary table that turned through  $180^\circ$  every 30 s. The two analyzers and rotary tables, designated detectors A and B, were mounted back to back and were synchronized so that both ion and electron spectra were sampled over a solid angle of  $2\pi \text{ sr}$  every 30 s. To assure unsaturated measurements during electron beam operations, the geometric factors of ESA B were set at  $\sim 100$  times smaller than those for ESA A. The energy resolution for electron channels is  $\delta E/E \approx 7\%$ .

The FPEG instrument consists of a flexible electron beam system capable of generating 100 mA in either DC or pulsed modes. Beam electrons had an initial energy of  $\sim 1$  keV as they were emitted through an aperture of 0.56-cm radius. At the aperture the beam had a magnetically controlled divergence of  $7.5^\circ$  [Banks and Raitt, 1988]. The vector magnetic field at the location of shuttle was measured once each second by a three-axis flux gate aspect magnetometer (AMAG).

Figure 1 schematically represents FPEG and SPREE mounted on the mission peculiar equipment support structure (MPESS), located aft of the TSS 1 satellite in the shuttle bay [Dobrowolny and Stone, 1994]. The two instruments are almost coplanar and separated by  $\sim 1.3$

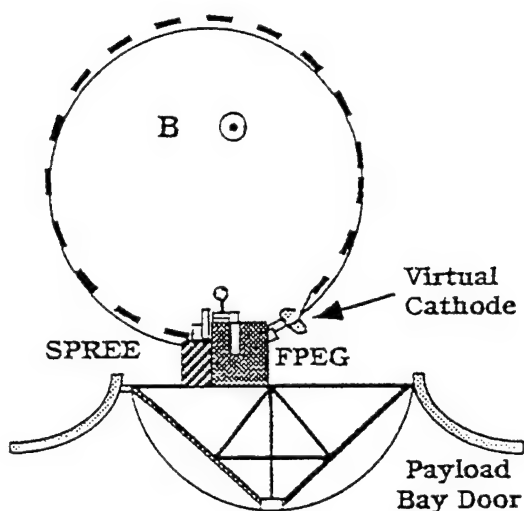


Figure 1. Schematic representation of the relative positions of SPREE and FPEG on TSS 1. The trajectories of 1-keV-beam electrons following perturbed (dashed line) and unperturbed (solid line) orbits in the Earth's magnetic field are provided for illustration.

m. In considering beam-electron trajectories, we adopt a shuttle-based coordinate system with the origin at the FPEG aperture. The  $X$ ,  $Y$ , and  $Z$  axes are positive toward shuttle's nose, right wing, and nadir, respectively. The center of the FPEG beam makes an angle of  $23^\circ$  in the  $Y$ ,  $Z$  plane above the  $Y$  axis. In this coordinate system, the approximate locations of apertures for SPREE ESAs A and B when looking over the shuttle's left wing are  $(-0.113, -1.311, -0.140)$  and  $(-0.473, -1.300, -0.140)$  m, respectively. We designate the fan direction angles for the aperture of ESA A as  $0^\circ$  when it faces  $-Y$ ,  $90^\circ$  facing  $+X$ , and  $180^\circ$  facing  $+Y$ . The look direction of ESA B rotates from  $180^\circ$  through  $270^\circ$  when facing  $-X$ , to  $360^\circ$ .

## Observations

We report on SPREE measurements acquired during two periods on August 3, 1992 (Julian day 216), from 2006:30 to 2011:35 UT and from 2006:46 to 2017:15 UT. During these events, the shuttle was in darkness approaching the geographic equator from the south at an altitude of  $\sim 300$  km, and FPEG was operating in its DC mode. Although electrons with beam energies reached both SPREE ESAs, only data from ESA B are presented. Owing to its larger geometric factor, ESA A was in saturation while facing in the direction of electron beam return. Plate 1 shows color spectrograms of electron fluxes measured in zones 0 and 2 of ESA B during the 90-s interval from 2007:00 to 2008:30 UT. During this period the instrument operated in the fast sweep mode sampling 8 energy spectra  $s^{-1}$ . In Plate 1 the energy range of the instrument is plotted on the  $Y$  axis, and time on the  $X$  axis. Flux intensities are represented by color in units of electrons  $cm^{-2} s^{-1} sr^{-1} eV^{-1}$ . Plate 1 is annotated at 30-s intervals with UT and the rotary fan direction angles. As described above,

at  $180^\circ$ , detector B's fan pointed toward FPEG, and at  $360^\circ$  directly away from it. The central look direction for zone 0 is parallel to the MPRESS mounting surface while zone 2 is centered  $20^\circ$  up in elevation. Below the measurements, Plate 1 indicates the look direction of the sensor apertures with respect to the magnetic field. The ingoing surface normal to the apertures gives the pitch angles of the measured particles for the two zones. During this sequence FPEG operated in a 30 s on, 15 s off duty cycle. While FPEG was off, electron flux levels were below the detector's sensitivity threshold. We note in passing that measured fluxes of pickup ions were significantly enhanced by electron beam operations and by thruster firings.

Plate 1 illustrates several key characteristics of this event. First, in zone 0, with the detection fan at rotary table angles of  $\sim 360^\circ$  and FPEG emitting, SPREE measured electron spectra that were sharply peaked at 1 keV for pitch angles of  $\sim 90^\circ$ . We postulate that the spectra result from the direct return of the beam electrons to the shuttle at the location of ESA B after they have executed almost a full gyrocycle after emission from FPEG. The return electrons were observed twice in the interval, as the rotary table swept toward then away from its point of maximum rotation. Second, the spectral peak at 1 keV occurs over a narrow angular range. We estimate that the angular extent is  $\sim 6^\circ$  full width at half maximum (FWHM) in the rotation angle of the table. This is in fact an upper bound, since this angular width is less than the  $8.5^\circ$  acceptance angle of the detector. The angular extent is somewhat broader in zonal angle, with the flux at 1 keV decreasing by only 60% in the  $10^\circ$  between zones 0 and 1. Third, when the 1-keV peak is observed, intense electron fluxes are seen at all energies below 1 keV measured by SPREE. While the electron flux at the peak drops off at higher elevation zones, below a few hundred eV it remains approximately constant. Fourth, between 10 and 60 eV, intense fluxes were seen in both zones at all rotation angles while FPEG was emitting. This electron flux is largest when the 1-keV peak was detected, but slightly lower when the zone 0 detector fan was looking toward FPEG, probably due to partial shadowing of electron trajectories by the SETS structure.

That we are observing directly returning beam electrons is supported in Figure 2, which shows an accurate model of the shuttle. The solid line represents the unperturbed trajectory of a 1-keV electron emitted in the center of the FPEG beam at 2007:54 UT. At this time the measured magnetic field was  $(-28, 123, -3281, -3750)$  nT in the shuttle coordinate system described above. We note that the center of the beam should return to the left side of shuttle slightly below and forward of SPREE's location in the shuttle bay.

Figures 3 and 4 provide examples of the differential number flux spectra measured during the period of interest. Figure 3 contains electron spectra detected in the 5 even-numbered zones at the time of the 1-keV flux maximum observed in zone 0. At this time all five zones were measuring pitch angles close to  $90^\circ$ . The figure shows that the highest intensity of 1-keV flux was



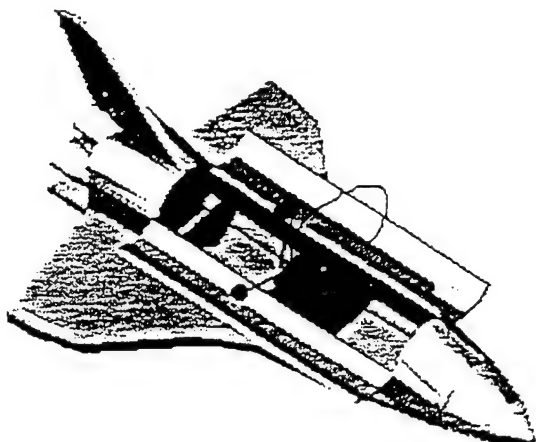


Figure 2. Scale model of the shuttle showing the unperturbed trajectory of an electron emitted in the center of the FPEG beam.

observed in zone 0 and that the intensity fell sharply with increasing zone. In this case the flux at 1 keV is  $2.8 \times 10^{10}$  electrons  $\text{cm}^{-2} \text{s}^{-1} \text{sr}^{-1} \text{eV}^{-1}$  in zone 0,  $6.14 \times 10^8$  in zone 2, and below  $10^8$  in zone 4. The figure also shows that the spread in energy of electrons about the 1-keV peak is much broader than the nominal 30-eV thermal spread of the emitted beam. In zone 0 the flux increase starts in the 671-eV channel with measurable fluxes continuing through the 1184-eV channel. At lower energies the maximum flux occurs at 8.3 eV, the lowest energy channel of SPREE, with values as high as  $4 \times 10^{11}$  electrons  $\text{cm}^{-2} \text{s}^{-1} \text{sr}^{-1} \text{eV}^{-1}$ . For the lower-

energy electrons, the flux generally decreased with increasing energy. A power law fit to this portion of the differential number flux spectrum shows that the flux varies as  $\sim E^{-2}$ . Note that while the flux at the 1-keV peak decreases sharply with increasing zone number, the flux in the lower-energy portion of the spectrum shows little if any variation. As a result the integral number flux over the full SPREE energy range falls from  $9.6 \times 10^{12}$  electrons  $\text{cm}^{-2} \text{s}^{-1} \text{sr}^{-1} \text{eV}^{-1}$  in zone 0 to only  $\sim 2.4 \times 10^{12}$  electrons  $\text{cm}^{-2} \text{s}^{-1} \text{sr}^{-1} \text{eV}^{-1}$  in zone 2 and all higher-numbered zones. The integral energy flux varies more strongly with zone, dropping from  $6.9 \times 10^{12}$  keV  $\text{cm}^{-2} \text{s}^{-1} \text{sr}^{-1}$  in zone 0 to between 5 and  $9 \times 10^{11}$  keV  $\text{cm}^{-2} \text{s}^{-1} \text{sr}^{-1}$  in zone 4 and all higher zones. Also note that no electron spectral peaks occur at low energies, as would be expected if the shuttle charged positive during FPEG operations. We conclude that if shuttle charged positive, it was by  $<9$  V.

Figure 4 shows the even-zone electron spectra taken when ESA B looked  $\sim 90^\circ$  away from the direction of the beam return. Here, intense fluxes are still observed at low energies with the highest differential number flux in the 10- to 15-eV channels. The maximum fluxes of a few times  $10^{10}$  electrons  $\text{cm}^{-2} \text{s}^{-1} \text{sr}^{-1} \text{eV}^{-1}$  are much lower than those observed near the direction of beam return. At low energies the spectra do not consistently follow the power law as seen near the return beam direction. Rather they either exhibit power law shapes or have clear peaks in the energy range from 20 to 50 eV. The peaked spectra are not well fit by Maxwellian distributions. Despite the variation in spectral shape

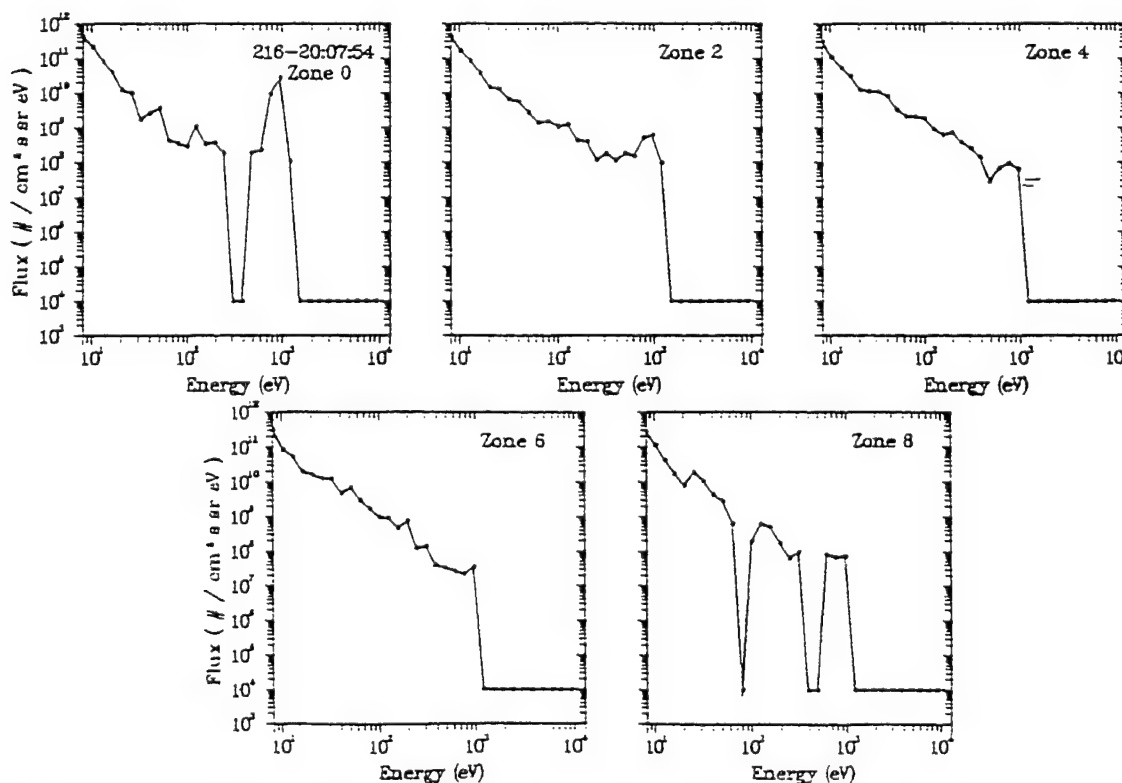


Figure 3. Directional differential fluxes measured in the even-numbered zones when ESA B faced in the direction of maximum beam return.



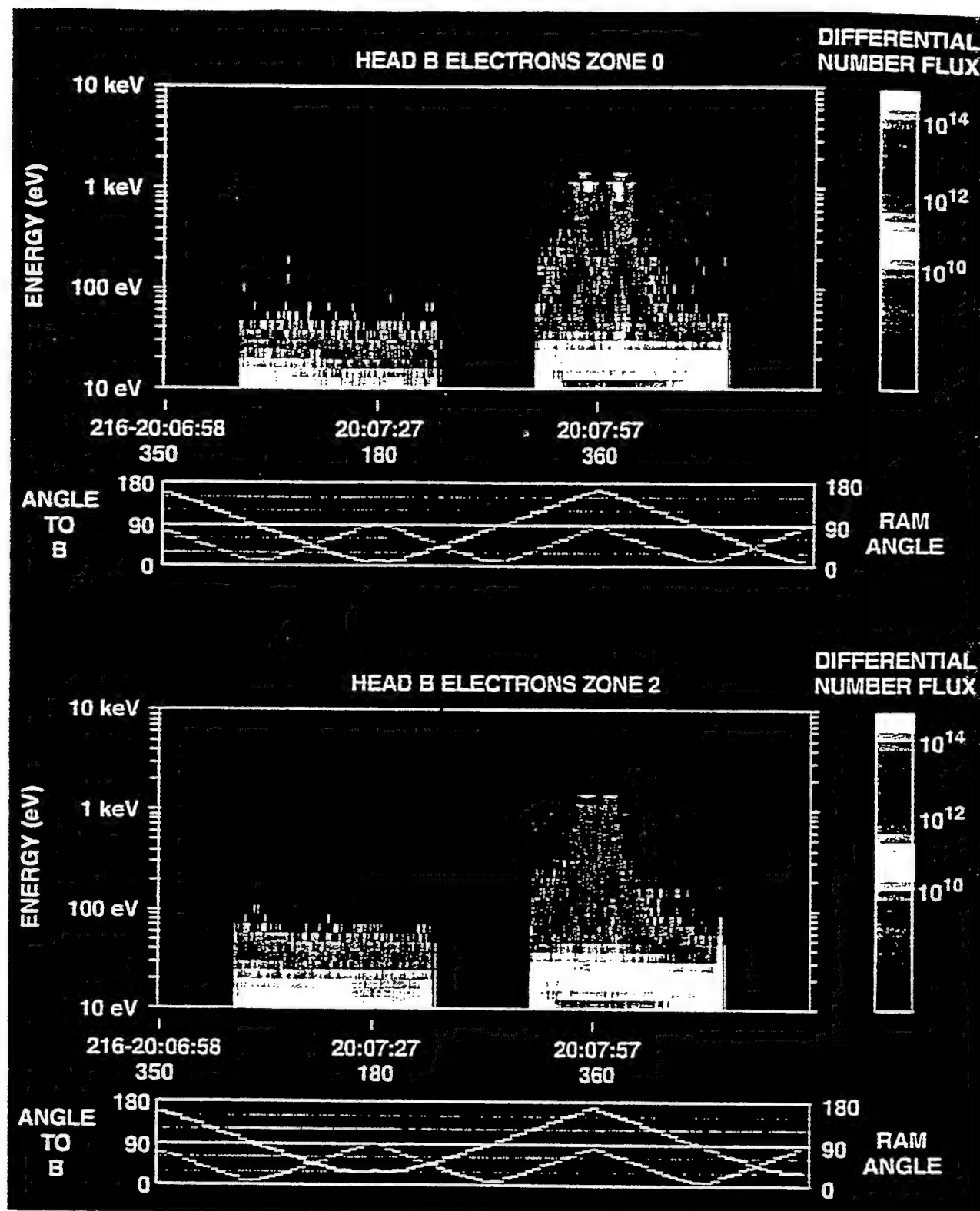


Plate 1. Directional differential fluxes of energetic electrons measured by ESA B, zone 0 (top panel) and zone 2 (bottom panel) near 2008 UT in an energy-versus-time spectrogram format. The angles of the fan direction and of the detector with respect to the Earth's magnetic field are indicated.

over the zones, the integral number flux of the spectra varies only between  $0.42$  and  $1.0 \times 10^{12}$  electrons  $\text{cm}^{-2} \text{s}^{-1} \text{sr}^{-1}$ , and the integral energy flux between  $0.7$  and  $2.3 \times 10^{10}$  keV  $\text{cm}^{-2} \text{s}^{-1} \text{sr}^{-1}$ .

Integrating the SPREE measurements over energy and solid angle, we estimate that the current density for the returning electron beam was  $\sim 18 \text{ nA cm}^{-2}$ . The current density coming from the more isotropic, lower-

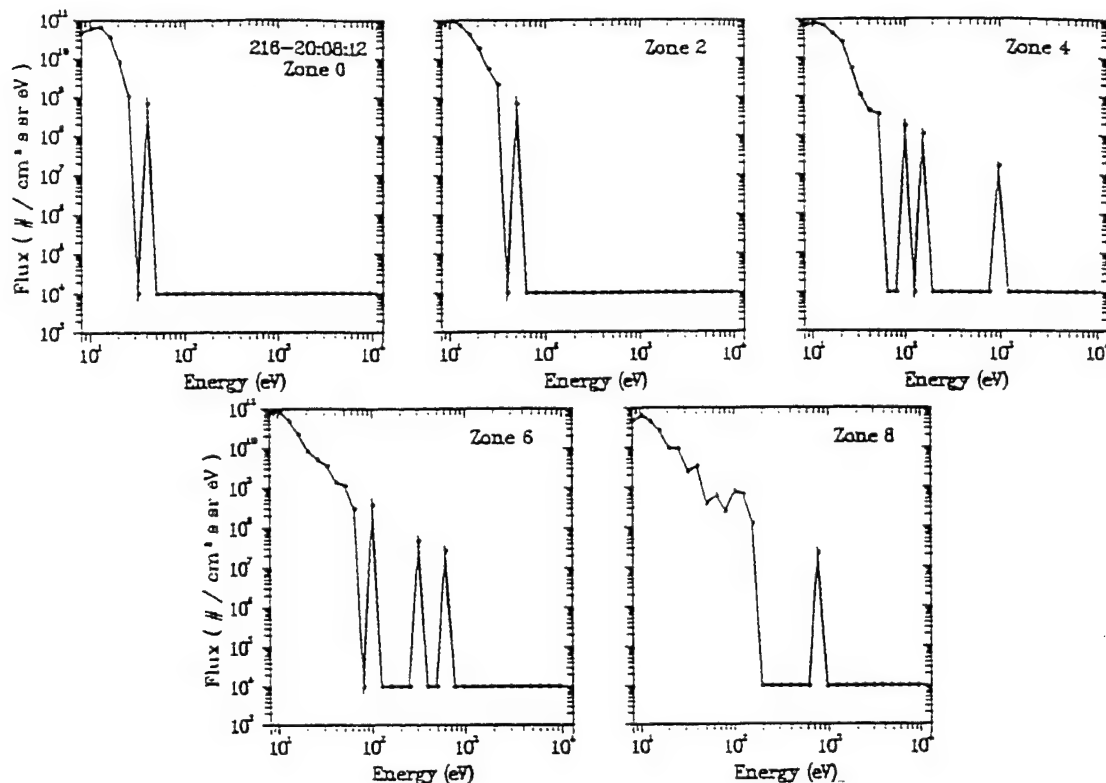


Figure 4. Directional differential fluxes measured in the even-numbered zones when ESA B faced 90° away from the direction of maximum beam return.

energy portion of the spectrum was between 0.5 and 2  $\mu\text{A cm}^{-2}$ . Thus the low-energy portion of the spectrum supplies the majority of the return current to the shuttle needed to balance the 100 mA emitted by FPEG. For an average return current from the low-energy electrons of 1  $\mu\text{A cm}^{-2}$  a conducting surface area of only 10 m<sup>2</sup> is needed. Approximately this amount of conducting surface is available near the SPREE instruments.

The number density of the two components was also estimated from the SPREE measurements. For the high-energy beam component we calculate a density of  $\sim 18$  electrons cm<sup>-3</sup>. The low-energy component density is between  $10^4$  and  $5 \times 10^4$  electrons cm<sup>-3</sup>. The smaller of these low-energy electron densities was calculated for the period prior to 2007:35 UT; the higher value came from the period starting at 2007:48 UT. This difference in density is probably an effect of a thruster firing which altered the ambient neutral gas density. The key point to note is that at the location of SPREE the density of low-energy electrons greatly exceeds that of the beam particles, and is comparable to the ionospheric densities expected near the shuttle's location.

Between 2006:30 and 2011:35 UT, there were a total of eight DC pulses of 35-s duration in which the same general behavior was observed. During four of these pulses, the orientation of SPREE was such that intense returns of beam electrons were measured. In total, six measurements were made of the peak return flux at  $\sim 1$  keV. Over the entire interval, the pitch angle at the center of the FPEG emission varied from 91° to 85.3°. Table 1 lists the characteristics of the 1-keV fluxes for each of the six observations. Column 1 gives the time of each observation, columns 2 and 3 the position at which beam electrons from the center of the FPEG emission following unperturbed trajectories would cross the  $Y = -1.3$  m plane containing the SPREE apertures, column 4 the pitch angle for the center of the FPEG emission, and column 5 the peak integral number flux over the energy range from 380 eV to 1850 eV. One can see that over the interval the center of the unperturbed beam would have moved from a position  $\sim 1.3$  m forward of the SPREE location to a position  $\sim 1.71$  m aft and from 0.16 to 0.61 m in the  $Z$  direction. Despite this movement, the intensity of the

Table 1. Beam Return Characteristics

UT	$X_m$	$Z_m$	$\alpha$	Flux ( $\times 10^{12} \text{ cm}^{-2} \text{ s}^{-1}$ )
2007:54	1.30	0.16	91.0°	7.17
2008:54	-0.17	0.33	89.4°	6.88
2009:54	-0.96	0.47	87.4°	7.46
2010:54	-1.71	0.61	85.3°	8.85
2016:54	-5.86	2.35	69.7°	2.25
2017:00	-61.3	2.17	68.2°	1.74

return flux was relatively unchanged. At 1 keV the flux varied between  $1.46$  and  $2.37 \times 10^{12}$  electrons  $\text{cm}^{-2} \text{s}^{-1} \text{sr}^{-1} \text{eV}^{-1}$  with an average value of  $2.11 \times 10^{12}$  electrons  $\text{cm}^{-2} \text{s}^{-1} \text{sr}^{-1} \text{eV}^{-1}$ . The integral number flux ranged between  $5.91$  and  $9.00 \times 10^{12}$  electrons  $\text{cm}^{-2} \text{s}^{-1} \text{sr}^{-1}$  with an average value of  $7.52 \times 10^{12}$  electrons  $\text{cm}^{-2} \text{s}^{-1} \text{sr}^{-1}$ . There is no falloff in these values with increasing  $X$  and  $Z$  distances from the SPREE aperture. This finding indicates that the intensity of the beam is relatively uniform over a spatial extent of at least 3 m at the plane containing the SPREE aperture after the electrons have executed  $\sim 1$  gyrotum.

By the onset of the second interval at 2016:46 UT, the shuttle's orientation has changed such that the FPEG was emitting at pitch angles of  $\sim 70^\circ$ . Plate 2 is an energy-versus-time spectrogram of the differential number flux of electrons measured in zone 1 from 2016:30 to 2018:00 UT. During this interval the largest differential number flux at 1 keV was measured in this zone. The figure illustrates that even for this relatively large pitch angle for FPEG emission, a significant flux at approximately 1 keV is still observed when the SPREE is sampling at pitch angles close to  $90^\circ$ . The two observations of the peak 1-keV flux are listed in Table 1. The 1-keV flux and the integral number flux have decreased by factors of about 6 and 3.3, respectively, despite the fact that an unperturbed trajectory for electrons at the center of the FPEG emission should have mapped almost 6 m tailward of the SPREE in one gyrotum. Again, this indicates the high degree of spreading of the beam that must be occurring. While the level at 1 keV has decreased at pitch angles of  $90^\circ$ , the fluxes

at low energies for rotary table angles away from the direction of beam particle return are still comparable to the measurements shown in Plate 1.

We examined three other intervals during the TSS 1 mission when the FPEG was operated in the DC mode at beam emission pitch angles of approximately  $90^\circ$ . In these three cases the magnetic field direction was approximately out of the shuttle bay. In particular, all three events have approximately the same spectral shape and range in density for the isotropic low-energy component of the electrons.

### Summary and Discussion

While the shuttle was oriented such that FPEG fired almost perpendicular to the Earth's magnetic field, SPREE detected part of the beam returning after the electrons executed almost a full gyrocycle. The electron spectrum is strongly peaked at 1 keV. Electrons were also observed with energies several hundred eV above and below the emitted beam energy. Since the energy resolution of any channel  $\delta E/E$  is 7%, the observed spread in energy cannot be purely an instrumental effect. The intensity of the beam electrons decreased from  $100 \text{ mA cm}^{-2}$  at FPEG's aperture to  $18 \text{ nA cm}^{-2}$  at the location of SPREE. At lower energies the electron flux is nearly isotropic, with energy spectra that either have power law shapes or exhibit peaks between 20 and 50 eV. The density estimated for this low-energy component varied between  $1$  and  $5 \times 10^4$  electrons  $\text{cm}^{-3}$ . The return current provided by this plasma component is sufficient to balance the 100 mA emitted by FPEG, and to maintain low shuttle potentials.

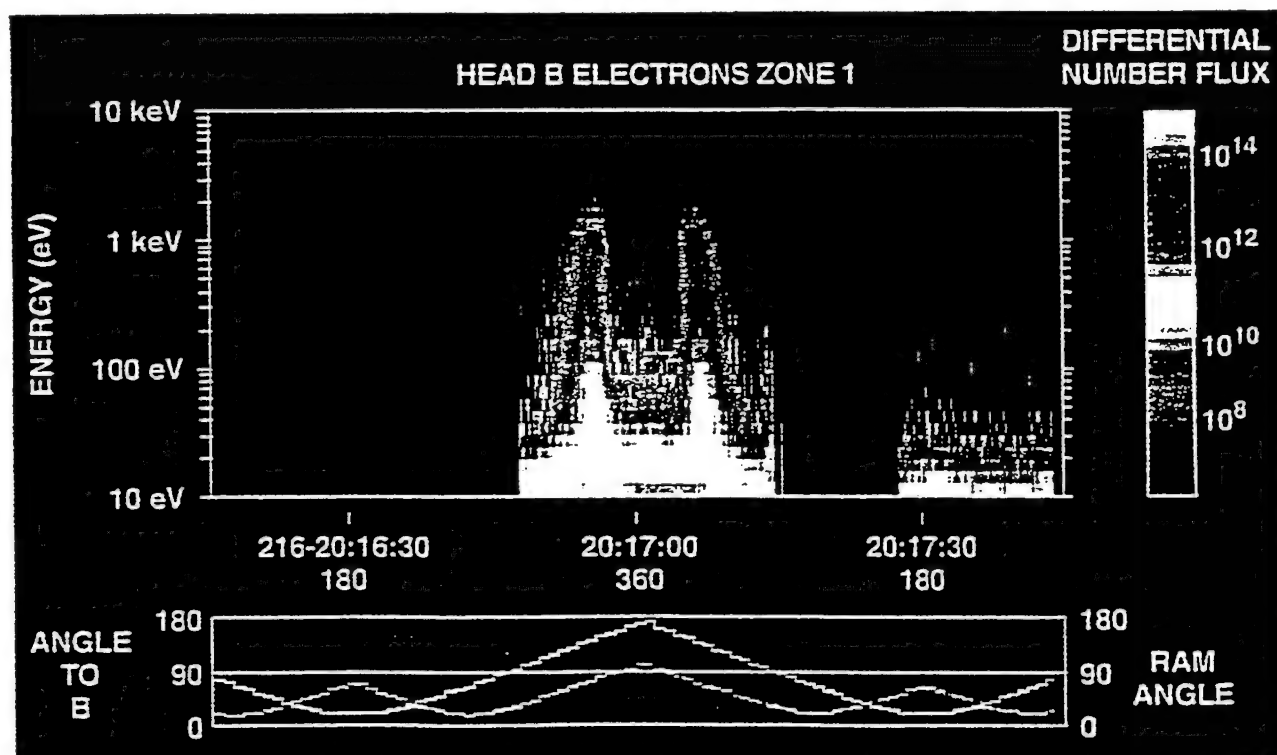


Plate 2. Directional differential fluxes measured by ESA B in zone 1 near 2017 UT, presented in the same format as Plate 1.

The remainder of this section is divided into two subsections. The first discusses the kinematics of beam electrons and, given the magnetic field configuration, the conditions required for beam electrons to reach the location of SPREE. The second subsection compares the present measurements with those reported from previous sounding rocket and shuttle flights, concentrating on the observations of low-level charging of the shuttle during FPEG operations, and enhanced fluxes of low-energy electrons indicating heating of the ambient ionospheric population. We then propose a qualitative framework for understanding shuttle-environment interactions during electron beam operations.

### Kinematics of Beam Electrons

Data shown in Plates 1 and 2 indicate that when FPEG emitted at pitch angles near  $90^\circ$  some beam electrons impacted the shuttle near the location of SPREE. The fluxes measured by SPREE are most intense when the ESAs sampled pitch angles almost perpendicular to the Earth's magnetic field. In the following analysis we concentrate on conditions near 2007:58 UT when an intense beam return was measured by ESA B (Plate 1 and Figure 3). We find that simple considerations of electron trajectories cannot account for the observations. At the time of the observations, the magnetic field intensity was 28,561 nT, the electron gyroperiod was  $1.25 \mu\text{s}$  and the gyroradius of a 1-keV ( $1.36 \times 10^7 \text{ m s}^{-1}$ ) electron,  $\leq 3.72 \text{ m}$ . For the purpose of illustration, we approximate the magnetic field as being in the  $-X$  direction. Figure 1 contains a to-scale sketch of an electron's trajectory after being emitted from FPEG at an angle of  $23^\circ$  above the shuttle's right wing. Allowing only for gyromotion, we see that the electron impacts the SPREE mounting bracket below the detectors. Figure 2 also shows that at 2007:58 UT the center of the beam crosses the plane of the SPREE detectors ( $Y = -1.3 \text{ m}$ ) well forward of the detectors. In fact, all electrons emitted within the nominal cone of  $7.5^\circ$  about the beam's center impact the SPREE mounting bracket or the payload bay door. None should reach the apertures of either ESA. Using the real magnetic vector  $\mathbf{B} = (-28,123, -3281, -3750) \text{ nT}$ , we find that electrons near the center of the FPEG beam have pitch angles of  $\sim 94^\circ$ . After 0.93 gyrotorn they cross the  $Y = -1.3 \text{ m}$  plane forward of ESA A by 1.5 m. The closest any electron emitted within the  $7.5^\circ$  beam cone should get to SPREE, as it crosses the  $Y = -1.3 \text{ m}$  plane, is 0.45 m forward of ESA A's aperture.

We first investigated whether the observations could be explained by the beam being emitted in a cylindrically symmetric cone whose angular FWHM is  $7.5^\circ$ . Computer simulations indicate that such a beam divergence might arise because of Coulomb repulsion as electrons emerge from a beam generator [Winglee and Pritchett, 1988]. The spreading takes place on the spatial scale of a beam Debye length, as the density of the beam decreases from its injection value to that of the ambient plasma. For a 1-keV,  $100 \text{ mA cm}^{-2}$  beam, the electron density is  $10^9 \text{ cm}^{-3}$ , and its Debye length is

$\sim 2 \text{ cm}$ . If we assume that the ambient density is  $10^5 \text{ cm}^{-3}$ , then to conserve current the beam radius must expand from 0.56 cm to  $\sim 20 \text{ cm}$ . Thus the half-angle spread about the center of the beam is  $> 80^\circ$ . If the beam is truly charge neutral, then the distribution of electrons must be uniform throughout this cone. However, it is reasonable to expect that while the beam flux is cylindrically symmetric and therefore uniform in azimuth angle, it depends strongly on the colatitude angle  $\beta$  with respect to the center of the beam. We assume that the flux  $F$  has a power law functional relation to  $\beta$  given by  $F(\beta) = F_0 \cos^N(\beta)$ . Regarding  $F(\beta = 7.5^\circ)$  as some fraction of the central flux  $F_0$ , we can calculate  $N$ . Since the  $7.5^\circ$  half-angle cone represents the FWHM, then  $F(7.5^\circ) = 0.5$ , and  $N = 80$ . For this case,  $F(\beta = 15^\circ) = 0.06 F_0$ , and  $F(\beta = 30^\circ) = 10^{-5} F_0$ .

In making calculations there are three natural coordinate systems, those of the shuttle, the beam, and the magnetic field. Appropriate transformations between these coordinate systems are needed. Consider first the beam whose centroid is  $23^\circ$  above the shuttle's right wing. We define a coordinate system  $(X', Y', Z')$  obtained by rotating counterclockwise  $23^\circ$  about the shuttle's  $X$  axis. In these coordinates the center of the beam is emitted along the  $Y'$  axis. The direction of any beam electron's initial velocity can be expressed in terms of two angles, which we designate  $\beta$  and  $\gamma$ . Here,  $\beta$  is a colatitude angle measured from the  $Y'$  axis. The azimuth angle  $\gamma$  is measured from the  $X'$  axis in the  $X', Z'$  plane. If we designate the speed of beam electrons as  $V_0$ , the velocity of electrons in the  $(X', Y', Z')$  coordinate system is

$$\begin{bmatrix} V_{X'} \\ V_{Y'} \\ V_{Z'} \end{bmatrix} = V_0 \begin{bmatrix} \sin \beta \cos \gamma \\ \cos \beta \\ -\sin \beta \sin \gamma \end{bmatrix} \quad (1)$$

In the shuttle coordinate system the initial velocity vectors of beam electrons are

$$\begin{bmatrix} V_X \\ V_Y \\ V_Z \end{bmatrix} = V_0 \begin{bmatrix} \sin \beta \cos \gamma \\ \cos 23^\circ \cos \beta - \sin 23^\circ \sin \beta \sin \gamma \\ -\sin 23^\circ \cos \beta - \cos 23^\circ \sin \beta \cos \gamma \end{bmatrix} \quad (2)$$

In the shuttle's frame of reference the Earth's magnetic field is constant and stationary over the period of a single electron gyration. The magnetic field can be represented in terms of standard colatitude and azimuth angles  $\theta$  and  $\phi$ .

$$\begin{bmatrix} B_X \\ B_Y \\ B_Z \end{bmatrix} = B \begin{bmatrix} \sin \theta \cos \phi \\ \sin \theta \sin \phi \\ \cos \theta \end{bmatrix} \quad (3)$$

For calculating electron trajectories it is useful to define a coordinate system  $(X'', Y'', Z'')$  in which  $\mathbf{B}$  is in the  $-X''$  direction. The matrix  $\mathbf{R}$  needed to accomplish this transformation and its inverse  $\mathbf{R}^{-1}$  are given in Appendix 1. The initial velocity of beam electrons in this coordinate system is obtained by  $\mathbf{V}_{X''} = \mathbf{R} \mathbf{V}_X$ . In

this system the velocity of a beam electron as a function of time is

$$\begin{bmatrix} V_{X''} \\ V_{Y''} \\ V_{Z''} \end{bmatrix} = \begin{bmatrix} -V_{||} \\ V_{\perp} \cos(\Omega t + \Psi) \\ -V_{\perp} \sin(\Omega t + \Psi) \end{bmatrix} \quad (4)$$

where the parallel and perpendicular subscripts indicate electron speeds parallel and perpendicular to the magnetic field and  $\Psi$  represents the initial phase angle. Comparing values of  $V_{X''}$  obtained by letting  $R$  operate on (2) with the representation in (4), we find that

$$V_{||} = V_0 [\cos \theta (\cos 23^\circ \sin \beta \sin \gamma - \sin 23^\circ \cos \beta) + \sin^2 \theta \cos \phi \sin \phi \sin \beta \cos \gamma + (\cos 23^\circ \cos \beta - \sin 23^\circ \sin \beta \sin \gamma)] \quad (5)$$

Since  $V_{||} = V_0 \cos \alpha$ , (5) allows a simple determination of the pitch angle  $\alpha$  for any values of  $\beta$  and  $\gamma$ . Similarly, using  $V_{Y''}$  obtained by letting  $R$  operate on (2) with its representation in (4) allows a determination of  $\Psi$ . We next integrate (4) to get the particle trajectory as a function of time

$$\begin{bmatrix} X'' \\ Y'' \\ Z'' \end{bmatrix} = \begin{bmatrix} V_{||} t \\ \rho [\sin(\Omega t + \Psi) - \sin \Psi] \\ \rho [\cos(\Omega t + \Psi) - \cos \Psi] \end{bmatrix} \quad (6)$$

where  $\rho$  represents the beam electron gyroradius. The locations of beam particles in shuttle coordinates are obtained by applying the inverse transformation  $X = R^{-1}X''$ .

We have solved the equations of motion numerically for a large class of initial particle emission angles ( $\beta, \gamma$ ) to determine the  $(X, Z)$  where they crossed the  $Y = -1.3$  m plane. The results of this analysis are summarized in the form of a map in Figure 5. Here we have plotted the crossing locations for particles with  $\beta = 0^\circ, 7.5^\circ, 15^\circ$ , and  $30^\circ$  in increments of  $10^\circ$  in  $\gamma$  from  $0^\circ$  to  $360^\circ$ . The  $(X, Z)$  locations of ESAs A and B are represented symbolically in the figure. For  $\beta > 30^\circ$  the crossing locations move further away from the ESAs.

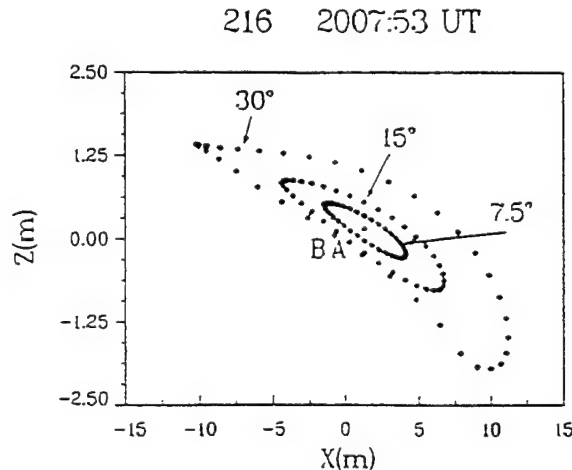


Figure 5. Maps of  $X, Z$  locations where beam electrons cross the  $Y = -1.3$ -m plane for  $\beta = 0^\circ, 7.5^\circ, 15^\circ$ , and  $30^\circ$ . The increments of  $\gamma$  are  $10^\circ$ . Locations of SPREE detectors A and B are indicated.

Figure 5 uses the magnetic field measured by AMAG and shows that both detectors are located outside of all mapping contours. Our calculations demonstrate that this is true for all values of  $\beta$ . From this we see that with the existing magnetic field, beam electrons following unperturbed orbits cannot reach either ESA.

How then may we understand the fact that beam electrons reach both SPREE detectors if they cannot do so following unperturbed orbits? We offer a qualitative explanation based on published results of computer simulations [Winglee and Pritchett, 1988; Pritchett, 1991]. As mentioned above, the simulations all show that as beam electrons emerge from their source, they slow down as they approach a virtual cathode. Electrons that eventually escape are able to penetrate the region of negative space charge and accelerate to their initial kinetic energy. During the transition through the virtual cathode the velocities and gyroradii of beam electrons decrease relative to their unperturbed values. After passing through the space charge a reaccelerated electron continues in a gyroorbit similar to its unperturbed trajectory. Figure 1 shows that the effect of passing through the region of smaller gyroradii is to shift the electron's center of gyration in the  $-Z$  direction. This in turn shifts the points where their trajectories cross the  $Y = -1.3$  m plane. Relatively small shifts in orbital gyrocenters bring particles with  $\beta > 15^\circ$  and  $\gamma \approx 250^\circ$  into the vicinity of the SPREE detectors. The relatively small variations in the flux of 1-keV electrons measured by SPREE while the pitch angle of FPEG emissions changed, suggests that electron scattering near the FPEG aperture is quite robust.

#### Comparison With Previous Space Flights

SPREE data indicate that the shuttle charged to positive potentials of  $\leq 9$  V during DC firings. By comparison, several recent sounding rocket flights carrying electron beam experiments and conducting tethered probes returned data indicating that beam firings can produce large positive potentials. MAIMIK emitted an 8-keV electron beam with currents between 20 and 800 mA. At the higher emitted currents the emitting payload charged to potentials in excess of the beam's energy [Maehlum et al., 1988]. The CHARGE 2 rocket emitted a 1-keV beam with currents between 6 and 36 mA. Its tethered payloads charged to significant fractions of the beam energy [Myers et al., 1989] except when the attitude control system (ACS) ejected large quantities of  $N_2$  into the local environment. Collected return currents increased and the vehicle potentials decreased to small values [Gulchrist et al., 1990]. During the ECHO 7 flight the beam-emitting payload charged between several hundred volts and  $>5$  kV. ACS gas releases decreased charging to several times the ionization potential of  $N_2$  [Burke et al., 1990].

We suggest two possible effects that contribute to the shuttle potential remaining near zero during DC beam operations. First, the total conducting area of the shuttle, between 25 and 35  $m^2$ , is much larger than that of sounding rockets. For such a collecting area, a plasma



density of  $\sim 10^5 \text{ cm}^{-3}$  is sufficient to balance the output electron current of 100 mA from FPEG. Such a density is normal at shuttle altitudes during daylight portions of its orbit. Under nightside conditions the ambient plasma density should be  $\sim 10^4 \text{ cm}^{-3}$ , too low to balance the FPEG current. Second and more important, FPEG firings create a dense, isotropic electron population at energies up to  $\sim 100 \text{ eV}$  which is sufficient to balance the emitted current. The data suggest that firings at pitch angles close to  $90^\circ$  produce a perturbed, cylindrical volume with radial dimension of the order of the 1-keV electron gyroradius. Within the cylinder an isotropic population of low-energy electrons is produced. This isotropic electron population has a density of  $1 \text{ to } 5 \times 10^4 \text{ cm}^{-3}$  and carries a return current to shuttle of  $0.5 \text{ to } 1 \mu\text{A cm}^{-2} \text{ sr}^{-1}$ . Since this is much higher than the ambient return current, a conducting area of  $\sim 10 \text{ m}^2$  is needed to balance FPEG emissions. This is an upper bound on the required conducting area, since we have not included the contributions of electrons with energies below the lower-energy limit of SPREE detection. The grounded, conducting thermal blanketing near SPREE has approximately this surface area. The large-scale spreading of the electron beam suggested by our study indicates that the region of the low-energy, isotropic fluxes could easily extend to other conducting areas on the shuttle.

Such a current balance picture still leaves a problem. If electrons within the cylindrical volume balance the FPEG current, there still must be a current of 100 mA passing from the ambient plasma into the cylinder to maintain charge neutrality. If we assume that the cylinder has the dimension of a 1-keV electron gyroradius, the ambient plasma density is  $10^4 \text{ cm}^{-3}$ , and electrons are transported into the cylinder at approximately their thermal speeds, then the cylinder would only have to be  $\sim 15 \text{ m}$  long for transport across the surface to balance the current return to the shuttle.

There also remain questions regarding the processes that create the low-energy electrons. There are several empirical constraints. First, the intensity of the isotropic component is approximately the same in the four cases examined, even though two were in sunlight and two in darkness. This finding implies that the creation of this population does not depend strongly on the initial, ambient plasma density. Second, for the two night cases the density of the isotropic component was equal to or exceeded the expected ambient plasma density. Thus the creation of this superthermal population must involve the ionization and subsequent heating of the neutral gas near the shuttle. Third, an explanatory model must account for fluxes that are 2 to 3 orders of magnitude larger than the suprathermal return electrons detected by *Arnoldy et al.* [1985] on the beam-emitting ECHO 5, which made no independent measurements of the vehicle potential. The suprathermal electrons measured by ECHO 5 were accompanied by a population of  $\sim 0.5\text{-keV}$  ions that had been accelerated perpendicular to the magnetic field. The authors

argue that these accelerated ions play a significant role in the plasma processes accompanying beam injection. No accelerated ions were detected in any of the SPREE cases.

It is also possible that initially different local environments of the shuttle and sounding rockets play significant roles. The shuttle moves at orbital speeds of  $\sim 7.5 \text{ km s}^{-1}$ , almost perpendicular to the direction of the magnetic field. This is the most favorable relative orientation of the shuttle's velocity vector and the magnetic field for generating intense lower hybrid turbulence [*Cairns and Gurnett, 1991a*]. These waves grow from the absorption of free energy contained in ring or arc distributions of pickup ions, created in the charge exchange interactions [*Cairns and Gurnett, 1991a*]. *Machuzak et al.* [1993] suggested that these lower hybrid waves heat ambient electrons and are responsible for electron high-energy ( $\leq 100 \text{ eV}$ ) tails detected in the shuttle bay by *McMahon et al.* [1983]. Many of these electrons had sufficient energies to create secondary ionization. Sounding rockets, on the other hand, have relatively small, suborbital velocities across magnetic field lines. Thus even in the presence of significant outgassing and charge exchange, conditions should stay below the threshold of instability for generating lower hybrid waves by the modified two-stream interaction. Without lower hybrid waves, the thermal energies of ambient electrons remain near ionospheric levels. Thus at beam turn-on the initial ionospheric electron environment of shuttle may be much warmer than that of a sounding rocket.

After beam turn-on a wide variety of wave modes are observed in the vicinity of shuttle [*Gurnett et al., 1988*] and sounding rockets [*Winckler et al., 1989*]. While a detailed examination of the various wave modes is beyond the scope of this observational paper, we note that their free energy source resides either directly in the beam or in the perturbed local plasma. The beam affects background electrons through Coulomb collisions and Landau damping of beam-generated waves. The ambient plasma may be perturbed in two ways. First, if part or all of the beam escapes, then a return current carried by ambient electrons must flow away from the host vehicle. The directed energy of the return current electrons is mostly along the magnetic field. If the flow speed of the current carriers exceeds various critical values, the plasma becomes unstable to the growth of ion cyclotron or ion acoustic waves [*Kindel and Kennel, 1971; Feng et al., 1992*]. Second, if the beam particles are not space-charge neutralized along the beam trajectory, ambient ions experience irregular electric field structures. In crossing such space-charge structures, nearby ions are accelerated and follow irregular orbits [*Winckler and Erickson, 1990*]. In the acceleration region they develop arc distributions which are sources of enhanced lower hybrid waves. In either case the waves damp through their interactions with local electrons, further heating them. It appears that the initially warmer distribution of electrons near shuttle than



near sounding rockets may provide a critical difference for producing the enhanced suprathermal electrons detected by SPREE.

## Appendix

For simplicity in calculations it is useful to transform the measured magnetic field into a coordinate system in which the magnetic vector is in the  $-X''$  direction. The transformation  $R$  is effected by two rotations. The first is through an angle  $(\phi - \pi)$  about the  $Z$  axis. The second is through an angle of  $(\pi/2 - \theta)$  about the intermediate  $Y$  axis. In this coordinate system the orbital calculations are very simple. The results may then be transformed back into the shuttle frame by using  $R^{-1}$ . The rotation matrix and its inverse are given by

$$R = \begin{pmatrix} -\sin \theta \cos \phi & -\sin \theta \sin \phi & -\cos \theta \\ \sin \phi & -\cos \phi & 0 \\ -\cos \theta \cos \phi & -\cos \theta \sin \phi & \sin \theta \end{pmatrix}$$

and

$$R^{-1} = \begin{pmatrix} -\sin \theta \cos \phi & \sin \phi & -\cos \theta \cos \phi \\ -\sin \theta \sin \phi & -\cos \phi & -\cos \theta \sin \phi \\ -\cos \theta & 0 & \sin \theta \end{pmatrix}$$

**Acknowledgments.** This work was supported in part by the U.S. Air Force Office of Scientific Research task 2311PL04 and by Air Force contract F19628-92K-0006 with Boston College. The authors also acknowledge the work of N. Bonito, C. Roth, K. Bounar, and W. McNeil in developing the graphics software for display and analysis of the SPREE data.

The Editor thanks C. J. Pollock and L. A. Frank for their assistance in evaluating this paper.

## References

- Abe, Y., K. N. Erickson, and J. R. Winckler, ELF electric turbulence near an electron beam-emitting rocket in the auroral ionosphere: ECHO 6, *Planet. Space Sci.*, **36**, 235, 1988.
- Aguero, V., P. M. Banks, B. Gilchrist, I. Linscott, W. J. Raitt, D. Thompson, V. Tolat, A. B. White, S. Williams, and P. R. Williamson, The shuttle electrodynamic tether system (SETS) on TSS 1, *Nuovo Cimento Soc. Ital. Fis. C*, **17**, 49, 1994.
- Arnoldy, R. L., and C. Pollock, The energization of electrons and ions by electron beams injected in the ionosphere, *J. Geophys. Res.*, **90**, 5197, 1985.
- Banks, P. M., and W. J. Raitt, Observation of electron beam structure in space experiments, *J. Geophys. Res.*, **93**, 5811, 1988.
- Banks, P. M., P. M. Williamson, and K. L. Oyana, Electrical behavior of a shuttle electrodynamic tether system (SETS), *Planet. Space Sci.*, **29**, 139, 1981.
- Borovsky, J. E., The dynamic sheath: Objects coupling to plasmas on electron-plasma-frequency time scales, *Phys. Fluids*, **31**, 1074, 1988.
- Burke, W. J., G. Murphy, and P. R. Malcolm, ACS gas effects on the charging of ECHO 7, paper presented at AIAA 21st Fluid Dynamics, Plasma Dynamics and Lasers Conference, Am. Inst. of Aeronaut. and Astronaut., Seattle, Wash., 1990.
- Bush, R. I., G. D. Reeves, P. M. Banks, T. Neubert, P. R. Williamson, W. J. Raitt, and D. A. Gurnett, Electromagnetic fields from pulsed electron beam experiments in space: Spacelab 2 results, *J. Geophys. Res.*, **92**, 1015, 1987.
- Cairns, I. H., Transition from ring to beam arc distributions of water ions near the space shuttle orbiter, *J. Geophys. Res.*, **95**, 15,167, 1990.
- Cairns, I. H., and D. A. Gurnett, Control of plasma waves associated with the space shuttle by the angle between the orbiter's velocity and the magnetic field, *J. Geophys. Res.*, **96**, 7591, 1991a.
- Cairns, I. H., and D. A. Gurnett, Plasma waves observed in the near vicinity of the space shuttle, *J. Geophys. Res.*, **96**, 13,913, 1991b.
- Denig, W. F., N. C. Maynard, W. J. Burke, and B. N. Maehlum, Electric field measurements during supercharging events on the MAIMIK sounding experiment, *J. Geophys. Res.*, **96**, 3601, 1991.
- Dobrowolny, M., and N. H. Stone, A technical overview of TSS 1: The first tethered satellite mission, *Nuovo Cimento Soc. Ital. Fis. C*, **17**, 1, 1994.
- Farrell, W. M., D. A. Gurnett, P. M. Banks, R. I. Bush, and W. J. Raitt, An analysis of whistler mode radiation from the Spacelab 2 electron beam, *J. Geophys. Res.*, **93**, 153, 1988.
- Feng, W., D. A. Gurnett, and I. H. Cairns, Interference patterns in the Spacelab 2 plasma data: Oblique electrostatic waves generated by the electron beam, *J. Geophys. Res.*, **97**, 17,005, 1992.
- Frank, L. A., W. R. Paterson, M. Ashour-Abdalla, D. Schriver, W. S. Kurth, D. A. Gurnett, N. Omidi, P. M. Banks, R. I. Bush, and W. J. Raitt, Electron velocity distributions and plasma waves associated with the injection of an electron beam into the ionosphere, *J. Geophys. Res.*, **94**, 6995, 1989.
- Gilchrist, B. E., P. M. Banks, T. Neubert, P. R. Williamson, N. B. Myers, W. J. Raitt, and S. Sasaki, Electron collection enhancement arising from neutral gas jets on a charged vehicle in the ionosphere, *J. Geophys. Res.*, **95**, 2469, 1990.
- Gough, M. P., D. A. Hardy, M. R. Oberhardt, W. J. Burke, L. C. Gentile, B. McNeil, K. Bounar, D. C. Thompson, and W. J. Raitt, Correlator measurements of megahertz wave-particle interactions during electron beam operations on STS 46, *J. Geophys. Res.*, in press, 1995.
- Gurnett, D. A., W. S. Kurth, J. T. Steinberg, P. M. Banks, R. I. Bush, and W. J. Raitt, Whistler-mode radiation from the Spacelab 2 electron beam, *J. Geophys. Res.*, **93**, 162, 1988.
- Hallinan, T. J., H. C. Stenbaek-Nielsen, and J. R. Winckler, The ECHO IV electron beam experiment: Television observations of artificial auroral streaks indicating strong beam interactions in the high-latitude magnetosphere, *J. Geophys. Res.*, **83**, 3263, 1978.
- Hess, W. N., M. G. Trichel, T. N. Davis, W. C. Beggs, G. E. Kraft, E. Stassinopoulos, and E. J. R. Maier, Artificial auroral experiment: Experiment and principal results, *J. Geophys. Res.*, **76**, 1442, 1971.
- Hunton, D. E., and J. M. Calo, Low energy ions in the shuttle environment: Evidence for strong ambient-contaminant interactions, *Planet. Space Sci.*, **33**, 945, 1985.
- Kindel, J. M., and C. F. Kennel, Topside current instabilities, *J. Geophys. Res.*, **76**, 3055, 1971.
- Machuzak, J. S., W. J. Burke, J. M. Retterer, D. E. Hunton, J. R. Jasperse, and M. Smiddy, Effects of thruster firings

- on the shuttle's plasma and electric field environment, *J. Geophys. Res.*, **98**, 1513, 1993.
- Maehlum, B. N., J. Troim, N. C. Maynard, W. F. Denig, M. Friedrich, and K. M. Torkar, Studies of the electric charging of the tethered electron accelerator mother-daughter rocket MAIMIK, *Geophys. Res. Lett.*, **15**, 725, 1988.
- McMahon, W., R. Salter, R. Hills, and D. Delorey, Measured electron contribution to shuttle plasma environment, in Proceedings of the AIAA Shuttle Environment and Operations Meeting, *Rep. AIAA-83-2598*, pp. 52-58, Am. Inst. of Aeronaut. and Astronaut., Washington, D. C., 1983.
- Myers, N. B., W. J. Raitt, B. E. Gilchrist, P. M. Banks, T. Neubert, P. R. Williamson, and S. Sasaki, A comparison of current-voltage relationships of collectors in the Earth's ionosphere with and without electron beam emissions, *Geophys. Res. Lett.*, **16**, 365, 1989.
- Narcisi, R., E. Trzcinski, G. Federico, L. Wlodyka, and D. Delorey, The gaseous and plasma environment around the space shuttle, in Proceedings of the AIAA Shuttle Environment and Operations Meeting, *Rep. AIAA-83-2659*, pp. 183-190, Am. Inst. of Aeronaut. and Astronaut., Washington, D. C., 1983.
- Oberhardt, M. R., D. A. Hardy, I. Katz, M. P. Gough, and D. C. Thompson, Vehicle charging as measured by the shuttle potential and return electron experiment aboard the TSS-1, paper presented at AIAA 31st Aerospace Sciences Meeting and Exhibit, Am. Inst. of Aeronaut. and Astronaut., Reno, Ne., 1993.
- Oberhardt, M. R., D. A. Hardy, W. E. Slutter, J. O. McGarity, D. J. Sperry, A. W. Everest, A. C. Huber, J. A. Pantazis, and M. P. Gough, The shuttle potential and return electron experiment (SPREE), *Nuovo Cimento Soc. Ital. Fis. C*, **17**, 67, 1994.
- Okuda, H., and J. Berchem, Injection and propagation of a nonrelativistic electron beam and spacecraft charging, *J. Geophys. Res.*, **93**, 175, 1988.
- Pritchett, P. L., A three-dimensional simulation model for electron beam injection experiments in space, *J. Geophys. Res.*, **96**, 13,781, 1991.
- Reeves, G. D., P. M. Banks, A. C. Fraser-Smith, T. Neubert, R. I. Bush, D. A. Gurnett, and W. J. Raitt, VLF wave stimulation by pulsed electron beams injected from the space shuttle, *J. Geophys. Res.*, **93**, 162, 1988.
- Reeves, G. D., P. M. Banks, T. Neubert, R. Harker, and D. A. Gurnett, VLF wave emissions by pulsed electron beams in space, 2, Analysis of Spacelab 2 results, *J. Geophys. Res.*, **95**, 6505, 1990.
- Sasaki, S., N. Kawashima, M. Yanagisawa, T. Obayashi, W. T. Roberts, D. L. Reasoner, W. W. L. Taylor, P. R. Williamson, P. M. Banks, and J. L. Burch, Ignition of beam plasma discharge in the electron beam experiment in space, *Geophys. Res. Lett.*, **12**, 647, 1985.
- Stone, N. H., U. Samir, K. H. Wright Jr., D. L. Reasoner, and S. D. Shawhan, Multiple ion streams in the near vicinity of the space shuttle, *Geophys. Res. Lett.*, **10**, 1215, 1983.
- Tanaka, M., and K. Papadopoulos, Creation of high-energy electron tails by means of the modified two-stream instability, *Phys. Fluids*, **26**, 1697, 1983.
- Winckler, J. R., Controlled experiments in the Earth's magnetosphere with artificial electron beams, *Rev. Mod. Phys.*, **64**, 859, 1992.
- Winckler, J. R., and K. N. Erickson, Plasma heating, electric fields and plasma flow by electron beam ionospheric injection, *Adv. Space Res.*, **10**(7), 119, 1990.
- Winckler, J. R., et al., ECHO 7: An electron beam experiment in the magnetosphere, *EOS Trans. Am. Geophys. Union*, **70**, 657, 1989.
- Winglee, R. M., and P. L. Pritchett, Space charge effects during the injection of dense electron beams into space plasmas, *J. Geophys. Res.*, **92**, 6114, 1987.
- Winglee, R. M., and P. L. Pritchett, Comparative study of cross-field and field-aligned electron beams in active experiments, *J. Geophys. Res.*, **93**, 5823, 1988.
- Wulf, E., and U. von Zahn, The shuttle environment: Effects of thruster firings on the gas density and composition in the payload bay, *J. Geophys. Res.*, **91**, 3270, 1986.

---

W. J. Burke, D. A. Hardy, and M. R. Oberhardt, Geophysics Directorate, Phillips Laboratory (AFMC), 29 Randolph Rd., Hanscom AFB, MA, 01731. (e-mail burke@plh.af.mil)

L. C. Gentile, Boston College Institute for Space Research, 885 Centre Street, Newton, MA 02159. (e-mail gentile@plh.af.mil)

W. J. Raitt and D. C. Thompson, Center for Atmospheric and Space Sciences, Utah State University, Logan, UT, 84322. (e-mail raitt@cc.usu.edu)

(Received July 8, 1994; revised December 8, 1994; accepted January 24, 1995.)

The U.S. Government is authorized to reproduce and sell this report.  
Permission for further reproduction by others must be obtained from  
the copyright owner.

# Evidence for magnetic disconnection of mass ejections in the corona

David F. Webb<sup>1</sup>

Institute for Space Research, Boston College, Newton Center, Massachusetts

Edward W. Cliver

Geophysics Directorate, Phillips Laboratory, Hanscom Air Force Base, Massachusetts

**Abstract.** Coronal mass ejections (CMEs) involve the expulsion of significant amounts of mass and magnetic flux into the heliosphere, a process which implies an unobserved continuous buildup of the net interplanetary magnetic flux. Some form of disconnection of the flux near the Sun, either directly associated with the CME or occurring elsewhere in the corona, appears to be required to prevent this buildup. Field line reconnection in the wake of CMEs is also a fundamental aspect of some types of magnetically driven eruptive flare/CME models. However, to date there have been very few reports of CMEs which exhibited evidence for disconnection, despite the detection of several thousand CMEs over nearly 2 decades of observations. We report on the results of a systematic search for candidate magnetic disconnection features, defined as transient large-scale, concave-outward bright regions usually following the CME leading edge, using both ground-based solar eclipse and spaceborne coronagraph data. We conclude that  $\geq 10\%$  of all CMEs observed in the corona have possible disconnection structures. We propose a simple classification scheme for these features based on their morphology. The most common type of candidate disconnection feature (65% of all the features) had a circular or ovoid shape; 35% of the features consisted of concave-outward partial arcs. The average leading edge speed and latitudinal span of these CMEs were slightly less than those of typical CMEs. The results are discussed in the context of recent studies of magnetic disconnection and reconnection in the corona.

## 1. Introduction

Solar coronal mass ejections (CMEs), defined as observable changes in coronal structures occurring on time scales of minutes to hours and involving new, discrete bright features in the field of view of a coronagraph [Hundhausen *et al.*, 1984], have been an important field of coronal studies since Skylab. CMEs are of interest because they involve discrete injections of mass and magnetic fields into the solar wind. The most energetic CMEs are associated with interplanetary shock waves and are geophysically important [Webb, 1993; Gosling, 1993].

The basic properties of the CMEs themselves have been determined from the data sets compiled from the Skylab [MacQueen *et al.*, 1974], P78-1 SOLWIND

[Sheeley *et al.*, 1980], and SMM [MacQueen *et al.*, 1980] orbiting coronagraphs. Recent reviews by Kahler [1987, 1992], Harrison [1991], Webb [1992], and Hundhausen [1995] discuss the general properties of CMEs. The basic structure of many CMEs has been determined to consist of three components: a bright leading edge, followed by a dark, low-density cavity and a bright core of denser prominence material [Illing and Hundhausen, 1985; Webb and Hundhausen, 1987].

Both observational and theoretical efforts to understand the development of CMEs have concentrated on the early phases of these events. Most CME-related theory has been directed toward understanding the conditions that give rise to CMEs (see recent reviews by Steinolfson [1991], Low [1993], and Dryer [1994]). Less effort has been made toward understanding how the large-scale magnetic field structures opened during a CME evolve after the CME has passed through the corona into the heliosphere [see MacQueen, 1980; Kahler, 1987]. In their summary of Skylab CMEs, Gosling *et al.* [1974] found that the CMEs seemed to retain their connection to the sun for several days following the passage of the CME itself. The Skylab observations fostered the concept that CMEs are planar loop structures having "legs." However, many CMEs

<sup>1</sup>Also at Geophysics Directorate, Phillips Laboratory/GPSG, Hanscom Air Force Base, Massachusetts.

do not show a simple looplike structure, and more detailed analyses suggest that CMEs have a more three-dimensional form [Webb, 1988].

Anzer and Poland [1979] examined the changes in the "legs" of several Skylab CMEs and concluded that these structures remain visible for more than a day, first dimming then brightening. Recently, Kahler and Hundhausen [1992] studied the late phase of 16 SMM CMEs and concluded that the bright structures following many CMEs can be more plausibly interpreted as the tops of helmet streamers which trace neutral sheets in the corona. Such streamers might have reformed following the reconnection of coronal fields during and after the CME. An outstanding example of the reformation of a large helmet streamer as observed by the Yohkoh satellite and the Mauna Loa K-coronameter has been reported by Hiei *et al.* [1993].

A fundamental question concerning magnetic fields ejected from the Sun was discussed by Gold [1962] and subsequently applied to CMEs by Gosling [1975] and MacQueen [1980]. They argued that the continual ejection of such magnetic structures from the Sun should cause the net magnetic flux permeating the interplanetary medium to increase indefinitely. Since no such buildup is observed, the paradox could be resolved by having the extended CME field lines pinch off and disconnect, forming a set of closed loops near the solar surface and an outward propagating closed magnetic structure in the outer corona. The CME magnetic flux would then be convected out of the heliosphere by the solar wind. Recently, McComas *et al.* [1992a] have used in-situ measurements at 1 AU to address the flux buildup problem. We will address this problem further in the Discussion section.

Evidence for newly closed magnetic loops near the solar surface following CMEs includes X-ray long-decay events which, as they cool, become visible in EUV, then H $\alpha$  [MacCombie and Rust, 1979]. These loops exhibit no motion, appearing to cool in place. Mass is convected upward from the chromosphere to fill the newly reconnected flux tubes [Forbes *et al.*, 1989]. That these X-ray arcades can last for many hours suggests that reconnection must continue in the low corona long after the departure of the CME. Nonthermal emission detected at hard X-ray and radio wavelengths is also often observed from the low-lying arcades. This emission may arise from electrons accelerated below the CME at an X-type reconnection point or current sheet [Cliver *et al.*, 1986]. Another class of coronal activity suggestive of disconnection is the moving metric type IV radio event, which has been interpreted as emission from accelerated particles trapped in a plasmoid which may lie within the CME [e.g., Kundu *et al.*, 1989].

The Kopp and Pneuman [1976] model explicitly addressed the magnetic field configuration in the late phase of eruptive flares and featured the gradual reconnection of field lines opened by some unspecified process. The model was successful in explaining the formation of new loops, the kinematics of the growth of the loops and separation of the bright footpoints, and

the energy release pattern. Since then, related theoretical efforts have involved modifications to the basic model and have continued to assume a key role for reconnection during eruptive events [e.g., Forbes *et al.*, 1989; cf. Svestka and Cliver, 1992]. It must be noted, however, that these models are intended to explain the small-scale "postflare" loop and eruptive prominence phenomena, and do not necessarily apply to the larger-scale structures involved in CMEs.

Anzer and Pneuman [1982] were among the first to specifically attempt to wed the postflare loop concept to CMEs in general. In their model, field lines stretched open during the eruption of a prominence and its surrounding CME reconnect beneath the CME. This process forms a magnetic loop system over the magnetic inversion line at the surface (the long-duration flare) and an upper loop system disconnected from the Sun (the CME). The two systems are connected at an X-type reconnection point, presumably lying just above the uppermost flare loop, which rises as the system evolves. More recent magnetically driven CME models have involved numerical simulations of a sudden release of magnetic energy stored and built up in the corona. Mikic and Linker [1994] review such efforts and, in particular, describe the dynamical evolution of arcades due to shear flows in the photosphere. Using MHD simulations with finite resistivity, they find that when a critical shear value is exceeded, the rising arcade field lines open forming a current sheet. Rapid reconnection at the current sheet leads to fast flows, dissipation of magnetic energy, and the ejection of a plasmoid (a CME; see their Figure 6).

Other simulations [e.g., Forbes, 1990] imply that reconnection in the current sheet below a filament or flux rope may occur very rapidly, ejecting the filament. The rising flux rope creates flows which tend to stretch the current sheet until it becomes thin enough to undergo rapid reconnection. X-ray images obtained from Yohkoh of an eruptive limb event on December 2, 1991 have been interpreted as evidence of such rapid reconnection (P. Martens, private communication, 1993). The images appear to show the ejection of a plasmoid in association with a two-ribbon flare. Martens has compared this observed structure with modeled field lines derived from the Martens and Kuin [1989] circuit model. That model uses a current filament added to a background field of line-dipoles to represent the evolution of a flux rope. The excellent agreement of the model field with the Yohkoh images of this event, including an observed vertical structure with a long current sheet, lends support to the postflare/plasmoid scenario.

Assuming that the coronal plasma outlines magnetic field structures, one signature of the upper disconnection process in the low or middle corona would be an outward moving circular or ovoid "plasmoid." Figures 1 and 2 show some examples of such features as they might appear within a few solar radii of the solar limb. Figure 1a shows a broad, circular-shaped CME wherein the contrast across a bright band (denser-than-ambient)



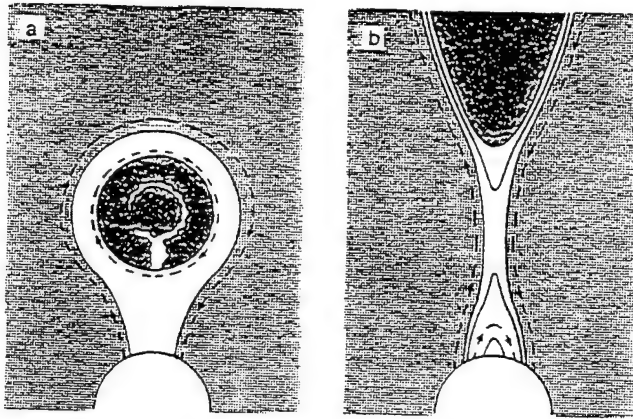


Figure 1. Schematic showing the evolution of a large, looplike CME exhibiting signatures of magnetic disconnection in the low or middle corona as it might appear within a few solar radii of the solar limb. Solid lines outline bright, denser plasma regions, and dashed lines suggest the direction of the constraining magnetic field lines. (a) An early phase in which the contrast across a bright band below a dark interior void region suggests an outward-curved disconnected structure. (b) The base of such a feature as it might appear farther out in the corona or late in the event. In terms of our morphological classification, Figure 1a exemplifies a class 1 DE which is circular or ovoid-shaped and can have a darker, circular interior void. An inner bright ring structure, often prominence material, may occasionally appear within the darker interior. Figure 1b represents a class 2a feature, a large broad arc curved concave-outward from the Sun such as in the I&H event. Also drawn is the possible interconnection between the large-scale, rising plasmoid structure and smaller-scale reconnecting loops near the surface. The figure is not to scale, and these lower structures might be obscured by the occulting disk of a coronagraph.

below a darker interior void region suggests an outward-curved disconnected structure. Such a configuration is similar to the familiar "three-part" CME, which is suggestive of the liftoff of pre-existing prominence and its surrounding coronal cavity. Farther out in the corona or late in the event, only the base of such a feature might be visible (e.g., in the field of view of a coronagraph) or it might not be obviously connected to the leading edge such that only the outward arc appears (Figure 1b). The vertical elongated structures shown beneath the arcs in Figures 1b and 2b represent extended neutral sheets. Many CMEs arise in pre-existing streamers [Hundhausen, 1993]; the evolution of a disconnected plasmoid/CME ejected through a streamer might appear as in Figure 2. Since the widths of streamers and CMEs range over many tens of degrees, we might expect the widths of disconnection structures to have a similar range, as shown in these figures.

We note that these pictures are meant to represent sketches of possible disconnection structures that might be viewed by coronagraphs. Coronagraphs measure the coronal density via Thomson-scattered emission, which peaks near the plane of the sky. Thus these features

are two-dimensional projections in the plane of sky of the actual structures. The appearance of these structures will depend on the line of sight, especially if the CME outlines an extended arcade of erupting loops. In addition, in three dimensions, reconnection might not lead to completely disconnected field lines. An erupting helical flux rope emerging from the photosphere might remain connected at its endpoints and not be topologically completely disconnected, at least until a later phase. Gosling [1993] has recently sketched such a model of flux rope formation and ejection as a CME.

Despite 2 decades of coronagraph observations, there have been only a few reports to date of apparently detached structures in the corona similar to those sketched in Figures 1 and 2 that might signify magnetic disconnection in CMEs. The dearth of such observations may result, at least in part, from the lack of a systematic survey of the later phase of CME evolution in the corona. In this paper we report on the results of this kind of search for disconnection events, making use of both ground-based solar eclipse observations and spaceborne coronagraph data. The preliminary results of this study were reported by Webb and Cliver [1989].

Note that in the highly conducting corona the plasma is expected to approximately outline the magnetic field, as we have indicated in Figures 1 and 2. However, we cannot observe the field lines directly, but can only infer their topology [e.g., Nling and Hundhausen, 1983]. Therefore hereafter, the term "disconnection event or structure" is meant to imply not the definitive identification of such a magnetic structure but only a "candidate" disconnection event or structure. We use the term "disconnection" to denote the large-scale (tens of

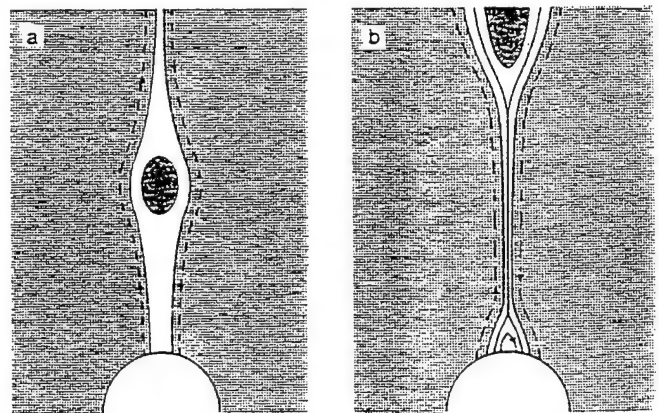


Figure 2. (a) The possible evolution of a narrow, disconnected plasmoid-type CME being ejected through a pre-existing streamer, within which CMEs often arise. (b) The base of such a feature as it might appear farther out in the corona or late in the event. According to our classification scheme, Figure 2a exemplifies a small, oval class 1 DE with a darker, circular interior void, and Figure 2b a class 2b small, partial outward-curved arc. The rising plasmoid and expected smaller-scale reconnecting loops near the surface are shown connected by a thin neutral sheet, which might later appear as an isolated bright ray.

degrees) detachment of a magnetic structure from the sun, and the term "reconnection" to describe the physical process of reforming closed loops from field lines opened during a CME. The latter process operates over smaller size scales of a few degrees and is descriptive of the postflare phenomenon near the surface.

In section 2 we review the observational evidence for large-scale magnetic disconnection associated with CMEs that has appeared previously in the literature. In section 3 we present the results of our examination of images obtained during total solar eclipses and by orbiting coronagraphs. Individual events exhibiting disconnection characteristics are displayed and summarized in tables, and a morphological classification scheme is presented. We conclude with a summary and a discussion of our results in terms of other recent studies related to this topic.

## 2. Previous Observational Evidence of Magnetic Disconnection Events

Several types of transient features which suggest closed magnetic structures, either disconnected fields (plasmoids) or magnetic loops that remain connected to the Sun ("bottles"), have been identified in the interplanetary medium [see *Kahler*, 1987; *Gosling*, 1990; *Webb*, 1993]. These include magnetic clouds [*Klein and Burlaga*, 1982; *Zhang and Burlaga*, 1988] and observations of counterstreaming electrons [*Gosling et al.*, 1987; *Phillips et al.*, 1992] and protons [*Marsden et al.*, 1987; *Richardson and Reames*, 1993].

Each of the above features has been suggested as a signature of CMEs in the interplanetary medium, but the uniqueness of these signatures is controversial [e.g., *Webb*, 1993]. For example, counterstreaming electron events are often considered good CME proxies because they can be explained by closed field structures and CMEs originate from closed-field regions at the Sun [*Gosling*, 1990]. However, to date the interplanetary observational evidence is not sufficient to differentiate between the closed-field topologies, or even open-field configurations [*Joselyn*, 1988; *Suess*, 1993]. For example, *Kahler and Reames* [1991], using energetic particles as probes of magnetic clouds, concluded that bottle or open-field configurations were the only topologies consistent with their observations. In addition, Helios white light observations of interplanetary CMEs provide some evidence for increased mass flow well behind the leading edge, arguing against large-scale reconnection for these events [*Jackson and Leinert*, 1985]. A hybrid of the closed-field topologies is also possible; e.g., the stronger interior fields of a CME might disconnect to form a plasmoid or a flux rope while the outer fields remain connected to the Sun. For instance, *Gosling* [1990] found that  $\approx 30\%$  of counterstreaming electron events resembled flux ropes, which could result from reconnection of highly sheared field lines near the Sun.

Coronagraph observations suggest that disconnection is not typically observed near the Sun in the wake of CMEs. For example, no clear evidence of a discon-

nection event (DE) had been reported from the Skylab coronagraph data, and the Skylab CMEs were thought to retain their connection to the Sun [*Gosling et al.*, 1974; *Anzer and Poland*, 1979].

The first published example of a possible disconnection feature was reported by *Illing and Hundhausen* [1983] (hereinafter, I&H) who interpreted an event observed in the 1980 SMM data as a disconnected CME. It appeared as a bright front pointed concave-outward from the Sun that moved slowly outward through the corona (similar in form to our Figure 1b), following by several hours a succession of convex-outward loops. Still later a bright, narrow radial ray appeared, suggesting the formation of a neutral sheet following the closed, detached magnetic structure [see also *Hundhausen*, 1995].

Other concave-outward arcs similar to the I&H event, or dark internal "voids" with outward-curved forms imbedded within CMEs have been detected in more recent coronagraph data, suggesting that disconnection events may not be as rare as previously thought. *Illing* [1985] described nine other events serendipitously discovered in the Skylab and 1980 SMM images. Because of limited temporal coverage, it was unclear if all of these features trailed CMEs. *Anzer and Pneuman* [1982] showed illustrations of two Skylab CMEs on June 10 and August 26, 1973, which they suggested showed evidence of closed magnetic structures within CMEs formed by reconnection. The August 26 CME, in particular, contained a large dark region bounded near the Sun by a brighter, concave-outward structure. Our inspection of images of the June 10 CME revealed a bright ray centered on the CME axis that appeared some hours after the passage of the CME front. Another well-observed and studied Skylab CME on August 10, 1973 had a circular, bubble shape with a darker interior similar to the June 10 event [*Gosling et al.*, 1974; *Anzer and Poland*, 1979]. Following *Anzer and Pneuman*, we regard these Skylab CMEs as candidate disconnection events.

Although no survey for disconnection features has been made of the SOLWIND coronagraph data, we are aware of two published candidate events, on May 8, 1979 [*Michels et al.*, 1980a, b] and September 1, 1980 [*Sheeley et al.*, 1982]. In both events, dark, circular voids with concave-outward forms (similar to Figure 1a) were observed within the CMEs as far out as  $11 R_{\odot}$ . A third event on April 14, 1980 was shown by R. Howard at a meeting in 1988 [*Joselyn*, 1988]. The SOLWIND image showed a wineglass-shaped structure, suggestive of disconnection, in the late phase of the CME. However, the SMM images showed a classic looplike CME erupting over the north pole [see *Kahler*, 1987, Figure 1]; the western leg of the CME was superposed on a pre-existing bright streamer, which subsequently erupted.

Recently, *McComas et al.* [1991, 1992b] have presented evidence of other outward-moving "U-shaped" structures in the SMM coronagraph data. They suggest that some concave-outward structures may indicate the disconnection of previously open-field regions in streamers, resulting in the expulsion of a detached structure open to the heliosphere. *Linker et al.* [1992] have simu-



lated such reconnection in a model equatorial streamer. The simulation yielded a disconnected structure similar to the observations of McComas et al. We will return to this idea in the discussion.

A few ground-based observations during total solar eclipses have also revealed similar concave-outward structures. Cliver [1989] analyzed ground-based observations of what was reported to be a "comet," a concave-outward bright front atop a radial ray, seen moving outward from the Sun during the 1893 solar eclipse. He interpreted this structure as a disconnected CME and pointed out that candidate DEs were also observed at eclipses in 1860 [Eddy, 1974] and 1980 [Rusin and Rybansky, 1983; C. Keller, private communication, 1988].

### 3. Results of the Survey: A Search for Disconnection Events

Our approach to the search for possible disconnection features was to examine complete sets of images of major CMEs obtained from spaceborne coronagraphs, as well as ground-based data obtained during naturally occurring solar eclipses. We examined the coronagraph CME data sets at the High Altitude Observatory (HAO) obtained during the Skylab missions in 1973/1974 and the SMM mission in 1980. We note that these two coronal data sets were obtained during missions that were primarily flare-oriented, resulting in relatively low duty cycles (32% and 38%, respectively) for detection of CMEs with speeds of 400 km/s or less [Hundhausen et al., 1984]. We also examined all available and appropriate images from total eclipses over the interval from 1860, by which time the study of solar eclipses had become a serious scientific enterprise [Todd, 1900], to the mid-1980s.

To be included as a candidate disconnection feature, a transient coronal structure had to be brighter than the ambient, or background, corona with at least a portion of its form having a concave-outward shape. These structures are expected to be listed themselves as CMEs (i.e., new bright material appearing in the field of view) or to trail the leading edge of a CME. The disconnection structures could consist of partial arcs, like the I&H event and our Figures 1b and 2b, or nearly complete ring-shaped structures with apparent closure on their sunward side, like the Skylab events shown by Anzer and Pneuman [1982]. We interpret these latter structures as providing evidence for the ejection of plasmoids (our Figures 1a and 2a); their interior may or may not be darker than the outer ring, but the contrast across the structure suggests a concave-outward geometry on the sunward side. Note that the existence of the darker cavity in the classic "three-part" CMEs does not by itself constitute evidence of disconnection; a clearly delineated concave-outward geometry must be present. In addition, we considered newly-formed bright rays following and coaxial with the above features as evidence of disconnection.

#### 3.1. Spaceborne Coronagraph Observations

For the Skylab data we examined high-quality prints and archival 35-mm transparencies available at HAO for each of the 77 "major" CMEs defined by Munro and Sime [1985]. We found that 8 of the 77 (10%) Skylab CMEs were associated with such candidate disconnection structures.

We also surveyed the literature and the photographic image data available at HAO to search for candidate disconnection events in the 1980 SMM data. We compiled a final list of 10 candidate events, most of which had been identified previously by Illing [1985, private communication, 1985]. Not all of these were called "CMEs" on the "official" SMM CME list at HAO. Our survey was completed at HAO in 1988; at that time there were 74 CMEs listed for 1980, although this count was considered a lower limit [e.g., Webb, 1987]. Therefore, the 10 disconnection candidate events represent a rate that is 13.5% of all major SMM CMEs counted in 1980. The final SMM CME catalog [Burkpile and St. Cyr, 1993] has added many fainter transients to the list and now records 169 CMEs observed in 1980. We have not resurveyed the updated 1980 data but do not expect the rate of disconnection features to change significantly. Burkpile and St. Cyr list a category of "concave-outward" features in their catalog. The "relative frequencies" of this class of descriptors is 6.2% in 1980 and a mean of 6.6% for 1984-1989. If considered to be an occurrence rate, it underestimates the rate of all disconnection features. For example, outward-curved arcs are only one type of feature we consider as evidence of disconnection.

Table 1 lists all candidate disconnection events, and their associated CMEs, observed from spaceborne coronagraphs that are known to us. For completeness, in addition to the Skylab and 1980 SMM events mentioned above, we have included the three SOLWIND events in 1979 and 1980 discussed above. However, these events are not included in our statistical results, since the SOLWIND data were not part of our survey. The table lists the following data for each event (from left to right): the date and day of year, the spacecraft from which the DE was observed, the solar cycle number, the approximate year from maximum phase of the event, the estimated time of onset, time of first and last observations, limb position of the central axis, width and speed of the associated CME if known, whether the leading edge of the CME was looplike, whether it had a central bright region (CBR) [see Webb and Hundhausen, 1987], the DE classification, and comments and references. For most events there are two lines of data: the top line refers to the CME, and data in the second row pertain specifically to measurements of the disconnection event itself. For DE class 1 events, the leading portion of the CME is essentially part of the DE, so the width of the DE is roughly the same as the CME itself. Only a few speeds of disconnection structures have been measured. The DE classification is discussed in section 3.3 and Table 3.

Table 1. Known Candidate CME/Disconnection Events Observed From Spaceborne Coronagraphs

Date	Space craft	Cycle Number	Event Onset	First Observed	Last Observed	Limb Position	Event Width	Event Speed	CME Loop?	CME CBR?	DE Class	Comments/References
June 10, 1973	ATM	20	—	0150 0204	>0235	N22E	30 20	580 ~170	n y	?	2b	<i>Illing</i> [1985]. Material in streamer at edge of field
June 10, 1973	ATM	20	—	0929 >1000	1002	N21E	35	450	y	y	1a,b,c	<i>Hildner et al.</i> [1975a]; <i>Anzer and Pneuman</i> [1982]. Bright ray at 1600 UT
Aug. 9, 1973	ATM	20	—	1530 1705	1705	N08W	30	155	y		1a?,1b	bubble CME with void
Aug. 10, 1973	ATM	20	—	1331 1457	1518 1515	N08W	50	400	y		1a,b 2a?	classic bubble with void; <i>Gosling et al.</i> [1974]
Aug. 13, 1973	ATM	20	—	0655 0655	0818 0756	N36W	40	700	y	y	1c	CME followed by narrow void. Small "tennis racket" inside CME. Nice
Aug. 26-27, 1973	ATM	20	—	2302 >0206	>0212 0512	N27E	57	150	y?	n	1b	<i>Hildner et al.</i> [1975b]; <i>Anzer and Pneuman</i> [1982]
Dec. 12, 1973	ATM	20	—	0020 0459	0807 0807	S23E	25 23	225 —	y?	y	2b	filled-bottle streamer blowout. Bulb-shaped; bright ray at 0925 UT. Nice example
Jan. 21, 1974	ATM	20	—	0720 1211	1335	S20W	25	60	y?	y	2b	filled-bottle streamer blowout. Munro's slow event
May 8, 1979	SOL	21	0910	1028 1205	>1246 >1246	S40W	110	375	y	?	1b	<i>Michels et al.</i> [1980a, b]. Well observed CME. Maybe Helios event
Mar. 15-16, 1980	SMM	21	0900	1536 0604	2100 1358	S30E S27E	~53 ~40	35 175	y y	y	2a	<i>Illing and Hundhausen</i> [1983]. Follows loop and cavity in streamer. Bright ray remains
March 25, 1980	SMM	21	0425	0453	0738	S35W	15 15	682 —	?	n	2b	narrow plasmoid; well observed

Table 1. (continued)

Date	Space craft	Cycle Number	Event Onset	First Observed	Last Observed	Limb Position	Event Width	Event Speed	CME Loop?	CME CBR?	DE Class	Comments/References
March 28, 1980	SMM	21	0600	0735	1124?	S45W	21 >20	127	n	—	2a or 2b	wispy; poor example
April 5, 1980	SMM	21	1000	1211 1211	~0241 1352	S07E 00E	46 ~457	— 234	y	n	1b?; 2a	Illing [1985]. Huge, wispy CME. Nice, but faint
April 5, 1980	SMM	21	1310	0728 1545	~2149 1545	N73W N75W	44 ~5	47 >206	?	n	1b or 2b	Illing [1985]. Small loop atop streamer.
	SOL		1410	1503	1545	N80W	10	420E				SOL sees inverted Y
April 14, 1980	SMM SOL	21	0356	0449 0801	0847	N85E N70W	50 40	285 —	y ?	y n	—	SMM C-P: famous loop CME at north pole. Bright west leg and motion due to NW streamer event. SOL: sees event end with bright leg and wine glass. DE?
April 15, 1980	SMM	21	0956	1033 1159	1820 1351	N15E S08E	20 70?	290 —	?	n	1c?	squarish structure; prominence?
April 27, 1980	SMM	21	~0200	0212 0246	0703 0351	S05E	38 ~10	595 —	y	y	1a, 2b?	Stewart et al. [1982]. Central blob followed by cavity. Moving type IV radio burst
May 1, 1980	SMM	21	<1200	1653 2025	2127 2028	S19E	19	50 +	n	—	1b?; 2a?	complex event. Maybe 2 separate DEs
Aug. 8, 1980	SMM	21	(2030)	2129	2148	S50E	—	>490	?		1b or 2b	Illing [1985]. Loop follows void. Front missed? Not in Burkepile and St. Cyr [1993]
Aug. 16-17, 1980	SMM	21	1700	2122 2155	~0233 2319	N35E	29 ~18	70 —	n	—	1b or 2b	streamer blowout with inverted back
Sept. 1, 1980	SOL	21	0534	0735 0735	>0814 >0814	N15W	90	960E 1200	y?	n	1b	Sheeley et al. [1982]. Fast void in CME to 11 $R_S$ . CME fills quadrant

Table 2. Eclipse Observations of CMEs and Candidate Disconnection Events

Date	Location	Principal Observer	CME <sup>a</sup>	DE <sup>a</sup>	DE Class	PA <sup>b</sup>	Cycle No.	Cycle Phase	Event Width	Event Speed	Comments/References
July 18, 1860	Spain	Tempel	Prob.	Prob.	1a,b,c	SW	10	Maximum	~40	200-500	Eddy [1974]; Ranyard [1879]
Aug. 7, 1869	Shelbyville, Kentucky	Winlock Harvard Obs.	Prob	Prob	1a,b	55	11	Max - 2	23	—	This study; Ranyard [1879]; Ashe [1870]
Dec. 12, 1871	Russia, India Indonesia	Holiday, Tennant, Lindsay	Poss	?	—	85	11	Maximum	—	—	Ranyard [1874, 1879]
Aug. 29, 1886	West Indies	Pickering	Prob.	?	—	220	12	Max + 3	~25	—	Pickering [1886]; Todd [1900]
April 16, 1893	Chile, Brazil, Africa	Schaeberle	Prob	Prob	2b	200	13	Max + 1	—	—	Cliver [1989 and references therein]
May 29, 1919	Brazil, Peru, Africa	English	?	?	—	(SE)	15	Max + 1	(~45)	—	[1929]. Large prominence lifts outward?
Jan. 14, 1926	Africa, Philippines	English	?	No	—	(SW)	16	Max - 2	?	—	[1929]
June 8, 1937	Canton Island Pacific	NRL	Prob	I	—	(WL)	17	Maximum	~65	—	This study; Hildner [1977]
June 8, 1937	Canton Island	NRL	?	I	—	(EL)	17	Maximum	(~45)	—	This study
Sept. 21, 1941	Siberia	Bugoslavskaya	Prob	No	—	288	17	Max + 4	30	—	Shklovskii [1965]; Bugoslavskaya [1950]
July 10, 1972	Canada	Keller	?	?	—	215	20	Max + 3	—	—	C. Keller (private communication, 1987)

Table 2. (continued)

Date	Location	Principal Observer	CME <sup>a</sup>	DE <sup>a</sup>	DE Class	PA <sup>b</sup>	Cycle No.	Cycle Phase	Event Width	Event Speed	Comments/References
June 30, 1973	Kenya, Africa	Keller	Poss	Poss	2b	260	20	Max + 4	—	—	Koutchmy et al. [1973]; C. Keller (private comm., 1987) Martinez [1978]. Diffuse Y structure. Skylab: Possible CME <1144 UT, PA 269
Feb. 16, 1980	Indian Ocean Africa	many	Prob	Prob	1a,b,c	282	21	Maximum	45	610 ±100	Rusin and Rybansky [1983]; Rust [1983]; Clette et al. [1985]; C. Keller (private communication, 1987); Koutchmy et al. [1988]. "Tennis racket" event
Feb. 16, 1980	Africa	Keller	Prob	No	—	168	21	Maximum	~30	—	C. Keller (private comm., 1987)
Feb. 16, 1980	Africa	Keller	Prob	No	—	215	21	Maximum	27	(70)	Fisher and Poland [1981]; Clette et al. [1985]; C. Keller, (private comm., 1987). Remnants of MLSO M3 CME on Feb. 157
Feb. 16, 1980	Palem, India	Street and Lacey	Poss	I	—	103	21	Maximum	30	—	Fisher and Poland [1981]. Possible CME on HAO photos; depletion on K-corona and LASL eclipse images

<sup>a</sup>The degree of confidence of the identification of the CME and disconnection event. Categories are Probable (Prob.), Possible (Poss.), Questionable (?) or Maybe, No, and indeterminate (I) or can't tell.

<sup>b</sup>Position angle of the event at the limb in degrees measured from solar north to the east.

### 3.2. Total Solar Eclipse Observations

For a total eclipse observation to be considered for our survey, we required a photographic image or high-quality drawing of the eclipsed corona; structures had to be visible on the image at least into the middle corona (i.e., to a distance of  $\approx 1.5 R_S$  depending on the phase of the solar cycle.)

We examined observations, either photographs or drawings, from a total of 37 eclipses that met these criteria between 1860 and 1980. Our survey was complete in the sense that we were able to review data from every well-observed eclipse over the last 130 years. Data sets searched included compilations of coronal sketches and drawings by *Ranyard* [1879] and *Anonymous* [1929]. In addition, we examined the entire collection of glass plates of eclipse photographs compiled by J. Eddy at HAO [*Eddy and Goff*, 1971] and the photographic records from eight eclipses contained in the archives at Harvard College Observatory (HCO).

During 12 of the 37 eclipses a CME (identified with varying confidence levels) was visible on at least one image of the middle corona. A total of 16 CMEs were detected (two were visible during the 1937 eclipse and four during the 1980 eclipse). Table 2 lists the references and some observational details of these probable (9), possible (3), and questionable (4) CMEs and the associated DEs. This table is similar to Table 1 with the additions of the location of the eclipse observation (column 2), the name of the principal observer (column 3), and the degree of confidence we placed in the identifications of the CMEs (column 4) and DEs (column 5).

Five of the 12 probable and possible eclipse CMEs, in 1860, 1869, 1893, 1973 and 1980, were associated with candidate disconnection features. Of the other seven eclipse CMEs, three showed no evidence of disconnection, and the other four were indeterminate or uncertain because of obscuration by the bright inner corona. Note that 9 of the 12 eclipse CMEs, and all but one of the DEs, occurred within 2 years of the maximum phase of the sunspot cycle, with an average monthly sunspot number of 102. This is not unexpected, since we now know that the occurrence rate of CMEs tends to follow that of the cycle in both amplitude and phase [*Webb and Howard*, 1994].

Three of the five disconnection events had previously been described by *Cliver* [1989]. We found the fourth event in the Eddy plate collection and later confirmed its existence on the original plate in the HCO archives. The photograph was taken by J. Winlock of HCO during the August 7, 1869 eclipse at Shelbyville, Kentucky. We believe that this is the first photograph of a CME and candidate DE ever obtained. Figure 3 shows a tracing of the nearly circular disconnection structure that we made from the enlarged Eddy plate at HAO. The eclipse was well observed across the upper midwest United States and Canada, and many reports were generated; *Ranyard's* [1879] compendium provides the most complete summary of these. He includes a drawing of Winlock's 40-s exposure, which Winlock said provided

"a most satisfactory picture of the corona" (p. 612). After viewing the original negative during a visit to HCO in 1878, *Ranyard* concluded that "...it was evident that a great deal of structure was recognizable in the original negative which is not shown in the steel plate published in vol. vi. of the 'Annals of the Harvard College Observatory'." Apparently, the feature which we recognize today as a CME was discounted at the time as an artifact.

Aligned with the southern edge of the CME at a Position Angle of  $69^\circ$  is a prominence. This may have erupted earlier and been associated with the CME. *Ashe* [1870] was among the earliest observers of totality at Jefferson, Iowa, and reported what we might today recognize as an erupting prominence over the east limb. He described a moving "protuberance" whose "...lower part was deep red, getting lighter, and the part blown off was a brilliant white light." Later "it assumed the form of a great heap of cinders," and this feature was what was seen by all the observers later to the east. C. Abbe at Sioux Falls, Iowa also reported a "column of ...hot gas ascending high above ...red flames" near the surface [*Ranyard*, 1879, p. 600]. Others referred to a "curled" or "spiral" structure in the corona. The most likely description of the CME was made by G. Hough at Maltoon, Illinois, who saw "...a curved mass of light, in shape resembling the petal of a flower. On the upper edge of the disc was plainly seen an arch of light, parallel with the edge, and within the boundary of the corona" (p. 606).

The fifth possible DE is best seen on the enhanced airborne large field photograph obtained of the June 30, 1973 eclipse over Africa by the Los Alamos Scientific Laboratory (LASL) group. It appears as a Y-shaped structure in the southwest with its branching point at about  $4 R_S$ . It was described as a split streamer by *Martinez* [1978] and as a "detachment" by *Koutchmy et al.* [1973]. *Koutchmy's* expedition obtained two photographs of the eclipsed corona from Mauritania and from Chad 87 min apart. The motion of the "detachment" between these times enabled them to estimate its velocity as 90–140 km/s. The feature had apparently moved beyond the field of an HAO eclipse photograph obtained later in Kenya at 1250 UT. The corona was also observed from Skylab on the day of the eclipse. A pre-existing bright streamer appeared at the west limb at 0410 UT and had been disrupted by a possible CME on the next image at 1144 UT. The source of the CME might have been in an activated prominence at the southwest limb which was associated with a loop and cloud observed by the American Science and Engineering Skylab X-ray telescope at 1141 UT.

These results indicate that candidate disconnection events might occur, or at least might be detectable, during approximately 10–15% of all solar eclipses (in our sample, 5 times out of 37 eclipses). Surprisingly, the fraction of DEs to CMEs detected during eclipses was much higher (40%, 5 of 12) than that for the coronagraph sample. The detection rates of both CMEs and DEs seem particularly high considering that good eclipse observations represent snapshots of the corona



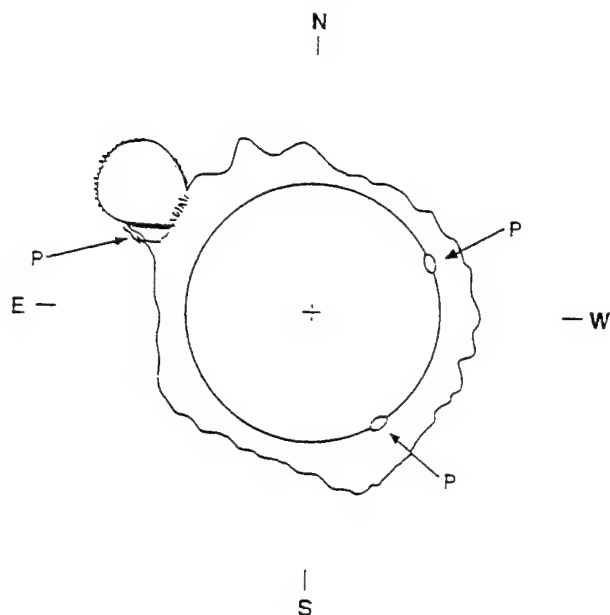


Figure 3. Tracing of the long-exposure (40 s) photograph of the August 7, 1869 eclipse obtained at Shelbyville, Kentucky by J. Winlock of HCO. The nearly circular candidate disconnection structure lies above the NE limb. We made this sketch from the enlarged plate in the Eddy collection at HAO, and confirmed the reality of the feature on the original plate in the HCO archives. This event is an example of a circular class 1 disconnection structure, with the CME exhibiting a nearly complete ring (class 1a) within which is there is some evidence of a darker void (class 1b). The sketch is interpretive only and is not intended to reproduce the faint, subtle detail on the original image. The compass points indicate solar coordinates. "P"s show locations of prominences.

taken on average once every 2 years. For example, the maximum CME rate derived from coronagraph observations is about 2.5/day, or 1 every 10 hr [Webb and Howard, 1994]. If we assume that an average-speed

CME will be visible in the corona for one hr, then we expect to see at most 3.5–4 CMEs during the 37 eclipses. However, we observed 9, or 2–3 times the expected rate.

These estimates suggest that for some reason, CMEs and disconnection features might be more readily detectable with natural eclipse observations than from spaceborne coronagraphs. A possible reason could be that natural eclipse observations, which don't require a coronagraph's occulting system with its associated stray light and vignetting problems, permit clear viewing of coronal features from the solar limb outward. This could be an important advantage if DEs are somehow easier to detect (e.g., have higher contrast) when they are nearer the surface than farther out in the corona. In addition, the use of modern techniques during eclipses, such as radially-graded filters, airborne infrared photographs and computer enhancement programs, greatly improves the detail observable in the lower corona and extends the field of view. These advantages were apparently decisive in detecting the four transients during the 1980 eclipse. Finally, we emphasize that the listing of CMEs and DEs in Table 2 represents our interpretation of the eclipse observations; others may disagree. A disadvantage in using eclipse images to identify dynamic phenomena is the brevity of natural eclipses. However, nearly all of the features we identified as CMEs or DEs were noted by others, although not recognized as CMEs or DEs at the time.

### 3.3. A Classification Scheme for Disconnection Structures

Counting only the probable identifications, there were a total of 23 events having features suggestive of disconnection detected in both the eclipse and coronagraph samples (Tables 1 and 2). We have developed a morphological classification scheme for these disconnection features which is presented in Table 3. The classification order is somewhat arbitrary but suggests a possible evolutionary sequence proceeding from complete

Table 3. Morphological Classification of Features Suggestive of Disconnection

Feature Class	Percent of Total Number of Events (23)	Percent of Total Number of Features (30)	Number of Features in Class	Description
1	54	65	19.5	Circular or ovoid structure (closed bubble or ring shape)
			a) 6	Outer CME structure is bubble or ring shape
			b) 9.5	Uniform dark void within CME
			c) 4	Bright bubble or ring shape within CME (erupting prominence material?)
2	46	35	10.5	Curved arc concave-outward from the Sun
			a) 2.5	Large-scale broad arc (like I&H event)
			b) 8	Small arc within pre-existing structure (usually part of a streamer disruption)

Narrow, sharply defined rays indicative of neutral sheets followed four of the class 1 or 2 events.

circular structures (class 1), which often include the leading edge of a CME and can consist of dark circular depleted regions or voids, to partial arcs or narrow U- or Y-shaped structures where the leading edge may have been missed (class 2), to newly-formed bright rays which suggest the formation of a thin neutral sheet late in the event. We have considered the rays to be not a separate class, but a late phase of a class 1 or 2 disconnection feature. This progression is illustrated in Figures 1 and 2, where wide and narrow complete class 1 CME/DEs are shown in Figures 1a and 2a, respectively, and as later-phase class 2 partial arcs and bright rays in Figures 1b and 2b. A given event could have characteristics which fall into one or both classes, particularly if it was observed for an extended period. There were a total of 30 classified features observed during the 23 events. In Table 3 the percentage of features in each class to the total number of *events* and to the total number of *features* is indicated in the second and third columns, respectively. The actual number of features in each class or subclass is given in column 3.

Class 1 features appeared in 54% (12.5 of 23) of all the events, and class 2 features in 46% (10.5 of 23). The most common type of disconnection feature (65%, 19.5 of 30) was a complete circular structure (class 1). Outward curved arcs (class 2), exemplified by the I&H event, comprised 35% (10.5 of 30) of all features. Small arcs (class 2b) were the most common features of this class and were often associated with pre-existing streamers, which disappeared following a CME characterized by the rapid outward expulsion of streamer material [see *Hundhausen*, 1993]. The class 2 subclasses were differentiated by the width of the arcs: class 2a

arcs were  $\approx 45^\circ$  wide and class 2b arcs were  $\leq 25^\circ$  wide, with a mean width of  $16.4^\circ$ . In either case the arc widths were slightly less than the widths of the leading part of any associated CME.

Examples of each of the main classes of events are shown in the figures. Figures 3 and 4 show examples of two similar class 1 circular features detected during two eclipses. The Shelbyville CME/DE structure in Figure 3 exhibits a nearly complete ring (class 1a) with its innermost boundary pinching in and blending with the bright inner corona  $0.3 R_S$  above the limb. Its center is at  $0.65 R/R_S$  and the outermost edge at  $1.0 R/R_S$ . The interior of the ring showed some evidence of a dark void (class 1b). The well-known "tennis-racket" CME observed during the February 1980 eclipse is shown in Figure 4 in three views from *Koutchmy et al.* [1988]. See *Rust* [1983] for an infrared photograph of this event obtained later (at 0850 UT) by the LASL airborne expedition. Class 1 DEs have three possible subcategories: an outer ovoid, an interior circular void region, and a bright interior ring. The 1980 event exhibited all three of these characteristics. This event is another likely example of the streamer-disruption type of ejection seen throughout the SMM period.

The large-scale, broad, concave-outward arc in the I&H event is the prototypical class 2a event (sketched in our Figure 1b; see Figures 3–5 of I&H). This arc was preceded by a series of loops that moved slowly through the corona up to 16 hr before the DE. The concave-outward arc was about  $40^\circ$  wide and moved at a speed of 175 km/s. Figure 5 shows an example of a smaller class 2b structure observed in 1980 from SMM. This event is typical of these features in that it occurred

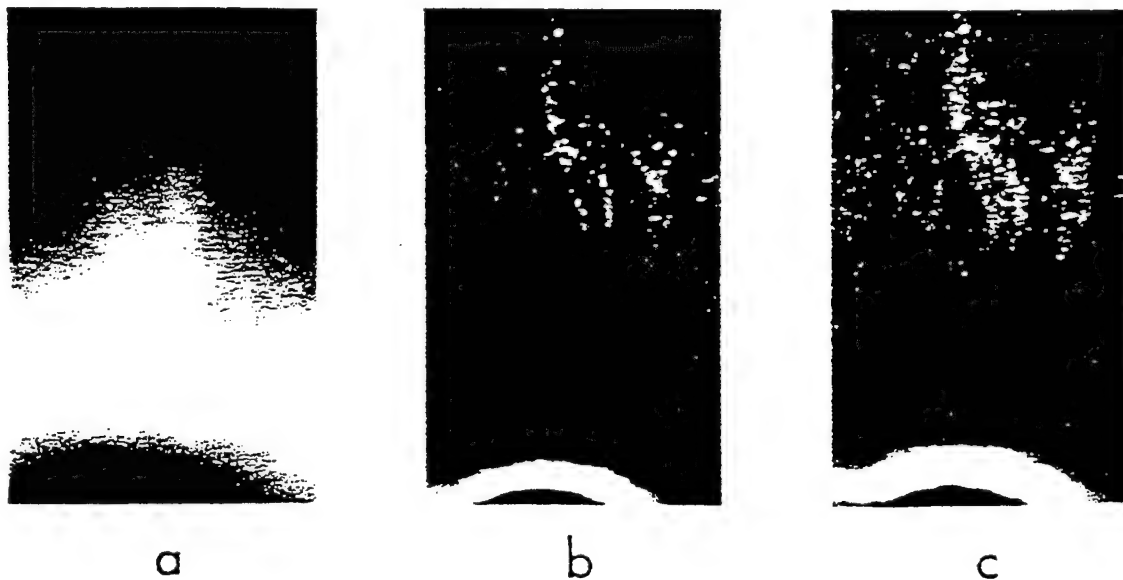


Figure 4. (a) A portion of the original image of the "tennis racket" CME obtained at 0823 UT by F. Diego during the February 16, 1980 eclipse. (b, c) Processed versions of the event using a second-order difference operator algorithm called MaD MAXII with two different weighting functions. The circular or ovoid structure exhibits all three class 1 characteristics: an outer complete ovoid, an interior void region, and a bright interior ring. From *Koutchmy et al.* [1988]; original print courtesy of S. Koutchmy.



Figure 5. An example of a smaller concave-outward arc feature (class 2b) observed on April 5, 1980 with the SMM coronagraph. Most of these features occurred within streamers in which the plasma brightened and then was at least partially expelled from the Sun. The dotted circle denotes the solar limb, and the arrow points to solar north. The transient structure at 1545 UT has been enhanced by the subtraction of a pre-event image at 1407 UT. The outermost edge of the transient is truncated by the edge of the field of view, producing an artificially bright edge on the image. Courtesy of J. Burkepile; see also Figure 17 of Burkepile and St. Cyr [1993].

within a streamer; apparently in such events material travels through the streamer and is expelled from the sun. The 1893 eclipse "comet" transient discussed by Cliver [1989], another example of a class 2b structure, bears a remarkable resemblance to this SMM DE.

We consider the narrow U- or Y-shaped structure observed during the June 1973 eclipse also to be an example of a class 2b event. Such features obviously form more acutely-angled concave-outward structures than the smooth U-shaped arcs typified by the I&H event. It can be argued that such structures should not be considered evidence for disconnection in the corona, since they do not exhibit a continuous outward-curved surface. They could be caused, for instance, by the superposition of two independent streamers at different distances along the line of sight. However, the 1973 structure exhibited coherent outward motion, both sides were of equal density, and it was probably associated with a streamer-disruption CME.

Newly-formed bright rays following CMEs are indicative of the formation of thin neutral sheets late in an event. In this study we considered the rays to be a late phase of a class 1 or 2 disconnection feature. We did not search specifically for such rays following CMEs, but such a search is probably warranted, especially con-

sidering the results of Kahler and Hundhausen [1992]. Examples of newly-formed ray structures are presented by I&H and by Kahler and Hundhausen.

We examined several basic characteristics of the CMEs associated with the DEs. The average leading edge speeds (312 km/s, 19 measurements) and average latitudinal spans (34°, 26 measurements) of these associated CMEs were slightly less than those of typical CMEs [see, e.g., Kahler, 1987, 1992; Burkepile and St. Cyr, 1993]. With a limited number of measurements, the disconnection features themselves tended to be narrower (27.5°, 21 measurements), slower (174 km/s, 5 measurements), and fainter than their accompanying CMEs.

## 4. Summary and Discussion

### 4.1. Summary

We find evidence that transient coronal structures similar to the prototypical I&H event can be detected in the middle to outer corona following a nonnegligible fraction,  $\geq 10\%$ , of all CMEs. We argue that these observations can be interpreted as plasma entrained on field lines which have become disconnected from the Sun following a CME. The speeds and widths of the accompanying CMEs were slightly lower than those of CMEs in general. The disconnection features themselves tended to be slower, narrower and fainter than the associated CMEs.

There are several types of coronal structures that we found to be suggestive of disconnection. An implication of our proposed morphological scheme is that, with incomplete observations, we could detect only portions of an evolutionary sequence proceeding from complete circular structures, which often included the leading edge of a CME, to partial arcs or narrow U- or Y-shaped structures where the leading edge may have been missed, to newly-formed bright rays indicative of the formation of neutral sheets late in the events (Figures 1 and 2). Complete circular or ovoidlike structures were the most common class of feature (65% of all features), and outward-curved arcs, like the I&H event, occurred less frequently in this sample (35%). Smaller arcs were the most common type of outward arc, and appeared to be frequently associated with pre-existing streamers which disappeared following "streamer-blowout" CMEs [Howard et al., 1985; Hundhausen, 1993].

### 4.2. Discussion

Field line reconnection is thought to be a fairly common time-dependent phenomenon on the Sun, especially within the complex and dynamic configurations occurring during flares and CMEs. As reviewed in section 1, a class of theoretical models [e.g., Forbes et al., 1989; cf. Svestka and Cliver, 1992] has been successful in explaining the "postflare" loop phenomena. In these models, field lines stretched open during the eruption of a prominence, and by inference its surrounding CME, reconnect beneath these structures to form loop arcades over the magnetic inversion line. Recent nu-

merical simulations involving magnetically driven CME models suggest that the formation of a current sheet is an important factor, within which rapid reconnection is accompanied by the formation and ejection of a plasmoid configuration from the Sun. The ringlike CMEs and concave-outward features identified in this study provide important evidence for the reconnection, current sheet and plasmoid formation consistent with these models.

However, alternative explanations for these features cannot be ruled out. For example, such features could arise from some peculiar viewing geometry of superimposed structures along the line of sight. They could be related to shock effects, especially from compressed plasma at slow and intermediate shock fronts [e.g., *Steinolfson*, 1992]. If the concave-outward features are a signature of magnetic disconnection, their role in the overall development of the CME is unclear. For instance, is it a major role in that essentially the entire CME field is disconnected, is it secondary in that only a small portion of the trailing edge or interior of the CME field disconnects, or is it a combination whereby all the CME field lines eventually disconnect through a succession of small-scale reconnections? *Kahler and Hundhausen* [1992] conclude that smaller-scale reconnection during and extending well after passage of the CME is the dominant process of the late phase. If disconnection plays a major role, why don't we see evidence for it during every CME? It is possible that large-scale disconnection might occur frequently during the passage of CMEs but be undetectable in coronagraph images because of its subtlety or faintness, the particular viewing geometry of the CME, the distance from the Sun at which it occurs, and/or obscuration by surrounding ambient coronal structures. For example, as suggested by *Cliver* [1989], such structures are likely to be more difficult to detect near solar minimum because of overlapping structures along the line of sight due to the minimal tilt of the streamer belt. On the other hand, during active phases of the cycle, CMEs arising from the highly-inclined streamer belt would tend to be viewed through the sides of arcades. Smaller-scale disconnection occurring only within the inner part of an extended arcadelike structure could easily be obscured by the bright, outer CME envelope. The disconnection time scale might also be important; for example, very slow disconnection might easily be missed against the slowly evolving coronal background. Finally, recent simulations of erupting streamers suggest that reconnection can occur at large distances from the Sun (e.g.,  $\geq 10 R_S$ ; *Z. Mikic*, private communication, 1994). In this case the disconnection features would occur too far out to be observed by present-day coronagraphs.

In this paper we have discussed disconnection events in terms of their relationship to CMEs. Like *I&H*, we have chosen to interpret such structures as providing evidence for magnetic reconnection of field lines during the later stages of CME evolution in the lower corona. This interpretation assumes that, as part of the CME, these field lines were initially closed near the solar sur-

face then locally opened up as the CME front, or leading edge, moved outward through the corona. In a recent series of papers, *McComas et al.* [1989, 1991, 1992b] present evidence for an alternative explanation for at least some outward-moving "U-shaped" structures seen in the 1984-1989 SMM coronagraph data. They suggest that most such events involve the disconnection of the previously open fields in helmet streamers, resulting in the expulsion of a detached U-shaped structure open to the heliosphere. Further they suggest that these structures can be identified in 1 AU in-situ data as "heat-flux dropout" events [*McComas et al.*, 1989]. This process might help to globally balance the magnetic flux added to the heliosphere by CMEs [*McComas et al.*, 1992a].

It is important to realize that the *McComas et al.* interpretation is distinctly different from that of *I&H* and our view in this paper. We view disconnection events as being directly associated with the trailing portions of CMEs. In a sequence of coronagraph images a CME, which is typically preceded by a bright, leading "loop," moves outward through the field of view, followed within tens of minutes or a few hours by a disconnected feature having approximately the width of the CME and radially aligned with its axis. In the *McComas et al.* picture, CMEs are not required, or if they do occur, the CME is remote from the affected streamer. Thus some distant dynamic process initiates X-type reconnection within the open fields of a pre-existing coronal streamer, resulting in the pinching off and expulsion of plasma and magnetic flux from the streamer. In our view, such a remote triggering process is ad hoc; e.g., in the *McComas et al.* [1991] event, it seems implausible that compressional waves could effectively propagate in opposite directions through many dense, intervening structures to trigger reconnection in a streamer  $180^\circ$  away.

*McComas et al.* [1991, 1992b] have presented only two examples of such events, both of which were narrow streamer-related transients listed as CMEs by the HAO group [*Burkepile and St. Cyr*, 1993]. Although neither event exhibited bright fronts, the observational cadence is such that their leading edges could have been missed. We have identified a number of such events in our sample of earlier coronal data. They fall into our subclass 2b (Table 3), which comprises at most about 45% (10 of 22) of our disconnection events. It is possible that some of these structures result from non-CME streamer disconnections. However, it seems more plausible that such events are narrow streamer-blowout CMEs in which the leading edge was not observed. Clearly, a detailed study of the time-cadence of the observations of these and additional class 2 events is required to definitively answer this question. The majority of our events are clearly associated with CMEs, typical in that they have concave-sunward leading fronts, and consisting of closed, plasmoidlike circular or bubble-shaped structures or large-scale, broad outward curving arcs.

*McComas et al.* [1992b] embrace the view of many Skylab researchers [e.g., *Gosling et al.*, 1974; *Anzer and Poland*, 1979] when they state, "Most CMEs appear to

leave long lasting 'legs' which slowly fade into coronal holes ...[which are] long lasting open field regions." In other words, there is little evidence of reconnection following CMEs. We do not agree with this view as applied to CMEs in general for the following reasons: (1) Coronal holes are not directly associated with mass ejections; occasional *transient* darkenings or depletions can appear in the low corona following some CMEs or X-ray transients [Rust, 1983], but these are not long-lived, stable structures like coronal holes. (2) Since most of our candidate events directly follow CME fronts, we maintain that at least 10% of all CMEs show evidence of disconnection. In fact, *McComas et al.* [1992b] themselves found a similar rate (11%, 6 of 52 CMEs) in a preliminary examination of 3 months of SMM CMEs in 1988. (3) In their study of the coronal magnetic topology following 16 CMEs, *Kahler and Hundhausen* [1992] found that structures consistent with neutral sheets and streamers generally form in the corona following passage of CMEs, implying that reconnection and the formation of closed structures has occurred. (4) The "post-flare loop" phenomena, often observed in association with CMEs, provides additional evidence of magnetic reconnection near the surface and suggests that it can continue in the corona long after the departure of the CME.

Postflare loop features, such as X-ray long-duration events, are more frequently associated with CMEs than the DEs discussed in this paper, suggesting that some form of reconnection is even more common low in the corona. For example, in the *Webb and Hundhausen* [1987] study, 38% of the SMM CMEs were associated with X-ray long-duration events. Therefore we find considerable evidence to support the view that the magnetic disconnection required for flux balance in the heliosphere can occur in direct association with the CMEs that otherwise might cause a buildup of the field.

The low-energy electron acceleration events termed "high coronal flares" (HCFs) by *Cliver and Kahler* [1991] provide evidence for intermittent reconnection, independent of CMEs, that could also contribute to flux balance by pinching off oppositely directed field lines drawn out into the interplanetary medium through the streamer belt [*McComas et al.*, 1992a]. However, the occurrence frequency of HCFs (several tens per day from observations of metric type III bursts) and their impulsive nature indicate a spatial scale much smaller than that of the DEs reported by *McComas et al.* [1991, 1992b].

Our study represents the first systematic search for candidate disconnection structures in the wake of CMEs. Using data from two different coronagraphs and from many natural eclipses, we found consistent rates of occurrence for such structures that are equivalent to at least 10% of all CMEs. *Burkepile and St. Cyr* [1993] give a lower rate (~6%) of "concave-outward" features associated with the SMM CMEs, but this rate is an underestimate in that it includes only one class of DE and they did not perform a separate search for disconnection structures [*McComas et al.*, 1992b]. We note that an

observed rate of CME/DEs near the Sun of  $\geq 10\%$  is not inconsistent with the fraction of counterstreaming electron events, purported to be proxies for interplanetary CMEs, that resemble flux ropes and are thus indicative of the reconnection of highly sheared field lines near the Sun [*Gosling*, 1990].

Recently, *McComas et al.* [1992a] have addressed the flux buildup problem, using in-situ measurements to estimate the amount of closed versus open flux at 1 AU. They used counterstreaming electron events as a CME proxy and found that in the absence of any reconnection, CMEs would double the ecliptic field magnitude every 9 months. They used heat flux dropout events as a proxy for disconnected flux in the ecliptic plane and concluded that these events by themselves were insufficient by a factor of 4 to balance the newly-added closed flux carried by CMEs. Since the estimates of *McComas et al.* [1992a] were by necessity rough, we cannot attach too much significance to this apparent discrepancy. Nevertheless, we note that these estimates are qualitatively in agreement with our view that interplanetary flux balance can be accomplished primarily by reconnection/disconnection of the fields directly associated with CMEs. However, because of the difficulties in detecting DEs discussed earlier, the question remains open and must be addressed in the future by better observations and measurements.

Finally, we wish to emphasize an important feature of CMEs and DEs. We have noted that many, if not most, CMEs arise in pre-existing coronal streamers. We interpret the evolution of plasma within a streamer entrained on field lines which become disconnected from the solar surface as resembling the picture sketched in Figure 2. In fact, we suggest that nearly half the disconnection features found in this study were of this type wherein material travels through a streamer and is expelled from the Sun, with the concomitant reconnection leaving a radial neutral sheet in its wake. We wish to highlight the remarkable resemblance of these coronal structures to the plasmoids which have been detected in the Earth's magnetotail [e.g., *Moldwin and Hughes*, 1991]. The "near-Earth-neutral-line" model of substorms has successfully explained these structures as arising from magnetic reconnection in the tail [*Hones*, 1977]. Although the physical conditions in the corona and the magnetosphere are quite different, the topological and evolutionary similarities of these two types of plasmoids point to a common process involved in magnetic disconnection.

Although the results reported in this paper are based on examination of a large number of events, they need to be verified with a more complete data set. In particular, the time cadences of the data sets used in this study were not ideal for a comprehensive survey. The Skylab and 1980 SMM data sets had relatively low duty cycles for synoptic coronal observations, and natural eclipses provide only snapshot views of the corona every few years. We plan a more comprehensive survey and study of the pre-existing structures from which CMEs arise and the late phase of CMEs using the extensive SMM



CME data set acquired with a steady cadence during the 5½ years between the repair of the SMM spacecraft in 1984 and its reentry in December 1989. These data were obtained with a high duty cycle rate of 87% for once-per-orbit observations of the corona. The results of these studies will provide an important baseline for observations of the evolution of streamers and CMEs that will be made with the SOHO mission, in particular with the expanded field of view that will be available with the LASCO coronagraph experiment.

**Acknowledgments.** This study was inspired by the pioneering efforts of Rainer Illing, who uncovered evidence for disconnection events in the HAO coronagraph data, and Jack Eddy, who archived many total eclipse photographs and first interpreted the 1860 feature as a transient event. We thank Eddy for assistance with the eclipse archive at HAO. D. Sime and A. Hundhausen helped us in our search of the Skylab and SMM data at HAO, and J. Burkepile assisted in displaying and copying the imagery. We are grateful to C. Keller of LASL for copies of his excellent airborne eclipse photographs, and M. Hazen of Harvard College Observatory for assistance with the Harvard eclipse data. We also thank Illing, S. Kahler, D. McComas, A. Hundhausen, C. St. Cyr, Z. Mikic, and B. Jackson for useful discussions. The work of D.F.W. was supported at Emmanuel College and Boston College by the Air Force Phillips Laboratory/Geophysics Directorate under contracts AF19628-87-K-0033 and AF19628-90-K-0006.

The Editor thanks T. G. Forbes and J. T. Gosling for their assistance in evaluating this paper.

## References

- Anonymous, Drawings of the corona from photographs of total eclipses from 1896 to 1922, *Mem. R. Astron. Soc.*, **64**, 363, 1929.
- Anzer, U., and G. W. Pneuman, Magnetic reconnection and coronal transients, *Sol. Phys.*, **79**, 129, 1982.
- Anzer, U., and I. Poland, Mass flow in loop type coronal transients, *Sol. Phys.*, **61**, 95, 1979.
- Ashe, E. D., On his photographs taken during the total solar eclipse, August 7th, 1879, *Mon. Not. R. Astron. Soc.*, **30**, 173, 1870.
- Bugoslavskaya, Y. Y., *Trud. Gos. Astron. Inst. im. Shternberga*, **19**, 3, 1950.
- Burkepile, J. T., and O. C. St. Cyr, A revised and expanded catalogue of mass ejections observed by the Solar Maximum Mission coronagraph, *NCAR/TN-369+STR*, Natl. Cent. for Atmos. Res., Boulder, Colo., 1993.
- Clette, F., P. Cugnon, and A. Koeckelenbergh, Observations of the solar corona in polarized white light during the total solar eclipse of February 16, 1980: Preliminary results, *Sol. Phys.*, **98**, 163, 1985.
- Cliver, E. W., Was the eclipse comet of 1893 a disconnected coronal mass ejection?, *Sol. Phys.*, **122**, 319, 1989.
- Cliver, E., and S. Kahler, High coronal flares and impulsive acceleration of solar energetic particles, *Astrophys. J.*, **366**, L91, 1991.
- Cliver, E. W., B. R. Dennis, A. L. Kiplinger, S. R. Kane, D. F. Neidig, N. R. Sheeley, Jr., and M. J. Koomen, Solar gradual hard x-ray bursts and associated phenomena, *Astrophys. J.*, **305**, 920, 1986.
- Dryer, M., Interplanetary studies: Propagation of disturbances between the sun and the magnetosphere, *Space Sci. Rev.*, **67**, 363, 1994.
- Eddy, J. A., A nineteenth-century coronal transient, *Astron. Astrophys.*, **34**, 235, 1974.
- Eddy, J. A., and J. G. Goff, An atlas of the white light corona, *Bull. Am. Astron. Soc.*, **3**, 261, 1971.
- Fisher, R. R., and A. I. Poland, Coronal activity below 2 R<sub>0</sub>: 1980 February 15-17, *Astrophys. J.*, **246**, 1004, 1981.
- Forbes, T. G., Numerical simulation of a catastrophe model for coronal mass ejections, *J. Geophys. Res.*, **95**, 11,919, 1990.
- Forbes, T. G., J. M. Malherbe, and E. R. Priest, The formation of flare loops by magnetic reconnection and chromospheric ablation, *Sol. Phys.*, **120**, 285, 1989.
- Gold, T., Magnetic storms, *Space Sci. Rev.*, **1**, 100, 1962.
- Gosling, J. T., Large scale inhomogeneities in the solar wind of solar origin, *Rev. Geophys. Space Phys.*, **13**, 1053, 1975.
- Gosling, J. T., Coronal mass ejections and magnetic flux ropes in interplanetary space, in *Physics of Magnetic Flux Ropes*, *Geophys. Monogr. Ser.*, vol. 58, edited by C. T. Russell, E. R. Priest, and L. C. Lee, p. 343, AGU, Washington, D. C., 1990.
- Gosling, J. T., The solar flare myth, *J. Geophys. Res.*, **98**, 18,937, 1993.
- Gosling, J. T., E. Hildner, R. M. MacQueen, R. H. Munro, A. I. Poland, and C. L. Ross, Mass ejections from the sun: A view from Skylab, *J. Geophys. Res.*, **79**, 4581, 1974.
- Gosling, J. T., D. N. Baker, S. J. Bame, W. C. Feldman, and R. D. Zwickl, Bidirectional solar wind electron heat flux events, *J. Geophys. Res.*, **92**, 8519, 1987.
- Harrison, R. A., Coronal mass ejection, *Philos. Trans. R. Soc. London, Ser. A*, **336**, 401, 1991.
- Hiei, E., A. J. Hundhausen, and D. G. Sime, Reformation of a coronal helmet streamer by magnetic reconnection after a coronal mass ejection, *Geophys. Res. Lett.*, **20**, 2785, 1993.
- Hildner, E., Mass ejections from the solar corona into interplanetary space, in *Study of Travelling Interplanetary Phenomena*, edited by M. A. Shea et al., p. 3, D. Reidel, Dordrecht, Mass., 1977.
- Hildner, E., J. T. Gosling, R. M. MacQueen, R. H. Munro, A. I. Poland, and C. L. Ross, The large coronal transient of 10 June 1973, *Sol. Phys.*, **42**, 163, 1975a.
- Hildner, E., J. T. Gosling, R. T. Hansen, and J. D. Bohlin, The sources of material comprising a mass ejection coronal transient, *Sol. Phys.*, **45**, 363, 1975b.
- Hones, E. W., Jr., Substorm processes in the magnetotail: Comment on "On hot tenuous plasma, fireballs, and boundary layers in the Earth's magnetotail" by L. A. Frank, K. L. Ackerson, and R. P. Lepping, *J. Geophys. Res.*, **82**, 5633, 1977.
- Howard, R. A., N. R. Sheeley, Jr., M. J. Koomen, and D. J. Michels, Coronal mass ejections: 1979-1981, *J. Geophys. Res.*, **90**, 8173, 1985.
- Hundhausen, A. J., Sizes and locations of coronal mass ejections: SMM observations from 1980 and 1984-1989, *J. Geophys. Res.*, **98**, 13,177, 1993.
- Hundhausen, A. J., Coronal mass ejections: A summary of SMM observations from 1980 and 1984-1989, in *The Many Faces of the Sun*, edited by K. Strong, J. Saba, and B. Haisch, Springer-Verlag, New York, in press, 1995.
- Hundhausen, A. J., C. B. Sawyer, L. House, R. M. E. Illing, and W. J. Wagner, Coronal mass ejections observed during the solar maximum mission: Latitude distribution and rate of occurrence, *J. Geophys. Res.*, **89**, 2639, 1984.
- Illing, R. M. E., A gallery of disconnection transients, *Bull. Am. Astron. Soc.*, **17**, 649, 1985.
- Illing, R. M. E., and A. J. Hundhausen, Possible observation of a disconnected magnetic structure in a coronal transient, *J. Geophys. Res.*, **88**, 10,210, 1983.



- Illing, R. M. E., and A. J. Hundhausen, Observation of a coronal transient from 1.2 to 6 solar radii, *J. Geophys. Res.*, **90**, 275, 1985.
- Jackson, B. V., and L. Leinert, Helios images of solar mass ejections, *J. Geophys. Res.*, **90**, 10,759, 1985.
- Joselyn, J., Solar events and their influence on the interplanetary medium, *EOS, Trans. AGU*, **69**, 796, 1988.
- Kahler, S., Coronal mass ejections, *Rev. Geophys.*, **25**, 662, 1987.
- Kahler, S. W., Solar flares and coronal mass ejections, *Annu. Rev. Astron. Astrophys.*, **30**, 113, 1992.
- Kahler, S. W., and A. J. Hundhausen, The magnetic topology of solar coronal structures following mass ejections, *J. Geophys. Res.*, **97**, 1619, 1992.
- Kahler, S. W., and D. V. Reames, Probing the magnetic topologies of magnetic clouds by means of solar energetic particles, *J. Geophys. Res.*, **96**, 9419, 1991.
- Klein, L. W., and L. F. Burlaga, Interplanetary magnetic clouds at 1 AU, *J. Geophys. Res.*, **87**, 613, 1982.
- Kopp, R. A., and G. W. Pneuman, Magnetic reconnection in the corona and the loop prominence phenomenon, *Sol. Phys.*, **50**, 85, 1976.
- Koutchmy, O., S. Koutchmy, C. Nitschelm, J. Sykora, and R. N. Smartt, Image processing of coronal pictures, in *Solar and Stellar Coronal Structure and Dynamics*, edited by R. C. Altrock, p. 256, NSO/ Sacramento Peak Observatory, Sunspot, N. M., 1988.
- Koutchmy, S., J. Fagot, N. I. Dzubenko, A. T. Nesmanovich, G. A. Rubo, and S. K. Veskhsvjatsky, Rapid variations observed during the total eclipse of the sun on June 30, 1973, *Nature*, **246**, 414, 1973.
- Kundu, M., N. Gopalswamy, S. White, P. Cargill, E. J. Schmahl, and E. Hildner, The radio signatures of a slow coronal mass ejection: Electron acceleration at slow-mode shocks?, *Astrophys. J.*, **347**, 505, 1989.
- Linker, J. A., G. Van Hoven, and D. J. McComas, Simulations of coronal disconnection events, *J. Geophys. Res.*, **97**, 13,733, 1992.
- Low, B. C., Mass acceleration processes: The case of the coronal mass ejection, *Adv. Space Res.*, **13**(9), 63, 1993.
- MacCombie, W. J., and D. M. Rust, Physical parameters in long-decay coronal enhancements, *Sol. Phys.*, **61**, 69, 1979.
- MacQueen, R. M., Coronal transients: A summary, *Philos. Trans. R. Soc. London, Ser. A*, **297**, 605, 1980.
- MacQueen, R. M., J. T. Gosling, E. Hildner, R. H. Munro, A. I. Poland, and C. L. Ross, The High Altitude Observatory white light coronagraph, *Proc. SPIE, Int. Soc. Opt. Eng.*, **44**, 207, 1974.
- MacQueen, R. M., A. Csoeke-Poeckh, E. Hildner, L. House, R. Reynolds, A. Stanger, W. Tepoel, and W. Wagner, The High Altitude Observatory coronagraph/polarimeter on the Solar Maximum Mission, *Sol. Phys.*, **65**, 91, 1980.
- Marsden, R. G., T. R. Sanderson, C. Tranquille, and K. P. Wenzel, ISEE 3 observations of low-energy proton bidirectional events and their relation to isolated interplanetary magnetic structures, *J. Geophys. Res.*, **92**, 11,009, 1987.
- Martens, P. C. H., and N. P. M. Kuin, A circuit model for filament eruptions and two-ribbon flares, *Sol. Phys.*, **122**, 263, 1989.
- Martinez, J., A better photograph of coronal streamers, *Sky Telescope*, **56**, 92, 1978.
- McComas, D. J., J. T. Gosling, J. L. Phillips, S. J. Bame, J. G. Luhmann, and E. J. Smith, Electron heat flux dropouts in the solar wind: Evidence for interplanetary magnetic field reconnection?, *J. Geophys. Res.*, **94**, 6907, 1989.
- McComas, D. J., J. L. Phillips, A. J. Hundhausen, and J. T. Burkepile, Observations of disconnection of open coronal magnetic structures, *Geophys. Res. Lett.*, **18**, 73, 1991.
- McComas, D. J., J. T. Gosling, and J. L. Phillips, Interplanetary magnetic flux: Measurement and balance, *J. Geophys. Res.*, **97**, 171, 1992a.
- McComas, D. J., J. L. Phillips, A. J. Hundhausen, and J. T. Burkepile, Disconnection of open coronal magnetic structures, in *Solar Wind Seven*, edited by E. Marsch and R. Schwenn, p. 225, Pergamon, New York, 1992b.
- Michels, D. J., R. A. Howard, M. J. Koomen, and N. R. Sheeley, Jr., Satellite observations of the outer corona near sunspot maximum, in *Radio Physics of the Sun*, edited by M. R. Kundu and T. E. Gergely, p. 439, D. Reidel, Hingham, Mass., 1980a.
- Michels, D. J., R. A. Howard, M. J. Koomen, N. R. Sheeley, Jr., and B. Rompolt, The solar mass ejection of 8 May 1979, in *Solar and Interplanetary Dynamics*, edited by M. Dryer and E. Tandberg-Hanssen, p. 387, D. Reidel, Hingham, Mass., 1980b.
- Mikic, Z., and J. A. Linker, Disruption of coronal magnetic field arcades, *Astrophys. J.*, **430**, 898, 1994.
- Moldwin, M. B., and W. J. Hughes, Plasmoids as magnetic flux ropes, *J. Geophys. Res.*, **96**, 14,051, 1991.
- Munro, R. H., and D. G. Sime, White-light coronal transients observed from Skylab May 1973 to February 1974: A classification by apparent morphology, *Sol. Phys.*, **97**, 191, 1985.
- Phillips, J. L., J. T. Gosling, D. J. McComas, S. J. Bame, and W. C. Feldman, Quantitative analysis of bidirectional electron fluxes with coronal mass ejections at 1 AU, in *Solar Wind Seven*, edited by E. Marsch and R. Schwenn, p. 651, Pergamon, New York, 1992.
- Pickering, W. H., Total eclipse of the sun, August 29, 1886, *Ann. Harvard Coll. Obs.*, **18**(5), 85, 1886.
- Ranyard, A. C., On a remarkable structure visible upon the photographs of the solar eclipse of December 12, 1871, *Mon. Not. R. Astron. Soc.*, **34**, 365, 1874.
- Ranyard, A. C., Observations made during total solar eclipses, *Mem. R. Astron. Soc.*, **41**, 1, 1879.
- Richardson, I. G., and D. V. Reames, Bidirectional 1 MeV  $\text{amu}^{-1}$  ion intervals in 1973-1991 observed by the Goddard Space Flight Center instruments in IMP 8 and ISEE 3/ICE, *Astrophys. J. Suppl.*, **85**, 411, 1993.
- Rusin, V., and M. Rybansky, Structure of the solar corona during the solar eclipse of 1980 February 16, *Bull. Astron. Inst. Czech.*, **34**, 257, 1983.
- Rust, D. M., Solar activity, *Rev. Geophys. Space Phys.*, **21**(2), 349, 1983.
- Sheeley, N. R., Jr., R. A. Howard, D. J. Michels, and M. J. Koomen, Solar observations with a new earth-orbiting coronagraph, in *Solar and Interplanetary Dynamics*, edited by M. Dryer and E. Tandberg-Hanssen, p. 55, D. Reidel, Hingham, Mass., 1980.
- Sheeley, N. R., Jr., R. A. Howard, M. J. Koomen, D. J. Michels, K. L. Harvey, and J. W. Harvey, Observations of coronal structure during sunspot maximum, *Space Sci. Rev.*, **33**, 219, 1982.
- Shklovskii, I. S., *Physics of the Solar Corona*, p. 12, Addison-Wesley, Reading, Mass., 1965.
- Steinolfson, R. S., Models of material ejection, in *Dynamics of Solar Flares*, edited by B. Schmieder and E. Priest, p. 171, Observatoire de Paris, DASOP, Paris, 1991.
- Steinolfson, R. S., Coronal shock waves, in Proceedings of the 26th ESLAB Symposium, *Spec. Publ. ESA SP-346*, p. 51, Eur. Space Agency, Neuilly, France, 1992.
- Stewart, R. T., G. A. Dulk, K. V. Sheridan, L. L. House, W. J. Wagner, C. Sawyer, and R. Illing, Visible light observations of a dense plasmoid associated with a moving type IV solar radio burst, *Astron. Astrophys.*, **116**, 217, 1982.
- Suess, S. T., The relationship between coronal and inter-

- planetary magnetic fields, *Adv. Space Res.*, **13**(9), 31, 1993.
- Svestka, Z., and Cliver, E. W., History and basic characteristics of eruptive flares, in *Eruptive Solar Flares*, edited by Z. Svestka, B. Jackson, and M. Machado, p. 1, Springer-Verlag, New York, 1992.
- Todd, M. L., *Total Eclipses of the Sun*, Little, Brown, Boston, Mass., 1900.
- Webb, D. F., Table of solar activity associated with coronal mass ejections observed by the SMM coronagraph/polarimeter in 1980, *NCAR/TN-297+STR*, Natl. Cent. for Atmos. Res., Boulder, Colo., 1987.
- Webb, D. F., Erupting prominences and the geometry of coronal mass ejections, *J. Geophys. Res.*, **93**, 1749, 1988.
- Webb, D. F., The solar sources of coronal mass ejections, in *Eruptive Solar Flares*, edited by Z. Svestka, B. Jackson, and M. Machado, p. 234, Springer-Verlag, New York, 1992.
- Webb, D. F., The heliospheric manifestations and geoeffectiveness of solar mass ejections, in *Solar-Terrestrial Predictions Workshop: IV*, edited by A. Hruska et al., p. 71, National Oceanic and Atmospheric Administration, Boulder, Colo., 1993.
- Webb, D. F., and E. W. Cliver, Evidence for magnetic disconnection of mass ejections in the corona, *Bull. Am. Astron. Soc.*, **21**, 857, 1989.
- Webb, D. F., and R. A. Howard, The solar cycle variation of coronal mass ejections and the solar wind mass flux, *J. Geophys. Res.*, **99**, 4201, 1994.
- Webb, D. F., and A. J. Hundhausen, Activity associated with the solar origin of coronal mass ejections, *Sol. Phys.*, **108**, 383, 1987.
- Zhang, G., and L. F. Burlaga, Magnetic clouds, geomagnetic disturbances, and cosmic ray decreases, *J. Geophys. Res.*, **93**, 2511, 1988.

---

E. W. Cliver and D. F. Webb, Geophysics Directorate, Phillips Laboratory/GPSG, 29 Randolph Road, Hanscom AFB, MA 01731-3010. (e-mail: webb@plh.af.mil)

(Received April 27, 1994; revised September 29, 1994; accepted October 17, 1994.)



## SOLAR AND GEOMAGNETIC DISTURBANCES DURING THE DECLINING PHASE OF RECENT SOLAR CYCLES

D. F. Webb

*Institute for Space Research, Boston College, Newton Center, MA 02159,  
U.S.A.*

The U.S. Government is authorized to reproduce and sell this report.  
Permission for further reproduction by others must be obtained from  
the copyright owner.

### ABSTRACT

On average, the distribution of geomagnetic disturbances over the solar activity cycle exhibits two peaks. It is commonly thought that these peaks represent two components of geomagnetic activity that have very different solar and heliospheric sources. A peak near solar maximum is associated with transient solar activity and a later peak during the declining phase is attributed to recurrent high speed streams from coronal holes. Coronal mass ejections (CMEs) are now considered to be the most important phenomenon associated with the first peak. However, the influence of such transient disturbances may also extend into the declining phase. It is becoming apparent that the coronal streamer belt and its extension as the heliospheric current sheet plays a major role in both kinds of geoactivity. For example, streamers are the source of many, if not most CMEs. During the declining phase, corotating stream interaction regions (CIRs) cause the strongest recurrent geomagnetic activity, often because CMEs cluster there. CIRs arise from interactions at the boundaries between streamers (slow wind) and coronal holes (fast wind). These aspects of geomagnetic disturbances during the declining phases of cycles are reviewed with emphasis on comparison of the present solar cycle with the previous two cycles.

### THE DISTRIBUTION OF GEOMAGNETIC ACTIVITY OVER THE SOLAR CYCLE

It has long been known that the level of geomagnetic activity at the earth tends to follow the sunspot cycle. Sunspots are considered a useful measure of the general level of magnetic activity on the sun, and the smoothed sunspot number rises and falls monotonically over the cycle. This activity is transmitted to Earth via the solar wind.

On average, however, the distribution of geomagnetic (GM) disturbances over the solar activity cycle exhibits two peaks, one near sunspot maximum and the other during the declining phase of the cycle. It is commonly thought that these two peaks represent the maximum phases of two components of GM activity that have very different solar and heliospheric sources. The first peak is considered associated with transient solar activity that tracks the solar cycle in both amplitude and phase. The later peak during the declining phase is usually attributed to recurrent high speed streams from coronal holes.

The close overall coupling between the sunspot and GM activity cycles can be seen in long-term plots comparing various indices of the two kinds of activity. For example, the so-called centennial series of the aa GM index has been used to show its long-term trend compared with sunspot numbers. The aa index measures GM activity at two antipodal stations and was determined for the years 1868-1967 by /1/. Mayaud /1/ presents plots of aa and sunspot number for these 10 solar cycles and /2/ show an updated version through cycle 21. There is a good overall correspondence between these parameters but with a distinct upward trend in the envelope of maximum and minimum aa values since 1900. This trend is unexplained but may be related to the 88 yr Gleissberg cycle in sunspot variations, e.g., /3/. However, no such trend is apparent from 1781-1880 in data derived from the magnetic declination compiled by Wolf (e.g., see Fig. 24 in /4/).

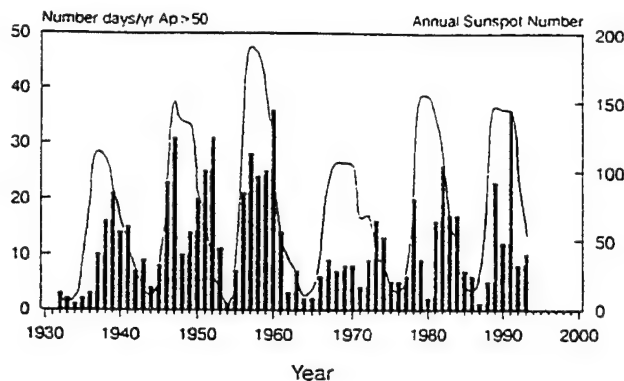


Fig. 1. Annual numbers of geomagnetic disturbed days,  $A_p > 50$ , (bars) vs. sunspots (light line) for solar cycles 17-22. Cycle numbers are marked above each curve. Courtesy NOAA, SEL.

On annual time scales the GM activity cycle clearly has more structure than the solar cycle. This is illustrated in Figure 1, which shows the annual number of disturbed days ( $A_p > 50$ ) vs sunspot number for the last 6 solar cycles, 17-22. The distribution of GM activity is more varied than sunspot number, but tends to track the sunspot cycles in amplitude. For example, the least "active" solar cycles, 17 and 20, also had the lowest levels of GM storms.

Figure 1 also demonstrates the double peaked nature of the GM activity cycle. There is evidence for two peaks in most cycles, with the first peak at or just before the sunspot peak and the second during the declining phase. The later peak is often higher than the first. Legrand and Simon [2] have studied the distribution of 192 "severe" storms ( $aa > 100$  nT) from 1868-1980 (their Fig. 10) and concluded that there are, on average, three intervals of activity during the sunspot cycle: a 1-2 yr period with no intense storms at sunspot minimum, a 6-yr interval of severe storms peaking one yr before sunspot maximum, and a 3-4 yr period of storms with a peak  $\sim 3$  yr after maximum. Gonzales et al. [5] performed a similar study of the distribution of  $aa$  and Dst storms over cycles 13-21, and found that both intense and moderate storms had similar distributions with the first peak occurring 8 mo before sunspot maximum and the later peak 2 yr after maximum.

The space age began in earnest in the 1960s. Since the beginning of solar cycle 20, we have had nearly continuous spacecraft measurements of the solar wind near the earth. So we can now compare and contrast the solar inputs and the interplanetary and GM responses over the last 3 solar cycles. Here we review the distribution of GM activity with an emphasis on the solar and interplanetary (IP) influences on this activity during the declining phase of the solar cycle, the primary focus of this Symposium. In the next section we briefly discuss transient solar and IP activity related to the first peak of GM activity, and the newly-realized importance of coronal mass ejections (CMEs) and IP shocks to GM storms. This is followed by a discussion of the important role of the coronal streamer belt as the locus of the heliospheric current sheet (HCS) and as a source of CMEs. The fourth section describes the solar and IP sources of the second peak of GM activity in the context of high speed streams and the slow speed boundaries which divide them. The evidence for a 22-year cycle in the level of recurrent activity is briefly discussed and related to the reversal of the solar dipole field. Finally, we compare the recurrent patterns in GM activity during the declining phases of the last 3 solar cycles, including the current cycle 22, and summarize the results.

#### SOLAR AND INTERPLANETARY SOURCES OF THE FIRST ACTIVITY PEAK

The dual-phase nature of GM activity is usually thought to arise from the superposition of two quite different sources of solar activity. In this section we discuss the transient solar and IP activity related to the first peak of GM activity and the newly-realized importance of CMEs and IP shocks to GM storms.

Overall, GM storms are statistically best correlated with the speed of the solar wind and with the

southward component ( $B_s = -B_z$ ) of the interplanetary magnetic field (IMF), e.g. /6, 7/. Lower correlations have been found between other combinations of solar wind parameters and GM indices. Longer periods of GM activity correlate best with solar wind speed, and shorter periods (min to hr) with enhanced  $B_s$ . This latter effect can be very pronounced in comparisons between short-term  $B_z$  fluctuations and the auroral electrojet index AE, particularly during the passage of high speed streams, e.g. /8/. The influence of periods of strong V and  $B_s$  impinging on the earth can be qualitatively understood because high speed is associated with high momentum flux, and  $B_s$  fields with an increased efficiency in transferring solar wind energy to the magnetosphere, probably through magnetic merging at the dayside magnetopause.

A GM storm is the long-term (hr to days) response of the magnetosphere to the passage of a structure in the solar wind. Compression of plasma and fields at the leading edge of the structure causes either a sudden or gradual commencement to the storm. Most sudden commencements occur during the maximum phase of the solar cycle since they are well correlated with IP shocks /9/. They are also associated with the most intense storms. Tsurutani, Gonzales and colleagues (e.g. /10/) have shown that the  $B_s$  fields associated with the most intense ( $Dst < -100$  nT) storms are caused by IP shocks and their sheaths, the so-called "driver gas" which follows, and/or a distorted HCS. All of these structures have been associated in other studies with coronal transients.

For years it was thought that solar flares were responsible for major IP particle events and storms. However, recently we have seen the development of an important new paradigm such that now CMEs, not flares, are considered the key causal link between solar activity and major transient IP and geomagnetic disturbances /11, 12/. CMEs are vast structures of plasma and magnetic fields that are expelled from the sun into the heliosphere. Fast CMEs propel fast shock waves ahead of them which trigger the sudden storm commencements when they reach the earth. These transient shocks also accelerate energetic particles which can penetrate the magnetosphere and create hazardous conditions to spacecraft and astronauts in Earth orbit. The CME itself constitutes the "driver gas" following the shock and can contain high speed plasma and strong magnetic fields which, when coupled to the magnetosphere, lead to intensification of the ring current, effectively causing the main phase of a storm.

The ISEE-3 spacecraft was placed at the L1 point in front of Earth from 1978 to late 1982 and collected vital data on solar-terrestrial interactions during the maximum phase of cycle 21. Several studies involving these data have been fundamental to our understanding of the causes of storms and the new paradigm. These include the papers by Tsurutani and his colleagues mentioned above in which they compared ISEE-3 solar wind and AE and Dst data sets during the ten largest storms from August 1978 to January 1980. Based on ISEE data, Gosling and McComas /13/ proposed that compression and draping in the leading edge of a CME and of the ambient IMF are prime causes of strong  $B_z$ . Field line draping alone can enhance  $B_z$ . If, in addition, there are strong  $B_s$  fields in the leading edge of the CME, a long period of strong  $B_s$  may ensue causing a severe storm at Earth. Crooker et al. /14/ emphasize that in-ecliptic compression and draping of the shock sheath fields can also result in enhanced  $B_s$  fields due to the Russell-McPherron effect.

Since sudden commencements are well correlated with IP shocks which in turn are driven by fast CMEs, it is inferred that the CME itself causes the sudden commencement storms. This was demonstrated statistically by /15/ using ISEE-3 bidirectional electron events as proxies for CMEs. They found that all but one of the 37 largest storms ( $K_p > 5$ ) from 1978-1982 were associated with the passage of bidirectional events and/or shocks (Figure 2). The most effective coupling with such storms is when both a CME and its shock pass over the earth; in this case the disturbance is encountered head-on where the flow parameters are maximized. However, Gosling et al. /15/ note that the association is much reduced for the more frequent smaller storms. Slower CMEs not driving shocks are probably associated with many of the smaller storms, but this has not yet been demonstrated with CME proxies. In an attempt to better define the characteristics of geoeffective CMEs, my colleagues and I are studying the characteristics of CMEs aimed at the earth using HELIOS photometer data. We have found that half of these CMEs can be associated with moderate to large storms. These CMEs have longer durations and higher speeds, masses and momenta, and are more often associated with shocks and other in-situ

characteristics of CMEs than those not related to storms. In another ISEE study Zhao et al. /16/ found that 78% of all periods with IMF  $B_s \geq 10$  nT for durations  $\geq 3$  hr were associated with one or more CME proxies. We also now know that the occurrence rate of CMEs closely tracks the solar activity cycle in both amplitude and phase /17/. This is consistent with the close association of CMEs with IP shocks and sudden storm commencements. When combined with the other information discussed above, it appears likely that CMEs and their related phenomena are the primary cause of the transient component related to the first peak of GM activity.

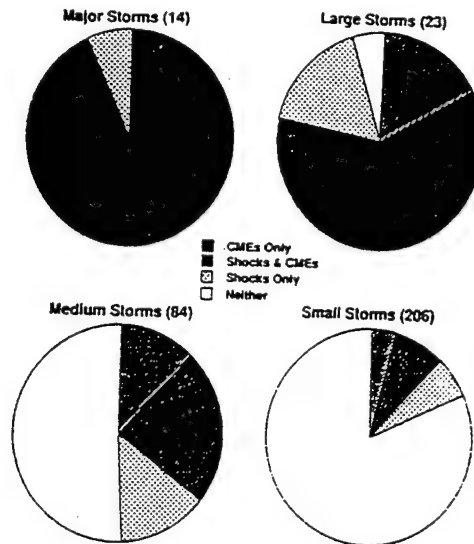


Fig. 2. Pie charts of the association of GM storms with Earth passage of CMEs and IP shocks from 1978-1982 /15/. ( ) indicate the number of storms in each category: Major,  $K_p \geq 8$ ; Large,  $7 \leq K_p \leq 7+$ ; Medium,  $6 \leq K_p \leq 6+$ ; Small,  $5 \leq K_p \leq 5+$ .

#### RELATION OF THE HELIOSPHERIC CURRENT SHEET TO STREAMERS AND CMEs

In order to understand all GM activity, including that which is recurrent, we need to place it in the context of the evolution of the sun's magnetic field and its associated activity over the cycle. We do so in this section by pointing out the close relationship among coronal streamers, the heliospheric current sheet (HCS) and CMEs and their evolution over the cycle. This connection is the foundation of a new consensus view of the solar-terrestrial interaction.

The simplest magnetic configuration of the sun occurs, not coincidentally, during activity minimum. At this time the sun's magnetic field can be approximated as a dipole whose axis is tilted slightly with respect to the axis of rotation. Large coronal holes cover the sun's polar regions with lobes extending equatorward. These open field regions are of opposite polarity. Separating them is a band about  $40^\circ$  wide centered over the heliomagnetic equator within which are mostly closed structures near the surface, i.e., active regions and sunspots. The coronal streamers extend over these regions forming a bright band around the sun. The high speed wind flowing from the polar holes constricts the oppositely-directed fields over the streamers to a narrow current sheet which, in a 3-dimensional view, takes on the appearance of a ballerina's skirt. The rotating, warped heliospheric current sheet appears as a sector boundary crossing at Earth, such that during one solar rotation the earth will be immersed in two large sectors of opposite polarity each with the relatively high speed wind of its parent hole.

During the cycle new magnetic flux emerges at higher latitudes leading to a more complex and disturbed corona. The streamer belt and heliomagnetic equator become more complicated and more inclined ("tilted") to the rotation axis, and more sectors and boundary crossings will be observed at Earth. Near maximum activity a simple, single current sheet surrounding the sun may not exist, although one recent study suggests that a 4-sector, single sheet pattern still exists even at maximum /18/. The tilted dipole model of the sun was shown by /19/ and others to empirically match the 3-dimensional corona during



SkyLab. Recent observations of the latitudinal dependence and evolution of CIRs at high latitudes from Ulysses show excellent agreement with improved 3-D tilted dipole models /20/.

On a global scale the slow wind is confined to the streamer belt and the HCS. It now appears that this belt is the source of most CMEs and other transient activity which affects the heliosphere, except possibly near maximum. This new understanding comes largely from results from the extended observations of CMEs made with the SOLWIND and SMM coronagraphs from 1979-1989. The temporal and latitudinal distributions of these CMEs are similar to those of streamers and prominences, being confined to low latitudes about the HCS near cycle minimum and becoming widely distributed in latitude near maximum /21/. This evolution is very different from that of active regions, flares or sunspots. Many energetic CMEs are actually the disruption of a pre-existing streamer, which increases in brightness and size for days before erupting as a CME. Afterwards the streamer and CME are gone, often replaced by a thin ray, probably a current sheet. Several recent studies /21, 22/ show that most CMEs are clustered within  $\sim 20^\circ$  of the coronal current sheet over much of the cycle. For example, in 1994 many streamers were blown out as CMEs, appearing on synoptic maps as "bugles" (see Fig. 12 in /21/). Thus, CMEs tend to arise in coronal streamers and these streamers form the locus of the HCS at the Sun.

Crooker et al. /23/ have recently developed a phenomenological model which consolidates the roles of coronal streamers, the HCS and sector boundaries, and CMEs over the solar cycle. They noted that the IMF at sector boundary crossings can be quite complex. They examined a sector boundary crossing at Earth on 21 April 1979 because it had the typical plasma structure of sector boundaries preceding high speed streams /24/, i.e., a sharp density peak and rapid velocity and temperature dips at the crossing. Crooker et al. found that the ISEE-3 IMF data revealed many directional discontinuities across the boundary indicating many time scales for its effective "thickness". In addition, a planar magnetic structure was detected in the ISEE data and a CME was observed earlier both remotely and in-situ within hours of the same boundary crossing at Helios-2 at 0.5 AU. These observations provide evidence that CMEs, magnetic clouds and other transient phenomena are often found near sector crossings in the solar wind. The authors contend that the classic description of the HCS as a single continuous sheet is often not correct.

Crooker et al. /23/ suggest that the sector boundary structure arises because the base of the HCS in the corona can be broad, encompassing multiple helmet streamers spanning tens of heliographic deg. In the heliosphere, these structures are compressed into a sandwich of multiple current sheets across the boundary between sectors. Figure 3 is a schematic of the model showing the HCS as a disk of variable thickness forming a conduit for transient outflow. In this view the HCS is more dynamic than previously thought, acting as a conduit for a range of activity from slowly evolving streamers to large CMEs. This process also compresses, amplifies and aligns pre-existing magnetic discontinuities in the HCS and at the leading edge of high speed streams /25/. These factors can also enhance the geoeffectiveness of CMEs.

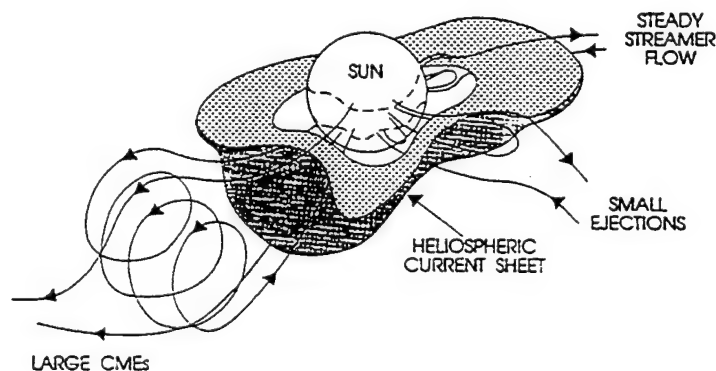


Fig. 3. Schematic model of HCS as a disk of variable thickness forming a conduit for transient outflow from streamer belt. After /23/.

However, there are some problems with this relatively straightforward picture. For example, Neugebauer et al. /25/ find that directional discontinuities and planar magnetic structures can occur elsewhere other than at sector boundaries. Ivanov et al. /26/ derive a model of the HCS and find that flares and CMEs sense the HCS as a barrier and are impeded by it. Thus, in their view GM activity is greatest for sources which arise farther from the HCS.

### SOURCES OF THE SECOND ACTIVITY PEAK

In this section we will discuss those aspects of the new paradigms, the streamer belt/HCS/CME interaction and the geoeffectiveness of CMEs, which are important for GM activity during the declining phase of the solar cycle. First we describe the periodicities other than the basic long-term solar 11-yr and 88-yr cycles which are important for GM activity during the declining phase. There are 3 other periodic patterns of activity on time scales longer than a day that are pertinent. The most important is, of course, the 27-day recurrence pattern imposed by the corotation of solar wind streams. The other two effects are secondary and are caused by periodic changes in the relationship between the earth's and sun's dipole fields; they are the double, or 22-yr cycle and the semiannual variation. We briefly review these periodicities then discuss in detail the 27-day recurrence pattern.

Maunder in 1905 /27/ was the first to convincingly demonstrate a recurrence pattern in GM activity of 27 days and to link it to the solar rotation rate. Hapgood /28/ has recently reviewed the evidence for this periodicity and performed significance tests of the recurrence of storm days ( $A_p \geq 30$ ) during the declining phases of cycles 17-21. Figure 4a shows the results of significance tests of the storm periods during the declining phase of each cycle. All of the  $\chi^2$  values are significant at the 99% confidence level and peak at a period of about 27 days with a width of 6 d. Figure 4b shows the distributions of both the number of recurrent storm days and their significance (against chance occurrence) vs the sunspot cycle. The declining phase of each of the 6 cycles has a strong ( $\chi^2 \geq 30$ ) 27-d peak.

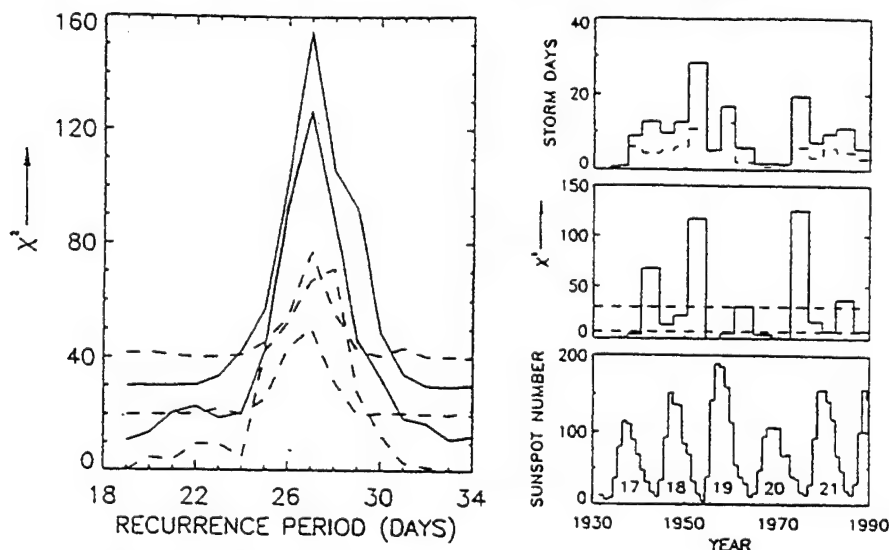


Fig. 4. Significance tests of storm day recurrence during declining phase of cycles 17-21 /28/. (a)  $\chi^2$  values of storm recurrence periods. (b) Distributions of recurrent storm days and their significance vs sunspot number.

Figure 4 also reveals that the peaks in the even-numbered cycles, 18 and 20, are much larger than those in the odd-numbered cycles. This is called the double or 22 year cycle and was first noted by Chernosky /29/, who examined 80 years of the Ci index. He found not only that the last half of even-numbered cycles tended to be more geomagnetically active than the first half, but that the activity started at a lower level than for odd-numbered cycles and peaked later. Russell and McPherron /30/ proposed that the 22-yr cycle was related to the 22 yr magnetic cycle of the sun. The solar field changes its polarity every cycle shortly after sunspot maximum as does the heliographic latitude dependence of the IMF polarity.

Therefore, after the maximum of alternate 11-yr periods the 'toward' polarity is dominant during the first half of the year and the 'away' polarity during the second half. These occurrences enhance the  $B_s$  component at Earth leading to stronger GM activity. On the contrary, during the alternate 11-year cycles the polarity is reversed and GM activity is weaker. This suggests that the present cycle 22 will have strong recurrent GM activity during its declining phase.

Russell and McPherron /30/ attributed the semiannual effect to the annual variation of the IMF polarity such that the IMF projects a southward component at the earth in a geocentric coordinate system whenever its polarity points toward the sun in the spring and away from the sun in the fall (also see /6/). The semiannual effect has been confirmed and analyzed by a number of methods, but usually only for average or total levels of GM indices. However, /14/ noted a pronounced semiannual variation of the occurrences of large storms and argued that much of this periodicity may be due to "compression and draping within the ecliptic plane in postshock flow preceding CMEs [which] greatly strengthens the Russell-McPherron effect there..." Others have emphasized that other effects in addition to the Russell-McPherron mechanism may also contribute to the semiannual distribution of storms.

With the advent of relatively continuous monitoring of the solar wind by spacecraft beginning in the mid 1960s we could study the relationship of various interplanetary parameters to GM activity on long time scales. We now have data coverage of most of four solar cycles with relatively complete coverage for cycles 20 and 21. A number of researchers have discussed the variations in average solar wind parameters during these two cycles and, in general, have found strong correlations between the speed of the wind and GM activity. For example, Gosling et al. /31/ first reported that the solar wind speed was unusually high during the latter half of cycle 20 in 1973-1975. The high speeds were associated with enhanced GM activity which lagged the sunspot peak by  $\sim 6$  yr. Crooker et al. /32/ found that the yearly Ap index was well correlated with  $V^2$  during cycle 20, but Crooker and Gringauz /7/ found it to be poorly correlated during cycle 21.

Slavin et al. /33/ and Hapgood et al. /34/ studied the long-term averages of the IMF over cycles 20 and 21. They found that the field strength and  $B_z$  were approximately 50% stronger in cycle 21 than 20, in accord with the signature of the total solar magnetic flux. The field strength peaked in 1982. Crooker and Gringauz /7/ concluded that during both cycles the Ap index correlated well with the product  $B_s V^2$ . The long-term variation of Dst was different from Ap and not as simply related to  $B_s$  or  $V$ . Hapgood et al. /34/ examined the variation of the dynamic solar wind pressure and found that it also peaked during the declining phase of the cycles, coincident with the speed peaks. However, in contrast to the wind speed, the peak pressure was higher in cycle 21 than 20, consistent with a steady density increase after 1970.

An important question is what are the solar sources of high speed solar wind and of high IMF strengths? Bartels called the solar sources of recurrent GM storms "M-regions", which were unknown for many years. With the advent of Skylab observations, M-regions were identified with coronal holes. Coronal holes were determined to be the primary sources of open field lines and high speed, low density flows in the solar wind. They were long-lived and corotated with the Sun. High speed wind streams were found to be largest and strongest during the declining phase of the cycle when the holes were largest and had lobes which extended toward the helioequator. The association between the number of near-equatorial coronal holes and storms was greatest during the declining phase of solar cycle 21 /35/. However, coronal holes cannot explain all recurrent storms. At its peak in 1984, near-equatorial holes could only account for less than half of all Ap > 30 storms /35/.

Recently, Crooker and Cliver /36/ have reexamined the M-region/recurrent storm relationship. They emphasize that the peak recurrent GM activity coincides with the passage of CIRs and their associated sector boundaries, as shown by /37/ and others. In the solar wind CIRs separate regions of high and low speed flows, which are identified with coronal holes and streamers, respectively, at the sun. Thus, the solar sources of the recurrent activity must include the boundaries between coronal holes and streamers.

At the sun the divergence and convergence of magnetic structures across these boundaries create temperature and velocity gradients (see Fig. 2 in /19/). Dessler and Fejer /38/ were the first to propose

that in the solar wind the interaction between these flows would create a region of enhanced turbulence which, in turn, would cause GM storms at Earth. We now know that this increased activity is caused by enhanced IMF due to compression at the leading edge of the high speed stream /36, 39/.

Figure 5 illustrates an example of this effect during a period of particularly prominent recurrent activity in the declining phase of cycle 20. This is a plot of the 27-day recurrence pattern of the Dst index during 1974. The solar wind data show two clearly separated high speed streams during the year; the boundaries between these two sectors are marked by vertical dashes. The peak GM activity follows the boundaries by 1-2 days, in agreement with their cause being compressed Bs fields in CIRs.

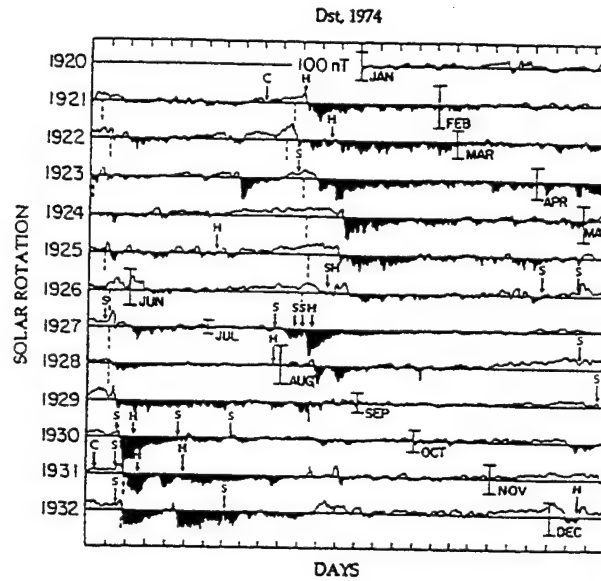


Fig. 5. 27-d recurrence plot of Dst index in 1974 /36/. Vertical dashes mark sector boundaries and arrows mark passage times of shocks (S), helium abundance enhancements (H), and magnetic clouds (C).

In the Crooker et al. /23/ model, the HCS is considered a conduit for CMEs so that the probability of encountering a CME in the ecliptic plane increases near sector boundaries. This prediction is strongly supported during the recurrent phase of the cycle, at least for cycle 20 /36, 8/. Figure 5 shows that the IP signatures of CMEs at Earth (vertical arrows) tend to cluster around the sector boundary crossings. It is important to emphasize that nearly all IP shocks (and therefore SCs) at 1 AU precede CMEs; corotating shocks associated with CIRs generally form beyond 1 AU (e.g. /39, 36/). CMEs also can contain Bs fields which can be compressed in the CIR. This compression is most effective for slow CMEs. In addition, Figure 5 demonstrates how effective the Russell-McPherron effect was during this period. Although there were two strong wind streams of opposite polarity in 1974 /40/, GM activity was clearly stronger in the second stream ("toward" polarity) during the first half of the year and in the first stream ("away" polarity) during the second half of the year. This is as predicted by the R-M effect /36/.

Finally, Crooker and Cliver /36/ note that there is a period of what they call "sustained" GM activity which follows and is weaker than the CIR-associated activity but can last 10 days or more. This weaker activity is associated with the high speed stream itself and, therefore, with the near-equatorial coronal hole. This activity is related to the continuous auroral activity called HILDCAAs caused by southward components of Alfvén waves in the streams /8/. Sustained activity can, of course, occur whether or not there is any distinct CIR-associated activity. Because of the interrelationship of CMEs with the streamer belt and the HCS, it is clear that forecasting the time of arrival of sector boundary crossings at the earth should improve forecasts of GM storm periods at nearly all phases of the solar cycle.

## PATTERNS IN THE PRESENT CYCLE (22)

Since the beginning of solar cycle 20 in 1965, we have had nearly continuous spacecraft measurements of the solar wind near the earth. Thus, we can now compare and contrast the solar inputs and IP and GM responses over the last 3 solar cycles. We have discussed some of the recurrent patterns in IP and GM activity during the declining phases of cycles 20 and 21. In this section we will discuss these aspects of the current cycle 22, in particular, the timing and strength of the recurrence patterns in GM activity compared with those of cycles 20 and 21.

Sheeley et al. /40/ and Sheeley and Harvey /41/ presented color-coded, 27-day displays comparing IMF polarity, solar wind speed and the GM disturbance index C9 from 1962-1979. These maps nicely demonstrate the dominance of the two-sector, 27-day corotation patterns during the declining phases of cycles 19 and 20. The data set beginning with Skylab in 1973 also includes coronal holes and their polarities, and shows that the holes also rigidly rotated during the declining periods and lay centered within the like-polarity IMF patterns. The solar wind coverage was spotty during the latter half of cycle 19 but suggests that the two-stream recurrence pattern set in before the end of 1962 and extended for at least 2 years nearly to the end of 1964. Cycle 20 showed a similar but stronger two-sector recurrence pattern starting in the fall of 1973 and extending through the spring of 1975, a period of 1½ yr.

The 27-day displays have been continued through cycle 21, but the solar wind data are not continuous /42/. We have also examined the GM activity patterns during the declining phases of cycles 21 and 22 for comparison with the earlier cycles. For cycle 21 we studied the 27-day pattern of activity using the 27-day displays and the annual plots of the Planetary Kp index in the Solar-Geophysical Data Bulletins from 1983 through 1985. The recurrence pattern of GM activity during the declining phase of this cycle was most apparent beginning in mid-1984 and extending to about May 1985, a period of about one year. However because of the incomplete IMF data coverage, we were unable to identify repeated crossings of the same sector boundary. In addition, the only continuous data available as an IP CME proxy are sudden commencements as indicators of IP shocks at 1 AU. With these limitations, we find that the overall pattern of GM activity recurrence in cycle 21 was similar to that of cycles 19 and 20. In particular it was similar to the period in 1974-75 with IP shocks and peak GM activity following the sector crossings by 1-2 days. However, the activity associated with one stream was stronger than the other and the overall patterns not as sharply defined as in 1974 (Figure 5). This is because the two-sector, high speed stream pattern was not as strong or as long-lived in 1984-85 as compared with 1974-75.

What can we say about how the present cycle compares with earlier ones, and about the timing and severity of GM activity during the declining phase? Referring back to Figure 1, we see that the present sunspot cycle had a rapid rise but was otherwise similar to the average envelope of previous cycles in terms of the distribution of both sunspot number and GM activity. The exceptions to this general pattern are that cycle 20 was abnormally low in both types of activity, and that cycle 21 had an unusual deficit of GM activity in 1980 during sunspot maximum. We note that because cycle 22 is an even numbered cycle, we can predict that the level of GM activity during the declining phase may be high due to enhanced values of the wind speed and/or IMF strength.

That we are well into the declining phase of cycle 22 is indicated by a number of key data sets. For example, McIntosh /43/ notes that the 10.7 cm solar radio flux is a good indicator of the duration of the maximum phase of coronal activity during the solar cycle, and that the end of this phase is usually signaled by an abrupt drop in intensity. This drop thus represents a good marker of the start of the declining phase of activity. The 10.7 cm plots of cycles 18-22 show that the duration of the maximum phase is consistently > 3 yr. The last 3 cycles have exhibited similar profiles, with flat maxima and sharp drops in intensity. The sharp drop signaling the start of the declining phase of cycle 22 occurred in March 1992, only 6 yr after cycle onset in 1986. This is shown in Figure 6 where the 10.7 cm flux for cycle 22 is presented along with the sunspot number and the GM A index. In this cycle the radio flux distribution matches well that of the sunspot number. Solar X-ray activity declined sharply at this time as seen in the whole-sun GOES plots and in plots of daily, full-disk averaged X-ray flux from Yohkoh. The last X-class X-ray flares occurred in late 1992 and the last Ground-Level Event was recorded at

Earth in November 1992.

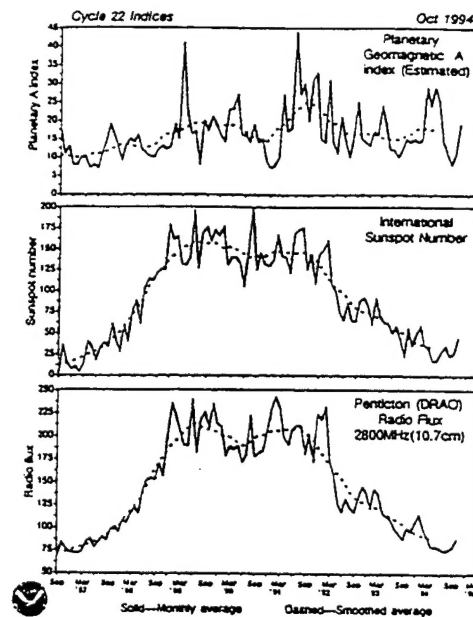


Fig. 6. Averaged plots of GM A index (top), sunspot number and 10.7 cm radio flux for cycle 22. Courtesy NOAA, Space Environment Laboratory.

The top panel in Figure 6 shows the distribution of GM activity in this cycle. Note that there were two sharp peaks in the cycle, the last in June 1991. Following the last peak the envelope of A declined slowly, then flattened out. Although we are still in the declining phase of cycle 22, we can get some idea when the pattern of recurrence began for this cycle. The annual plots of the Planetary Kp index establish that recurrent activity began possibly as early as the fall of 1993 and continues into the present (late 1994). Note in Figure 6 that 1994 saw a resurgence of GM activity which, along with the developing 27-day Kp pattern, reveals that the recurrent phase of GM activity in cycle 22 is well underway.

An onset of the recurrence pattern in the fall of 1993 is only 7 years after the start of the present cycle. Compared with the previous two cycles this recurrence onset is earlier than might be expected. This is consistent with the rapid rise in sunspot number of cycle 22 to an early onset of maximum, a period of just over 2½ yr, and with a 3.3-yr maximum phase. At least one prediction, based on the radio flux, is that the next minimum of solar activity will occur as early as the fall of 1995 /43/. If so, this would make the length of cycle 22 just over 9 yr, or the shortest cycle in the modern record (defined as since 1818 when the record of sunspot numbers is of good or better quality) /44/. For comparison the only cycle during this period with a length of less than 10 yr was cycle 8, with a length of 9.6 yr starting in 1833. Thus, it is possible that cycle 22 may become one of the shortest cycles on record!

### SUMMARY

The distribution of geomagnetic disturbances over the solar activity cycle statistically exhibits two peaks. It is thought that these represent two components of GM activity that have very different solar and heliospheric sources: one associated with transient solar activity that peaks with the sunspot cycle, and a later peak during the declining phase associated with recurrent high speed streams from coronal holes. It is clear that the first peak is dominated by transient solar activity. However, a new paradigm has developed in which coronal mass ejections and their associated shocks, rather than flares, are considered the key link between solar and GM activity at maximum.

The influence of CMEs appears also to extend into the declining phase. As we have shown, the coronal



streamer belt and its extension as the heliospheric current sheet appears to play a major role in both kinds of geoactivity. For example, streamers are the source of many, if not most CMEs. During the declining phase, the passage of CIRs by the earth are associated with the strongest recurrent GM activity, often because CMEs tend to cluster there. CIRs arise from interactions at the boundaries between streamers (slow wind) and coronal holes (fast wind). The sustained recurrent activity associated with high speed streams from coronal holes causes weaker activity and is due to Alfvén waves in the wind.

We compared and contrasted several aspects of GM disturbances during the declining phases of the last 3 solar activity cycles. The 27-day recurrence patterns of GM indices during the declining phases of cycles 21 and 22 were compared with the pattern seen in Dst during cycle 20 in 1974. The patterns were similar in all 3 cycles, but with important differences. In cycle 21 recurrence set in from mid-1984 to May 1985. Although the available space-based data is less than in cycle 20, it is evident that the 2 cycles differed in that in cycle 21 the IP shocks and associated major storms mainly followed one sector boundary instead of two and were not as pronounced.

In comparison with the previous two cycles, the recurrence pattern of the present cycle 22 started earlier than might be expected, only 7 years after cycle onset. This is in accord with the possibility that cycle 22 may become one of the shortest cycles in the modern record. Several data sets, including the 10.7 cm radio flux, sunspot number, GM activity indices, and a sharp decrease in flaring activity on the sun, indicate that we are definitely into the declining phase and the recurrent pattern of activity in cycle 22. Because of the 22-year solar magnetic cycle, the level of recurrent activity may be stronger in this even-numbered cycle.

I thank E. Cliver of the AF Phillips Lab/GPS and N. Crooker of Boston University for helpful comments on the manuscript. I am grateful to the COSPAR Bureau and to Phillips Lab/GPS (contract AF19628-90-K-0006) for supporting my participation in the COSPAR meeting.

#### REFERENCES

1. Mayaud, P.N., Analysis of storm sudden commencements for the years 1868-1967, J. Geophys. Res., 80, 111 (1975).
2. Legrand, J.P. and P.A. Simon, Geomagnetic storms and their associated forecasts, in Solar-Terrestrial Predictions - IV, ed. by J. Hruska et al., NOAA, Boulder, Vol. 3, 1993, p. 191.
3. Feynman, J. and P.F. Fougere, Eighty-eight year periodicity in solar-terrestrial phenomena confirmed, J. Geophys. Res., 89, 3023 (1984).
4. Svalgaard, L., Geomagnetic activity: dependence on solar wind parameters, in Coronal Holes and High Speed Wind Streams, ed. J. Zirker, Colorado Assoc. Univ. Press, Boulder, 1977, p. 371.
5. Gonzalez, W.D., A.L.C. Gonzalez, and B.T. Tsurutani, Dual-peak solar cycle distribution of intense geomagnetic storms, Planet. Space Sci., 38, 181 (1990).
6. Crooker, N.U., and G.L. Siscoe, The effect of the solar wind on the terrestrial environment, in: Physics of the Sun, ed. P.A. Sturrock et al., D. Reidel, Dordrecht, Holland, 1986, p. 193.
7. Crooker, N.U. and K.I. Gringauz, On the low correlation between long-term averages of solar wind speed and geomagnetic activity after 1976, J. Geophys. Res., 98, 59 (1993).
8. Tsurutani, B.T., W.G. Gonzales, A.L.C. Gonzales, F. Tang, D. Park, M. Okada, and J. Arballo, J. Geophys. Res., submitted (1995).
9. Smith, E.J., J.A. Slavin, R.D. Zwickl, and S.J. Bame, Shocks and sudden storm commencements, in Solar Wind-Magnetospheric Coupling, ed. by Y. Kamide and J.A. Slavin, Terra Scientific Publishing,

Tokyo, p. 345 (1986).

10. Tsurutani, B.T., W.D. Gonzales, F. Tang, S.T. Akasofu, and E.J. Smith, Origin of interplanetary southward magnetic fields responsible for major magnetic storms near solar maximum (1978-1979), J. Geophys. Res., 93, 8519 (1988).

11. Kahler, S.W., Solar flares and coronal mass ejections, Ann. Rev. Astron. Astrophys., 30, 113 (1992).

12. Gosling, J.T., The solar flare myth, J. Geophys. Res., 98, 18,937 (1993).

13. Gosling, J.T. and D.J. McComas, Field line draping about fast coronal mass ejecta: a source of strong out-of-the-ecliptic magnetic fields, Geophys. Res. Lett., 14, 355 (1987).

14. Crooker, N.U., E.W. Cliver, and B.T. Tsurutani, The semiannual variation of great geomagnetic storms and the postshock Russell-McPherron effect preceding coronal mass ejecta, Geophys. Res. Lett., 19, 429 (1992).

15. Gosling, J.T., D.J. McComas, J.L. Phillips, and S.J. Bame, Geomagnetic activity associated with Earth passage of interplanetary shock disturbances and coronal mass ejections, J. Geophys. Res., 96, 7831 (1991).

16. Zhao, X.P., J.T. Hoeksema, J.T. Gosling, and J.L. Phillips, Statistics of IMF Bz events, in Solar-Terrestrial Predictions - IV, ed. by J. Hruska et al., NOAA, Boulder, Vol. 2, 1993, p. 712.

17. Webb, D.F., and R.A. Howard, The solar cycle variation of coronal mass ejections and the solar wind mass flux, J. Geophys. Res., 99, 4201 (1994).

18. Zhao, X. and J.T. Hoeksema, The effect of coronal mass ejections on the structure of the heliospheric current sheet, in Proceedings of the Third SOHO Workshop, ESA, to be published (1995).

19. Hundhausen, A.J., An interplanetary view of coronal holes, in Coronal Holes and High Speed Wind Streams, ed. J. Zirker, Colorado Assoc. Univ. Press, Boulder, 1977, p. 225.

20. Gosling, J.T., S.J. Bame, D.J. McComas, J.L. Phillips, V.J. Pizzo, B.E. Goldstein, and M. Neugebauer, Latitudinal variation of solar wind corotating stream interaction regions: Ulysses, Geophys. Res. Lett., 20, 2789 (1993).

21. Hundhausen, A.J., Sizes and locations of coronal mass ejections: SMM observations from 1980 and 1984-1989, J. Geophys. Res., 98, 13,177 (1993).

22. Mendoza, B. and R. Perez-Enriquez, Association of coronal mass ejections with the heliomagnetic current sheet, J. Geophys. Res., 98, 9365 (1993).

23. Crooker, N.U., G.L. Siscoe, S. Shodan, D.F. Webb, J.T. Gosling, and E.J. Smith, Multiple heliospheric current sheets and coronal streamer belt dynamics, J. Geophys. Res., 98, 9371 (1993).

24. Borrini, G., J.T. Gosling, S.J. Bame, W.C. Feldman, and J.M. Wilcox, Solar wind helium and hydrogen structure near the heliospheric current sheet: a signal of coronal streamers at 1 AU, J. Geophys. Res., 86, 4564 (1981).

25. Neugebauer, M., D.R. Clay, and J.T. Gosling, The origins of planar magnetic structures in the solar wind, J. Geophys. Res., 98, 9383 (1993).

26. Ivanov, K.G., A.F. Harshiladze, and E.P. Romashets, Solar flares, magnetic clouds, and

- geomagnetic storms, Solar Phys., 143, 365 (1993).
27. Maunder, E.W., Magnetic disturbances, 1882 to 1903, as recorded at the Royal Observatory, Greenwich, and their association with sun-spots, M.N.R.A.S., 65, 2 (1905).
28. Hapgood, M.A., A double solar cycle in the 27-day recurrence of geomagnetic activity, Ann. Geophys., 11, 248 (1993).
29. Chernosky, E.J., Double sunspot-cycle variation in terrestrial magnetic activity, 1884-1963, J. Geophys. Res., 71, 965 (1966).
30. Russell, C.T. and R.L. McPherron, Semiannual variation of geomagnetic activity, J. Geophys. Res., 78, 92 (1973).
31. Gosling, J.T., J.R. Asbridge, and S.J. Bame, An unusual aspect of solar wind speed variations during solar cycle 20, J. Geophys. Res., 82, 3311 (1977).
32. Crooker, N.U., J. Feynman, and J.T. Gosling, On the high correlation between long-term averages of solar wind speed and geomagnetic activity, J. Geophys. Res., 82, 1933 (1977).
33. Slavin, J.A., G. Jungman, and E.J. Smith, The interplanetary magnetic field during solar cycle 21: ISEE-3/ICE observations, Geophys. Res. Lett., 13, 513 (1986).
34. Hapgood, M.A., M. Lockwood, G.A. Bowe, D.M. Willis, and Y.K. Tulunay, Variability of the interplanetary medium at 1 a.u. over 24 years: 1963-1986, Planet. Space Sci., 39, 411 (1991).
35. Joselyn, J.A., Geomagnetic activity forecasting: the state of the art, Rev. Geophys., in press (1995).
36. Crooker, N.U., and E.W. Cliver, Postmodern view of M-regions, J. Geophys. Res., 99, 23,383 (1994).
37. Wilcox, J.M. and N.F. Ness, Quasi-stationary corotating structure in the interplanetary medium, J. Geophys. Res., 70, 5793 (1965).
38. Dessler, A.J. and J.A. Feyer, Interpretation of Kp index and M-region geomagnetic storms, Planet. Space Sci., 11, 505 (1963).
39. Schwenn, R., Large-scale structure of the interplanetary medium, in Physics of the Inner Heliosphere, ed. R. Schwenn and E. Marsch, Springer-Verlag, New York, Vol. 1, 1990, p. 99.
40. Sheeley, N.R., Jr., J.R. Asbridge, S.J. Bames, and J.W. Harvey, A pictorial comparison of interplanetary magnetic field polarity, solar wind speed, and geomagnetic disturbance index during the sunspot cycle, Solar Phys., 52, 485 (1977).
41. Sheeley, N.R., Jr., and J.W. Harvey, Coronal holes, solar wind streams, and geomagnetic disturbances during 1978 and 1979, Solar Phys., 70, 237 (1981).
42. Sheeley, N.R., Jr., private communication (1994).
43. McIntosh, P.S., private communication (1994).
44. McKinnon, J.A., Sunspot numbers: 1610-1985, Report UAG-95, World data Center A, U.S. Dept. of Commerce, NOAA, Boulder (1987).